ANALYSES OF FLOOD EVENTS USING REGIONAL HYDROMETEOROLOGICAL MODELING SYSTEM

A THESIS SUBMITTED TO

THE GRADUATE SCHOOL OF NATURAL AND APPLIED SCIENCES

OF

MIDDLE EAST TECHNICAL UNIVERSITY

BY

ALPER ÖNEN

IN PARTIAL FULFILLMENT OF THE REQUIREMENTS

FOR

THE DEGREE OF MASTER OF SCIENCE

IN

CIVIL ENGINEERING

JANUARY 2013

Approval of the thesis:

ANALYSES OF FLOOD EVENTS USING REGIONAL HYDROMETEOROLOGICAL MODELING SYSTEM submitted by **ALPER ÖNEN** in partial fulfillment of the requirements for the degree of **Master of Science in Civil Engineering Department, Middle East Technical University** by,

Prof. Dr. Canan Özgen
Dean, Graduate School of **Natural and Applied Sciences** _____

Prof. Dr. Ahmet Cevdet Yalçıner
Head of Department, **Dept. of Civil Engineering** _____

Assoc. Prof. Dr. Ismail Yücel
Supervisor, **Dept. of Civil Engineering, METU** _____

Examining Committee Members:

Assoc. Prof. Dr. Zuhal Akyürek
Civil Engineering Dept., METU _____

Assoc. Prof. Dr. İsmail Yücel
Civil Engineering Dept., METU _____

Assoc. Prof. Dr. Elçin Kentel
Civil Engineering Dept., METU _____

Asst. Prof. Dr. Koray K. Yılmaz
Geological Engineering Dept., METU _____

Dr. Fatih Keskin
Civil Engineer PhD., Palme Mühendislik _____

Date: **22.01.2013**

I hereby declare that all information in this document has been obtained and presented in accordance with academic rules and ethical conduct. I also declare that, as required by these rules and ethical conduct, I have fully cited and referenced all material and results that are not original to this work.

Name, Last name: Alper Önen

Signature:

ABSTRACT

ANALYSES OF FLOOD EVENTS USING REGIONAL HYDROMETEOROLOGICAL MODELING SYSTEM

Önen, Alper

M.Sc., Department of Civil Engineering

Supervisor: Assoc. Prof. Dr. İsmail Yücel

January 2013, 134 pages

Extreme rainfall events and consequent floods are being observed more frequently in the Western Black Sea region in Turkey as climate changes. In this study, application of a flood early warning system is intended by using and calibrating a combined model system. A regional-scale hydro-meteorological model system, consisting of Weather Research and Forecasting (WRF) model, NOAH land surface model and fully distributed NOAH-Hydro hydrologic models, is used for simulations of 25 heavy-rainfall and major flooding events observed in the Western Black Sea region between years 2000 and 2011. The performance of WRF model system in simulating precipitation is tested with 3-dimensional variational (3DVAR) data assimilation scheme. WRF-derived precipitation with and without data assimilation and Multi Precipitation Estimates (MPE) are used in NOAH-Hydro model to simulate streamflow for flood events. Statistical precipitation analyses show that WRF model with 3DVAR improved precipitation up to 12% with respect to no-assimilation. MPE algorithm generally underestimates rainfall and it also showed lower performance than WRF model with and without data assimilation. Depending on reliability of precipitation inputs, NOAH-Hydro model produces reasonable flood hydrographs both in structure and volume. After model calibration is performed using assimilated precipitation inputs in Bartın Basin, NOAH-Hydro model reduced the average error in streamflow by 23.24% and 53.57% with calibration for testing events. With calibrated parameters, NOAH-Hydro model forced by WRF non-assimilated precipitation input also reduced the error in streamflow but with lower rates (16.67% and 40.72%). With a proper model calibration and reliable precipitation inputs, hydrologic modeling system is capable of simulating flood events.

Keywords: precipitation, streamflow, hydrology, flood, model

ÖZ

BÖLGESEL NİTELİKLİ HİDROMETEOROLOJİK MODEL SİSTEMİ KULLANIMI İLE TAŞKIN OLAYLARININ ANALİZLERİ

Önen, Alper

Yüksek Lisans, İnşaat Mühendisliği Bölümü

Tez Yöneticisi: Doç. Dr. İsmail Yücel

Ocak 2013, 134 sayfa

Şiddetli yağış ve buna bağlı olarak oluşan sel olayları, iklimsel değişiklikler nedeniyle Batı Karadeniz bölgesinde daha sık görülmeye başlanmıştır. Bu çalışmada, birleşik bir model sistemi kullanarak ve kalibre ederek, sel erken uyarı sistemi geliştirilmesi amaçlanmıştır. Hava Araştırma ve Tahmin (WRF) modeli, NOAH yer yüzey modeli ve tam dağılımlı NOAH-Hidro hidrolojik modellerinden oluşan bölgesel ölçekli bir hidro-meteorolojik model sistemi, 2000-2011 yılları arasında Batı Karadeniz bölgesinde gözlemlenen 25 olayı simule etmek için kullanılmıştır. Yağış simülasyonlarının yapıldığı WRF modeli 3 boyutlu değişkenli (3DVAR) asimilasyonu tekniği ile de test edilmiştir. WRF modelinden elde edilen asimilasyonlu ve asimilasyonsuz yağış verileri ile uydu tahmin yağışları (MPE), sel olayları sırasındaki nehir akışlarını simule etmek için NOAH-Hidro modelinde kullanılmıştır. İstatistiksel yağış analizleri sonucunda WRF modelinin asimilasyonlu yağışlarda asimilasyonsuzlara göre %12'ye kadar iyileşme gösterdiği görülmüştür. MPE algoritması genel olarak gözlem yağışlarından düşük tahminde bulunurken, asimilasyonlu ve asimilasyonsuz WRF modeline göre istatistiksel olarak düşük performans göstermiştir. Yağış girdilerinin güvenirliliği de göz önüne alındığında, NOAH-Hydro modelinin yapısal ve hacimsel olarak kabul edilebilir hidrograflar yarattığı gözlemlenmiştir. Asimilasyonlu yağışlar kullanılarak Bartın havzası için yapılan model kalibrasyonu sonucu, NOAH-Hidro modelinin deneme olayları için hata payını ortalama %23.24 ve %53.57 oranında azalttığı belirlenmiştir. Yapılan kalibrasyonun asimilasyonsuz yağışlardan oluşan hidrograflara uygulanması sonucu hata payı, asimilasyonluya göre daha az olmasına rağmen, kalibrasyonun burada da iyileştirme gerçekleştirdiği belirlenmiştir (%16.67 ve %40.72). Kapsamlı bir model kalibrasyonu ve güvenilir yağış girdileriyle bu hidrolojik model sisteminin, sel olaylarını başarılı bir şekilde elde edebileceği görülmektedir.

Anahtar kelimeler: yağış, nehir akımı, hidroloji, sel, model

To my family & friends

ACKNOWLEDGMENTS

First of all, I would like to thank my supervisor Assoc. Prof. Dr. İsmail Yücel for his guidance, advice, encouragement and patience with gratitude. I would also like to thank Asst. Prof. Dr. Koray K. Yılmaz for his guidance and assistance throughout the study.

I would like to thank my colleagues and sincere friends, Meriç Selamoğlu, Tuğçe Yıldırım, Ezgi Köker, Melih Çalamak and Cem Sonat for their never ending support and encouragement. I would also like to thank all professors and staff in Water Resources Laboratory for their continuous encouragement and goodwill.

I would like to show my gratitude to my close long-time friends who never actually believed I was achieving something for the last 3 years, Özgür Soysal Özdemir, Alper Korhan Atlıhan, Cansu Albayrak, Elif Ataol, İlhan Altuğ Aksoy and Remzi Çöl for their support. I would also like to thank my musician friends, Ayberk Garagon, Barış Yaman, Cansu Turgut and Kıvanç Tatar for the sincerity and friendship.

Lastly, I would like to show my deepest gratitude to my family. For their endless support and encouragement in any means, I would like to thank my parents, Yüksel and Ayhan Önen, my brother, Onursal Önen and beloved grandmother Nermin Şenerler for everything.

This research is supported by TÜBİTAK ARDEB ÇAYDAG Scientific and Technological Research Project Program (1001) (Project No: # 110Y036).

TABLE OF CONTENTS

LIST OF TABLES

LIST OF FIGURES

LIST OF SYMBOLS

$\partial h/\partial x$	:	Change in depth of the water surface above the land surface in the x-direction
A	:	Cross-sectional area
B, y^b	:	3DVAR Assimilation Scheme Setup Background Errors
biasp	:	Bias Percentage
Bw	:	Average Channel Base Width
C	:	Soil heat capacity
Ch SSlp	:	Channel Slope
C_m	:	Dimensional constant (1.0 for SI units)
CSI	:	Critical Success Index
D	:	Soil difusivity
ETS	:	Equitable Threat Score
FAR	:	False Alarm Rate
F_θ	:	Sources (e.g. infltration) and Sinks (e.g. evaporation)
g	:	Acceleration due to gravity
h	:	Surface head
HLINK	:	Channel Inıtial Water Depth
K	:	Soil hydraulic conductivity
K_t	:	Soil heat conductivity
MANN	:	NOAH-Hydro model Channel Rougness Factor
MannN	:	Channel Manning Coefficient
n	:	Manning's roughness coefficient
nash-sutcliffe	:	Nash- Sutcliffe Efficiency Index
n_{ov}	:	Roughness coefficient of the land surface
nrmse mean	:	Mean-normalized Root Mean Square Error
nrmse stdev	:	Standart Deviation-Normalized Root Mean Square Error
OVROUGHRT	:	NOAH-Hydro model Surface Roughness Factor
P	:	Wetted perimeter
POD	:	Probability of Detection
Q	:	Flow rate
$q_{i,j}$	:	Flow rate from grid cell i,j
q_{lat}	:	Lateral flow rate
Q_m	:	Modeled discharge
Q_o	:	Observed discharge

Q_o^t	:	Observed discharge at time t
R	:	Hydraulic radius (A/P)
R, RR	:	Correlation Coefficient
REFKDT	:	NOAH-Hydro model Infiltration Factor
RETDEPRT	:	NOAH-Hydro model Retention Depth Factor
RMSE	:	Root Mean Square Error
S_f	:	Friction slope
S_{fx}	:	Friction slope in the x-direction
S_{ox}	:	Terrain slope in the x-direction
St Order	:	Stream Order
T	:	Soil temperature
t	:	Time
$T_{i,j}$	:	Transmissivity of grid cell i,j
x	:	Streamwise coordinate
x^b	:	3DVAR Assimilation Scheme Setup Background
y^o	:	3DVAR Assimilation Scheme Setup Observations
z	:	Vertical coordinate
Z	:	Water surface elevation
α	:	$S_{fx}^{0.5} / n_{ov}$
β	:	Momentum correction coefficient
$\beta_{i,j}$	:	Water table slope
θ	:	Soil moisture
$\omega_{i,j}$	:	Width of the grid cell
3DVAR	:	3 Dimensional Variational
AGİ	:	Stream Gauge Station (Akım Gözlem İstasyonu)
AS	:	Assimilation
AWOS	:	Automated Weather Observing System
CAL. AS	:	WRF AS induced calibrated NOAH-Hydro model stream output
CAL. MPE	:	MPE induced calibrated NOAH-Hydro model stream output
CAL. NOAS	:	WRF NOAS induced calibrated NOAH-Hydro model stream output
DSİ	:	State Water Works (Devlet Su İşleri)
ECMWF	:	European Centre for Medium-Range Weather Forecasts
EİEİ	:	Electrical Study and Administration works (Elektrik Etüd İdare İşleri)
EUMETSAT	:	European Organisation for the Exploitation of Meteorological Satellites
IR/VIS	:	Infra-Red / Visible
LSM	:	Land Surface Model

MGM	:	General Directorate of Meteorological Works (Meteoroloji Genel Müdürlüğü)
MPE	:	Multi Precipitaiton Estimates
NetCDF	:	Network Common Data Form
NOAH AS	:	WRF AS induced NOAH-Hydro model stream output
NOAH NOAS	:	WRF NOAS induced NOAH-Hydro model stream output
NOAS	:	No-Assimilation
NWP	:	Numerical Weather Prediction
OBS	:	Observation (Precipitation and Stream Data)
USGS	:	United States Geological Survey
WRF	:	Weather Research and Forecasting
WRF AS	:	3DVAR Assimilation appiled WRF Precipitation Data
WRF NOAS	:	No Assimilation appiled WRF Precipitation Data

CHAPTER 1

INTRODUCTION

1.1 Introduction

Influences of global warming and climate change have been getting more dominant with more catastrophic events observed around the world. With global warming, major changes in rain and water cycles are being observed and frequency of meteorological disasters such as heavy rainfalls is increasing continuously. With warming climate, drought and flood risks are getting higher consequently. With climate models developed by Trenberth (1998, 1999), Allen and Ingram (2002), Neelin et al. (2006), and Held and Soden (2006) and local observation analyses, it is shown that, by climate warming, while water vapor input to atmosphere increases, total annual precipitation does not show discernible increases. In the last 50 years, when precipitation amounts on land is investigated, it is observed that even in regions showing lower annual mean precipitation, the percentage of extreme precipitation against total precipitation has increased (Trenberth et al., 2007). Corresponding to these facts, with increased extreme precipitation frequencies, flooding risks have also increased.

As occurring and evidencing on several geographical regions on the earth, these types of extreme events are also being observed throughout regions more prone to flooding in Turkey. In semiarid environments like Turkey, many small and medium steep streams are ephemeral, which can cause unexpected and extensive flood damage (Amengual et al., 2006). As an example, on 7-12 September 2009 in Marmara region, extreme precipitation and flooding has caused a death toll of 21 and economic damage around few million TL's. On regions having complex topography like Turkey, extreme events show significant temporal and spatial variations and generate extensive amounts of precipitation in short durations. Also based on basin morphologic properties, such events generate flash floods and excess surface runoff. Flash floods, by overloading the river capacity, causes inundation on low elevation basins and settlement regions and consequently increases risk of life and economic losses.

For this research, use of a numerical weather prediction (NWP) model is intended to establish a possible forecasting system. Currently, although such regional climate models can run at grid resolutions as high as a few kilometers to hundreds of meters, they are used mainly for research on short-term weather and hydrologic predictions (Roebber et al., 2004; Faccani et al., 2003). For mountainous and semi-arid hydro-climatologic regime dominant regions like Turkey, uncertainties in precipitation compared to uncertainties related to model parameters and theoretical concepts may become more important and significant. In NWP model, by using data assimilation, it is aimed to have improvements in short-term weather predictions particularly in precipitation. By forming initial analysis fields of NWP model via three dimensional variational data assimilation system (3DVAR) it is intended to increase accuracy and decrease the bias between actual observations and model predictions. With

data assimilation method, more accurate precipitation data are generated and they are used in hydrological model for extreme flooding event simulations. This study focuses on documenting performance of Weather Research and Forecasting (WRF) model with use of 3DVAR scheme on heavy rainfall events occurred in the West Black Sea region of Turkey. Similar studies that involve using WRF modeling system with 3DVAR have been applied in different parts of the world (Choi et al., 2011; Xiao et al., 2005).

Satellite-derived precipitation estimates also show remarkable potential in hydrological applications. This type of precipitation data such as from Multi Precipitation Estimates (MPE) covers large extent of area in high spatial (4-km) and temporal (15 minutes) resolutions. By providing continuous monitoring in precipitation, satellite-derived rainfall estimates become critical in data sparse regions and in operational applications for flash flood warning. Satellite data, especially with operational purpose, is being used occasionally in forecasting heavy precipitation events of convective systems. To establish more consistency in hydrological processes, in addition to precipitation products obtained from NWP with and without data assimilation, high resolution satellite-derived precipitation data are also used in hydrological model for flood simulations. By assessing the accuracy of these precipitation products against observations the performance of these products in producing flood hydrographs is tested.

In this thesis, Weather Research and Forecasting (WRF) model as a NWP, coupled with a land surface model is used with and without data assimilation to produce precipitation and surface hydrometeorological variables for a number of rainfall/flood events observed in partially mountainous Western Black Sea region in Turkey. Precipitation produced by this regional modeling system and MPE are inputted to the fully distributed and physically based hydrological model, NOAH-Hydro model, to generate flood hydrographs. With the implementation of combined system of atmosphere, land surface and hydrological processes in a regional scale, possible flooding events induced by extreme weather events are investigated.

1.2 The Scope of the Study

Hydrological forecasts have significant importance for decision-makers in taking preventive measures against extreme flooding events. Traditional flood forecasting systems based on rain gauge readings are insufficient for preparing necessary precautions against potential losses. Prediction of reliable runoff forecasts is very critical and important in heavy precipitation events. For this prediction, use of NWP models, is vital. By using forecasted heavy precipitation values through NWPs in a hydrological model, flood discharge values are being produced in advance. Showing atmospheric events, surface runoff of corresponding events and hydrologic processes on surface in a dynamic combined structure is possible with a regional hydro-meteorological model with atmosphere, land and hydrology components. From such a modeling system to make reliable hydrologic forecast, accurately described spatial and temporal precipitation data from the atmospheric component (NWP) of the regional system is required. In regional NWP models, data assimilation and use of high resolution land surface model are vital to increase the performance of precipitation forecast.

1.3 Description of Thesis

This thesis study consists of 5 chapters;

As introduction of this research, general information and aim of the study are presented in chapter 1.

Research methodology and details about data assimilation and hydrological model are given in chapter 2. In this chapter, different precipitation datasets used in research are also explained extensively.

In chapter 3, comparative statistical analyses of corresponding datasets are investigated.

In chapter 4, model calibration process, and evaluation results of calibration are presented.

Finally, in chapter 5, final results and conclusion are given.

CHAPTER 2

METHODOLOGY

2.1 General Information

In this chapter, data and processes used in this thesis are discussed in detail. On Section 2.2, selection of simulation events and corresponding rain and stream gauge stations representing selected extreme events are explained. On Section 2.3, regional hydrometeorological modeling system with its components (WRF-NOAH LSM) is presented. On Section 2.4, theory and processes of NOAH-Hydro model is described. On Section 2.5, data assimilation concept and processes with WRF model are introduced. Finally, on Section 2.6, information about satellite (MPE) precipitation is given.

As an overview of methodology used in this research, a flowchart is shown in Figure 2.1. Firstly initial and boundary layer conditions (project domain information) are inputted to the WRF and NOAH LSM explained in Section 2.3. In this process, 3DVAR data assimilation described in Section 2.5 is also introduced to WRF system to generate assimilated precipitation (WRF AS). Also non-assimilated precipitation (WRF NOAS) is also generated from WRF - NOAH LSM coupled model. By using the precipitation obtained in these steps, NOAH-Hydro model, explained in Section 2.4, is run to simulate streamflow with atmospheric, hydrologic and geographic inputs. With observations presented in Section 2.2 and MPE presented in Section 2.6, statistical analyses are performed both for precipitation and streamflow for selected events. MPE precipitation is also inputted in NOAH-Hydro model for streamflow simulations.

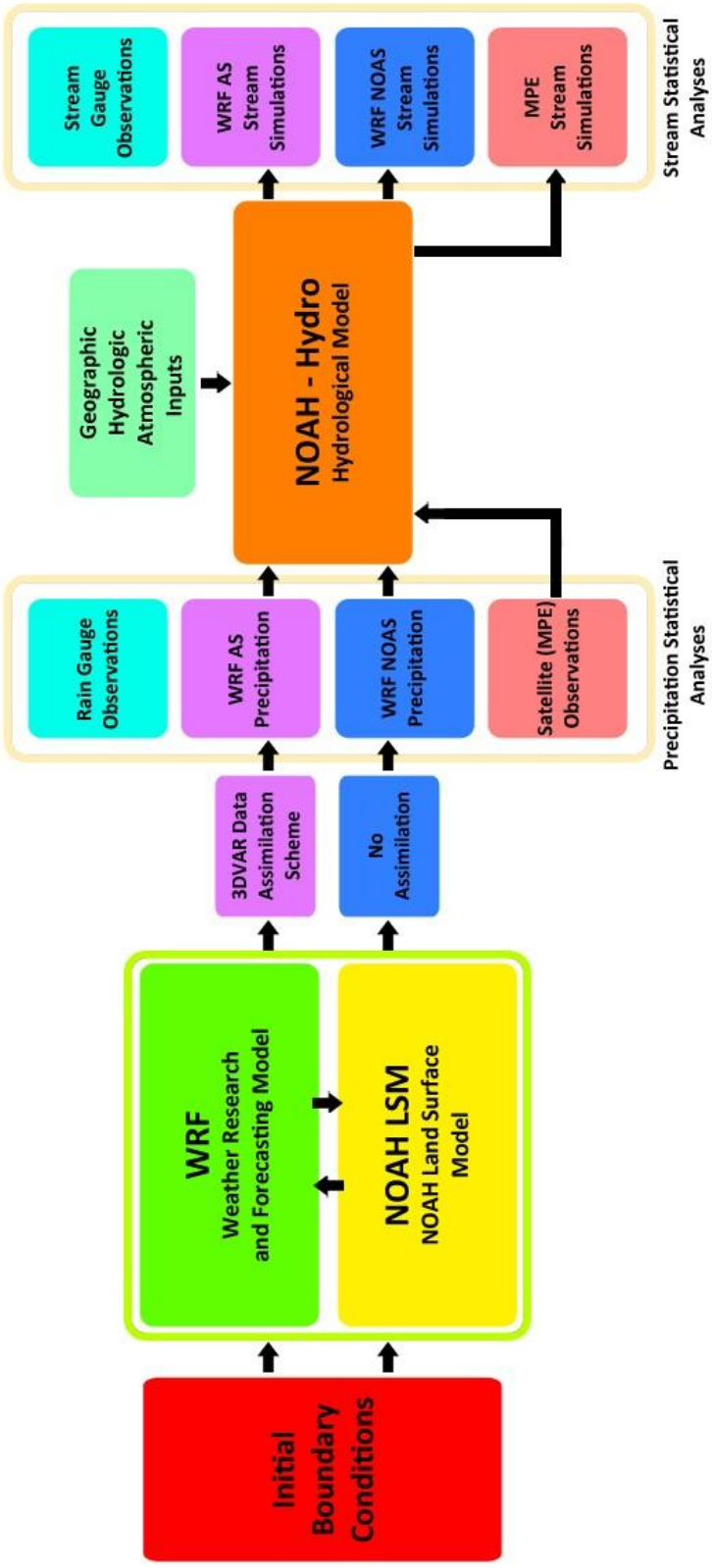

Figure 2.1: Methodology Overview

2.2 Hydrometeorological Events, Rain and Stream Gauge Stations Selection

When inspecting the long range of past records related to extreme meteorological events occurred throughout Turkey, more heavy rainfall and flood events are observed in Western Black Sea region with respect to rest of Turkey. Moreover, since Western Black Sea region has regular stream flow measurements and sub-basins of un-diverted rivers it is selected as study area of this thesis. As Extreme Events Information throughout Turkey obtained from General Directorate of Meteorology (MGM) is examined, 25 “heavy rain and flooding” tagged hydro meteorological events occurred in Western Black Sea region between years 2000 and 2011 are selected for this study and they are shown in Table 2.1 with their event locations. In this study, events shown in Table 2.1 are evaluated between beginning and end dates of the event according to observed hydrograph trends. In MGM extreme event information, for years 2001, 2003 and 2006, no heavy precipitation and flooding events are observed.

Table 2.1: Selected events, their periods and peak observation regions (MGM)

Event No.	Start Date	End Date	Peak Observation Regions
1	02-06-00	07-06-00	Bartın
2	04-08-02	12-08-02	Kastamonu, Devrekani
3	16-08-02	23-08-02	Kastamonu, Devrekani
4	11-08-04	16-08-04	Zonguldak, Ereğli
5	14-08-04	19-08-04	Bartın, Kastamonu
6	23-08-04	28-08-04	Bartın
7	28-04-05	05-05-05	Bartın, Bolu, Düzce, Amasra
8	02-07-05	09-07-05	Bartın
9	13-07-05	18-07-05	Bartın, Zonguldak
10	05-06-07	15-06-07	Kastamonu, Cide, Zonguldak, Devrek
11	30-07-07	04-08-07	Zonguldak
12	20-09-07	25-09-07	Zonguldak, Akçakoca
13	27-09-08	02-10-08	İnebolu, Bozkurt, Daray, Devrekani
14	12-07-09	17-07-09	Bartın, Kastamonu, Devrekani
15	26-07-09	29-07-09	Cide, İnebolu
16	06-09-09	12-09-09	Sakarya, Bolu
17	19-09-09	25-09-09	Bartın
18	25-06-10	02-07-10	Bartın, Bolu, Devrekani
19	06-07-10	11-07-10	Çankırı, Bolu, Ilgaz
20	31-08-10	04-09-10	Bartın
21	13-09-10	16-09-10	Bartın
22	01-10-10	04-10-10	Bozkurt
23	07-10-10	12-10-10	Bartın, Bozkurt
24	25-05-11	05-06-11	Devrekani, Tosya, Yenice
25	09-06-11	14-06-11	Bartın, Ereğli, Devrek

For each of the 25 events shown in Table 2.1, hourly rain gauge values are obtained from MGM. With 34 rain gauge stations distributed within Western Black Sea region, the comprehensive statistical analyses are performed. Automated Weather Observation Station (AWOS) and pluviographs used in these 34 stations are shown in Table 2.2 with station name, type and geographical coordinates. Also for hydrologic model evaluation and calibration, daily stream flow measurements are obtained from State Water Works (DSİ) and Electrical Study and Administration works (EİEİ). While selecting the stations, since parameter calibration process is generated on basin basis, major basins with respect to their

station counts to have enough hydrograph evaluation results are selected. For the research, 4 major basins are selected and numbered with respect to their sizes of area; 1- Filyos, 2-Devrekani, 3-Düzce and 4-Bartın. For these basins, 21 stream gauge stations are available. However, available measurements are limited and not sufficient enough to represent each selected event. In some events while many stations have data, in some other events, record amount is limited to one station or even none. Especially for 2010, no available stream flow data is obtained. In Table 2.3, available stream flow gauge stations are shown with their names, coordinates and corresponding basins. In Table 2.4, obtained periods for each station per event are shown. Recorded gauge readings represent daily average discharges.

Table 2.2: Rain Gauge Stations, type and cordinates

Station No. and Name	Station Type	Latitude (°)	Longitude (°)
17015 - Akcakoca	Pluviograph / AWOS	41.083	31.167
17020 - Bartin	Pluviograph / AWOS	41.633	32.333
17022 - Zonguldak	Pluviograph	41.450	31.800
17024 - Inebolu	Pluviograph	41.983	33.783
17026 - Sinop	Pluviograph	42.033	35.167
17066 - Kocaeli	Pluviograph	40.767	29.933
17069 - Sakarya	Pluviograph	40.683	30.417
17070 - Bolu	Pluviograph / AWOS	40.733	31.600
17072 - Duzce	Pluviograph / AWOS	40.833	31.167
17074 - Kastamonu	Pluviograph / AWOS	41.367	33.783
17080 - Cankiri	Pluviograph	40.617	33.617
17602 - Amasra	Pluviograph	41.750	32.383
17604 - Cide	Pluviograph	41.883	33.000
17606 - Bozkurt	Pluviograph	41.950	34.017
17618 - Devrekani	Pluviograph / AWOS	41.583	33.833
17646 - Cerkes	Pluviograph	40.817	32.900
17648 - Ilgaz	Pluviograph / AWOS	40.917	33.633
17650 - Tosya	Pluviograph / AWOS	41.017	34.033
17662 - Geyve	Pluviograph	40.517	30.300
17608 - Acısu-Radar	AWOS	41.181	31.799
17611 - Ereğli	AWOS	41.283	31.417
17613 - Devrek	AWOS	41.217	31.950
17615 - Ulus	AWOS	41.582	32.637
17617 - Yenice	AWOS	41.200	32.333
17620 - Boyabat	AWOS	41.467	34.767
17621 - Çaycuma	AWOS	41.400	32.083
17629 - Araç	AWOS	41.250	33.333
17642 - Gerede	AWOS	40.800	32.200
17693 - Seben	AWOS	40.417	31.583
17694 - Kıbrıscık	AWOS	40.417	31.850
17625 - Catalzeytin	AWOS	41.950	34.217
17637 - Boludağı	AWOS	40.717	31.417
17641 - Eskipazar	AWOS	40.967	32.533
17697 - Göynük	AWOS	40.400	30.783

Table 2.3: Stream gauge stations, coordinates and corresponding basins

Basin Name and No.	Total Station Count per Basin	Station Code	Station Name	Longitude (°)	Latitude (°)
1 - Filyos	10	DSİ 13-44	Bolu Ç. Devrek	31.9500	41.2167
		EİE 1314	Soğanlı Çayı-Karabük	32.6431	41.1697
		EİE 1319	Mengen Çayı-Gökcesu	31.9672	40.8964
		EİE 1327	Ulusu-Afatlar Köp.	32.2508	40.7422
		EİE 1334	Bolu Çayı-Beşdeğirmenler	31.9300	40.8867
		EİE 1335	Filyos Çayı-Derecikviran	32.0792	41.5481
		EİE 1336	Yenice Irmağı-Yenice	32.3239	41.2022
		EİE 1343	Korubaşı Deresi-Arak	32.2547	40.9411
		EİE 1349	Araç Çayı-Karabük	32.6581	41.2147
		EİE 1351	Devrek Çayı-Devrek	31.9567	41.2239
2 - Devrekani	3	DSİ 13-21	Devrekani Ç. Çorbacı	33.9500	41.6167
		DSİ 13-15	Devrekani ç. Cürümören	33.4667	41.5833
		DSİ 13-52	Kocaçay Cide	32.9500	41.8667
		EİE 1307	Devrekani Çayı-Azdavay	33.3011	41.6417
3 - Düzce	4	EİE 1302	Büyükmelen-Yakabaşı	30.9858	40.8561
		EİE 1338	Lahana Deresi-Ortaköy	30.9375	40.9978
		EİE 1339	Aksu Deresi-Çifttekese	30.9206	40.7156
		EİE 1340	Büyükmelen-Beyler	30.9550	40.9825
4 - Bartın	4	DSİ 13-14	Ulus Çayı Bayıryüzü	32.4667	41.5333
		DSİ 13-39	Kocanaz Ç. Boğazköy	32.3667	41.4667
		DSİ 13-49	Arıt Ç. Darıören	32.5167	41.6500

Table 2.4: Matching periods between available stream data and selected events.

		Event 1	Event 2	Event 3	Event 4	Event 5	Event 6	Event 7	Event 8	Event 9	Event 10	Event 11	Event 12	Event 13	Event 14	Event 15	Event 16	Event 17	Event 18	Event 19	Event 20	Event 21	Event 22	Event 23	Event 24	Event 25
DSİ 13-44	Start																									
	End																									
EİE 1314	Start			18.8.02				29.4.05	3.7.05	15.7.05																
	End			26.8.02				8.5.05	12.7.05	20.7.05																
EİE 1319	Start																									
	End																									
EİE 1327	Start																									
	End																									
EİE 1334	Start								4.7.05		6.6.07															
	End								12.7.05		10.6.07															
EİE 1335	Start		3.8.02	21.8.02	9.8.04	16.8.04	23.8.04	29.4.05	4.7.05	14.7.05		1.8.07														
	End		14.8.02	27.8.02	14.8.04	21.8.04	28.8.04	10.5.05	14.7.05	31.7.05		7.7.07														
EİE 1336	Start																									
	End																									
EİE 1343	Start																									
	End																									
EİE 1349	Start																									
	End																									
EİE 1351	Start								3.7.05	15.7.05	6.6.07															
	End								13.7.05	20.7.05	12.6.07															
DSİ 13-21	Start																									
	End																									
DSİ 13-15	Start																								15.4.11	
	End																								3.6.11	
DSİ 13-52	Start			20.8.02																						
	End			27.8.02																						
EİE 1307	Start			19.8.02				29.4.05			6.6.07															
	End			27.8.02				4.5.05			10.6.07															
EİE 1302	Start		7.8.02	19.8.02	9.8.04	15.8.04			3.7.05	15.7.05	6.6.07	1.8.07	21.9.07													
	End		12.8.02	23.8.02	15.8.04	21.8.04			13.7.05	20.7.05	11.6.07	5.8.07	27.9.07													
EİE 1338	Start									14.7.05		1.8.07	21.9.07													
	End									16.7.05		3.8.07	25.9.07													
EİE 1339	Start								3.7.05		6.6.07		19.9.07													
	End								13.7.05		11.6.07		29.9.07													
EİE 1340	Start		7.8.02	19.8.02	10.8.04	15.8.04					6.6.07	1.8.07	21.9.07													
	End		14.8.02	23.8.02	14.8.04	21.8.04					15.6.07	6.8.07	28.9.07													
DSİ 13-14	Start	3.6.00																								
	End	15.6.00																								
DSİ 13-39	Start				10.8.04	16.8.04	23.8.04		4.7.05	14.7.05																
	End				14.8.04	23.8.04	28.8.04		12.7.05	20.7.05																
DSİ 13-49	Start				10.8.04		23.8.04								13.7.09	26.7.09		20.9.09								
	End				14.8.04		28.8.04								17.7.09	29.7.09		24.9.09								

2.3 Hydrometeorological Model System

Within hydro-meteorologic model system, while the atmospheric weather events are simulated via a meso-scale NWP model, WRF (Skamarock et al., 2005), surface water and energy balance are calculated via NOAH land surface model (Chen and Dudhia, 2001). Surface, sub-surface and river routing are performed via NOAH-hydro hydrological model (Gochis et al., 2012). While WRF and NOAH LSM models are being operated in a coupled way, NOAH-Hydro is being operated as an offline model by importing atmospheric inputs and land surface static parameters from WRF-NOAH model.

WRF, a non hydro-static model, consists of cloud microphysics model that calculates hydro-meteorological parameters like rain and snow, convective parameterization, short- and long-wave radiation, boundary layer physics. WRF model has been tested in various atmospheric and hydro-meteorologic conditions on different regions around the world. (Liu et al., 1997; Colle et al., 2000; Brito et al., 2003). With this type of models, some studies such as rain and stream flow simulations in complex mountainous terrains and influence of topography on precipitation have also been performed (Yucel et al., 2002; Yucel et al., 2003; Gochis et al., 2003; Gochis et al., 2006). WRF model is also being used operationally by MGM for research purposes.

Model is setup with 2 nested domains at 12 km and 4 km resolutions, and for this study the inner 4 km domain is fitted to Western Black Sea region. In Figure 2.2, nested configuration with inner and outer domains and focus of the inner domain with positions of rain gauge stations (green nodes) are shown. While initial and boundary conditions of outer domain determined by 25 km resolution European Centre for Medium Range Weather Forecasts (ECMWF) analysis, boundary condition of inner domain is obtained from 12 km WRF outer domain. Each event given on Table 2.1 is simulated by WRF model and relevant physics used in these simulations for WRF model are given on Table 2.5. As convective tendencies are usually observed within 1 km – 4 km resolution scales, WRF inner grid resolution is decided to be 4 km. These selected physics options are generally preferable settings in WRF system. Especially in deciding microphysics and convective parameterizations, experimental simulations are performed before selection. For land surface model, most commonly used model of NOAH with WRF is chosen and this model is integrated with the hydrological model (NOAH-hydro model) being used in this study.

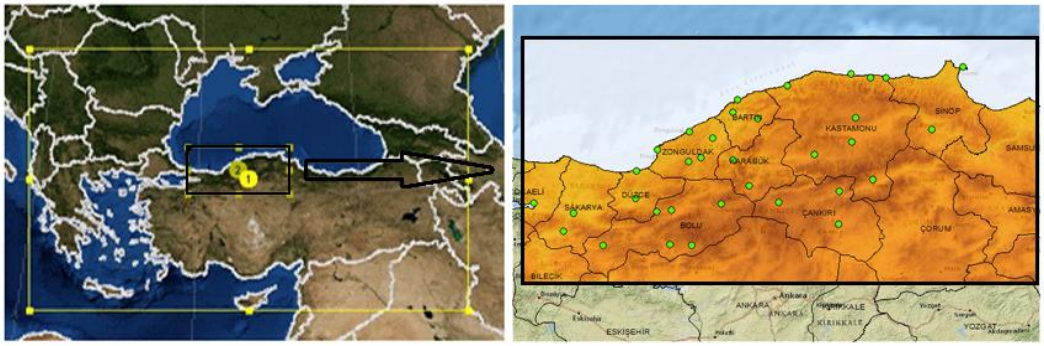

Figure 2.2: Outer and inner grids with detailed inner grid view

Table 2.5: WRF model physics and References

Category	Selected Property	References
Large Scale Precipitation (micro-physics)	Lim and Hong	Lim and Hong (2010)
Convective Cloud	Kain-Fritsch	Kain and Fritsch (1992)
Radiation	Dudhia, RRTM	Dudhia (1989)
Land Surface Layer	NOAH Surface Model	Chen and Dudhia (2001)
Boundary Layer	Yonsei University scheme	Hong et al. (1996)

As the lowest boundary of WRF model, NOAH land surface model calculates the soil – vegetation – atmosphere interactions between surface and atmosphere. In these processes, while moisture and heat fluxes between atmosphere and land-sea surfaces are determined, 1-dimensional surface and sub-surface water balance calculations are also made. To make these calculations, physical based NOAH land-surface model imports precipitation, humidity, surface radiation, temperature, wind speed and pressure values from WRF atmospheric model. Inside the model, multi-layered surface soil structure is represented by 16 different categories of soil types and 1-km grid resolution of land-cover data is represented by 24 class types of U.S. Geological Survey (USGS). In each land cover classification, land type is defined by albedo, surface roughness length, soil moisture, vegetation resistance factor, water vapor deficit parameters. Land cover map obtained from inner WRF domain (4 km) is shown in Figure 2.3. In this map, each 4-km grid classification is defined as dominant classification from 16 1-km resolution sub-grids positioned for every 4-km grid. USGS land cover classifications (Anderson et al., 1976) are given on Table 2.6. In Western Black Sea region, most common classifications are: (2) Dryland Cropland and Pasture, (11) Deciduous Broadleaf Forest, (5) Cropland/Grassland Mosaic and (6, 7, 8) Cropland/Woodland Mosaic, Shrubland and Mixed Shrubland/Grassland classes.

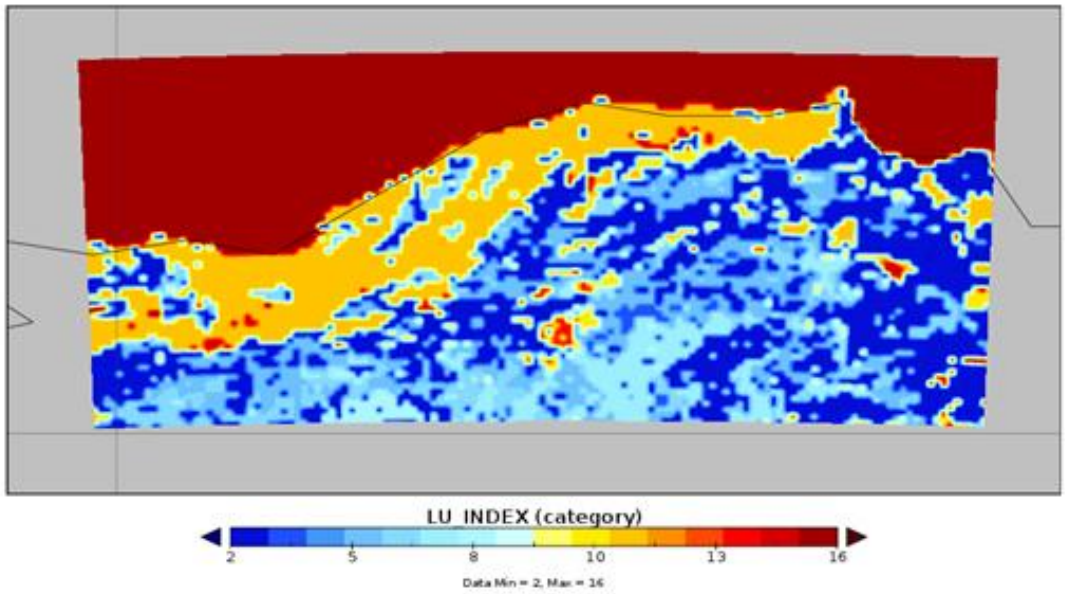

Figure 2.3: Land cover classification on 4-km WRF grid. Class variance between 2-16 are observed.

Table 2.6: USGS land use/land cover classification (Anderson et al., 1976)

Value	Description
1	Urban and Built-Up Land
2	Dryland Cropland and Pasture
3	Irrigated Cropland and Pasture
4	Mixed Dryland/Irrigated Cropland and Pasture
5	Cropland/Grassland Mosaic
6	Cropland/Woodland Mosaic
7	Grassland
8	Shrubland
9	Mixed Shrubland/Grassland
10	Savanna
11	Deciduous Broadleaf Forest
12	Deciduous Needleleaf Forest
13	Evergreen Broadleaf Forest
14	Evergreen Needleleaf Forest
15	Mixed Forest
16	Water Bodies
17	Herbaceous Wetland
18	Wooded Wetland
19	Barren or Sparsely Vegetated
20	Herbaceous Tundra
21	Wooded Tundra
22	Mixed Tundra
23	Bare Ground Tundra
24	Snow or Ice

NOAH model uses 1 vegetation layer on land surface and 8 soil layers in sub-surface. Land surface is represented by 1-km topography data. Topography layer representing Western Black Sea region on 4-km grid resolution is shown in Figure 2.4. Topography shows an altitude range between 0 m – 2065 m for the region and consists of 132 (east – west) x 63 (south – north) grids within study domain.

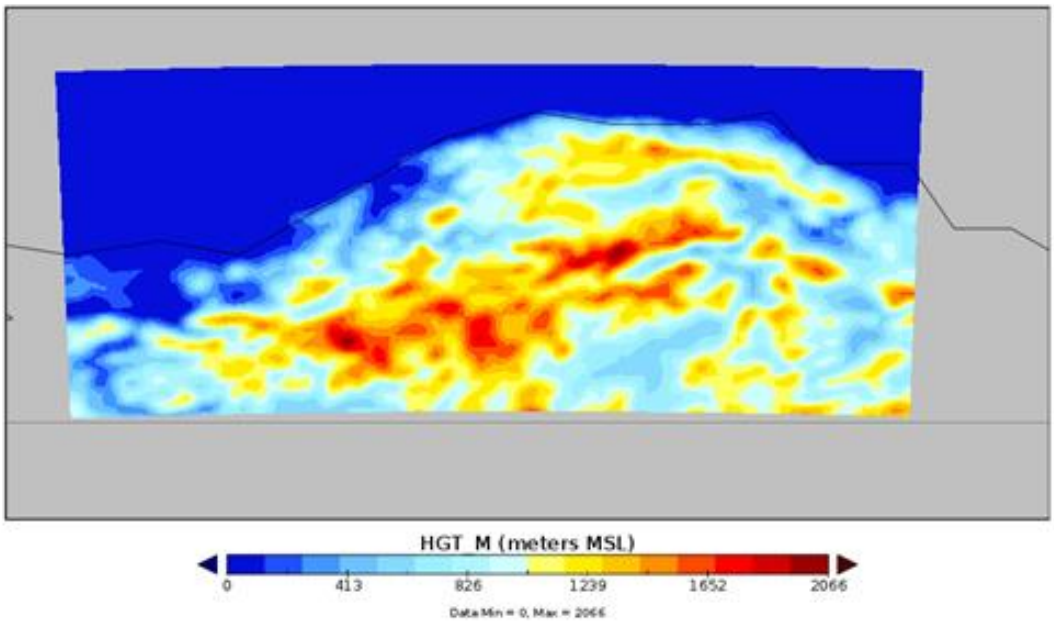

Figure 2.4: Study domain topography on 4-km grid resolution.

2.4 NOAH-Hydro Hydrological Model

Flood simulations are performed with completely physical and fully distributed grid based NOAH-hydro hydrological model by using WRF model outputs. In addition to properties in traditional NOAH model, NOAH-hydro model includes hydrologic processes like horizontal routing on surface and sub-surface flows, channel and reservoir routing, surface accumulation and evaporation. While horizontal runoff could be neglected on coarse scale grids (>10 km), on higher resolutions and topography dominant grids (i.e. <2 km) evaluation of horizontal runoff is essential for water budgets and flood calculations. In each routing step, solution of wave model is being calculated by taking energy losses and surface roughness factor into consideration along grid cells on x and y directions. As a result of these computations, water levels on grid surface and water amount transmitted from land to river channels are determined. Channel routing along the river network defined by grid cells is being simulated by application of St. Venant's equation, which provides solution to conservation of mass and momentum equations, to single direction shallow water wave flows. If there is a reservoir along river, model also applies reservoir routing.

As NOAH-hydro model and NOAH land surface models have same properties for physical and atmospheric inputs, to run NOAH-hydro model, both WRF atmospheric support data (precipitation, temperature, wind, humidity and incoming short, long wave radiation) and geo-static base layers of NOAH land surface model (topography, land cover, soil type) are needed. In addition to these data, hydrologic base layers like high resolution (250 m) topography, flow direction, stream network, stream order, basin boundaries are needed to use in land and channel routing modules. 250-m surface layers are generated by processing topography data in Geographic information system (GIS) environment. Inside the model algorithm, excess precipitation calculated by water and energy balance, soil moisture and hydraulic conductivity are downscaled from 4-km to 250 m resolution by grid disaggregation technique (Gochis et al., 2012) and are used in routing modules to perform surface, sub-surface and channel routing processes. After flow processes are completed, the grids are

aggregating back in larger initial resolution to match processing WRF model. An example grid/subgrid for this process is shown in Figure 2.5.

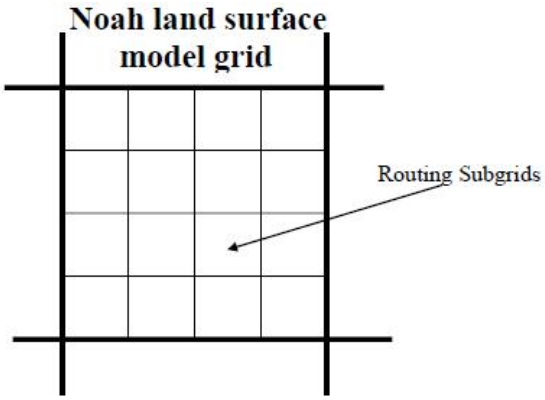

Figure 2.5: Example subgrids for WRF

As a general overview, architecture of NOAH-hydro model with geo-static, hydrologic and atmospheric data components are shown in Figure 2.6.

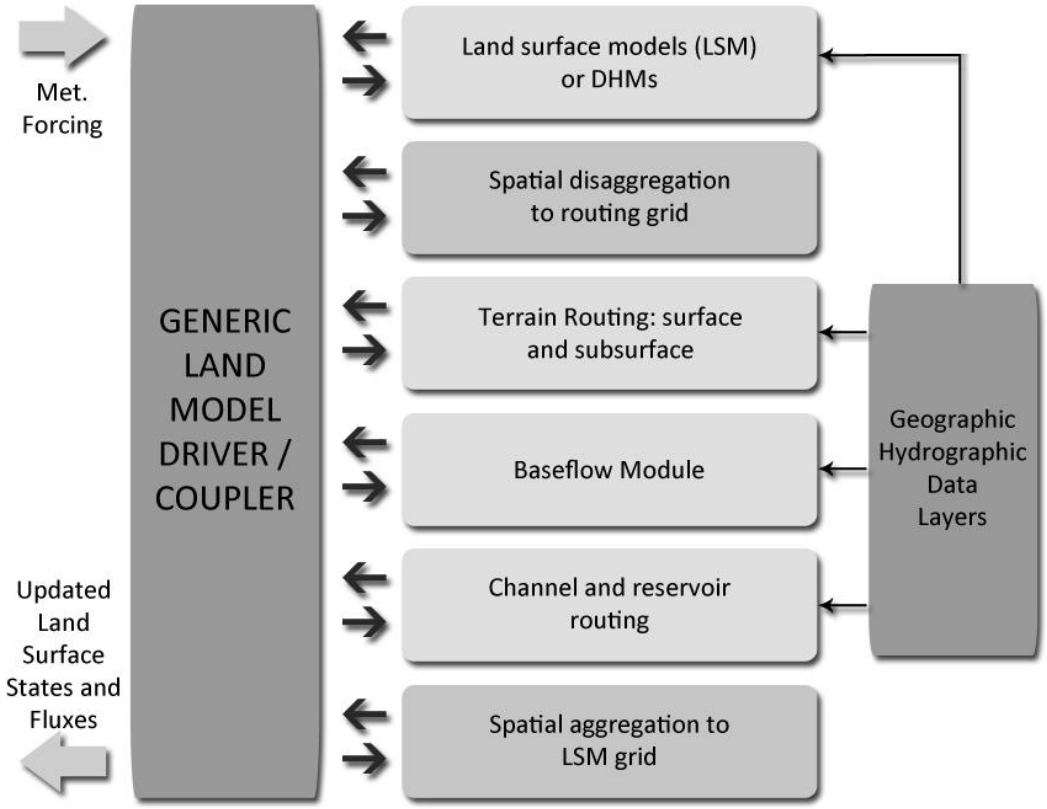

Figure 2.6: Schematic of the NDHMS architecture showing the various model components.

Architecture shown in Figure 2.6 is theoretically explained by Rummler et al., (2012). In NOAH-hydro, the 1-D NOAH LSM calculates the vertical fluxes of energy and moisture. The thermal state of the soil layers is calculated by a prognostic equation which describes the molecular heat flux:

$$C(\theta)\frac{\partial T}{\partial t} = \frac{\partial}{\partial z}\left(K_t(\theta)\frac{\partial T}{\partial z}\right) \tag{2.1}$$

Where:

T soil temperature [K]

C soil heat capacity [$Jm^{-3}K^{-1}$]

K_t soil heat conductivity [$Wm^{-1}K^{-1}$]

C, K_t functions of soil texture and soil moisture

Vertical water movement in the unsaturated zone of the soil column are described by the 1-D form of Richard's equation:

$$\frac{\partial \theta}{\partial t} = \frac{\partial}{\partial z}\left(D\frac{\partial \theta}{\partial z}\right) + \frac{\partial K}{\partial z} + F_\theta \tag{2.2}$$

where:

t time [s]

θ soil moisture [m^3m^{-3}]

z vertical coordinate [m]

D soil difusivity [m^2s^{-1}]

K soil hydraulic conductivity [ms^{-1}]

F_θ represents sources (e.g. infltration) and sinks (e.g. evaporation) [$m^3m^{-3}s^{-1}$]

D,K functions of soil texture and soil moisture

On each land surface model timestep, the column moisture states within the NOAH LSM (e.g. soil moisture, infiltration capacity excess) are disaggregated from the LSM grid to the high-resolution-routing grid using a sub-grid, spatial-weighting method described in Gochis and Chen (2003) and then passed on to the routing routines. The relevant input fields used in the routing modules include maximum soil moisture for each soil type, infiltration capacity excess, lateral saturated hydraulic conductivity for each soil type and the soil moisture content for each soil layer.

Subsurface lateral flow is calculated before the surface routing so that ex-filtration from fully saturated soil columns can be combined with existing infiltration capacity excess prior to surface routing. The method used to calculate the lateral flow of moisture in saturated soil columns is that of Wigmosta et al. (1994) and Wigmosta and Lettenmaier (1999). The quasi-steady-state saturated subsurface flow rate $q_{i,j}$ can be obtained by using the Dupuit-Forchheimer approximation:

$$q_{i,j} = \begin{cases} -T_{i,j} \tan \beta_{i,j} \omega_{i,j} & \beta_{i,j} < 0 \\ 0 & \beta_{i,j} \geq 0 \end{cases} \quad (2.3)$$

where:

$q_{i,j}$ flow rate from grid cell i,j [$m^3 s^{-1}$]
$T_{i,j}$ transmissivity of grid cell i,j [$m^2 s^{-1}$]
$\beta_{i,j}$ water table slope [.]
$\omega_{i,j}$ width of the grid cell [m]

Overland flow is calculated when the depth of ponded water in a grid cell exceeds a specified retention depth which is a tunable parameter on the order of one millimeter or so. Ponded water depths below the retention depth do not move and are subject to future infiltration or direct evaporation. A steepest descent directionality search based on total head gradient (i.e. elevation plus water depth) is used and the fully-unsteady spatially explicit diffusive wave formulation of Julien et al. (1995) with a later modification by Ogden (1997) calculates the propagation of shallow overland flow waves.

In NOAH-hydro the solution to the diffusive-wave simplification of the shallow water wave flow equation is calculated with a form of the Manning's equation (here as an example for the x-direction):

$$q_x = \alpha_x h^{5/3} \quad (2.4)$$

where:

α $S_{fx}^{0.5} / n_{ov}$ [.]
h surface head [m]
n_{ov} roughness coefficient of the land surface [.]

and

$$S_{fx} = S_{ox} - \frac{\partial h}{\partial x} \quad (2.5)$$

where:

S_{fx} friction slope in the x-direction [.]
S_{ox} terrain slope in the x-direction [.]
$\frac{\partial h}{\partial x}$ change in depth of the water surface above the land surface in the x-direction [.]

For channel routing, an explicit algorithm is used simulate in-channel streamflow processes. The routing is executed on a pixel-by-pixel basis along a predefined channel network with trapezoidal geometry. The channel parameters are side slope, bottom width and roughness which are defined a priori as functions of the Strahler stream order and tunable via model calibration. Channel inflow is received from overland flow and is currently limited in one direction and in the version used in this study there is no overbank flow or representation of inundation areas. The channel routing algorithm uses an implicit, one-dimensional, variable time-stepping diffusive wave formulation, which is a simplification of the more general St. Venant equations for shallow water wave flow. The mass and momentum continuity equations are given as:

$$\frac{\partial A}{\partial t} + \frac{\partial Q}{\partial x} = q_{lat} \quad (2.6)$$

$$\frac{\partial Q}{\partial t} + \frac{\partial (\beta Q^2 / A)}{\partial x} + gA \frac{\partial Z}{\partial x} = -gAS_f \quad (2.7)$$

where:

A flow area of the cross section [m^2]

t time [s]

x streamwise coordinate

q_{lat} lateral flow rate [m^3s^{-1}]

Q flow rate [m^3s^{-1}]

β momentum correction coefficient [.]

g acceleration due to gravity [ms^{-2}]

Z water surface elevation [m]

S_f friction slope [.]

The friction slope Sf is computed as:

$$S_f = \left(\frac{Q}{K}\right)^2 \tag{2.8}$$

where K [m^3s^{-1}] is the from the Manning's equation computed conveyance:

$$K = \frac{C_m}{n} A R^{2/3} \tag{2.9}$$

with:

n Manning's roughness coefficient [.]

A cross-sectional area [m^2]

R hydraulic radius (A/P) [m]

P wetted perimeter [m]

C_m dimensional constant (1.0 for SI units)

When ignoring the convective terms in the momentum equation, the result is the diffusive wave approximation of open channel flow Q [m^3s^{-1}]. The momentum equation then simplifies to:

$$Q = -SIGN\left(\frac{\partial Z}{\partial x}\right) K \sqrt{\left|\frac{\partial Z}{\partial x}\right|} \tag{2.10}$$

where the friction slope is substituted and the SIGN function is 1 for $\frac{\partial Z}{\partial x} > 0$ and -1 for $\frac{\partial Z}{\partial x} < 0$.

Finally the numerical solution is calculated by discretizing the continuity equation over a raster cell as:

$$A^{n+1}| - A^n = \frac{\Delta t}{\Delta x}(Q^n_{i+0.5} - Q^n_{i-0.5}) + \Delta t q^n_{lat} \quad (2.11)$$

where $Q^n_{i+0.5}$ is the flux across the cell face between point i and i + 1 and is computed as:

$$Q^n_{i+0.5} = -SIGN(\Delta Z^n_{i+1}) K^n_{i+0.5} \sqrt{\frac{|\Delta Z^n_{i+1}|}{\Delta x}} \quad (2.12)$$

where:

$\Delta Z^n_{i+1} = Z^n_{i+1} - \Delta Z^n_i$

$K^n_{i+0.5} = 0.5[(1 + SIGN(\Delta Z^n_{i+1}))K_i + (1 - SIGN(\Delta Z^{i+1}_n))K_{i+1}]$

4 km WRF inner model domain needs to overlap with the 250 m grid resolution of NOAH-hydro model domain. After grid disaggregation and overlapping, each 4 km x 4 km WRF grid consists of 256 grids of 250 m x 250 m routing grids. For the corresponding time period, as the surface runoff is calculated after routing, these data is re-aggregated into 4-km LSM grid (last component in Figure 2.5). For routing, 250 m grid resolution geographical (topography, longitude, latitude) and hydrologic parameter layers (flow direction, channel grid, stream order, basin mask, forecast points) are generated individually as NetCDF (Network Common Data Form) files and then, concatenated into a single NetCDF file as model input. In Figure 2.7, 250 m grid resolution topography layer is shown and this layer is directly overlapped with the 4-km WRF domain shown previously in Figure 2.4. Other layers; flow direction is shown in Figure 2.8, channel grid in Figure 2.9, stream order in Figure 2.10, basin masks in Figure 2.11, and finally, forecast points layer is shown in Figure 2.12. In Figure 2.12, detailed channel grid and stream gauge stations (forecast points) for selected basins are shown in detail. Points shown on forecast points layer represent the stream gauge stations given in Table 3.2 in the previous section. While channel routing is only available for defined basins and corresponding events, surface routing is being operated for the whole WRF domain.

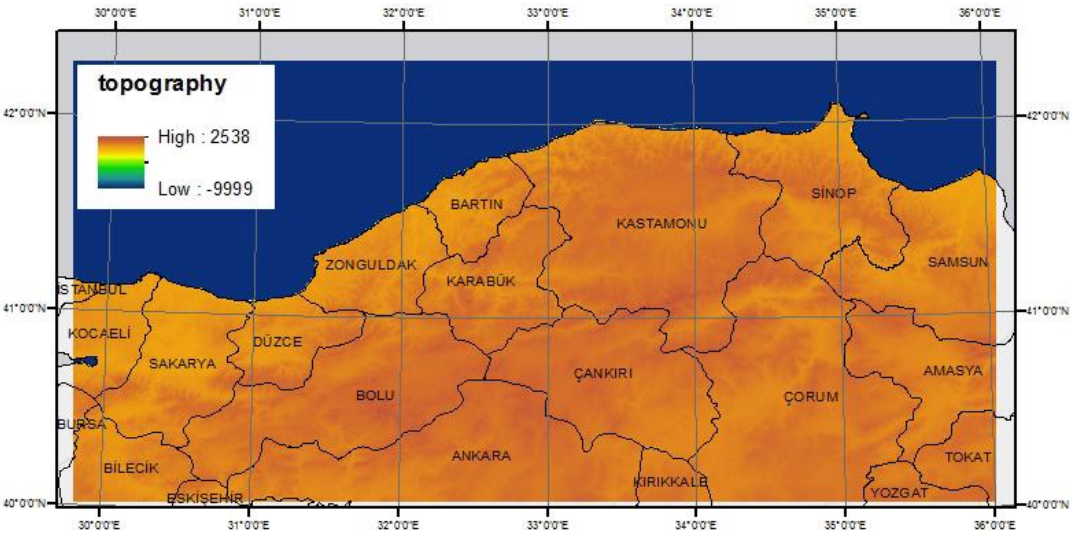

Figure 2.7: NetCDF 250 m Topography Layer

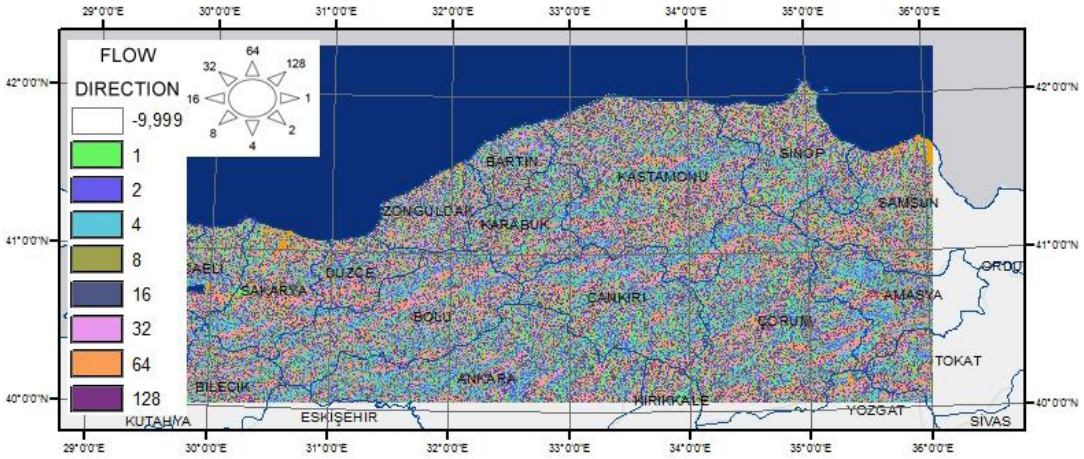

Figure 2.8: NetCDF 250 m Flow Direction Layer

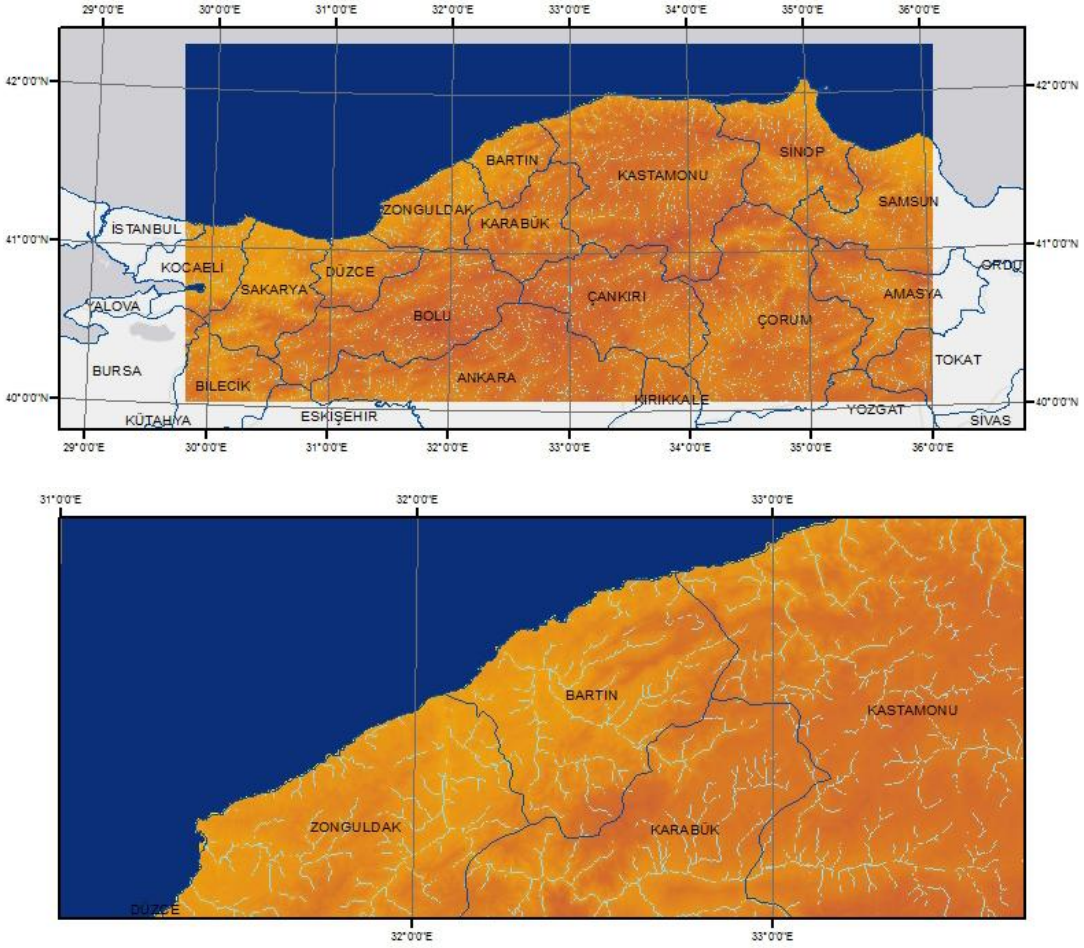

Figure 2.9: NetCDF 250 m Channel Grid Layer with zoomed details (below)

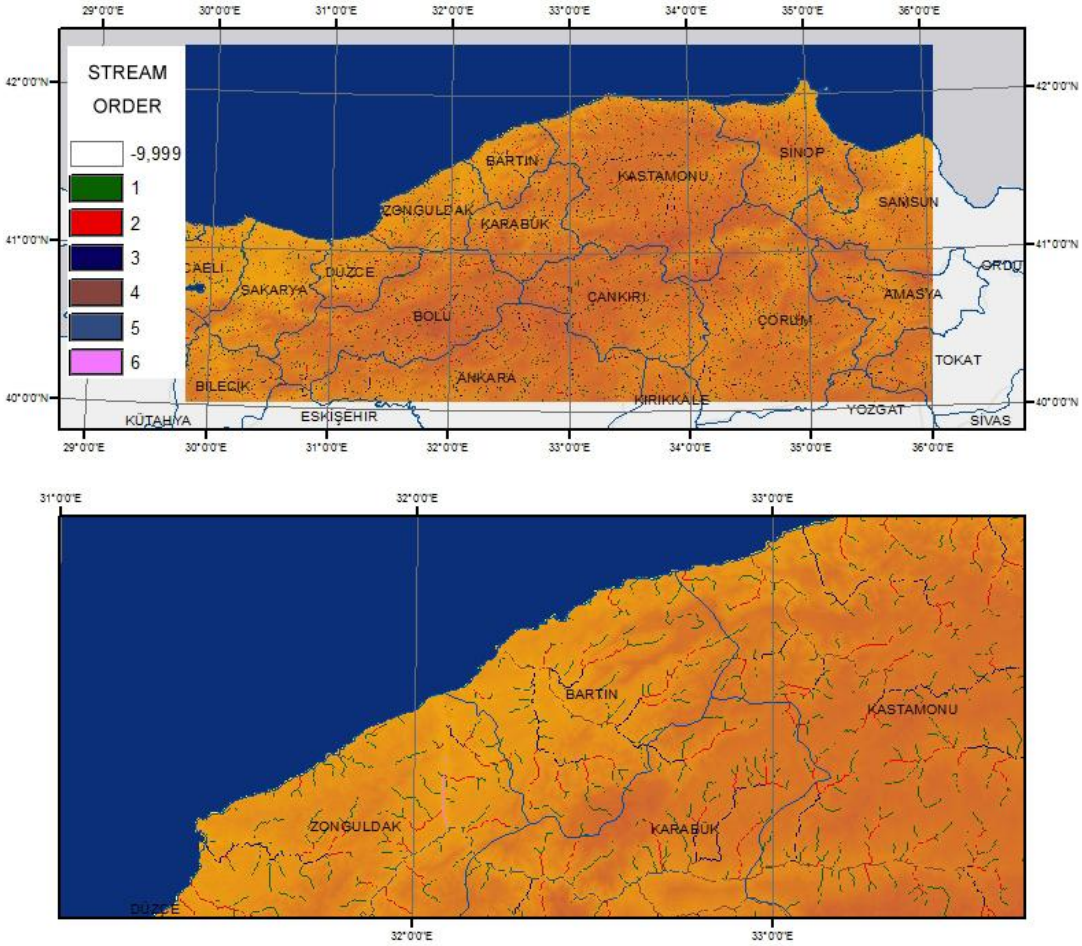

Figure 2.10: NetCDF 250 m Stream Order Layer with zoomed details (below)

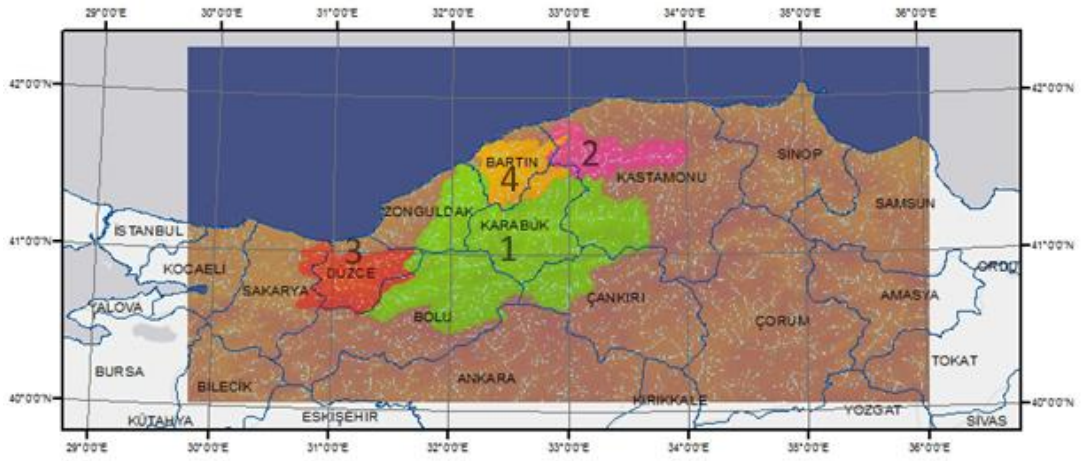

Figure 2.11: NetCDF 250 m Basin Mask Layer (1-Filyos, 2-Devrekani, 3-Düzce, 4-Bartın)

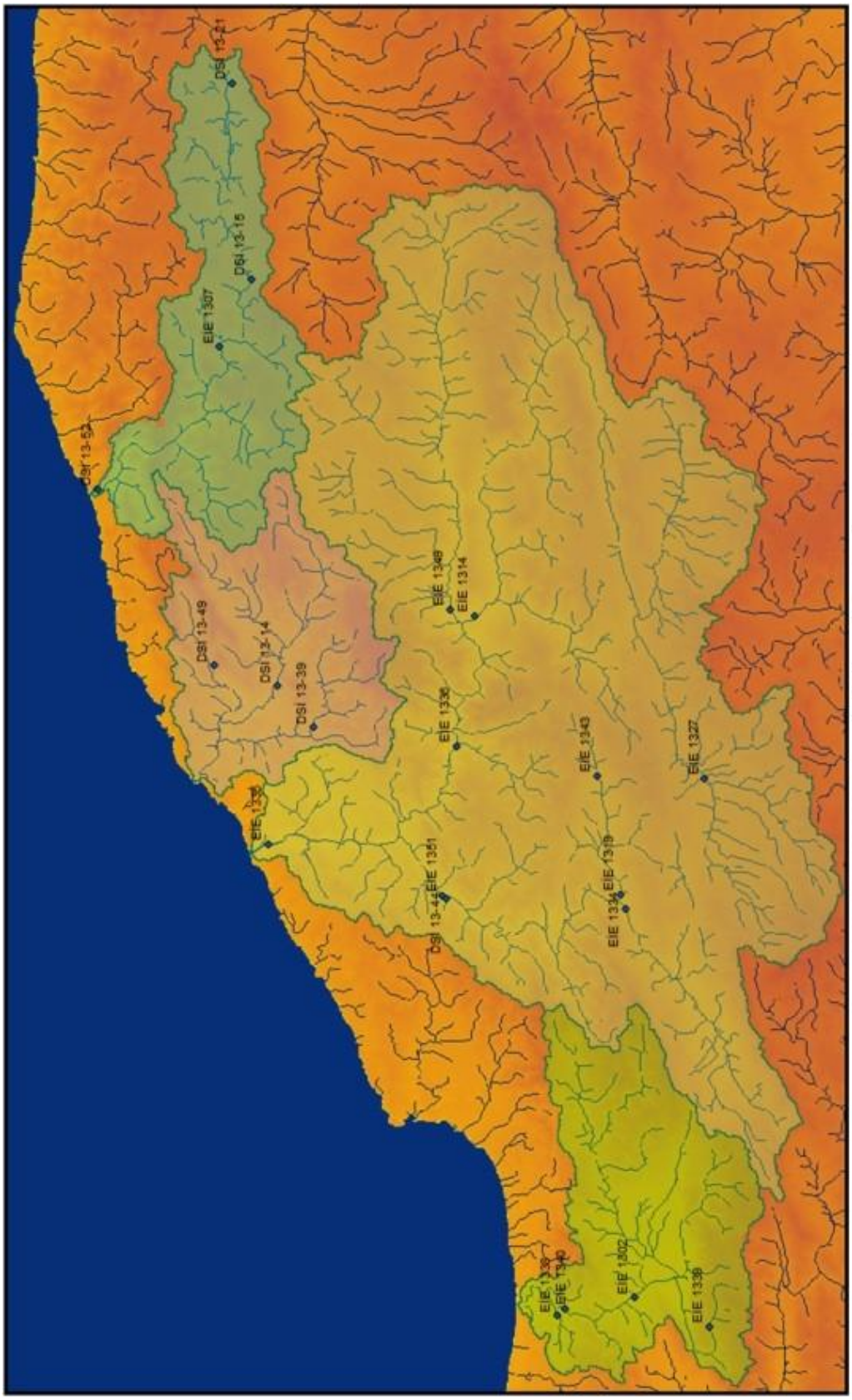

Figure 2.12: NetCDF 250 m Detailed Channel Grid and Forecast Points

2.5 3DVAR Data Assimilation

With WRF model, 3 dimensional variational (3DVAR) data assimilation is intended to use by implementing observation data into beginning sequence to improve the forecast accuracy for short-term simulations. For the selected events shown in Table 2.1 on previous section, WRF simulations are performed with and without assimilation and improvement in assimilation is investigated. WRF model is initiated by ECMWF analysis but with data assimilation, the model is started by new initial analysis, which is being obtained by a generalized inverse operator applied on observation. Steps in preparation of initial pre-operation simulation data and operation for WRF assimilation process are shown in Figure 2.13. This process is explained extensively in Barker et. al, (2003).

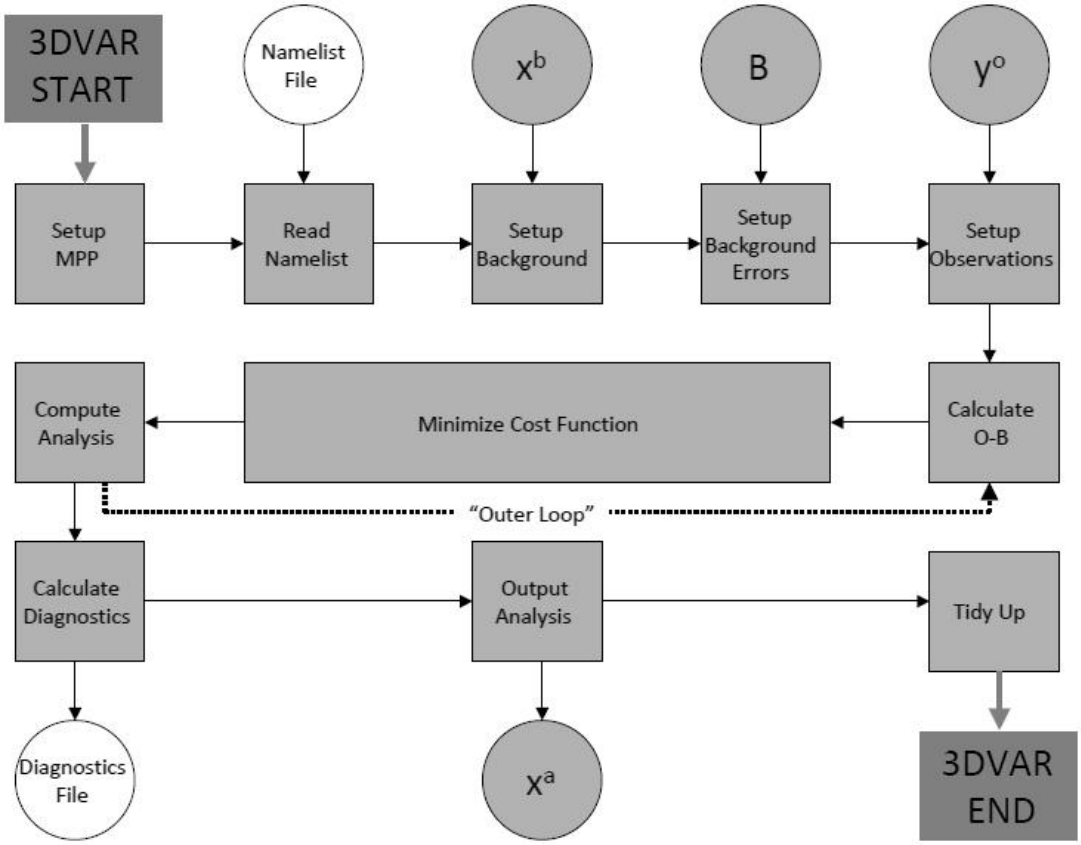

Figure 2.13: 3DVAR analysis scheme for WRF (Barker et. al, 2003)

As the first step, setup process for WRF model is being initialized by reading details of the run configuration in from a WRF namelist file. On the second step, 3DVAR run-time options are read in from another namelist file. These options are time-based operational options. In third step, setup background (x^b) is initialized for the model. On next step, setup background errors (B) are evaluated. In calculation of error covariance matrices, firstly WRF model is being run for each case by using corresponding ECMWF data in 12-hourly periods for 3 days then by taking averages of observation differences by NMC method (Parrish and Derber, 1992), matrices are formed. In these matrices, components of the background error (eigenvectors, eigenvalues, length scales and balance regression coefficients) are read and stored.

On the next step, setup observations enter the algorithm as the most important factor for this assimilation process. Observations y^o are obtained and additional covariance matrices are calculated from these data. In this research, as event periods are between years 2000 – 2011, amount of observation data show increase for outer domain with respect to time.

On the calculate O-B (Observation – Background Error) step, for valid data, the innovation vector $y^o – y^b$ is calculated. A “maximum error check” is applied to all values within the innovation vector which compares the O-B value against a maximum value defined as a multiple of the observation error for each observation.

After O-B data is calculated, minimization of cost function is being processed. The minimization of the 3DVAR cost function proceeds iteratively in 3 steps. Diagnostic output includes cost function and gradient norm values for each iteration.

On Calculate Analysis step, after the control variables that minimize the cost function are found, a final transform of the analysis increments to model space is performed. The increments are added to the background values to produce the analysis. Finally, checks are performed to ensure certain variables are within physically reasonable limits (e.g. relative humidity is greater than zero and less that 100%). The increments are adjusted if analysis values fall outside this range. On the next step, Compute Diagnostics, assimilation statistics (minimum, maximum, mean and root mean square) are calculated and output for study. As a final algorithmic step, both analysis and analysis increments are created as outputs on Output Analysis step. Lastly in Tidy Up stage, dynamically allocated memory is de-allocated and summary run-time data output is generated. As a result of this algorithm, new initial data to be run in model are defined and with respect to new data, model boundary conditions are updated. For this research, new boundary conditions and analyses values are defined and made ready for the necessary WRF simulation runs. As an example, initial surface temperature, pressure distribution and wind vectors has been shown in Figure 2.14 for 25 October 2008 00:00 GMT (simulation start time). As non-assimilated and 3DVAR assimilation applied initial data have been compared, the difference in model dynamics are significantly traceable hence the effect of assimilation becomes clear.

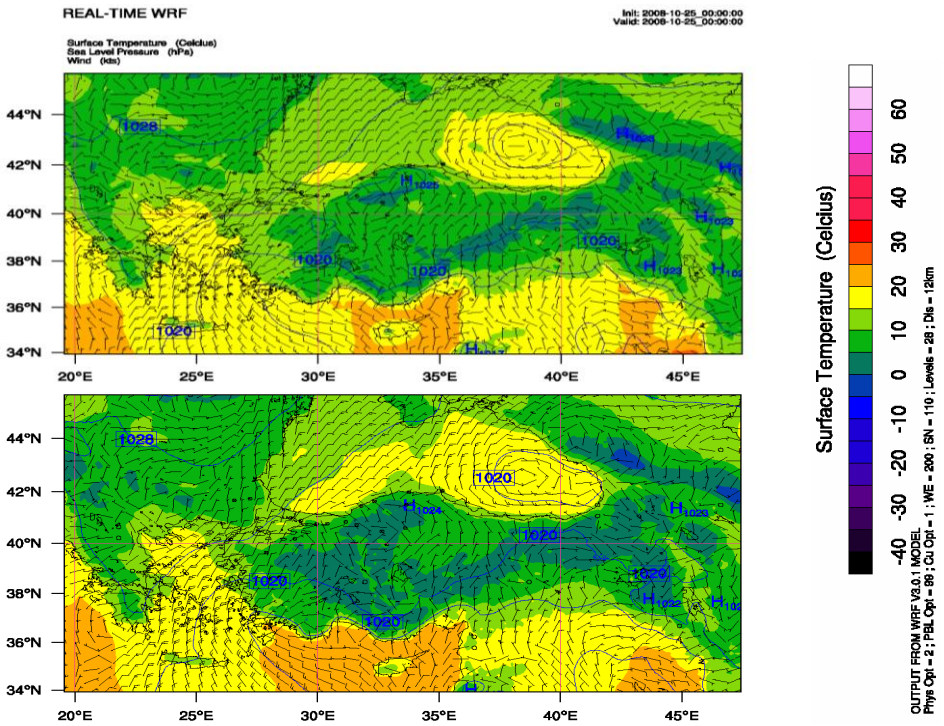

Figure 2.14: Initial surface temperature, pressure distribution and wind vectors for 25 October 2008 00:00 GMT (Top - Non assimilated, Below – 3DVAR assimilation applied)

2.6 Satellite (MPE) Precipitation Data

In convective rain systems and relative flood events analyses, Infra-red and Visible (IR/VIS) techniques of GEO stationary satellite systems are occasionally being operated. With respect to these techniques, MPE (Multi Precipitation Estimates; Heinemann et al., 2002) is an instantaneous rain rate product based on cloud-top temperature measurements. Polar orbiting microwave sensors are used to calibrate rain estimates obtained from IR technique of GEO satellite. Since microwave rain rates are available for 1 or 2 times in a day for the same grid, this algorithm is being used on precipitation forecast calibration for data obtained from continuous METEOSAT products being recorded in 15-minutes periods. MPE data in this research have been obtained from General Directorate of Meteorological Works (MGM) for whole satellite cycle (3712 x 3712 4-km resolution grids) in 15 minutes period for the events observed after 2005. As compared with hourly WRF outputs, time match has been established by aggregating 15-minutely MPE products into hourly readings by computing weighted averages of corresponding values. For simulations performed for this research, GRIB formatted MPE readings have been converted into NetCDF format with WRF model projection by computer algorithms. As an example to this conversion, for the event number 16 (08.09.2009) 19:00 UTC, the precipitation distribution on study domain has been shown in Figure 2.15. In this figure, GRIB output for the corresponding date has been shown above; while integrated MPE rainfall on WRF domain for the same date has shown below in this figure. To implement into NOAH-hydro model, MPE readings have also been converted from mm/hour to mm/sec.

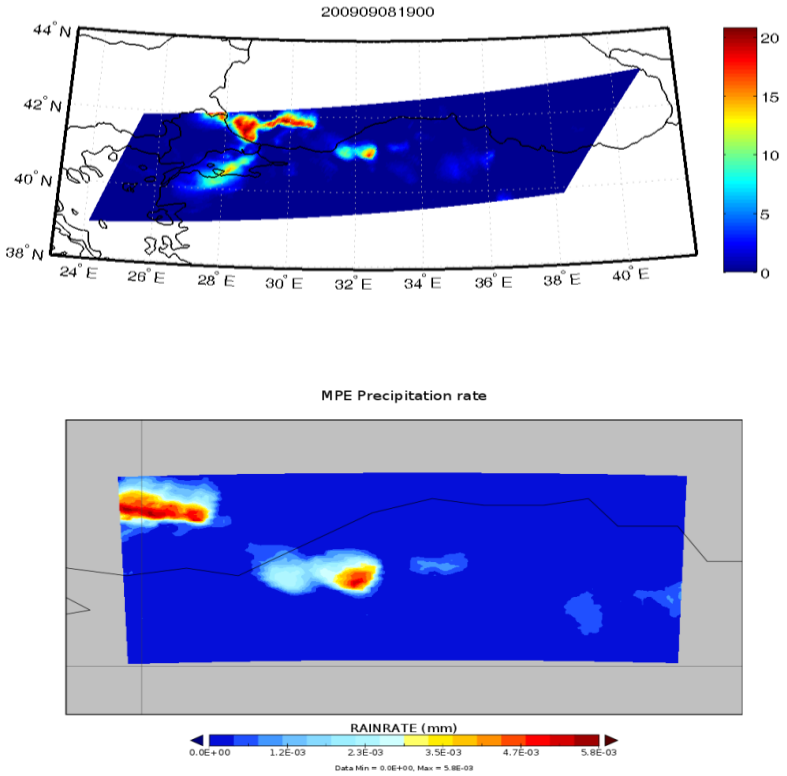

Figure 2.15: MPE GRIB output in mm/hour (top) and WRF MPE input in mm/sec (below) for 08.09.2009 19:00 GMT in their own projections.

CHAPTER 3

PRECIPITATION ANALYSIS

3.1 Introduction

In this chapter, a detailed precipitations analysis in which WRF-derived precipitation with and without data assimilation (WRF AS, WRF NOAS), satellite-derived precipitation (MPE) and gauged precipitation used are presented. WRF AS, WRF NOAS, MPE, and observed precipitation values are first analyzed as area-averaged time series for hourly, 3-hourly, 6-hourly, and 24-hourly for each event. Second, they are evaluated by calculating their general statistics using all events together and third, event- and station- based statistical analyses are performed. Precipitation data obtained from WRF and MPE are at hourly and 4-km resolution while hydrograph analyses are performed at mean daily time scale.

3.2 Area Averaged Time Series

Area-averaged precipitation of WRF AS, WRF NOAS, MPE and observations are formed using 34 rain gauges at hourly, 3-hourly, 6-hourly, and daily time scales for each of 25 events. These area-averaged series are generated by taking mean values of all available readings for every hourly time step. 3, 6 and 24 hourly series are cumulatively calculated from 1 hourly series. With these series, the performances of WRF and MPE in capturing the fluctuations observed in measured precipitation along with event periods are checked visually. Figures 3.1 – 3.25 respectively show the area-averaged time series of each event from 1 to 25 at 1-,3-,6-, and 24-hourly time intervals. WRF AS, WRF NOAS and MPE show variable skills against observations from event to event. In general, WRF model shows some skill in capturing the timing of the rainfall events and up to some extent the magnitude of precipitation. As the time interval aggregates rainfall fluctuations are smoothed and thus the ability of WRF model becomes more obvious whether it is able to follow the observed temporal rainfall trend. Overall assimilation shows discernible improvements with various degrees in WRF-derived precipitation (WRF AS) in all events. Especially on events 5, 9, 17 and 23, assimilation shows substantial improvements with respect to no-assimilation (WRF NOAS) precipitation. When MPE rainfall trends are examined, it is observed that MPE generally shows a tendency to significantly underestimate precipitation with respect to both observation and WRF. Only in few events, MPE manages to match observation rainfall trends and magnitudes better than WRF model.

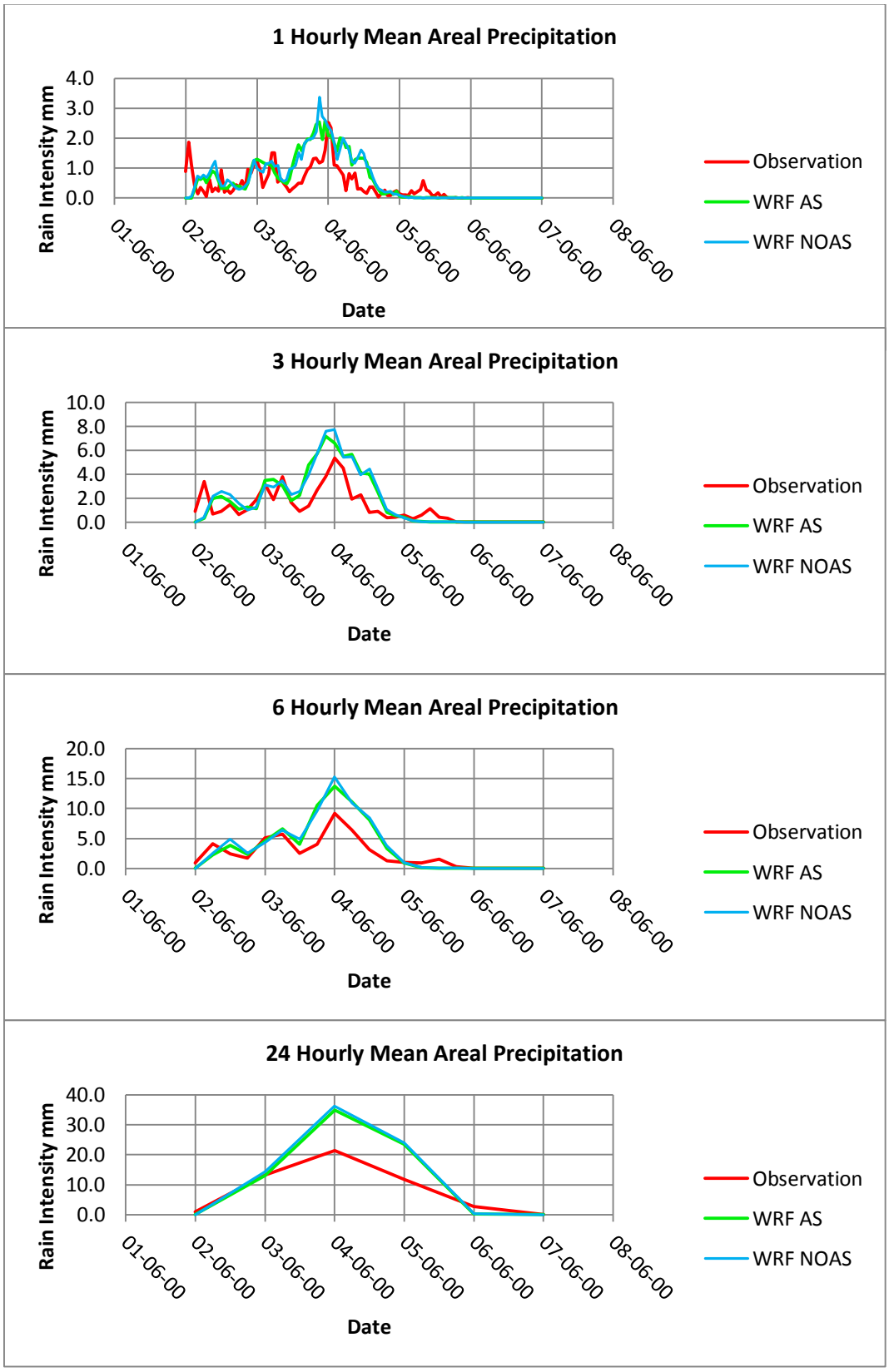

Figure 3.1: 1, 3, 6 and 24 hourly mean areal time series for Event 1

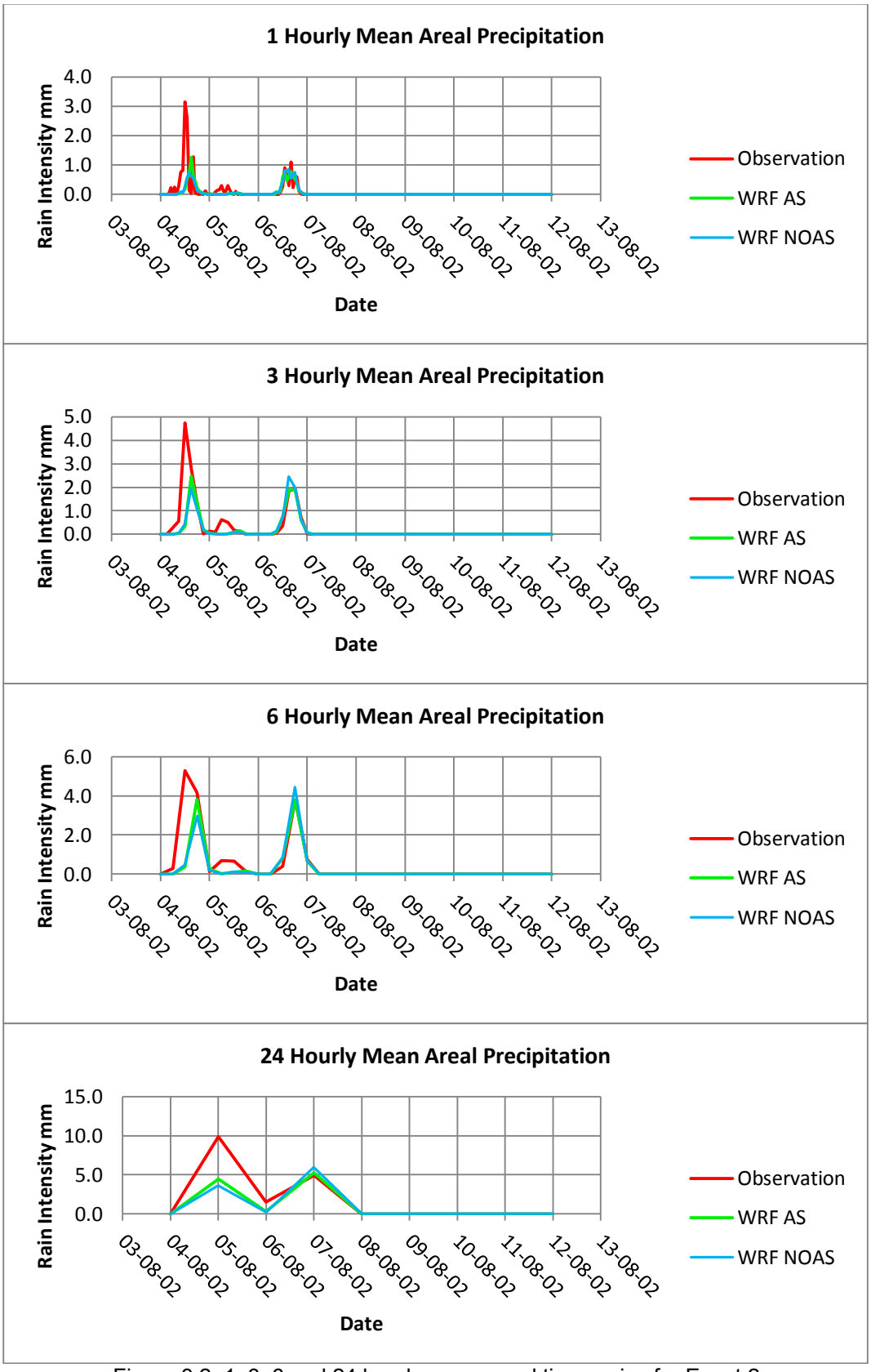

Figure 3.2: 1, 3, 6 and 24 hourly mean areal time series for Event 2

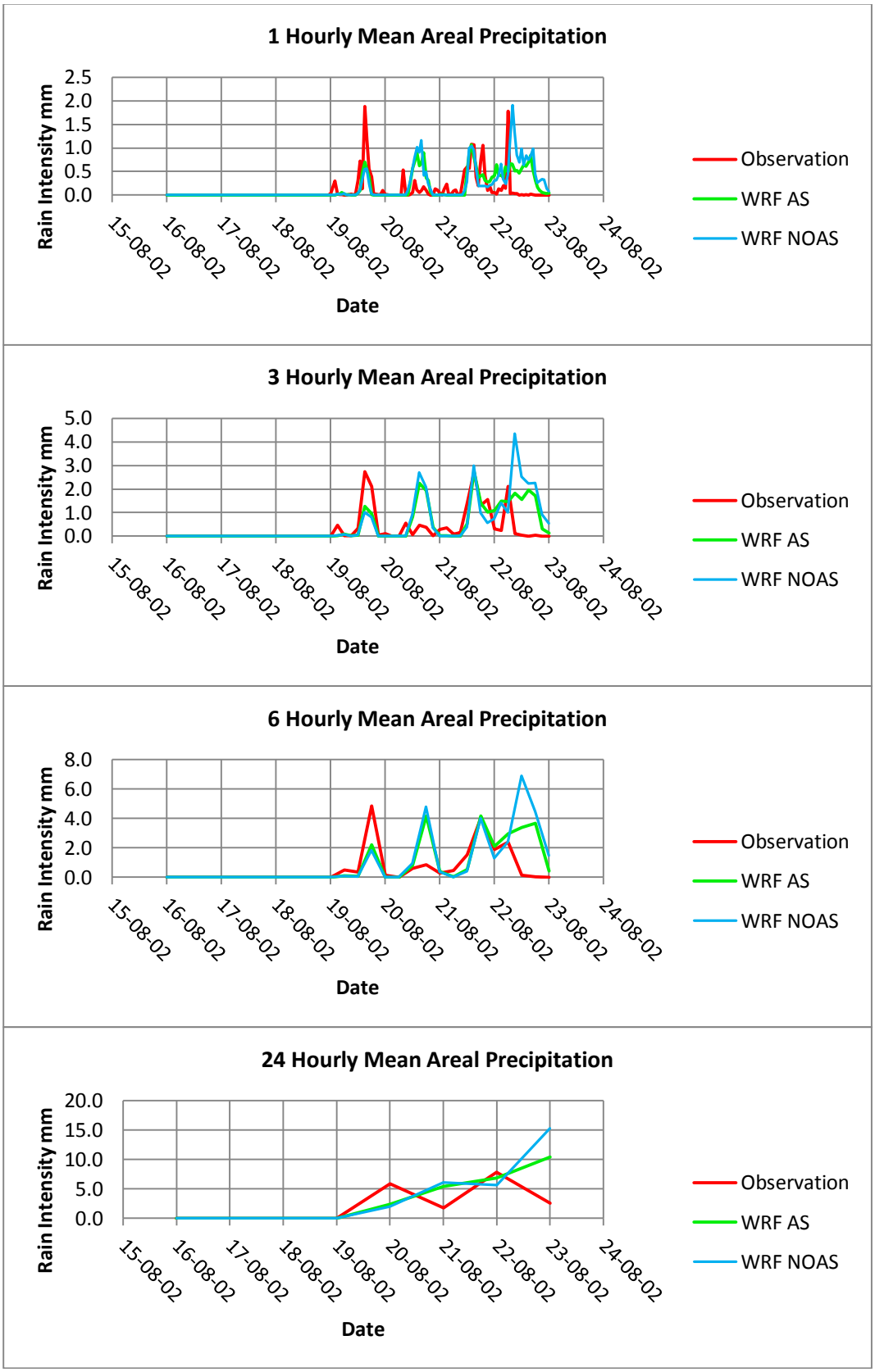

Figure 3.3: 1, 3, 6 and 24 hourly mean areal time series for Event 3

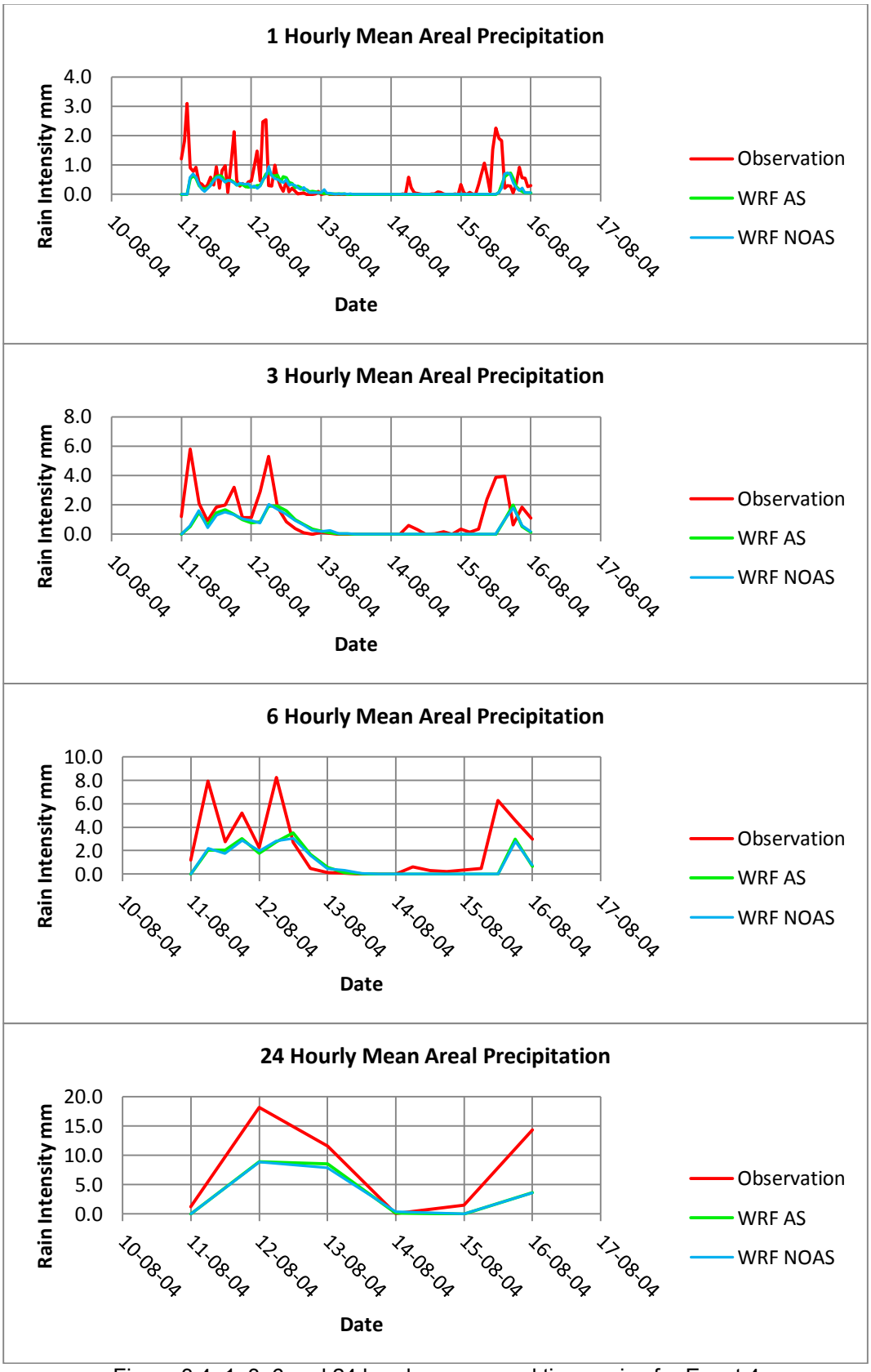

Figure 3.4: 1, 3, 6 and 24 hourly mean areal time series for Event 4

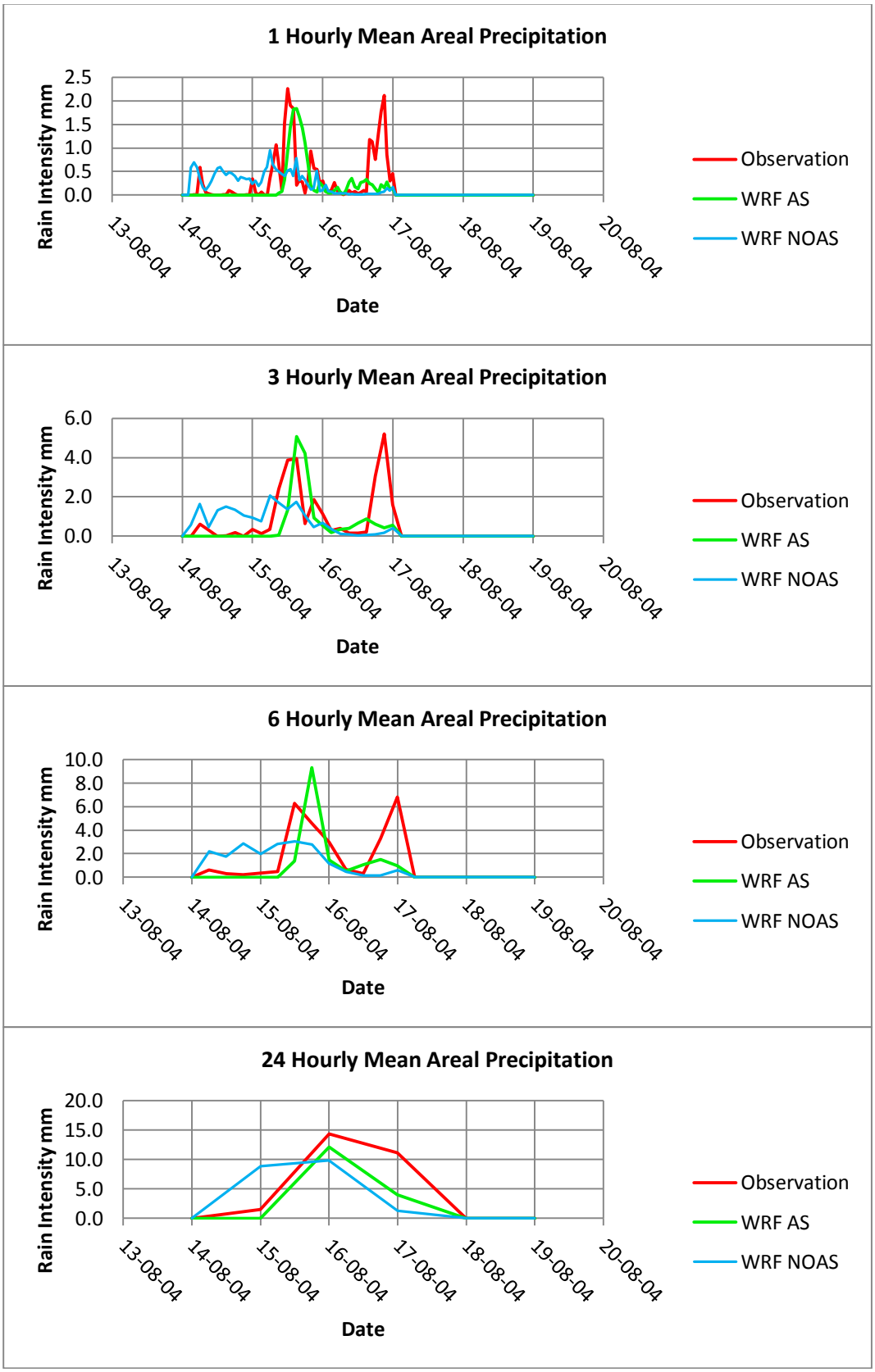

Figure 3.5: 1, 3, 6 and 24 hourly mean areal time series for Event 5

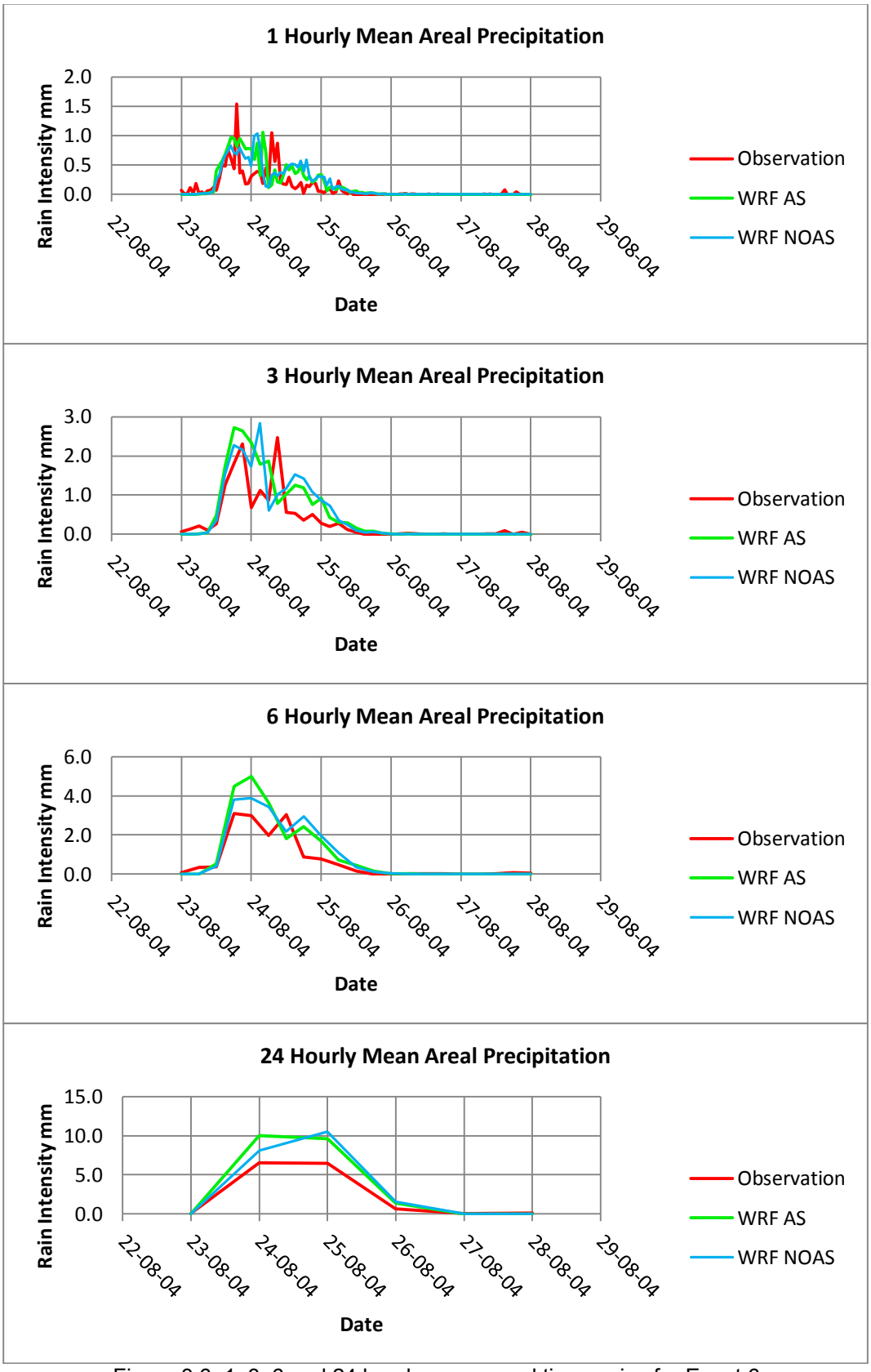

Figure 3.6: 1, 3, 6 and 24 hourly mean areal time series for Event 6

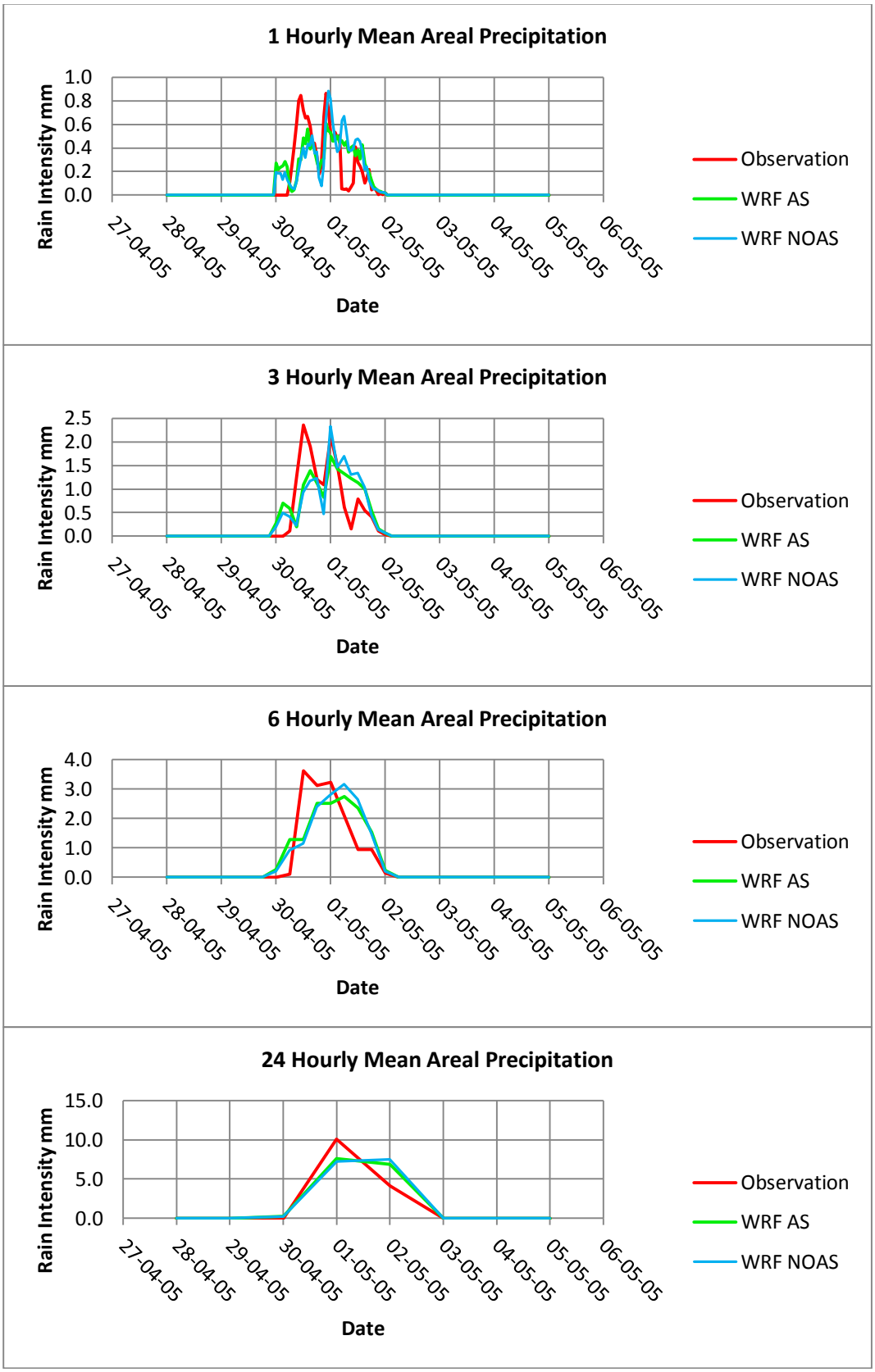

Figure 3.7: 1, 3, 6 and 24 hourly mean areal time series for Event 7

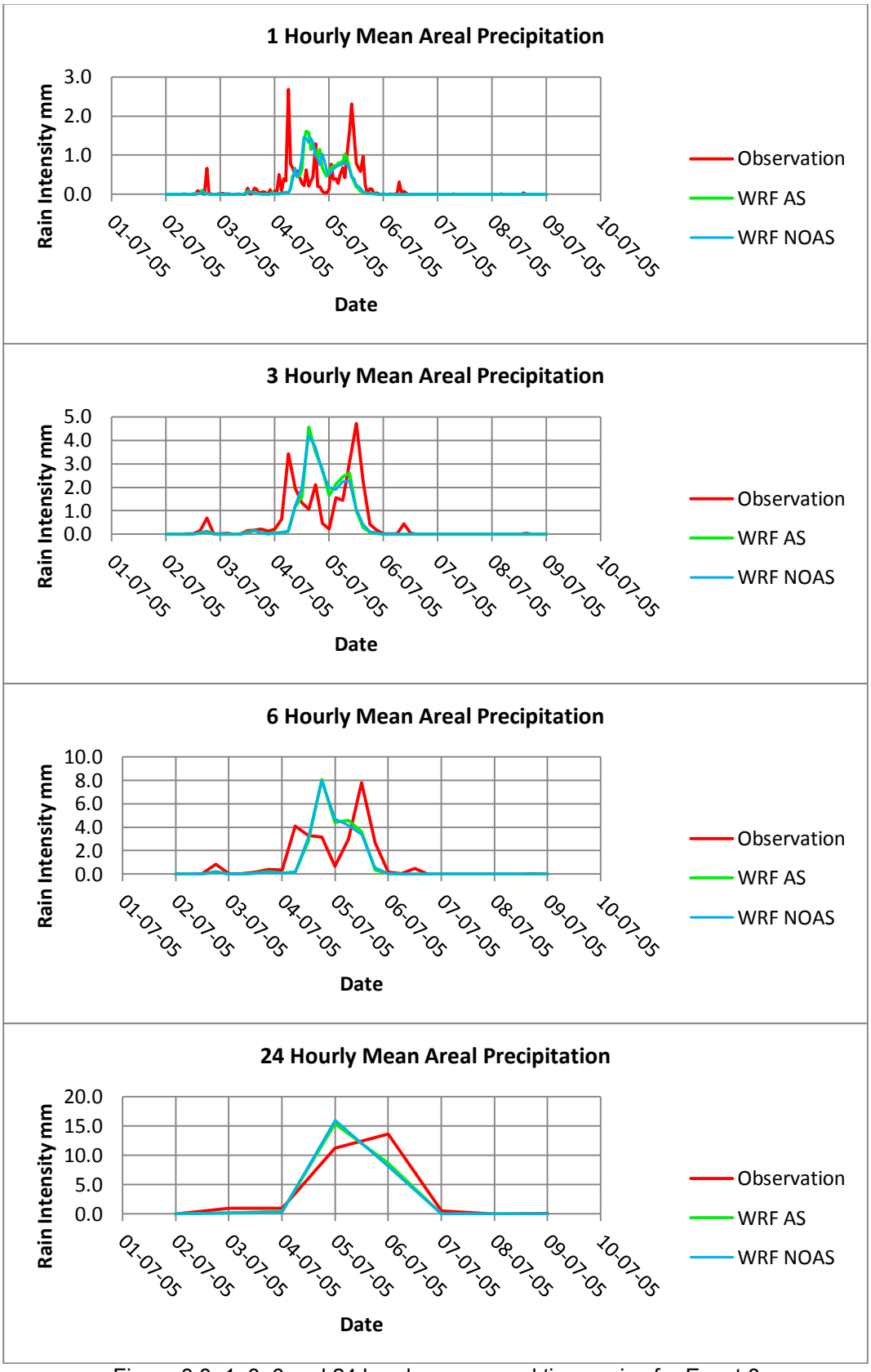

Figure 3.8: 1, 3, 6 and 24 hourly mean areal time series for Event 8

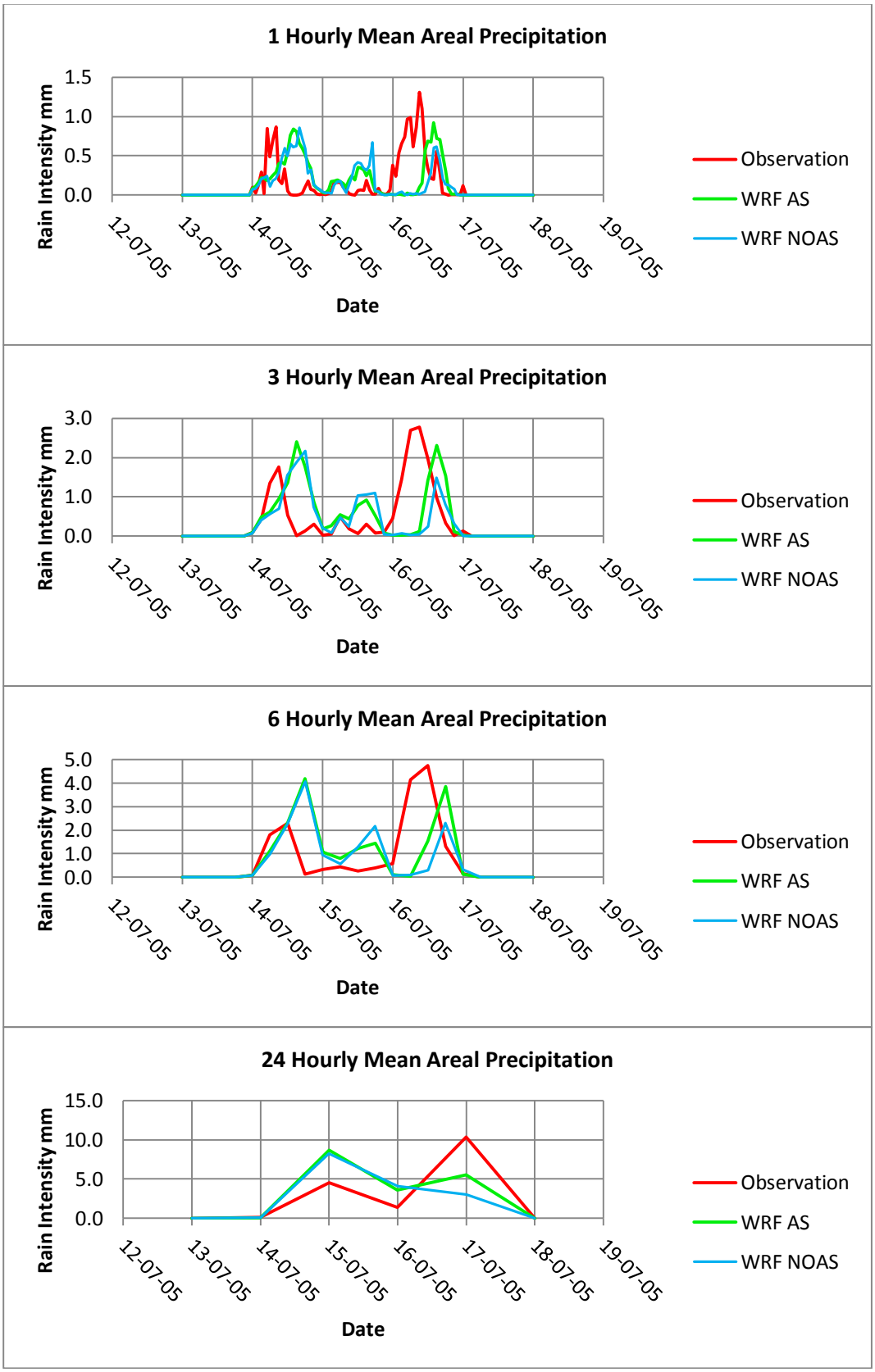

Figure 3.9: 1, 3, 6 and 24 hourly mean areal time series for Event 9

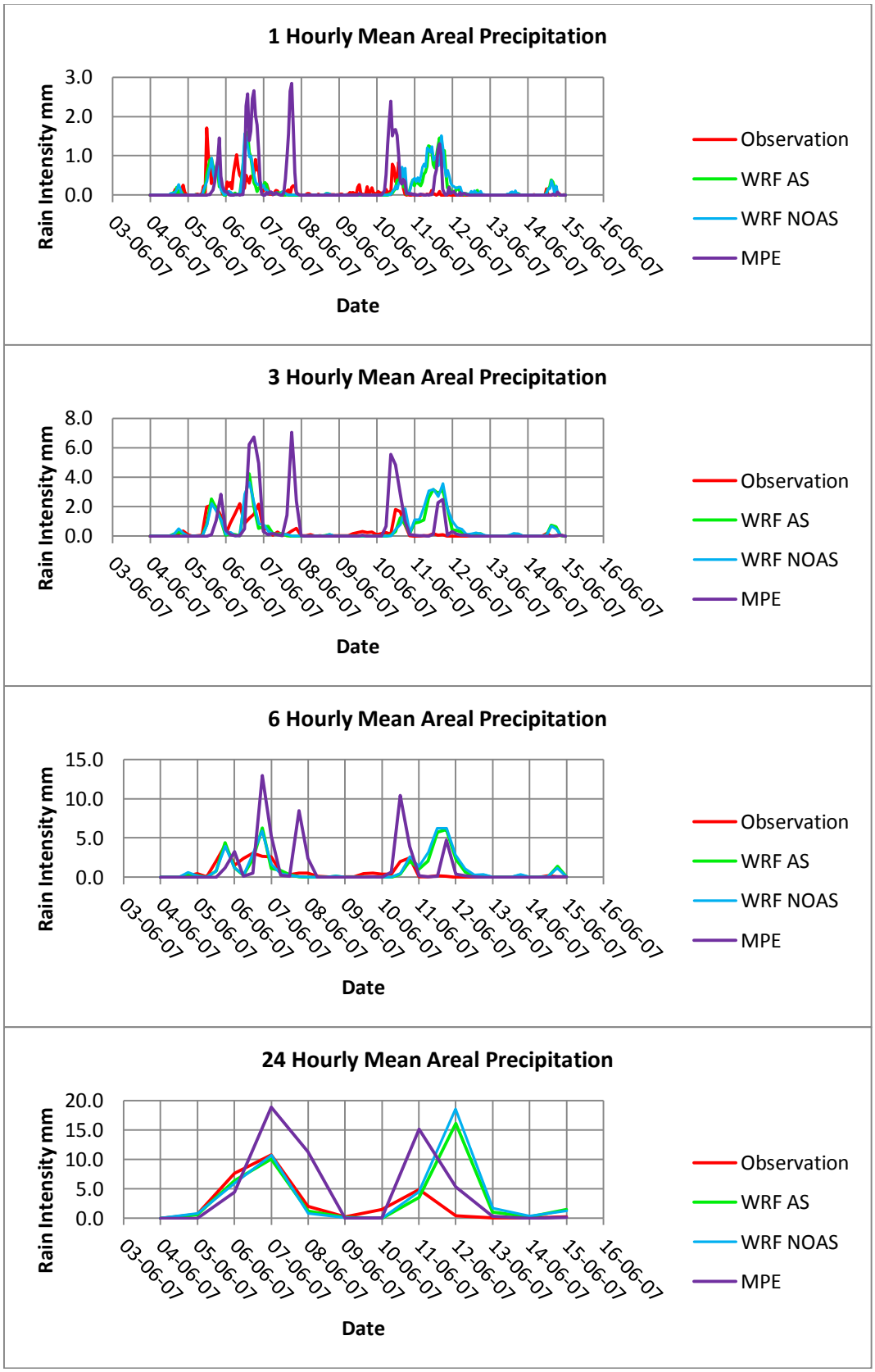

Figure 3.10: 1, 3, 6 and 24 hourly mean areal time series for Event 10

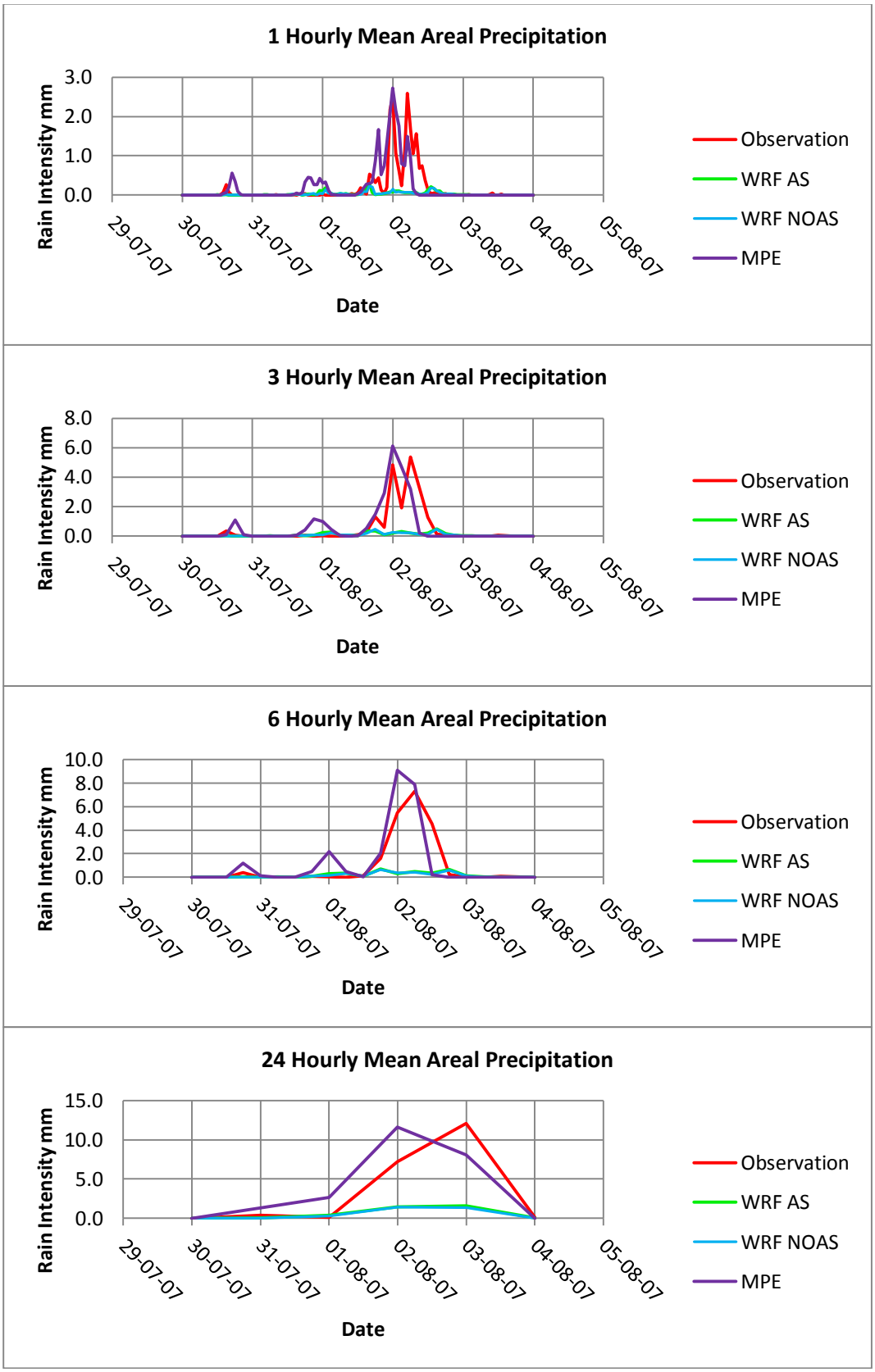

Figure 3.11: 1, 3, 6 and 24 hourly mean areal time series for Event 11

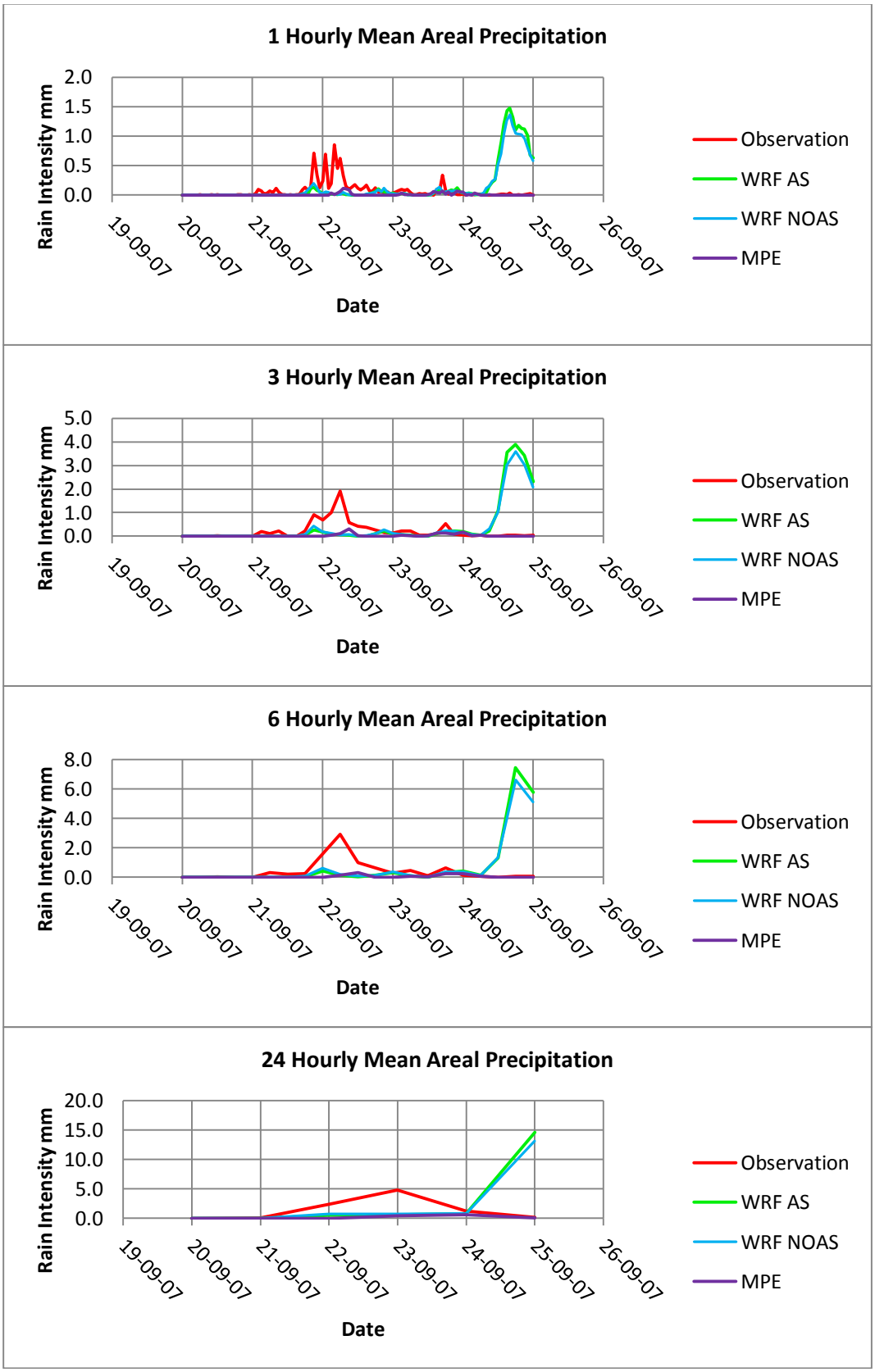

Figure 3.12: 1, 3, 6 and 24 hourly mean areal time series for Event 12

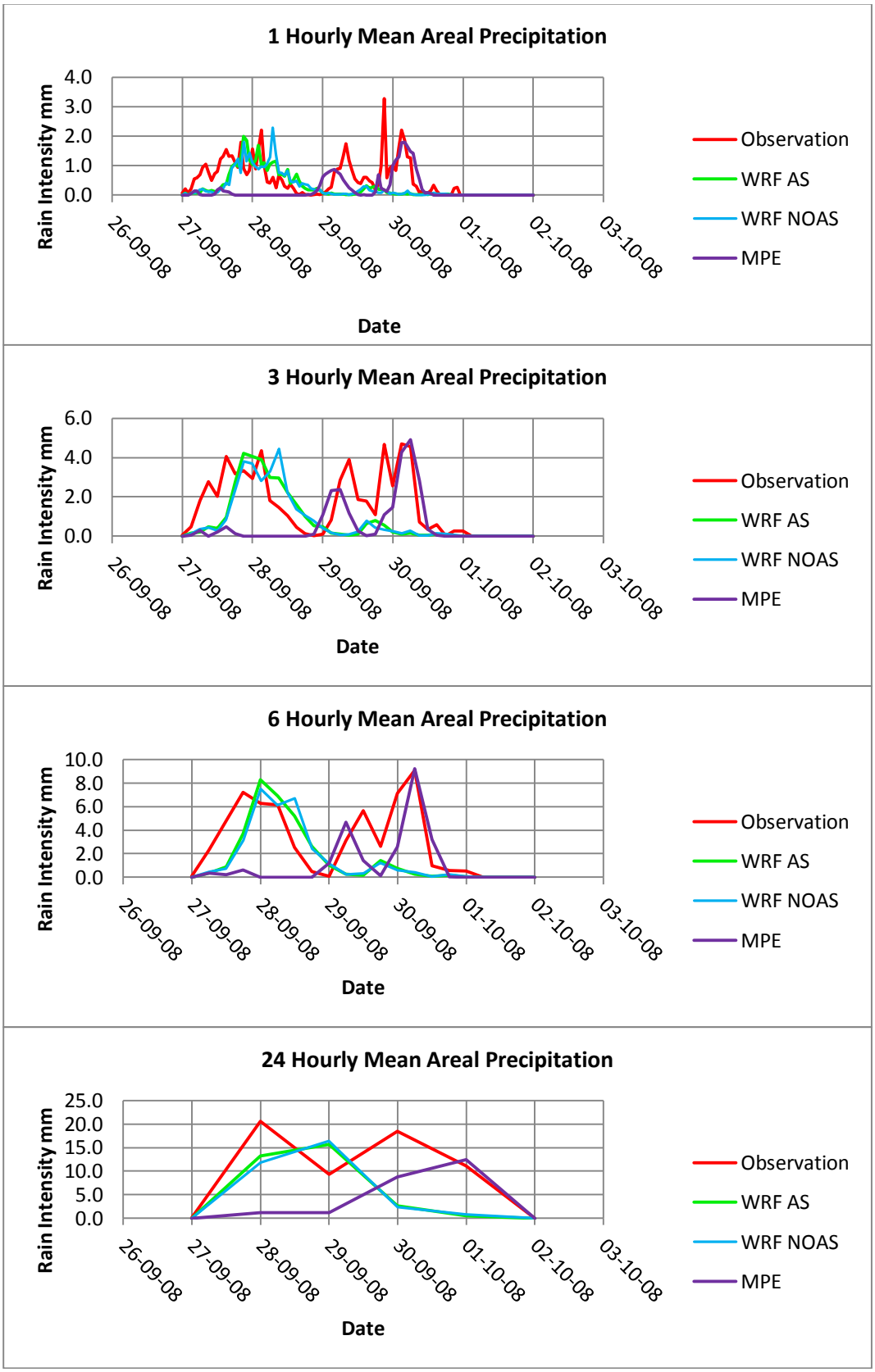

Figure 3.13: 1, 3, 6 and 24 hourly mean areal time series for Event 13

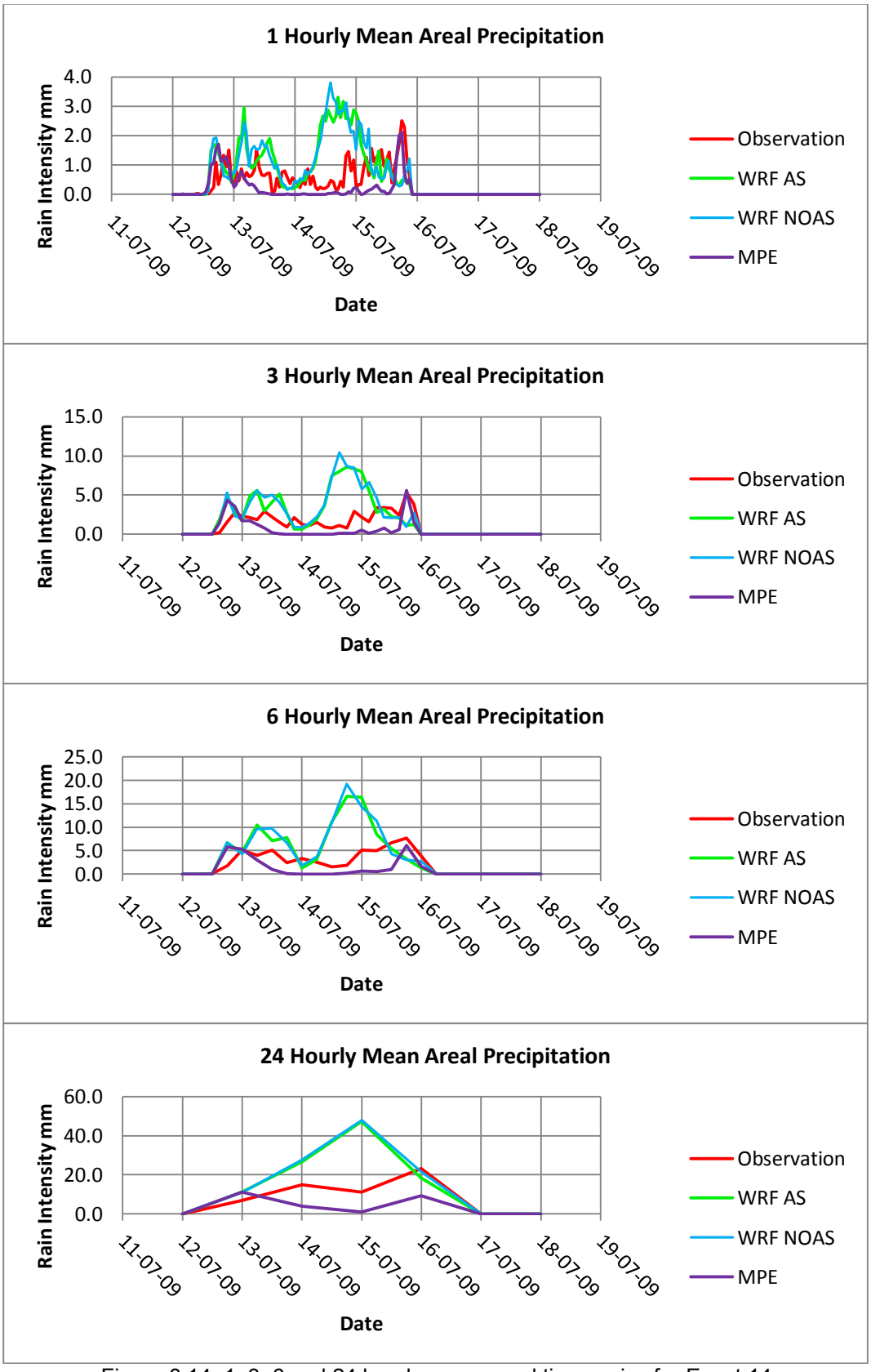

Figure 3.14: 1, 3, 6 and 24 hourly mean areal time series for Event 14

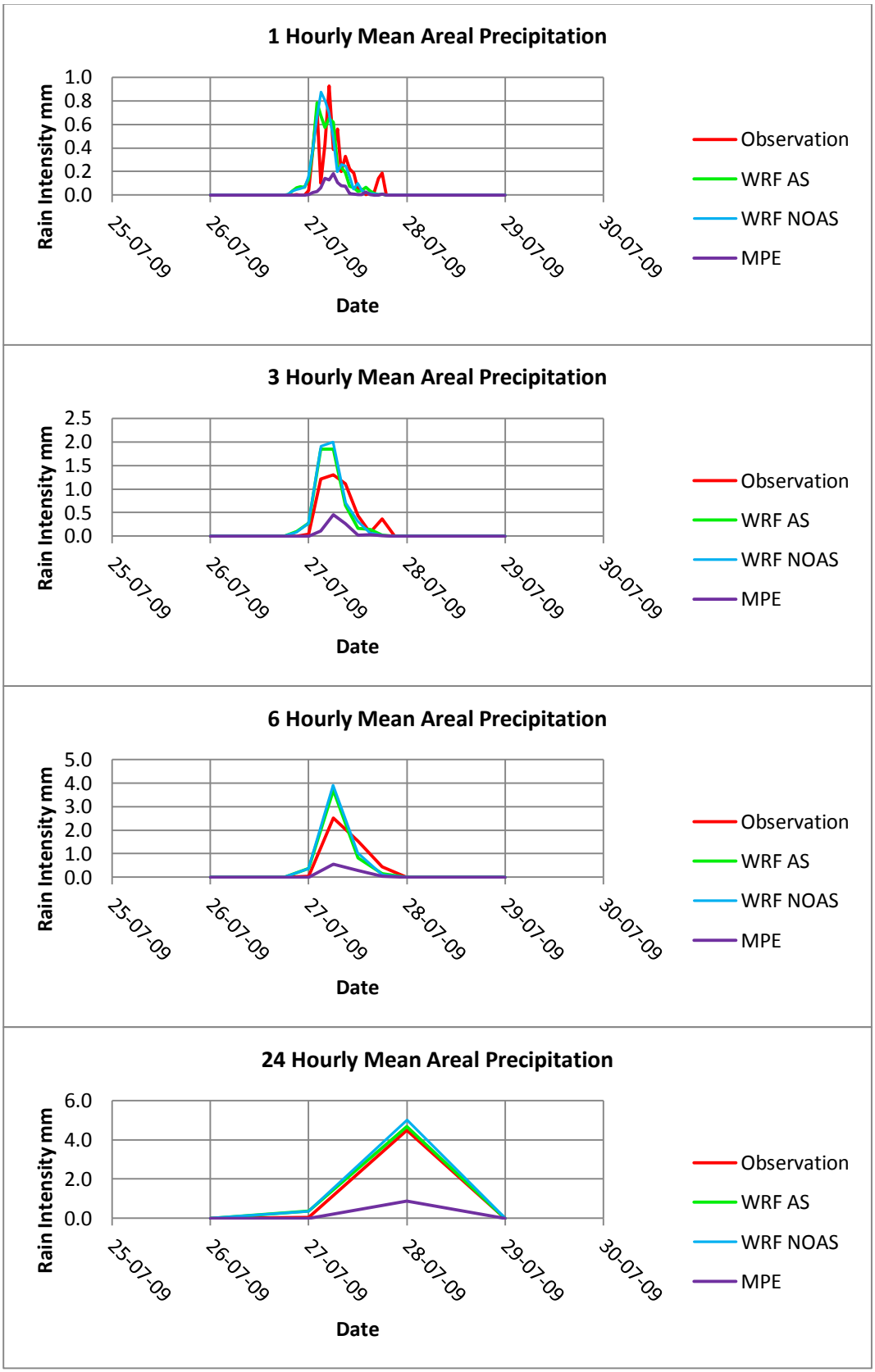

Figure 3.15: 1, 3, 6 and 24 hourly mean areal time series for Event 15

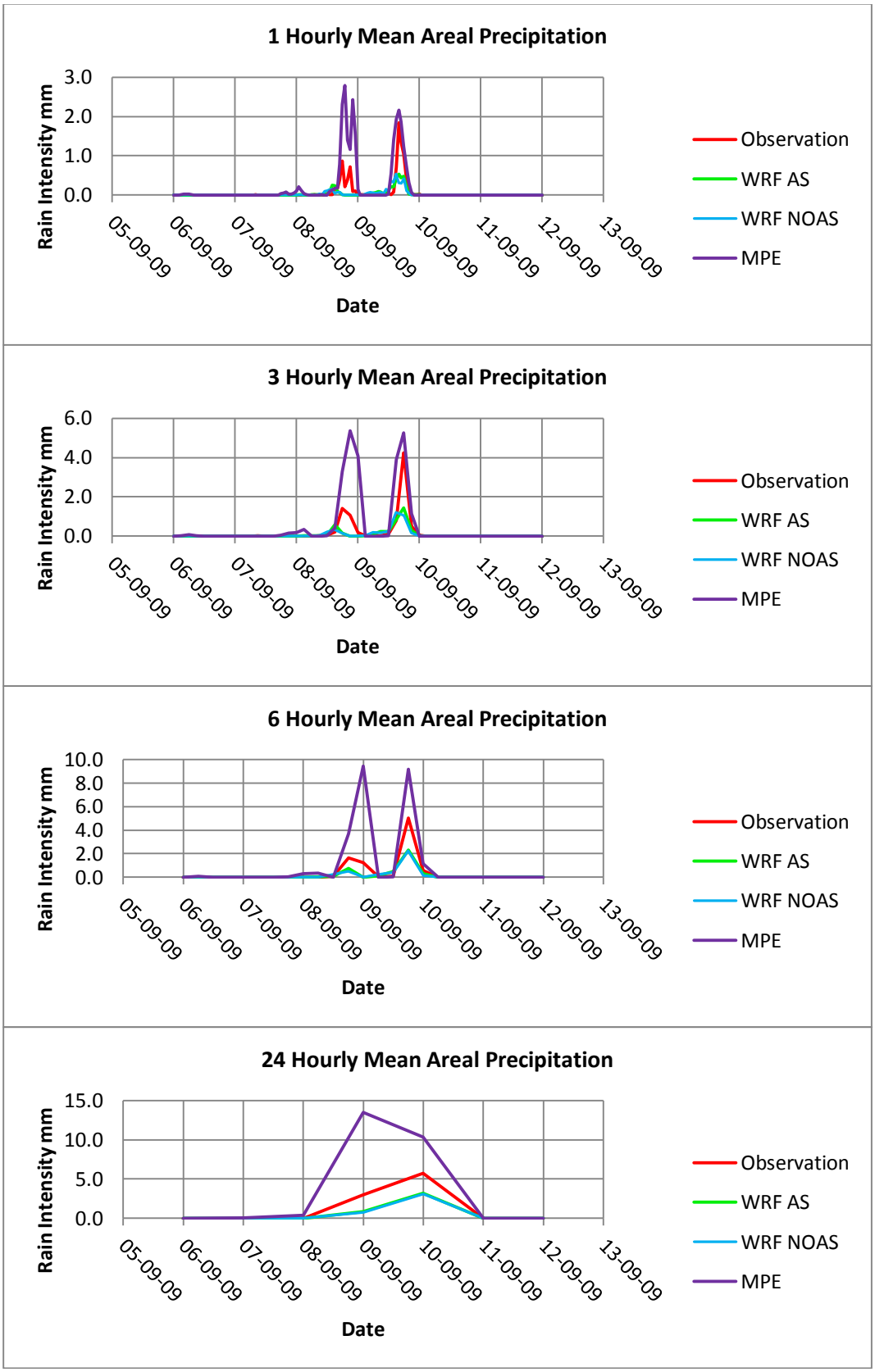

Figure 3.16: 1, 3, 6 and 24 hourly mean areal time series for Event 16

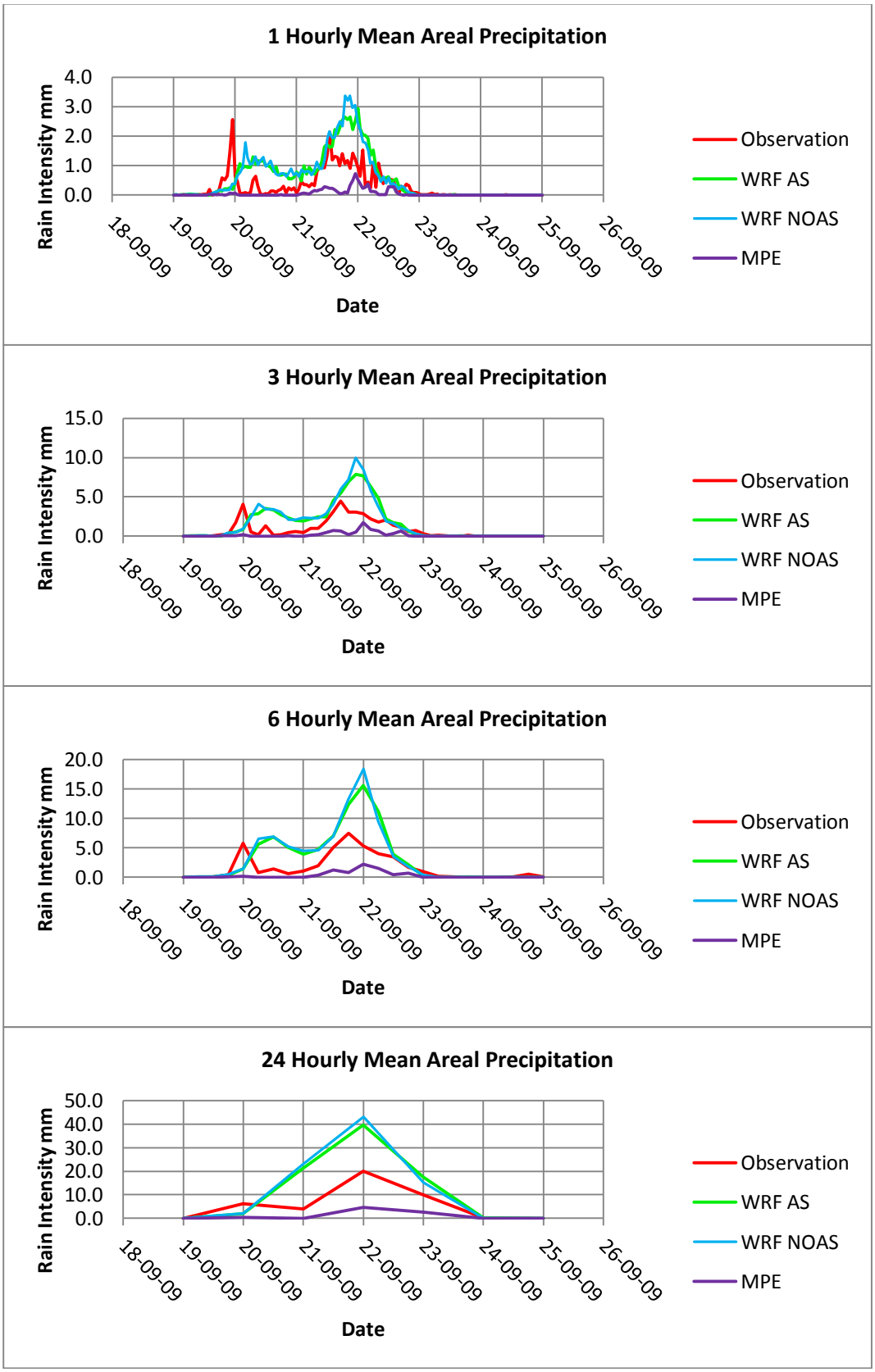

Figure 3.17: 1, 3, 6 and 24 hourly mean areal time series for Event 17

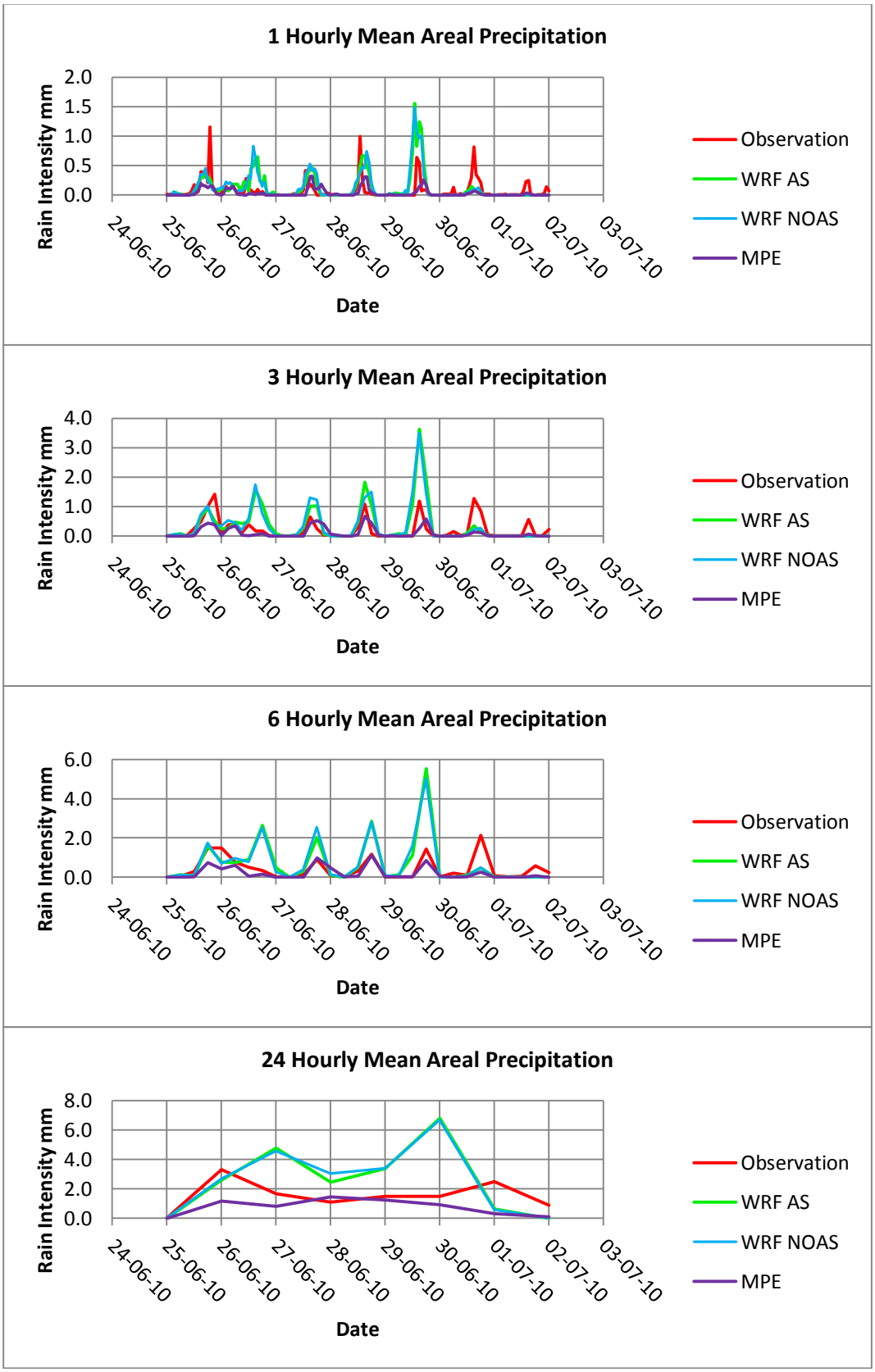

Figure 3.18: 1, 3, 6 and 24 hourly mean areal time series for Event 18

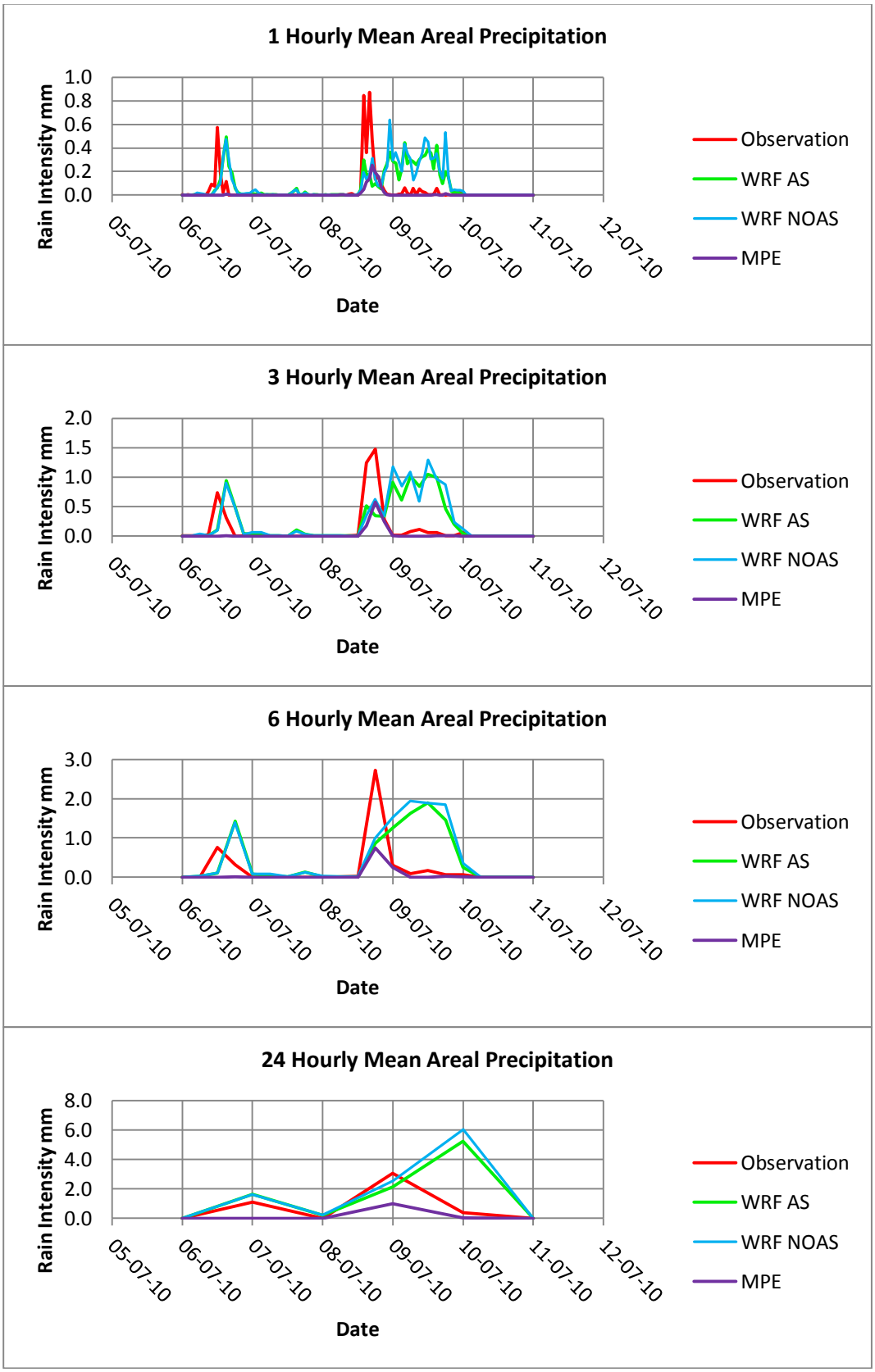

Figure 3.19: 1, 3, 6 and 24 hourly mean areal time series for Event 19

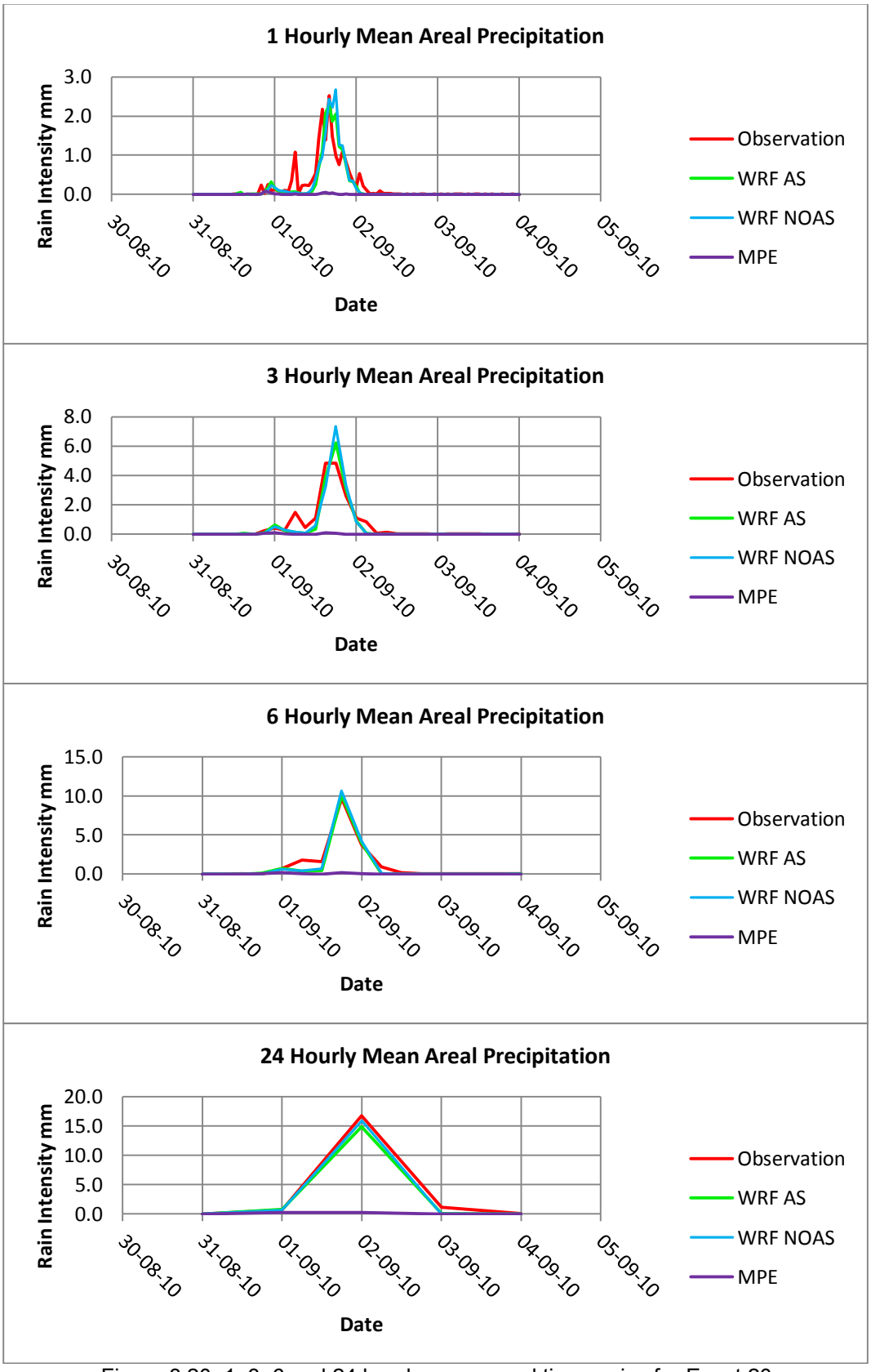

Figure 3.20: 1, 3, 6 and 24 hourly mean areal time series for Event 20

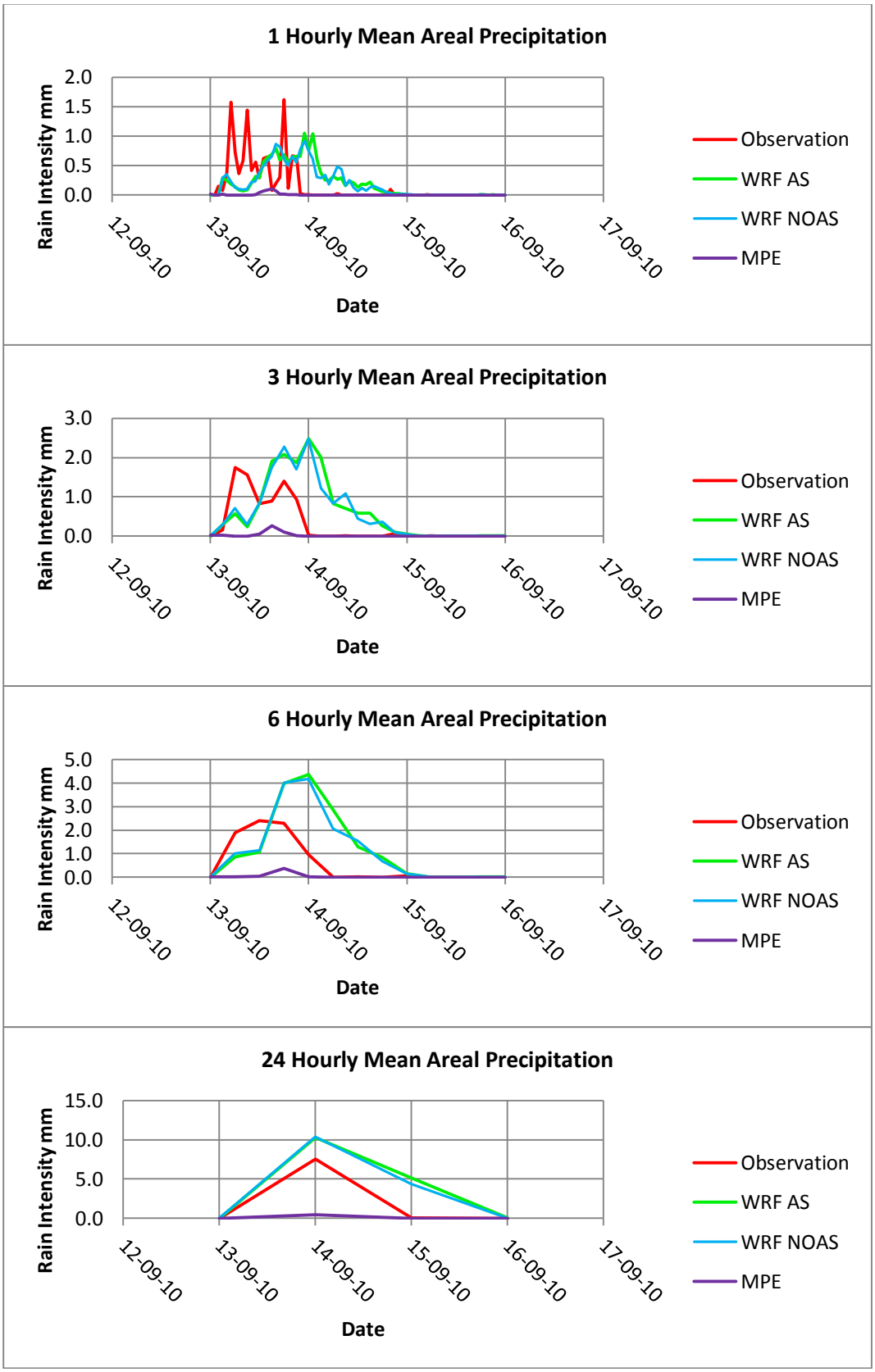

Figure 3.21: 1, 3, 6 and 24 hourly mean areal time series for Event 21

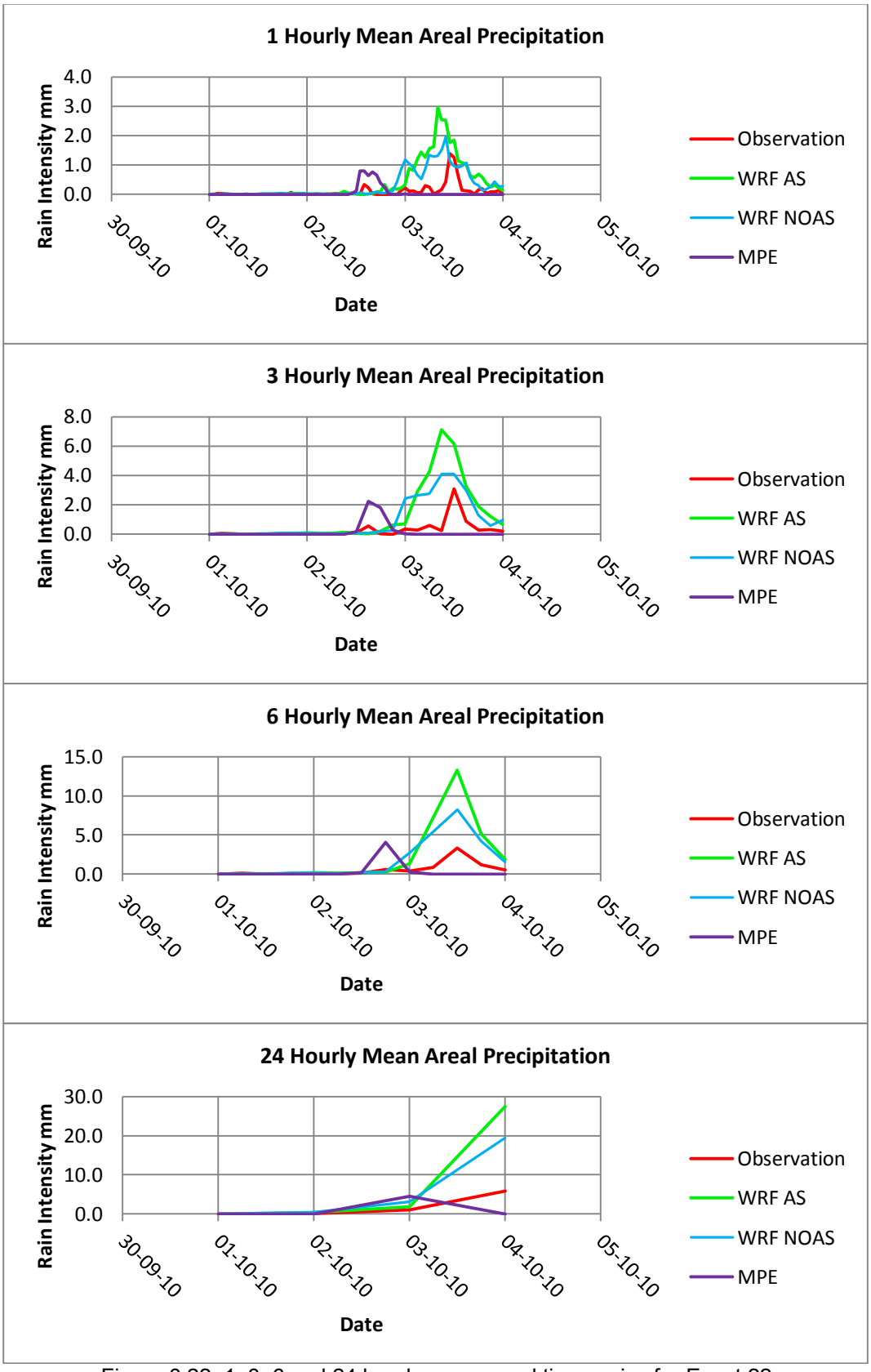

Figure 3.22: 1, 3, 6 and 24 hourly mean areal time series for Event 22

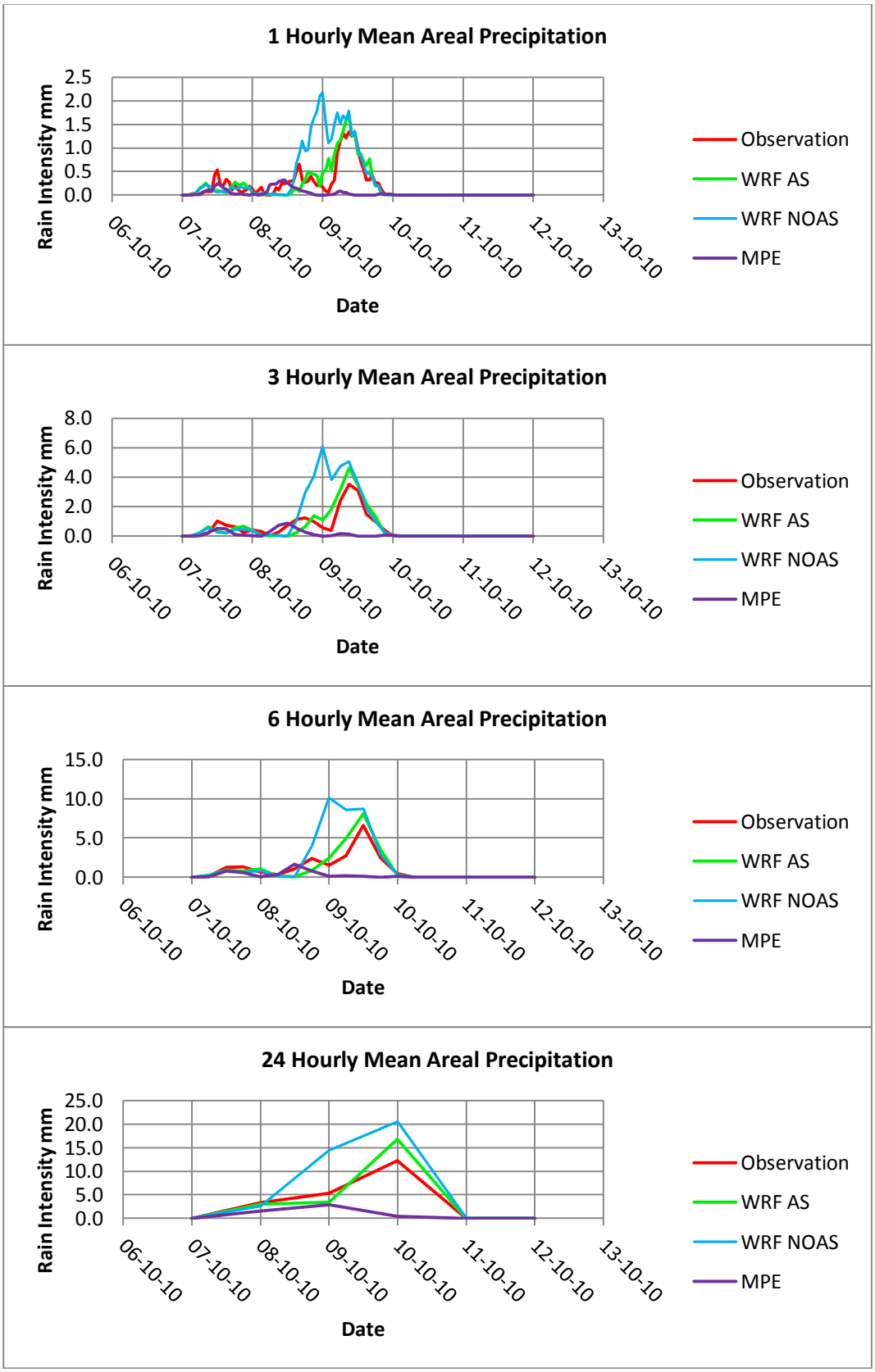

Figure 3.23: 1, 3, 6 and 24 hourly mean areal time series for Event 23

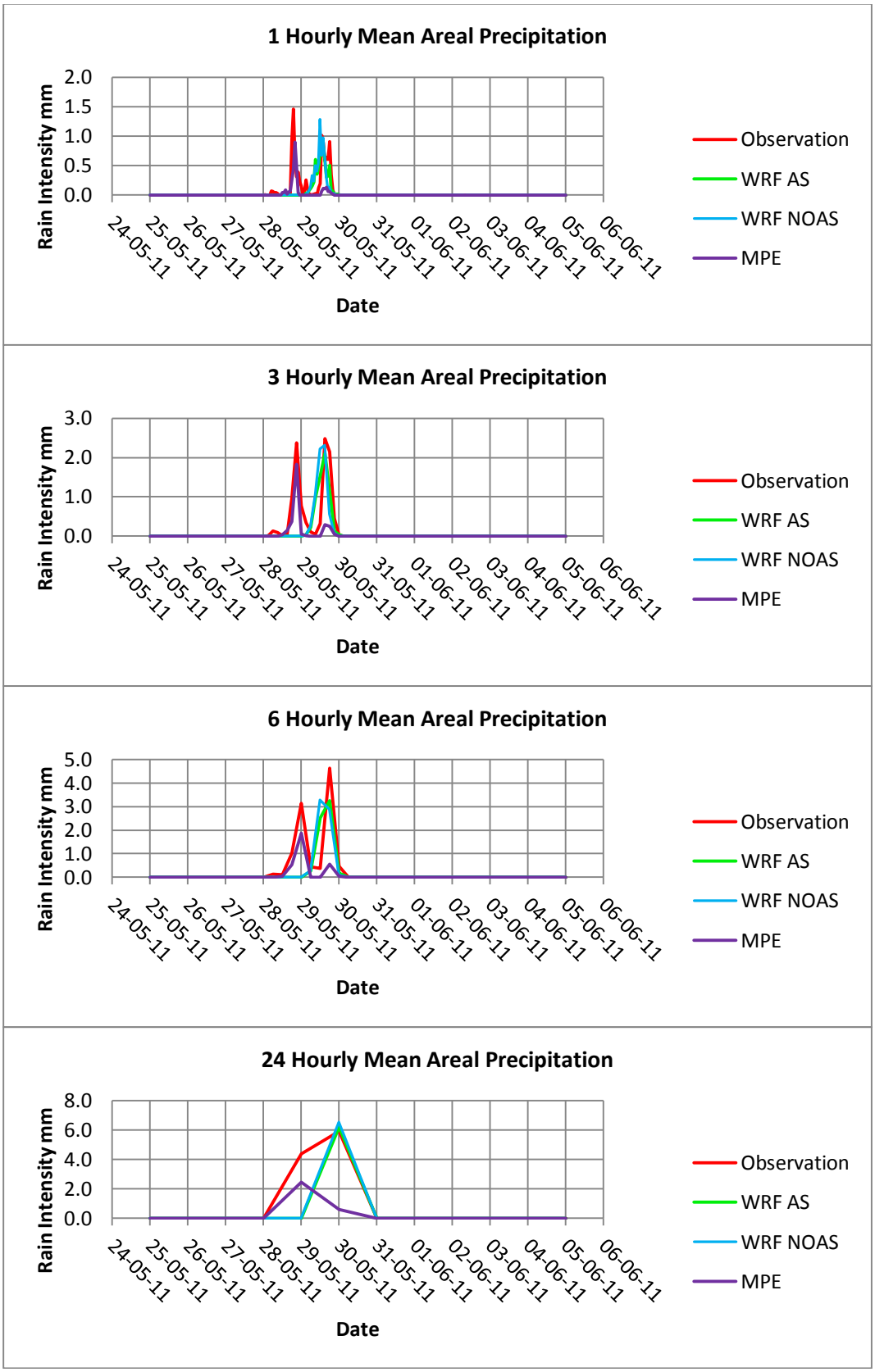

Figure 3.24: 1, 3, 6 and 24 hourly mean areal time series for Event 24

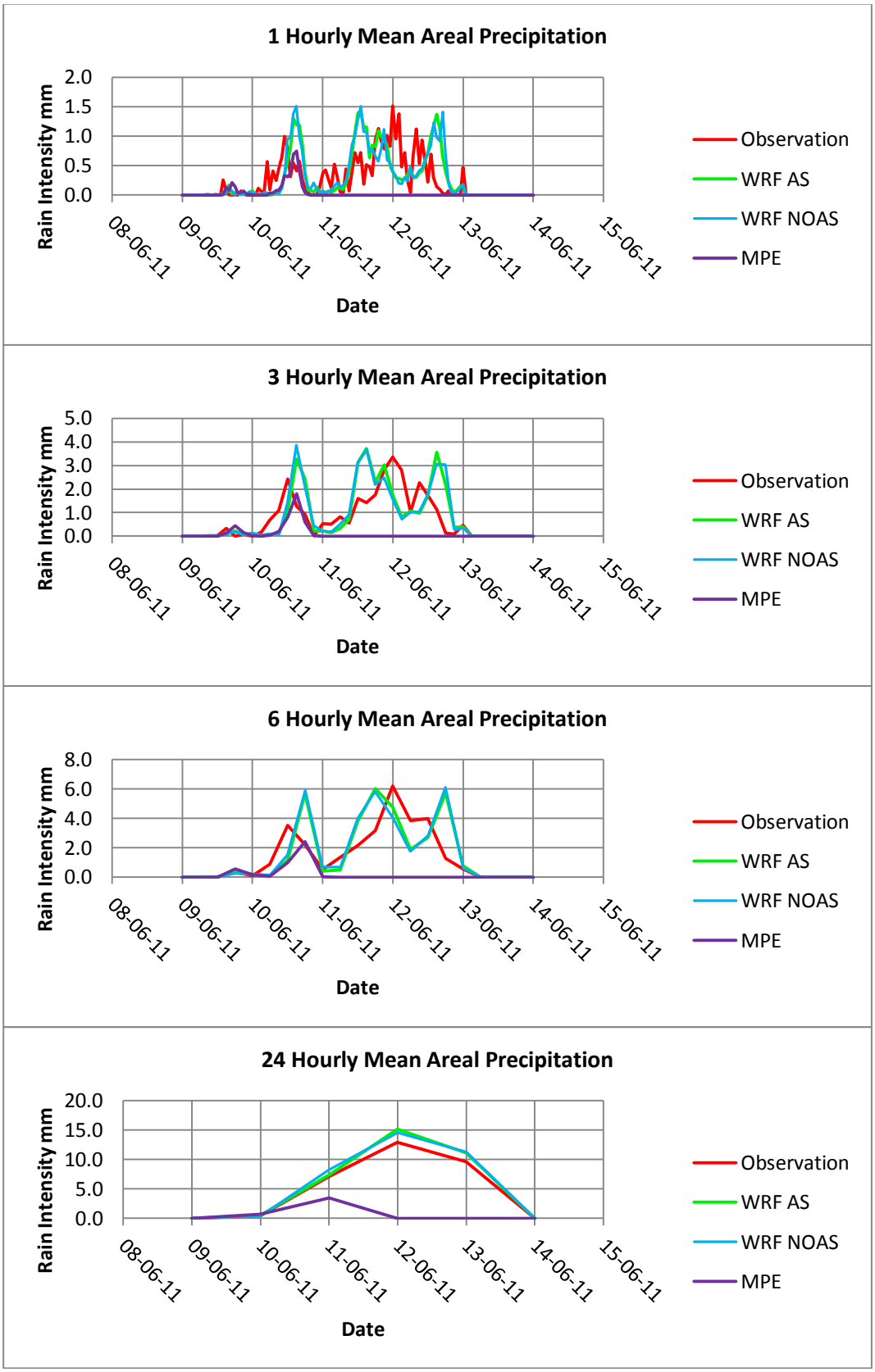

Figure 3.25: 1, 3, 6 and 24 hourly mean areal time series for Event 25

3.3 Statistical Analyses Using All Events

Using all event data together a scatter analysis is first performed to examine whether there exists a solid relationship between the data pairs of WRF- observation and MPE-observation along with different time intervals. Degree of the scattering among data pairs as well as the tendency of overestimation and underestimation against observations is determined from these analyses. Figures 3.26 – 3.29 show the scatter plots of observation versus WRF AS, WRF NOAS and MPE for 1, 3, 6, 24 hourly intervals, respectively. In these figures, the regression equations and correlation coefficient values of each data pair are also given.

As it is expected the least relationship between data pairs is obtained at hourly scatter plot with no discernible difference between WRF and MPE versus observations. As the time interval increases from 1 to 24-hour scatter decreases and trendlines of each precipitation product shows a closer pattern to 1:1 line and therefore, they are resulting in higher correlation values. In addition, in all time intervals, WRF AS shows consistently better correlation coefficient than WRF NOAS. According to scatter plots, more scattered behaviour of WRF NOAS particularly related with extreme overestimation and underestimation data points seems to be modified by data assimilation in WRF (WRF AS). These cases are more evident in 3-, 6-, and 24-hourly scatter diagrams. While MPE gives slightly higher correlation values than WRF with and without assimilation at 1-, 3-, and 6-hourly intervals it provides lower correlation coefficient at daily analysis.

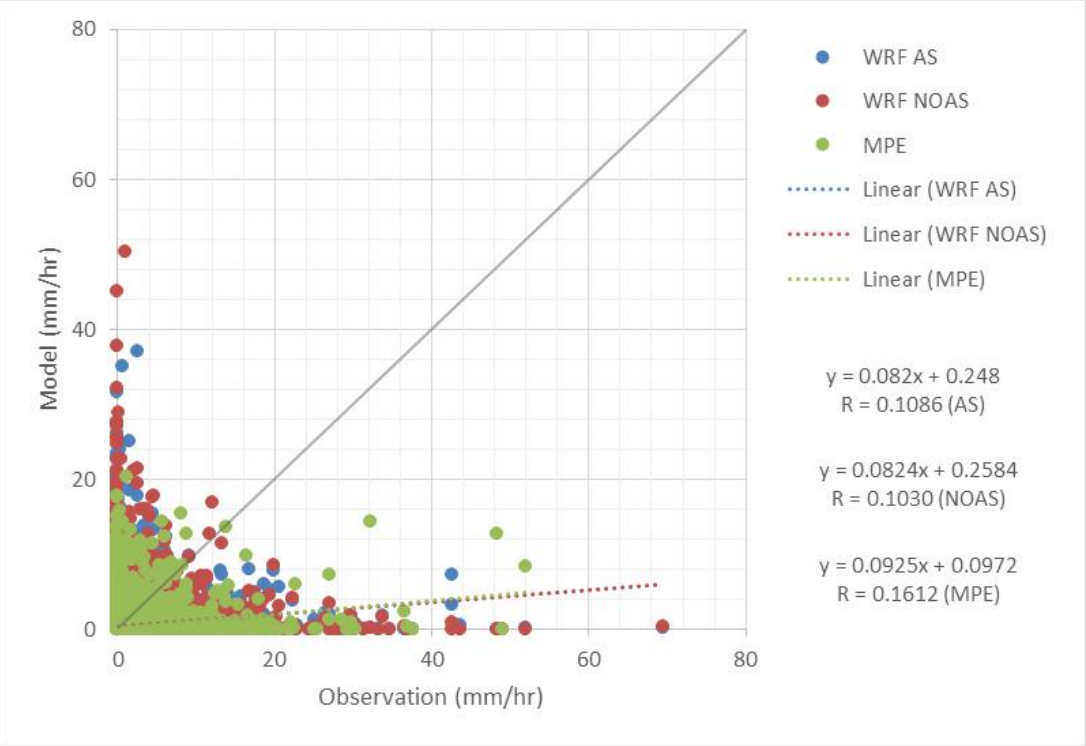

Figure 3.26: Scatter Diagrams for 1-Hourly Periods

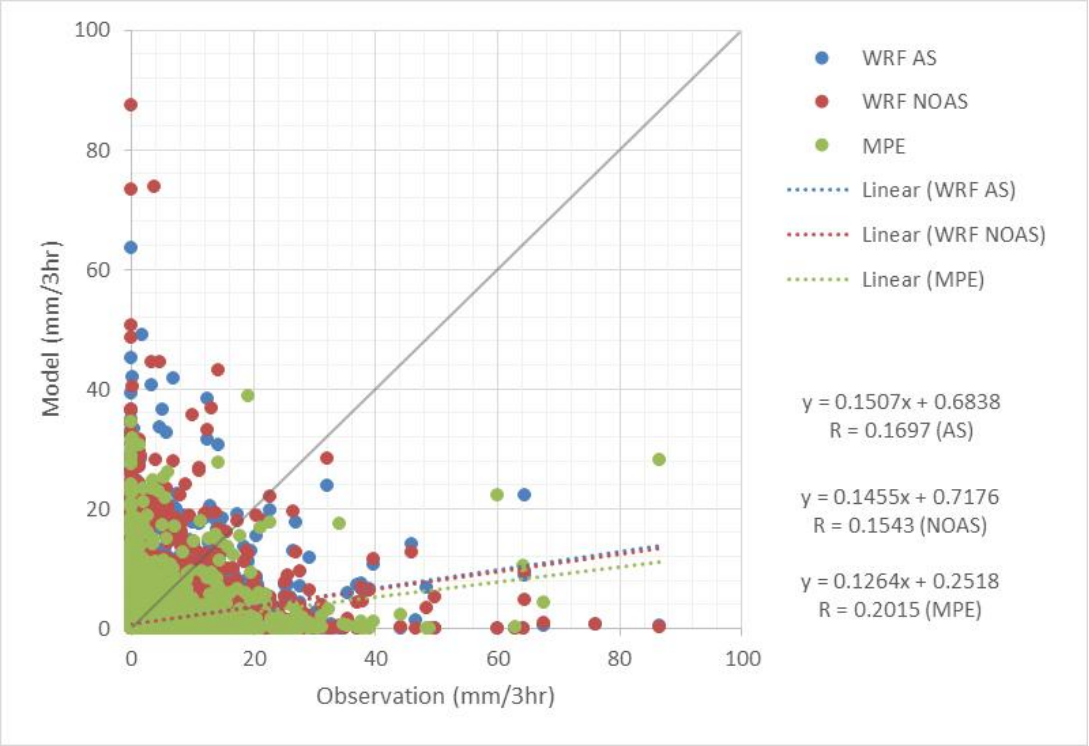

Figure 3.27: Scatter Diagrams for 3-Hourly Periods

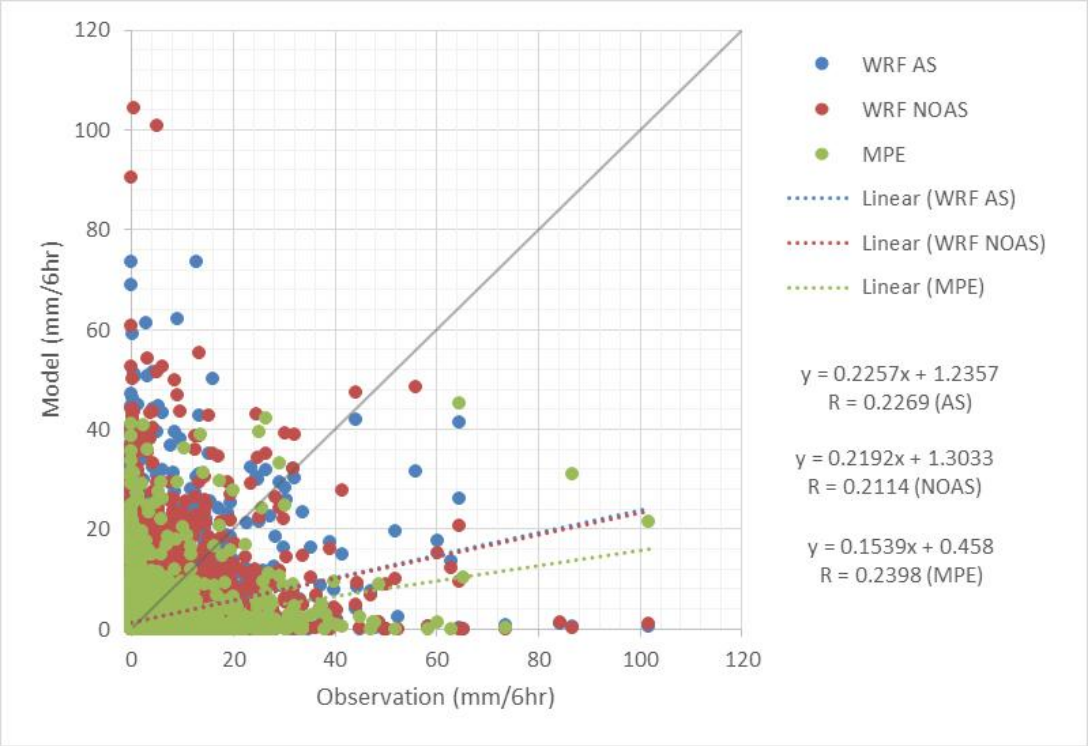

Figure 3.28: Scatter Diagrams for 6-Hourly Periods

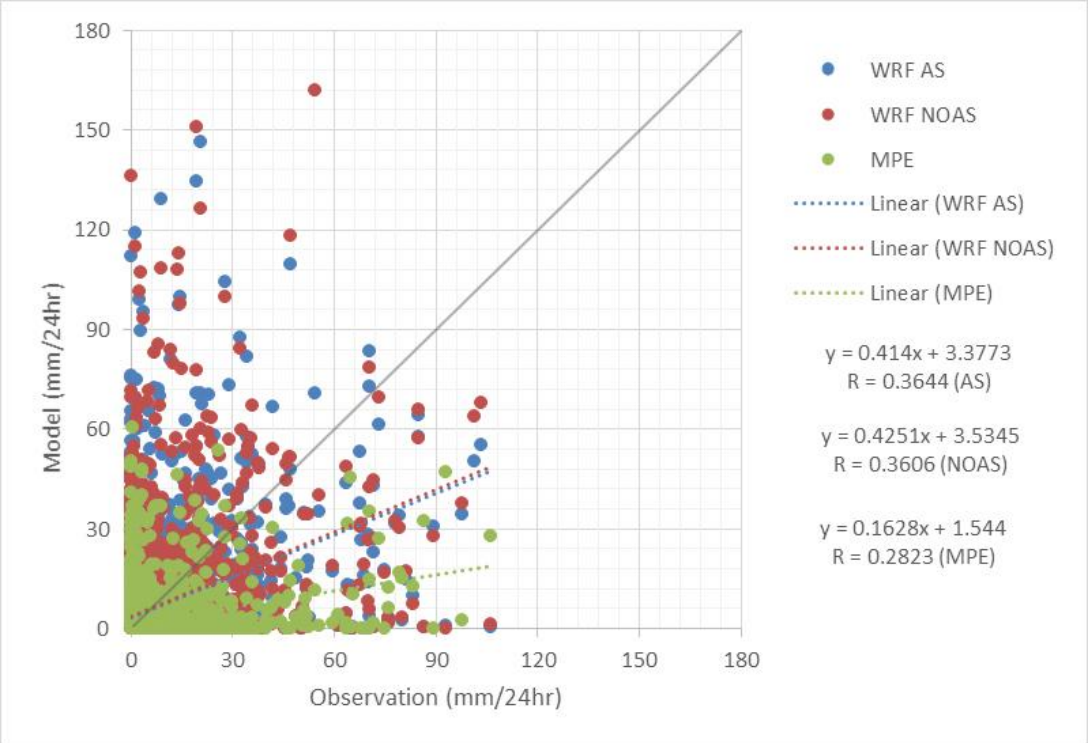

Figure 3.29: Scatter Diagrams for 24-Hourly Periods

The root mean square error (rmse), bias and correlation coefficient (R) of WRF and MPE precipitations are calculated for 1-, 3-, 6-, and 24-hourly periods and the results are shown in Table 3.1. According to results, assimilation shows consistent significance on WRF precipitation at all time intervals. With assimilated WRF outputs (WRF AS) lower rmse, bias values and higher correlation coefficients wit respect to WRF NOAS are obtained. Correlation coefficients increase with increasing time interval from 1 to 24 hours. MPE underestimates the precipitation that is shown with negative biases. These negative biases become more significant at higher time intervals toward 24-hour. When comparing to WRF model MPE shows better statistics in 1-, 3-, and 6-hourly rains but it shows lower correlation than WRF at daily precipitations because of the more pronounced effect of high negative biases at this interval. In the same table, the conditional rain (only non-zero observed precipitation cases and their respective model outputs) comparison statistics are also shown to test the performance of models for actual observed precipitation (>0) instants. With conditional rains, statistical performances of WRF and MPE decreases further with higher rmse and biases, and lower correlation. As the underestimation behaviour of MPE becomes more significant WRF with and without data assimilation also exhibits some underestimation characteristics with conditional rain analysis.

Table 3.1: Regular and Conditional Rain Statistics Summary for 1, 3, 6 and 24 hourly periods

Obs. Interval		WRF AS		WRF NOAS		MPE	
		Regular	Conditional	Regular	Conditional	Regular	Conditional
1 Hour	**BIAS (mm)**	0.0389	-1.0240	0.0493	-1.0048	-0.0885	-1.2968
	RMSE (mm)	1.6171	3.8412	1.6590	3.8774	1.3200	3.4998
	R	0.1088	0.0664	0.1030	0.0615	0.1613	0.1562
3 Hours	**BIAS (mm)**	0.1300	-1.1792	0.1604	-1.1097	-0.2733	-2.1068
	RMSE (mm)	3.6279	6.6968	3.7630	6.8647	2.9886	6.0921
	R	0.1696	0.1296	0.1541	0.1092	0.2016	0.2078
6 Hours	**BIAS (mm)**	0.2581	-1.0870	0.3174	-0.9508	-0.5249	-2.8489
	RMSE (mm)	5.8472	9.4730	6.0361	9.8639	4.7591	8.4245
	R	0.2270	0.1819	0.2114	0.1559	0.2397	0.2450
24 Hours	**BIAS (mm)**	0.8478	-0.2519	1.0530	0.0237	-1.8022	-5.3121
	RMSE (mm)	13.3393	18.5403	13.7038	19.0404	10.8916	16.3499
	R	0.3645	0.2939	0.3605	0.2910	0.2822	0.2038

Additionally, to quantify the improvement obtained with data assimilation in WRF precipitation the error reduction rate at each time interval is calculated and shown in Table 3.2. According to the calculated error reduction rates in this table, most improvement in WRF precipitation is observed on 3-hourly interval for regular analysis (3.59 %) and on 6-hourly interval for conditional analysis (3.96 %). In general, for regular rain and conditional rain analysis the average improvement is calculated as 3% and 2.5%, respectively.

Table 3.2: WRF rmse improvements for 1, 3, 6 and 24 hourly periods

Obs. Interval	Normal	Conditional
1 Hour	2.53%	0.94%
3 Hours	3.59%	2.45%
6 Hours	3.13%	3.96%
24 Hours	2.66%	2.63%

In a further statistical analysis, Probability of Detection (POD), False Alarm Rate (FAR), Critical Success Index (CSI) (Chokngamwong, R. and L. Chiu, 2007), Equitable Threat Score (ETS) and its bias (ETS Bias) scores (Lee et al., 2004) are determined for several threshold rainfall limits. With calculation of these scores the performance of WRF and MPE in capturing these different threshold rainfall values is observed. These statistical parameters are defined as below:

$$POD = A/(A+B) \quad (3.1)$$

$$FAR = C/(A+C) \quad (3.2)$$

$$CSI = A/(A+B+C) \quad (3.3)$$

$$ETS = (A-H)/(A+B+C-H) \quad (3.4)$$

$$ETS\ Bias = (A+B)/(A+C) \quad (3.5)$$

where:

$H = (A+B)(A+C)/(A+B+C+D)$,

and A is the number of matching precipitation data while both observation and model (WRF and MPE) shows precipitation; B is the number of occurrence where observation shows precipitation and model shows zero precipitation and C is the number of occurrence where model shows precipitation and observation shows zero precipitation. Also for ETS calculations, the additional parameters are; D is the number of occurrence where both observation and model shows zero precipitation.

In these analyses, if score values of POD, CSI, and ETS equal to 1 or (100%) they give perfect result and if score value of FAR equal to 0 it is a perfect result. For ETS bias, scores greater than 1 show overestimation while scores less than 1 indicate underestimation for the model being evaluated. 1-Hourly POD, FAR, CSI, ETS, ETS Bias threshold charts are shown in Figure 3.30a-b; 3-Hourly POD, FAR, CSI, ETS, ETS Bias threshold charts in Figure 3.31a-b; 6-Hourly POD, FAR, CSI, ETS, ETS Bias threshold charts in Figure 3.32a-b; 24-Hourly POD, FAR, CSI, ETS, ETS Bias threshold charts are shown in Figure 3.33a-b. With thresholds, observation and model responses to various precipitation amounts are tested.

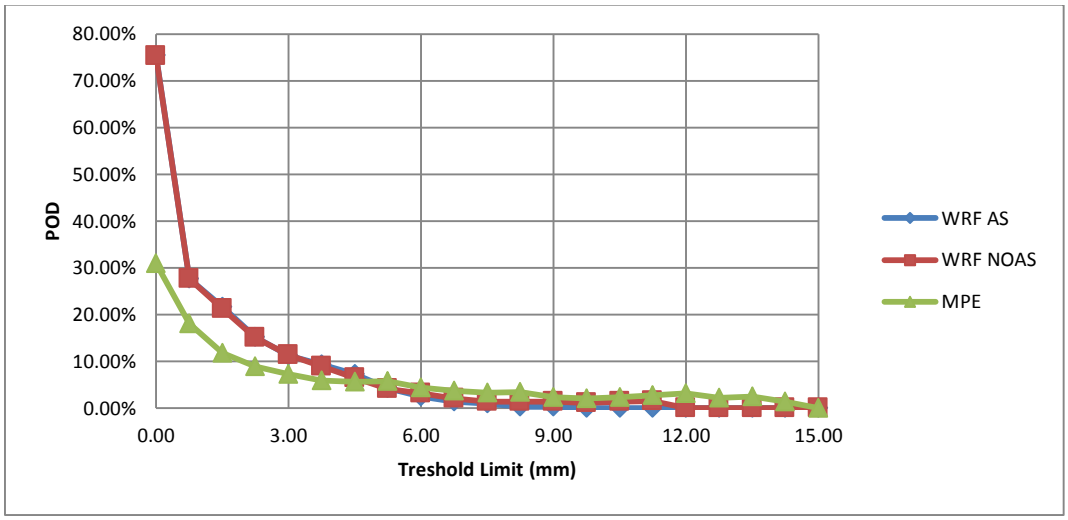

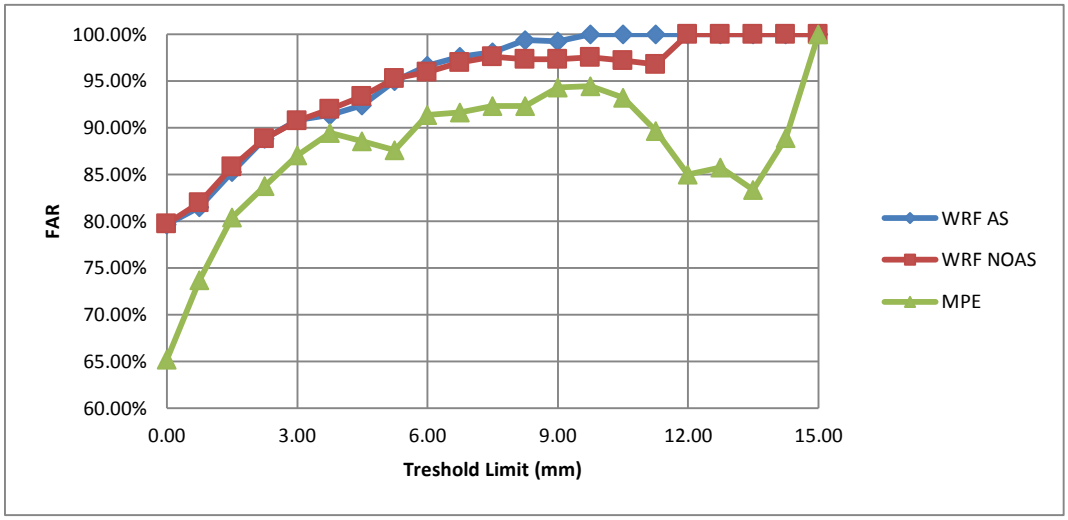

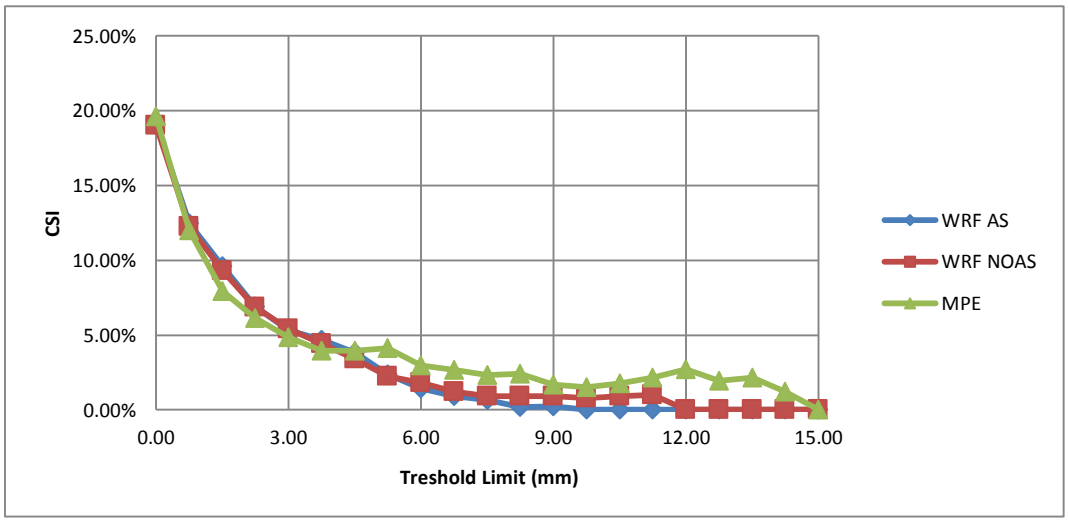

Figure 30a: 1 Hourly POD, FAR, CSI Charts

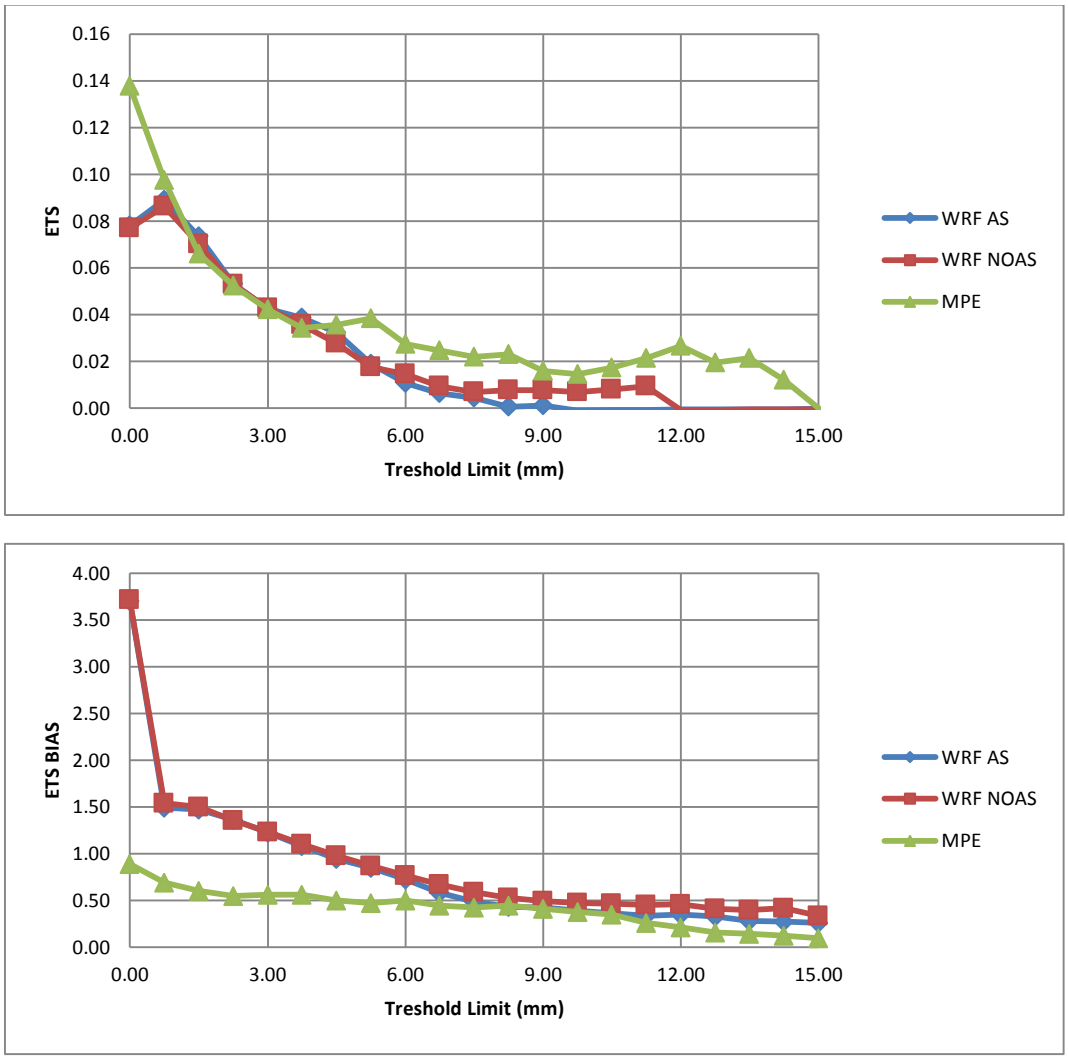

Figure 30b: 1 Hourly ETS, ETS BIAS Charts

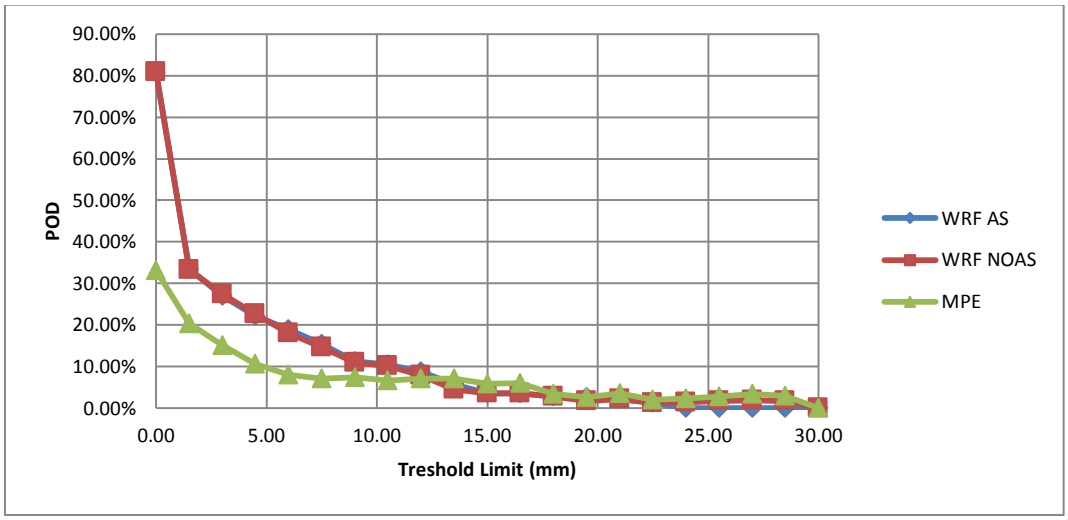

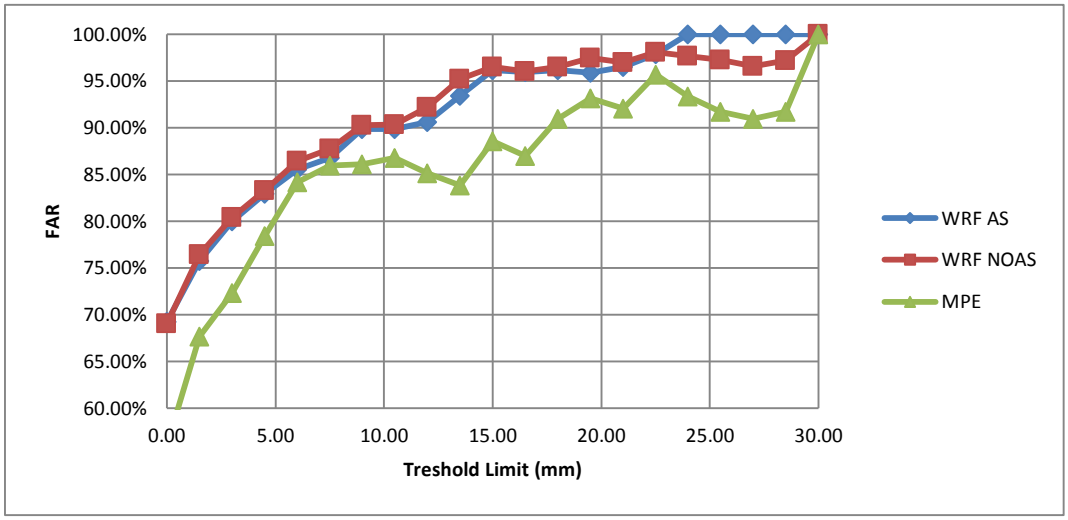

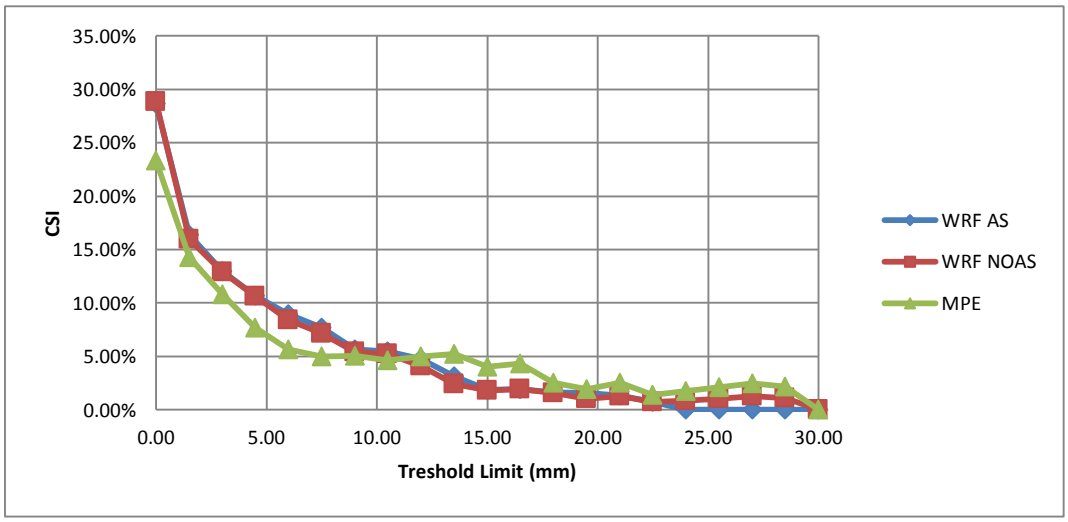

Figure 31a: 3 Hourly POD, FAR, CSI Charts

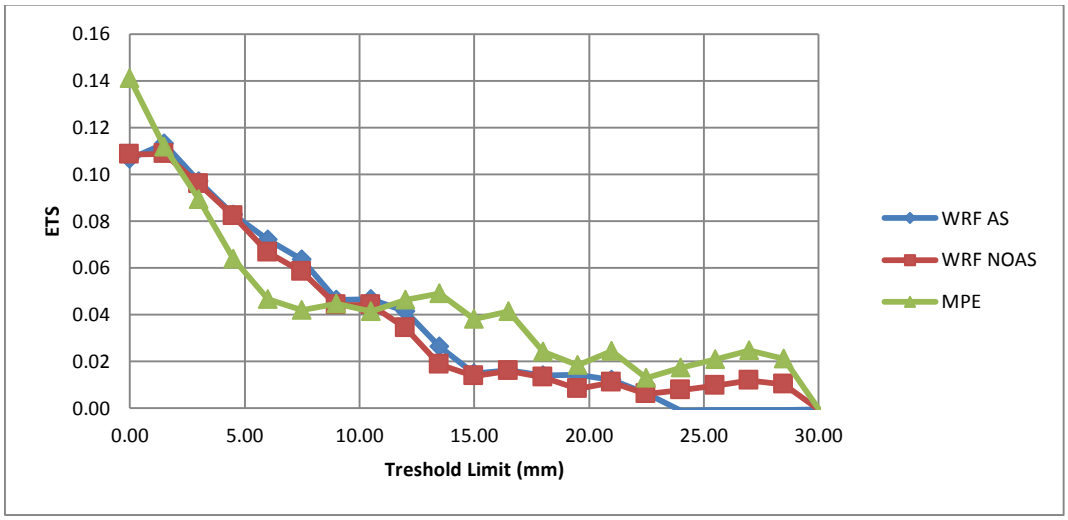

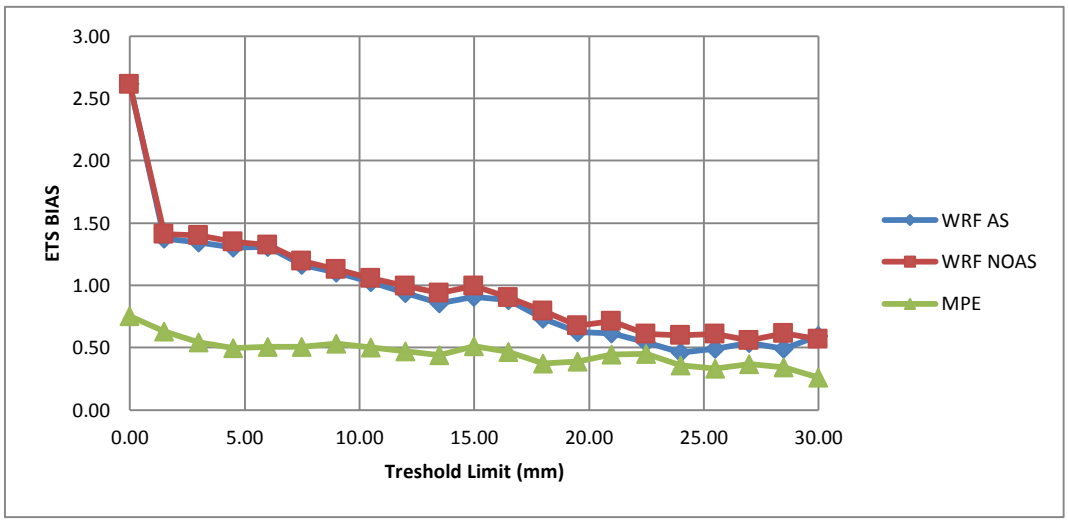

Figure 31b: 3 Hourly ETS, ETS BIAS Charts

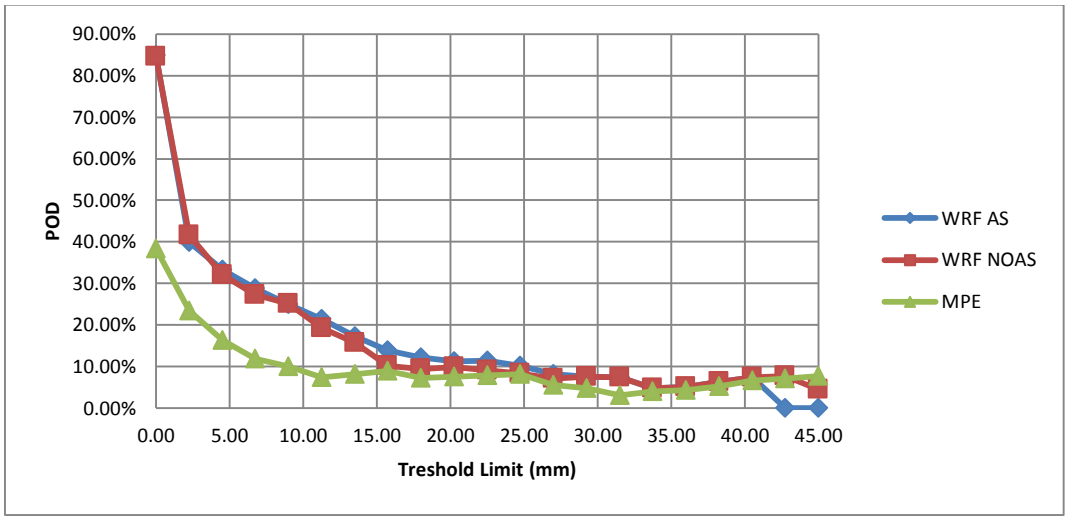

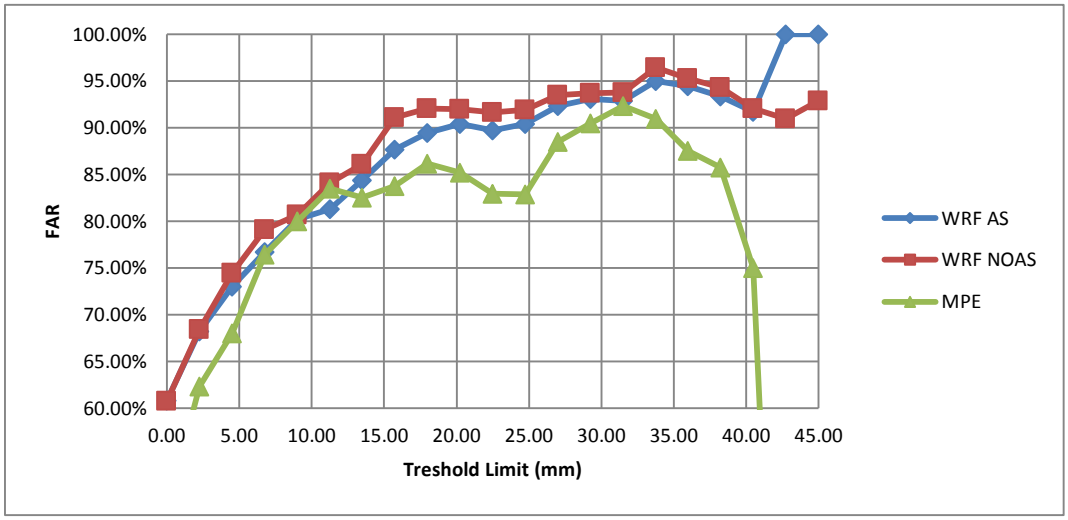

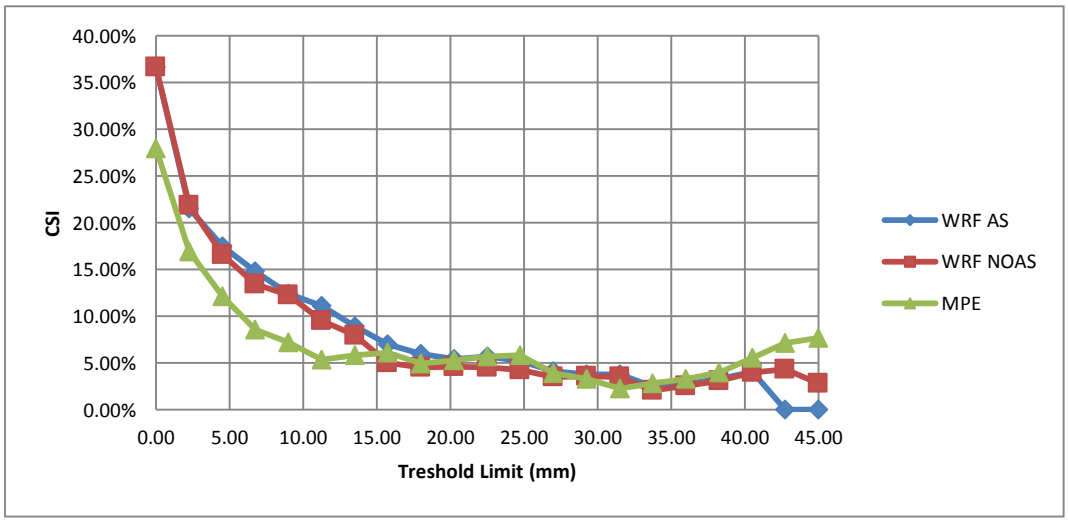

Figure 32a: 6 Hourly POD, FAR, CSI Charts

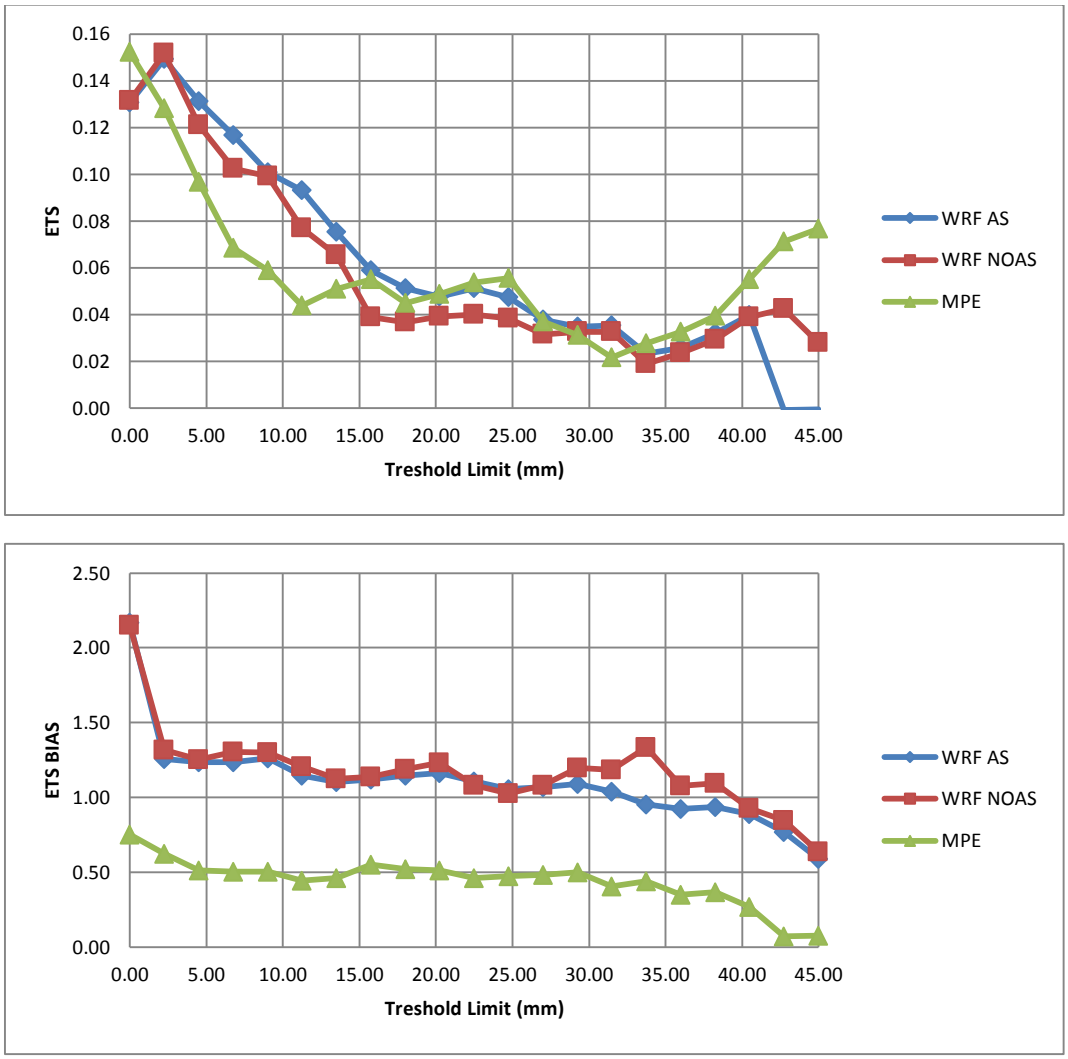

Figure 32b: 6 Hourly ETS, ETS BIAS Charts

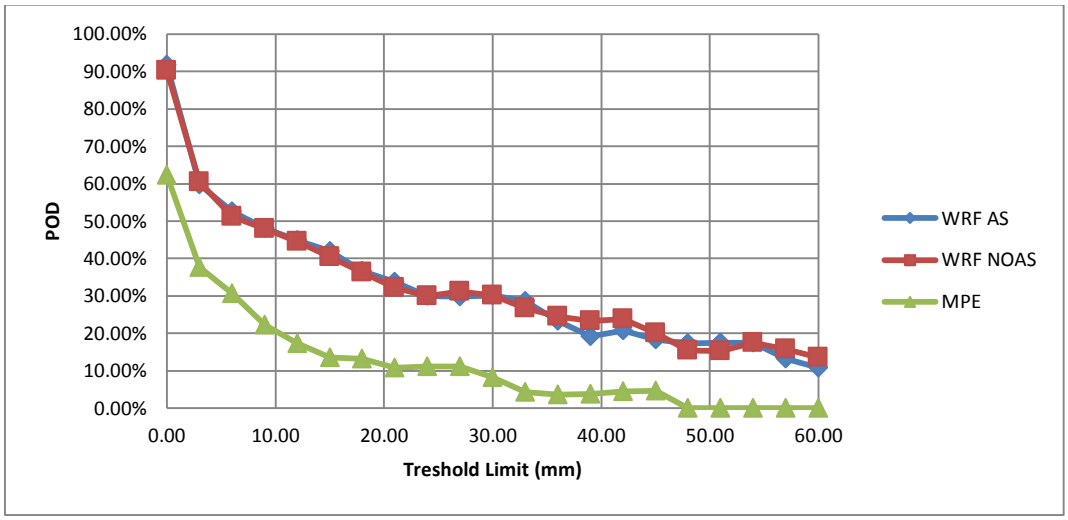

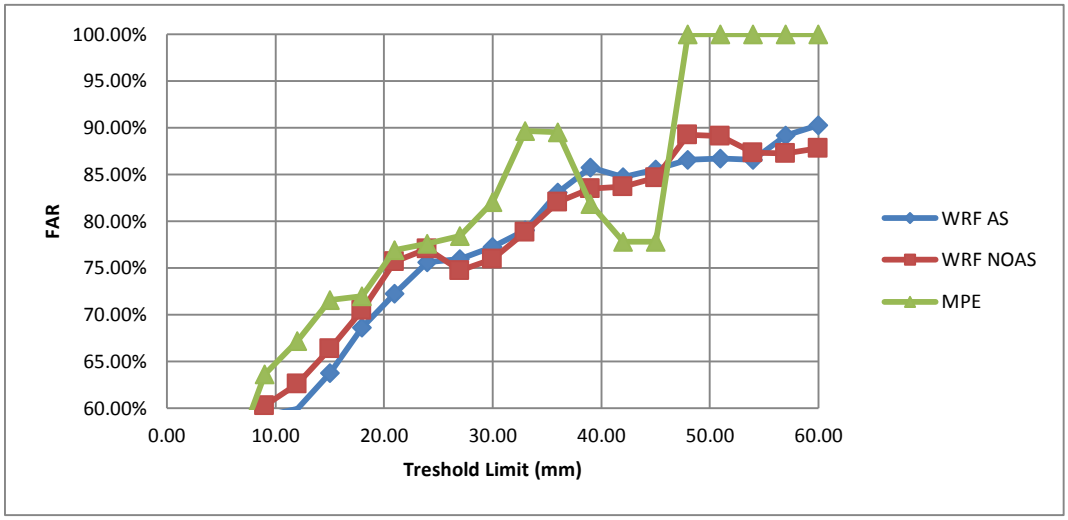

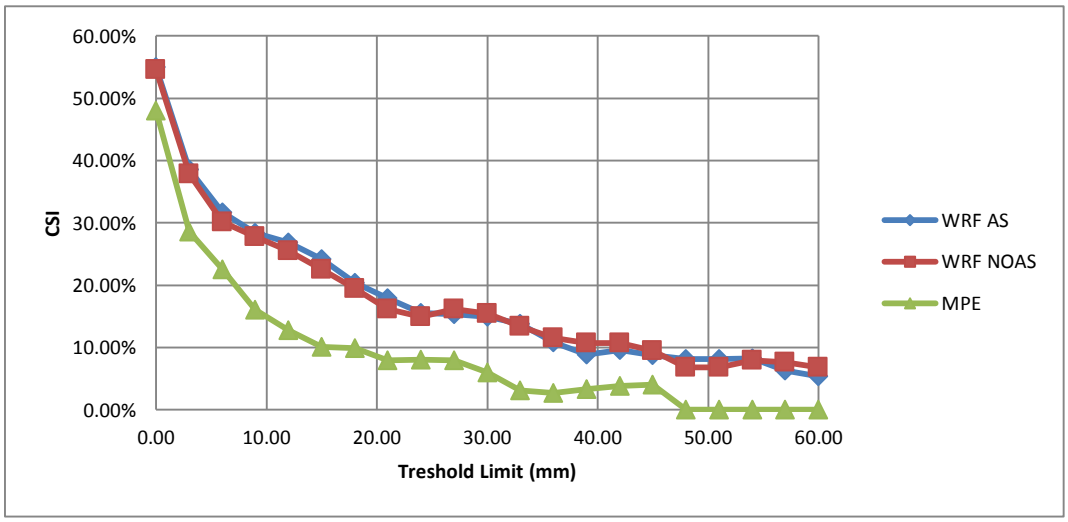

Figure 33a: 24 Hourly POD, FAR, CSI Charts

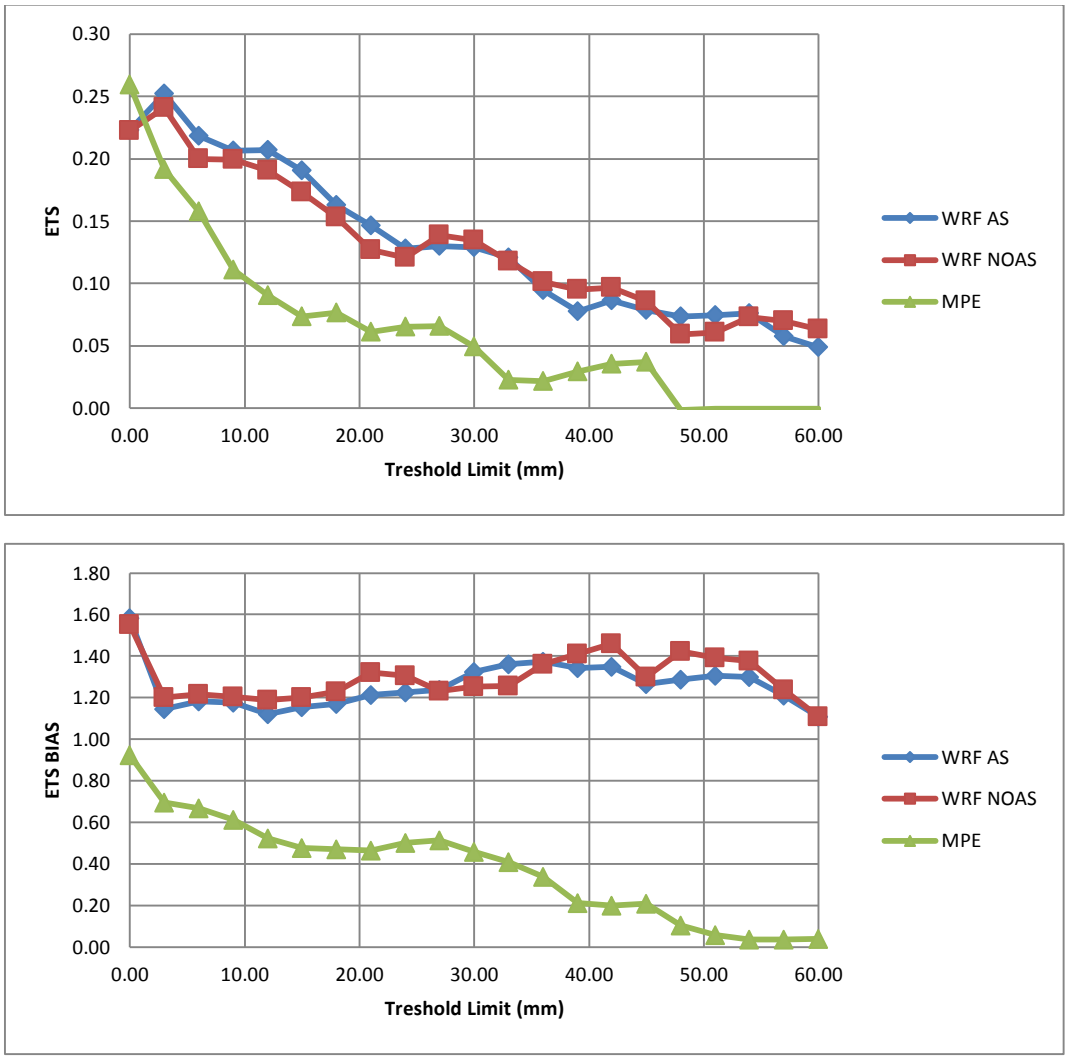

Figure 33b: 24 Hourly ETS, ETS BIAS Charts

In these plots, for a given threshold a high POD corresponds to high CSI, ETS and low FAR and ETS bias. On a general overview, with the increase of threshold limits, decrease in POD, CSI and ETS and increase in FAR acts as the logical behaviour for the corresponding analyses. For 3, 6 and 24-hourly analyses, WRF AS shows higher success scores than WRF NOAS along with threshold values, while 1-hourly analyses holds rather a fluctuating pattern for WRF comparison. Also satellite MPE outputs express relatively higher CSI and ETS values than WRF outputs towards the higher threshold values on 1-, 3-, and 6-hourly analysis, though on daily analysis, MPE consistently provides lower success scores (POD, CSI, ETS) than WRF along with all threshold values. In addition, FAR scores of MPE are always greater than that of WRF at all threshold values. The lower success scores at smaller threshold values in hourly analysis indicate that MPE misses the light intensity of rain events. With ETS Bias scores less than 1 MPE also shows in these charts its underestimation behaviour. ETS bias scores of MPE are substantially lower than that of both WRF outputs at all threshold values and all time intervals. Underestimation behaviour of MPE systematically appears at all threshold values while WRF model shows the similar behaviour only towards higher threshold values in 1-, 3-, and 6-hourly rainfall intervals. Also as a comparison, ETS charts show significantly more visible improvements than CSI for WRF outputs for different thresholds.

3.4 Statistical Analyses Using Event and Station Based Datasets

In event-based analyses, using 34 stations and their corresponding grid points, spatial variation of precipitation for each event is examined. The effect of local influences on the performance of WRF model and satellite-generated precipitation among events is determined by investigating the spatial variation of precipitation for each event. For each event, bias, root mean square error (RMSE), and correlation coefficient (R) are calculated and shown in Figures 3.34 - 3.37, respectively for 1-, 3-, 6- and 24- hourly rainfall intervals as WRF AS, WRF NOAS and MPE. Almost in all events, generally, decrease in Bias and RMSE and more visible increase in R are observed on WRF AS with respect to WRF NOAS. As a result of this, while assimilation shows a minor effect on magnitude of precipitation, it shows an important impact on general precipitation trend in a desired direction. As seen from MPE bias values (negative biases) MPE algorithm shows generally a dry trend based on events (they are described with event numbers from 10 to 25). The dry bias character of MPE results in falsely lower RMSE values with respect to WRF in many cases. In most cases, WRF AS generates significantly better statistical results than WRF NOAS and MPE. Spatial influences on rainfall show variability from event to event because there might be different precipitation type and regime exist among events.

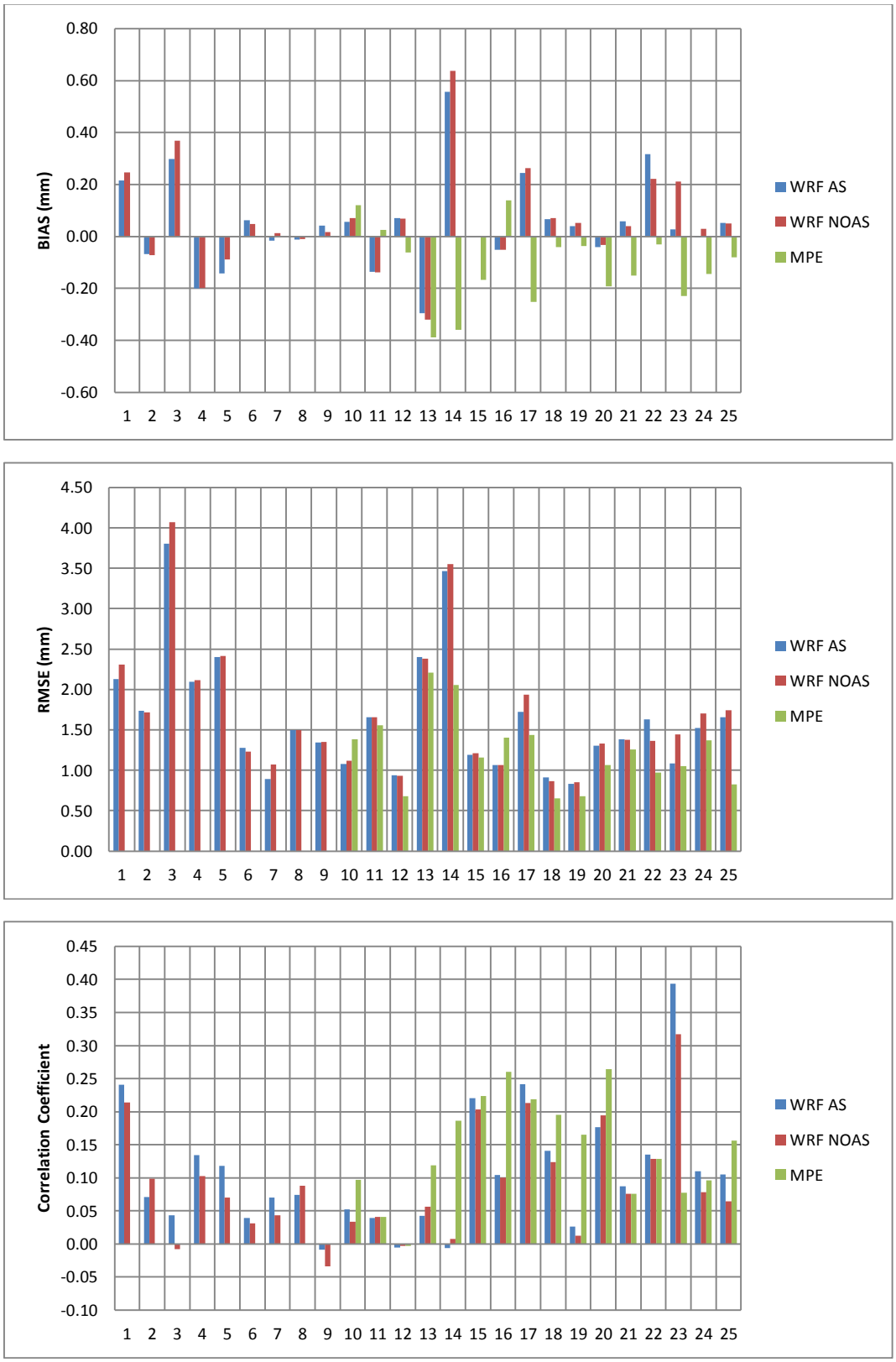

Figure 3.34: Event Based 1-Hourly Bias, RMSE and R Charts

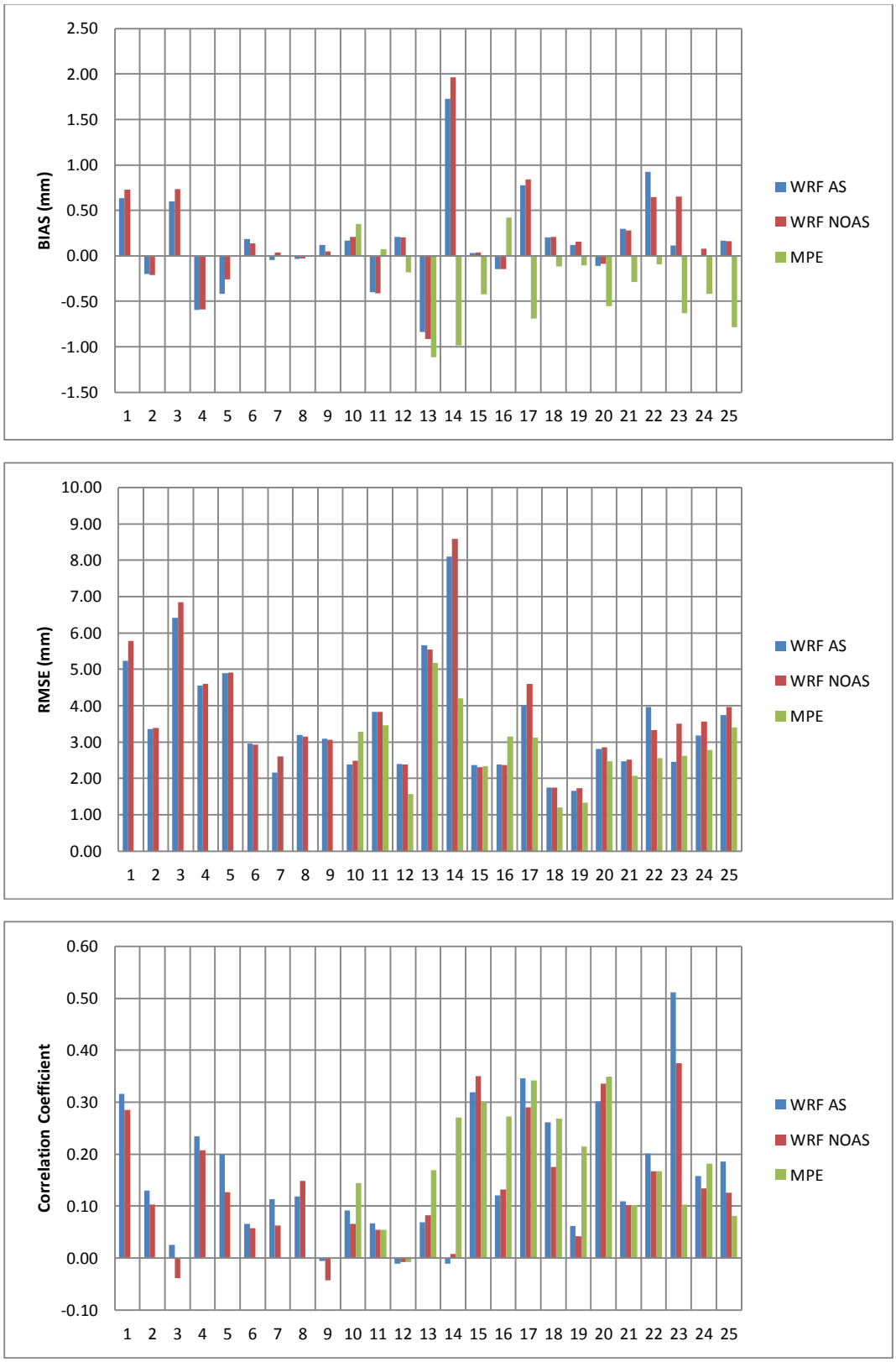

Figure 3.35: Event Based 3-Hourly Bias, RMSE and R Charts

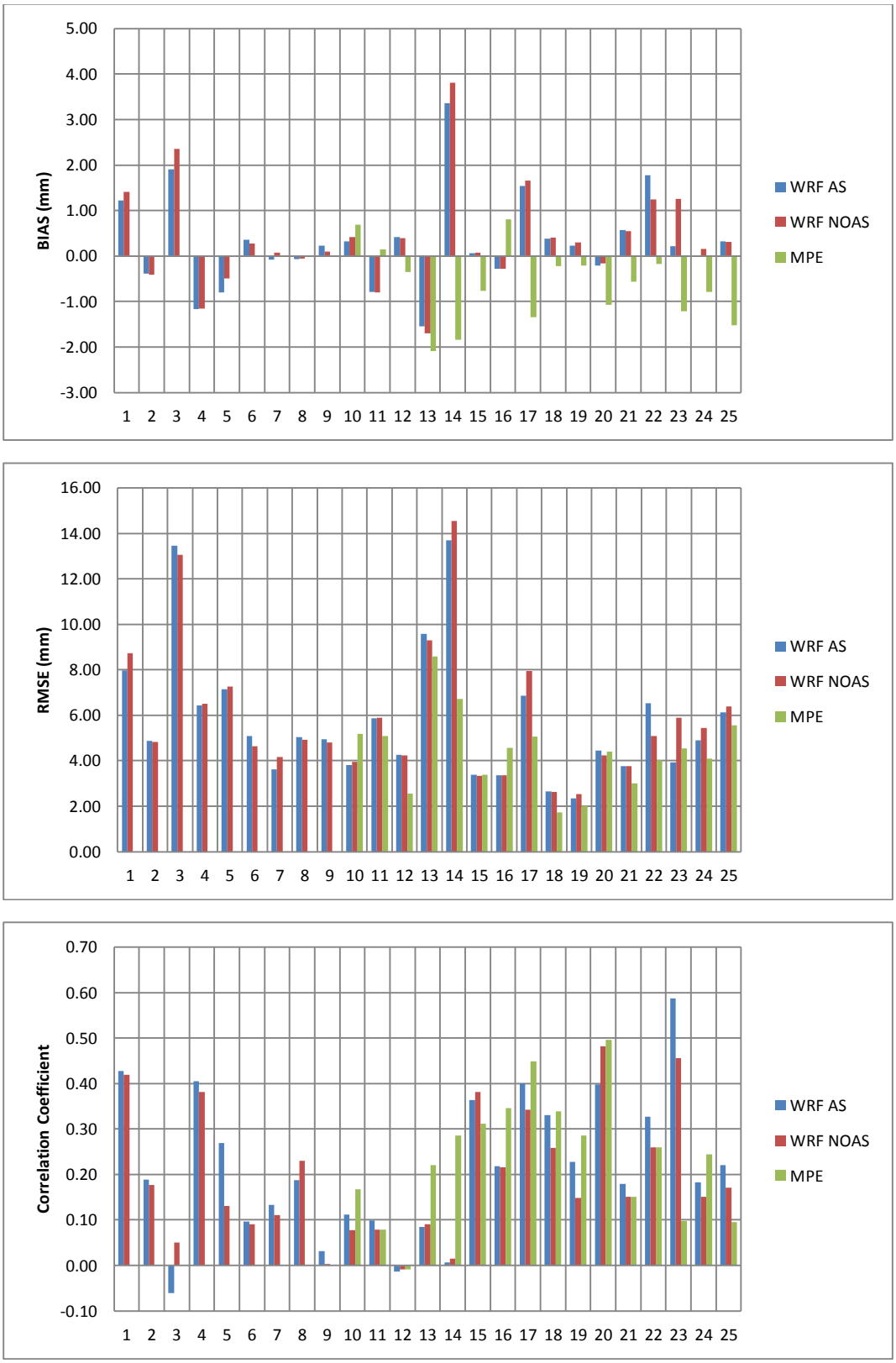

Figure 3.36: Event Based 6-Hourly Bias, RMSE and R Charts

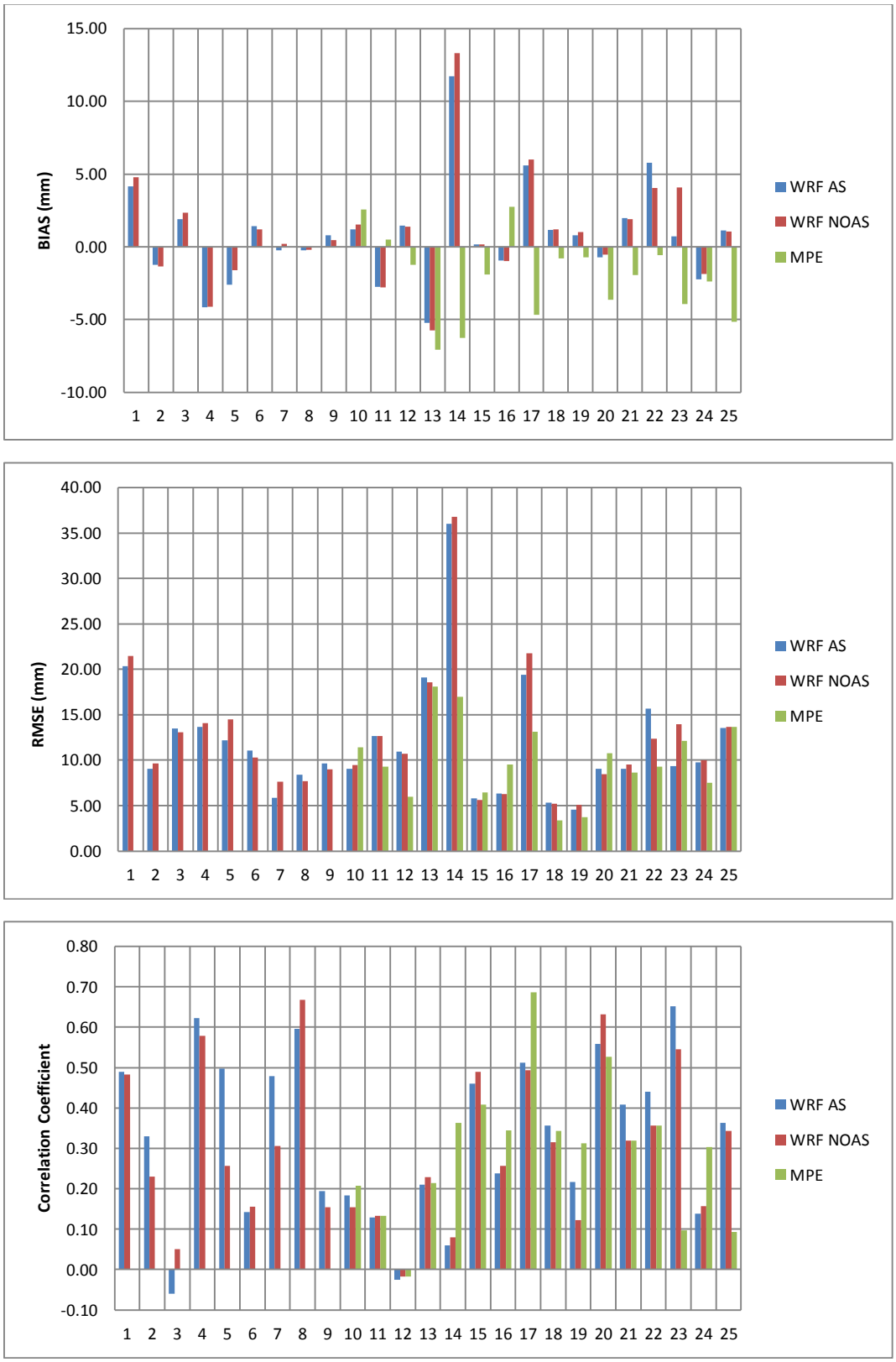

Figure 3.37: Event Based 24-Hourly Bias, RMSE and R Charts

In station based analysis, each of 34 stations is examined individually by combining 25 different event periods to generate a temporal evaluation In Figures 3.38, 3.39, 3.40, and 3.41 , Bias, RMSE, and Correlation coefficient charts for 1-, 3-, 6-, and 24-hourly intervals, respectively are shown for WRF AS, WRF NOAS and MPE at each station. Like in event based analyses, station based analyses also show significant improvement in WRF precipitation with data assimilation. Especially in 3-hourly analyses, improvements are very significant with correlation coefficient values. As explained previously in hourly analysis (1, 3, and 6) MPE provides better statistics than WRF model in many stations because of its underestimation behaviour but in daily analysis its skill decreases largely due to more pronounced effect of negative biases. However, even though MPE does provide substantially lower precipitation amount with respect to observations it shows a good skill in timing of precipitation events because of significant high correlation coefficients observed at many stations. With station- and event-based analyses it can be concluded that assimilation in WRF interprets the temporal effects better than spatial effects. In this study, as summer-time precipitation events are selected for analyses, the corresponding events are convective system origin and in such cases, uncertainties of spatial effects results in lower statistical reliability than temporal effects.

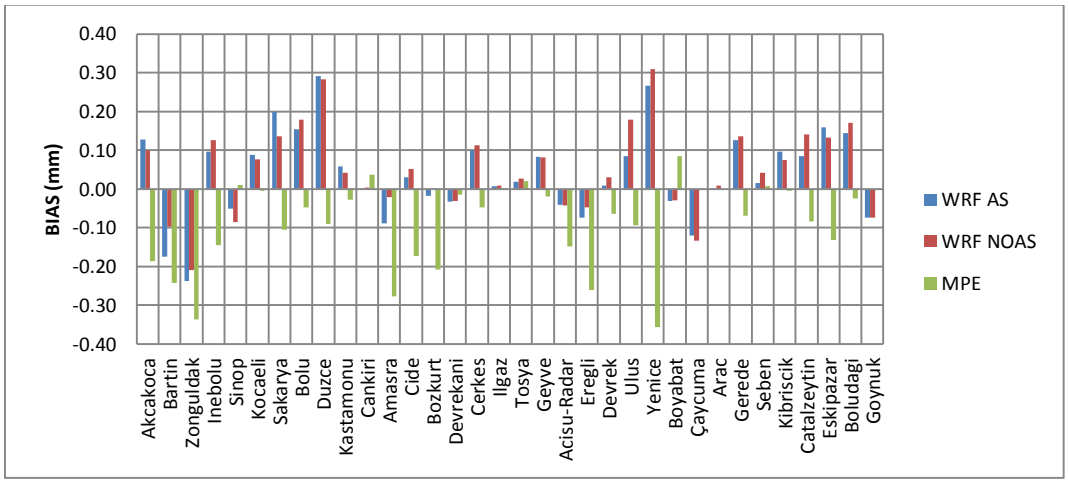

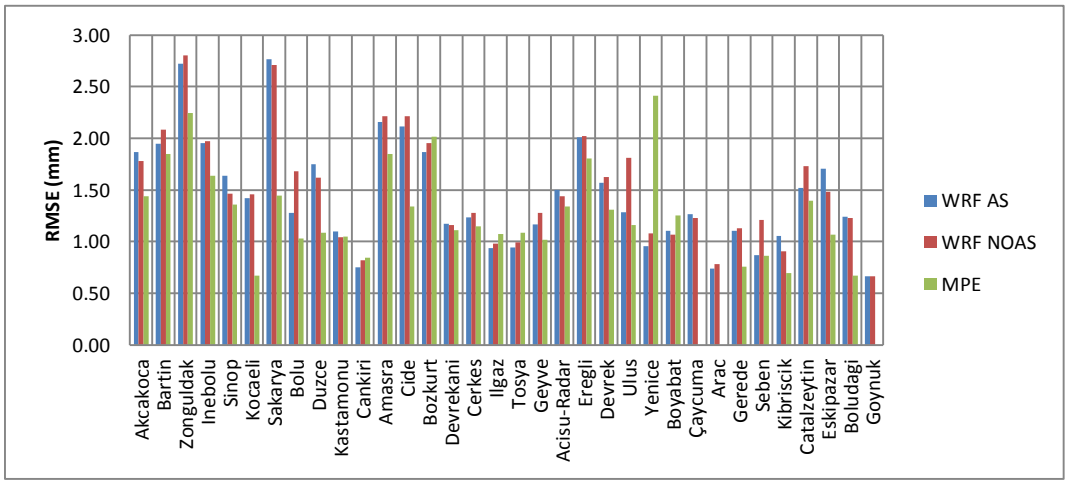

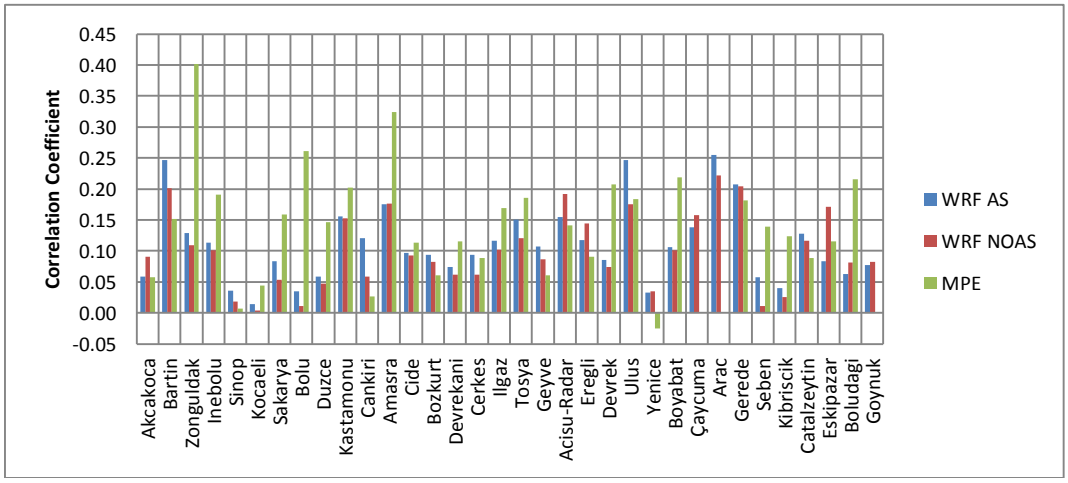

Figure 3.38: Station Based 1-Hourly Bias, RMSE and R Charts

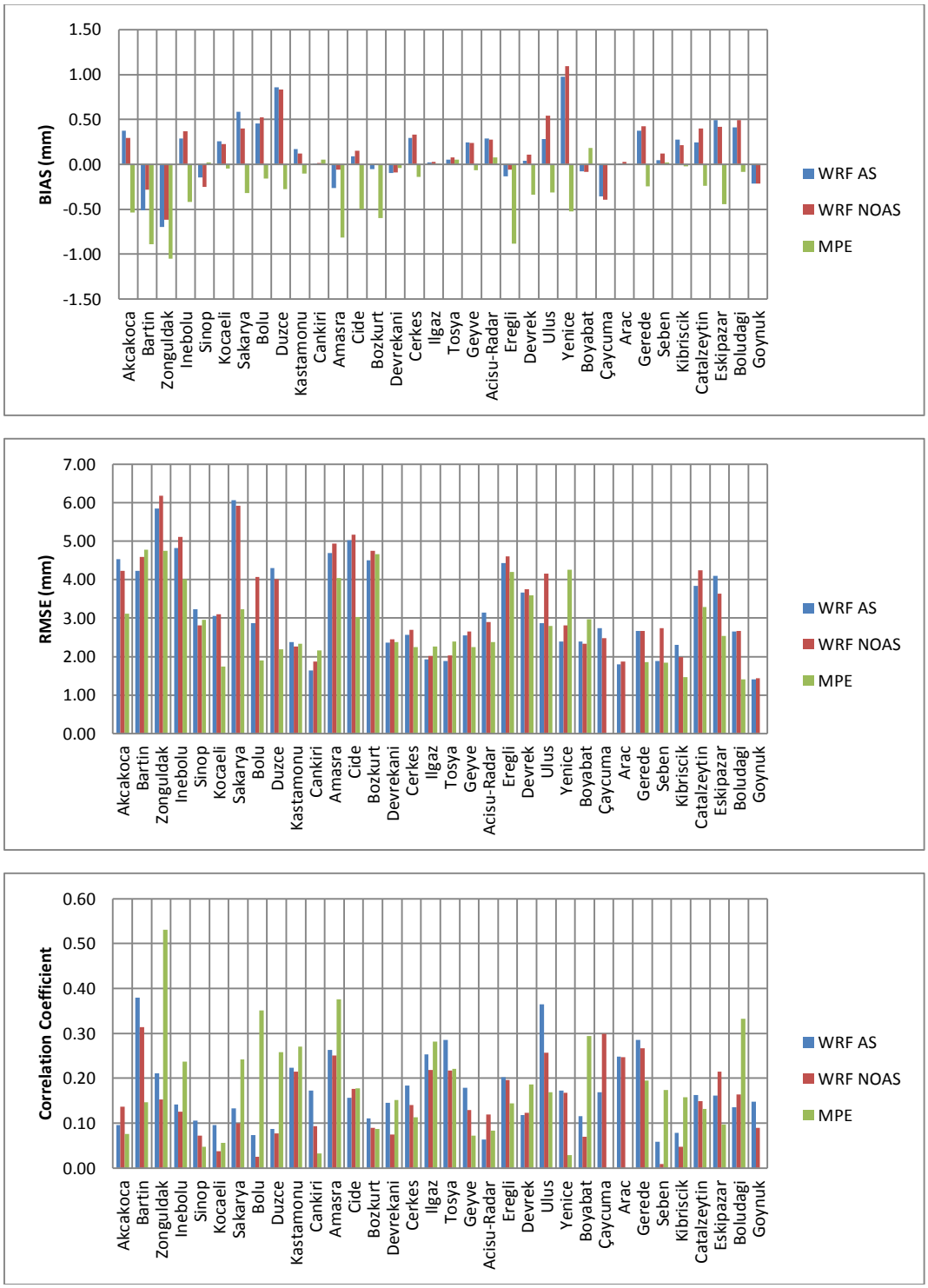

Figure 3.39: Station Based 3-Hourly Bias, RMSE and R Charts

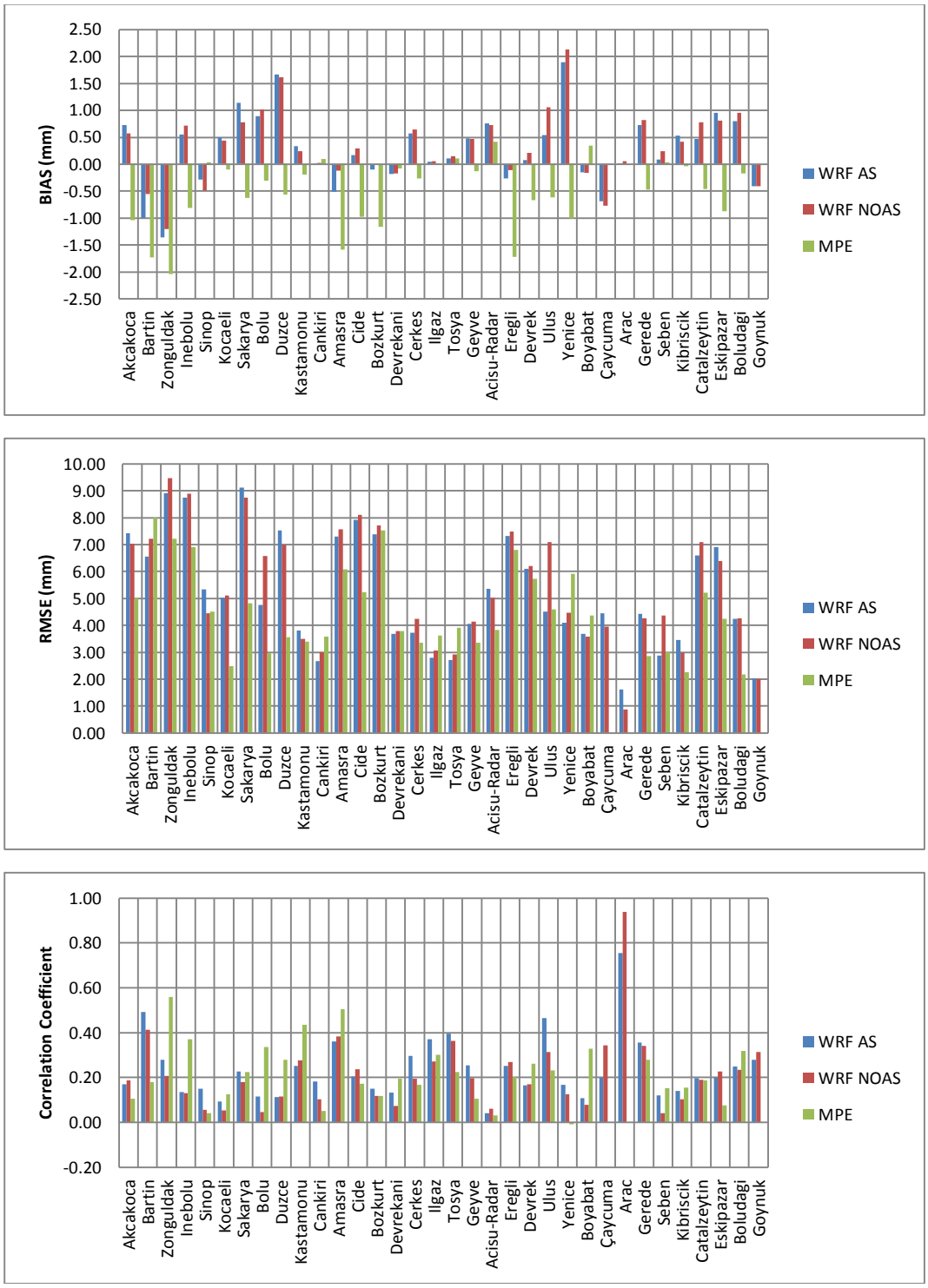

Figure 3.40: Station Based 6-Hourly Bias, RMSE and R Charts

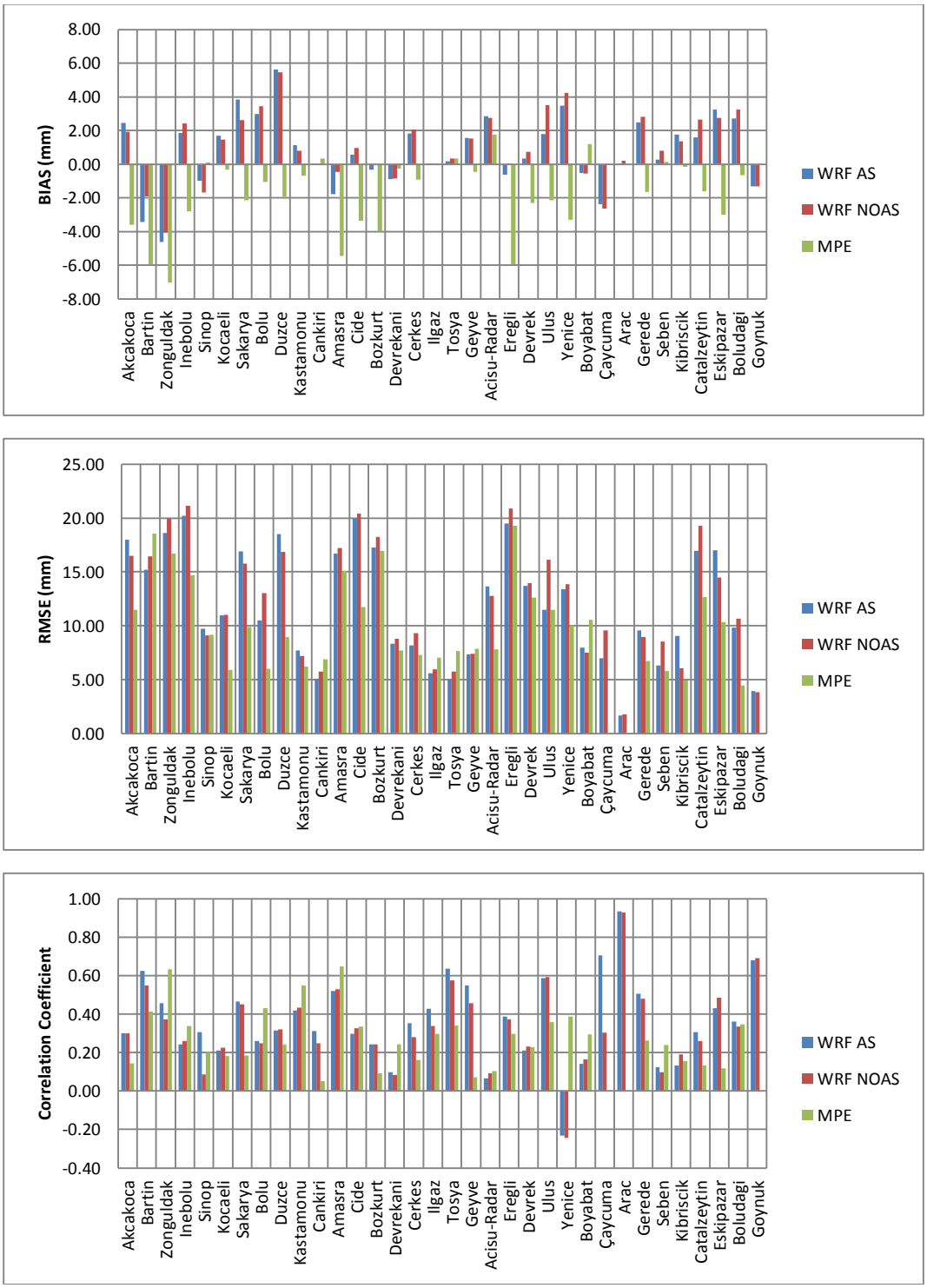

Figure 3.41: Station Based 24-Hourly Bias, RMSE and R Charts

Average RMSE values of 1-, 3-, 6-, and 24–hourly intervals from WRF AS, WRF NOAS, and MPE are given for event- and station-based analyses in Table 3.3. The lower RMSE values are obtained with WRF AS results in all time intervals. The station based analyses in WRF

show lower error rates than event based analyses while in MPE results it is vice versa. Comparing to spatial effects in precipitation the temporal effects are better resolved by WRF model. Resulting from higher error scores of station based analyses, it can be commented that uncertainty in spatial variability over the domain increases with complex topography and convective rain characteristics.

Table 3.3: Mean RMSE scores (mm) for WRF AS, WRF NOAS and MPE

	Event Based			Station Based		
	WRF AS	WRF NOAS	MPE	WRF AS	WRF NOAS	MPE
1 Hourly	1.641	1.693	1.235	1.453	1.497	1.291
3 Hourly	3.559	3.701	2.794	3.256	3.385	2.871
6 Hourly	5.765	5.897	4.405	5.21	5.368	4.527
24 Hourly	11.973	12.302	9.997	11.783	12.175	10.082

For both event- and station-based analyses, the mean error reduction rates in RMSE for each time interval are calculated and shown in Table 3.4. In both event- and station-based analyses, 3-hourly rain interval showed the highest improvement rates with 5.13 % in event-based and 4.29 % in station-based when data assimilation is used in WRF model. In some cases because of the chaotic status of the atmosphere, the assimilation degrades precipitation against observations as these cases are seen in analyses. When such cases are extracted from analyses the direct effect of assimilation on precipitation amount can be observed and that results in more enhanced error reduction rates in analyses. For example, those rates are increased from 5.13% to 11.39% in 3-hourly interval. In a very similar study by Liu et al, (2012), a small basin with more observation data available is used to test assimilation performance. In this study, the WRF model with and without 3DVAR assimilation is run and domain averaged daily precipitations at 10 km resolution are found to be 8.52 mm and 0.15 mm, respectively. Based on observation, bias percentage values are equal to -71% and -99% with and without assimilation. As these results are compared with results presented in this study, it is observed that similar improvements are obtained.

Table 3.4: Event and Station based time dependent RMSE improvement averages

Analysis Type	**Data Type**	**Hourly Time Period**			
		1 Hourly	3 Hourly	6 Hourly	24 Hourly
Event Based Analysis	All	4.31%	5.13%	3.72%	4.21%
	Excl. NOAS better values	7.80%	9.19%	9.29%	10.12%
Station Based Analysis	All	2.79%	4.29%	3.81%	4.08%
	Excl. NOAS better values	8.99%	11.39%	11.46%	11.20%

3.5 Event and Station Based POD, FAR, CSI Correlations

While improvements provided by assimilation are given per event and per station basis in previous analyses, the performances of WRF AS, WRF NOAS and MPE among stations and events are evaluated by interrelating POD, FAR, and CSI among each other (Kidd et al. 2011). In Figures 3.42a -3.42b, 1-, 3-, 6- and 24-hourly charts for POD, FAR and CSI are shown for each event. According to these charts, WRF model shows higher POD and lower FAR values than MPE algorithm in a more scattered pattern, and as the time interval increases from 1-hour to 24-hour, desired pattern of significant increase in POD and decrease in FAR are witnessed. Thus, CSI values, which is a function of both POD and FAR, converges towards 1, shown within contours. Scattering among the events occurred because of the spatial impacts, vary from event to event. In addition, WRF calculates the precipitation based on physical parameterization while satellite algorithm determines the precipitation based on empirical equation. This causes WRF model to predict rainfall in a more scattered way than the MPE algorithm. In Figures 3.43a - 3.43b, POD, FAR, CSI charts (Kidd et al. (2011)) of 1-, 3-, 6-, and 24-hourly analyses are shown for each station. In these charts, WRF and MPE precipitations shows a clustering among themselves and as seen in event based charts, the consistency of statistical results increases with respect to increase in rainfall analysis from 1 to 24 hour. With a clustering feature of rainfall statistics it is indicated that WRF or MPE captures the temporal variation in precipitation similarly. For both event and station based analyses, MPE shows higher FAR and lower CSI values, while POD values give close results when compared to WRF model outputs.

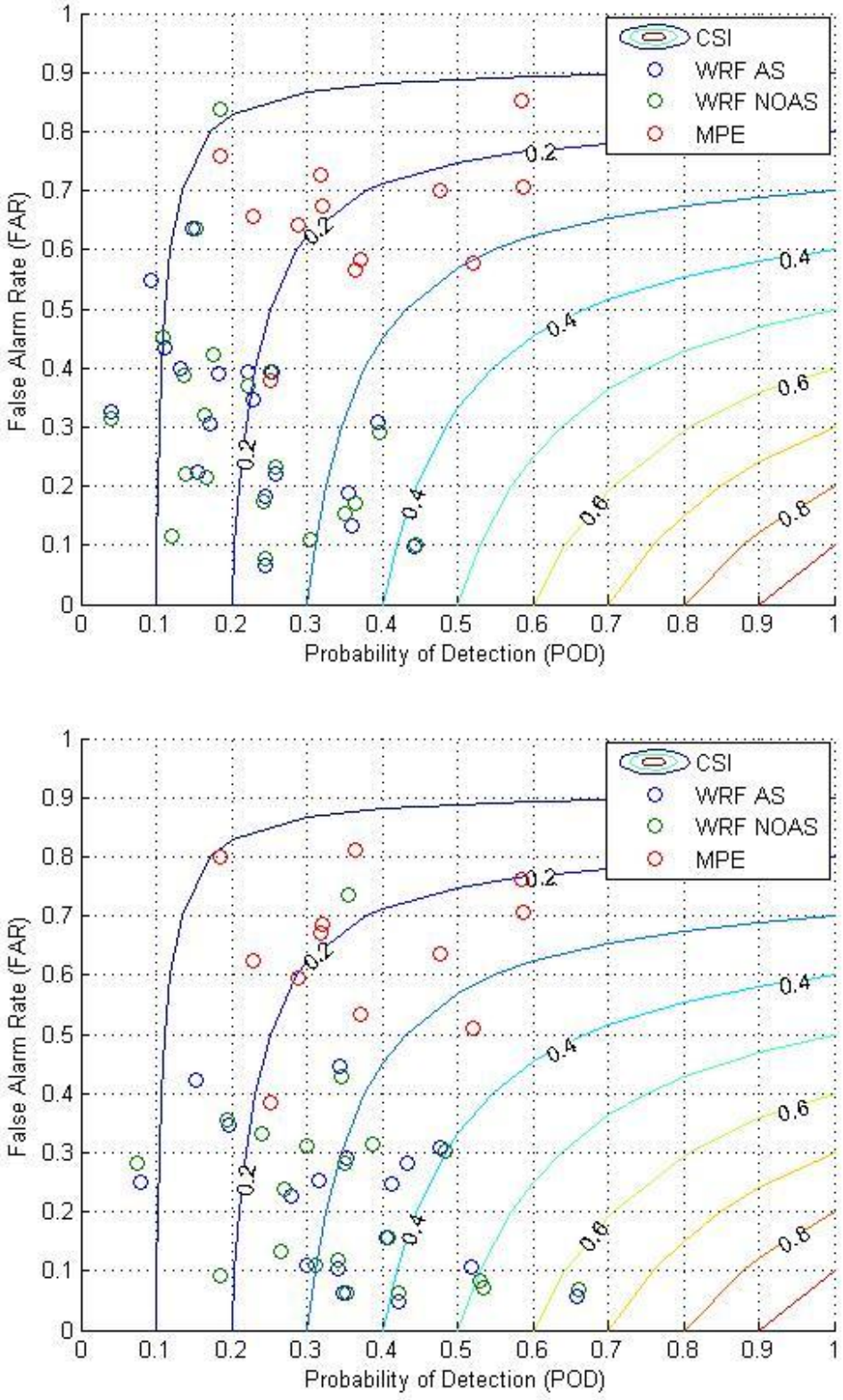

Figure 3.42a: Event Based 1 (top) and 3 (bottom) Hourly POD, FAR, CSI Charts

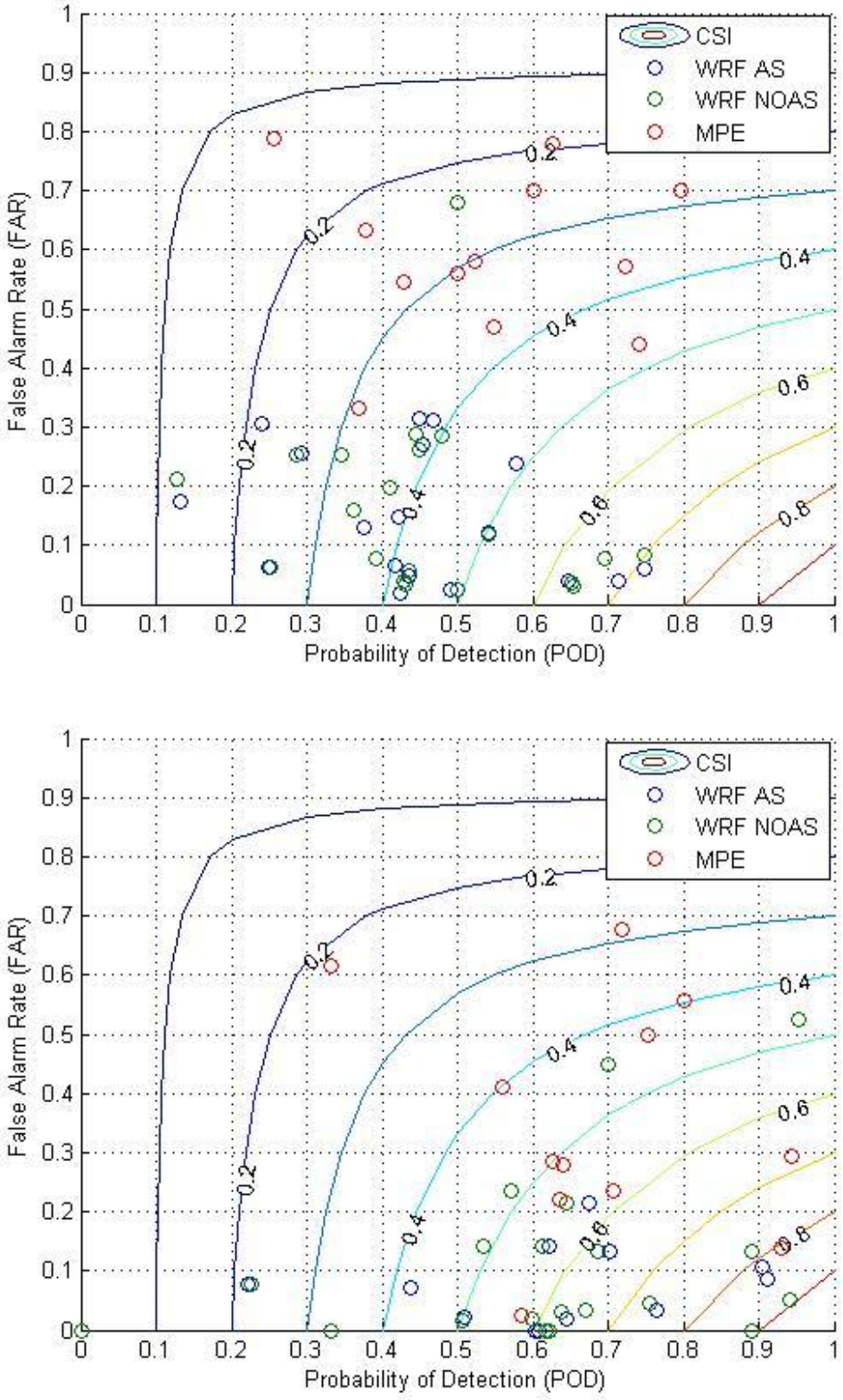

Figure 3.42b: Event Based 6 (top) and 24 (bottom) Hourly POD, FAR, CSI Charts

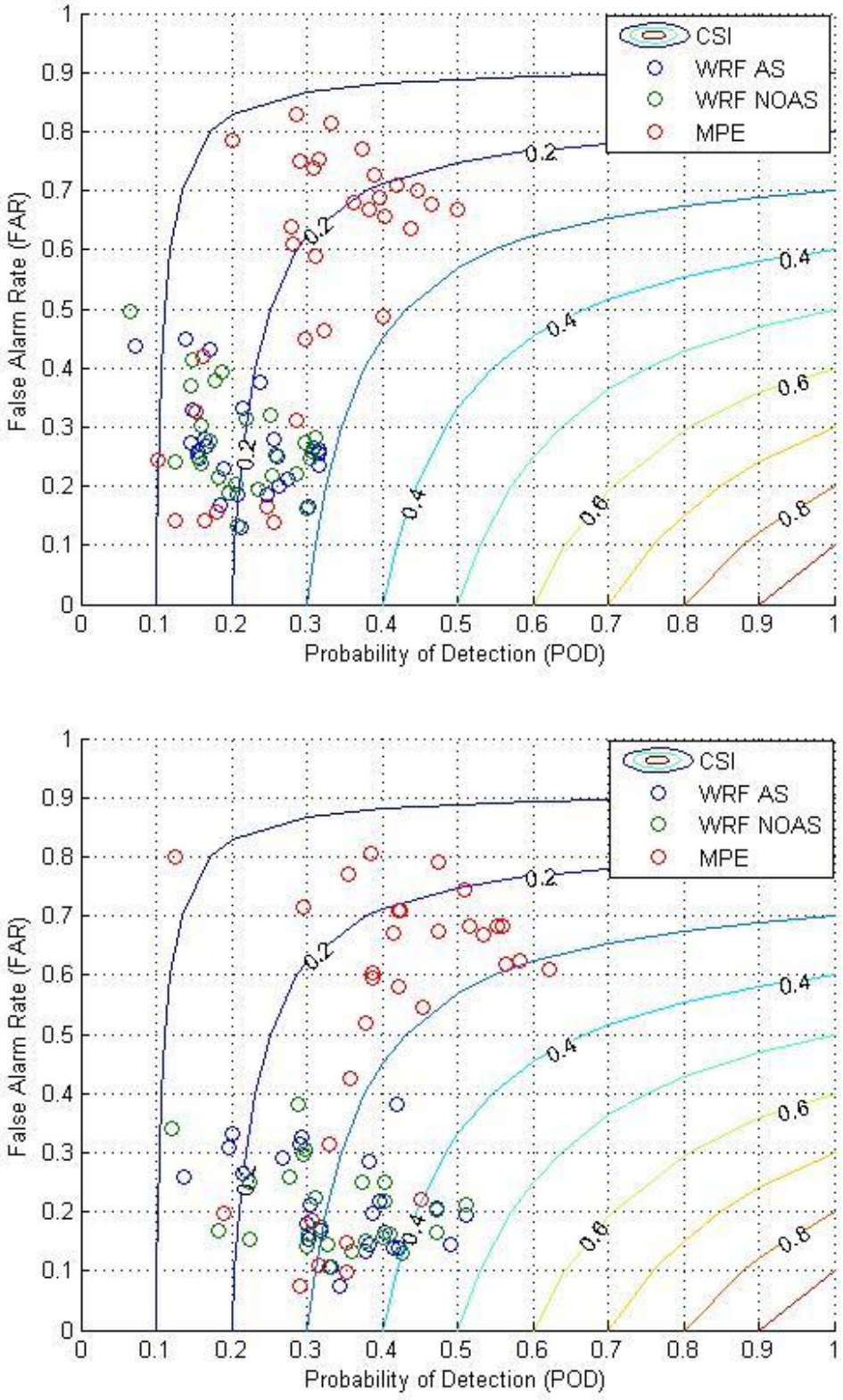

Figure 3.43a: Station Based 1 (top) and 3 (bottom) Hourly POD, FAR, CSI Charts

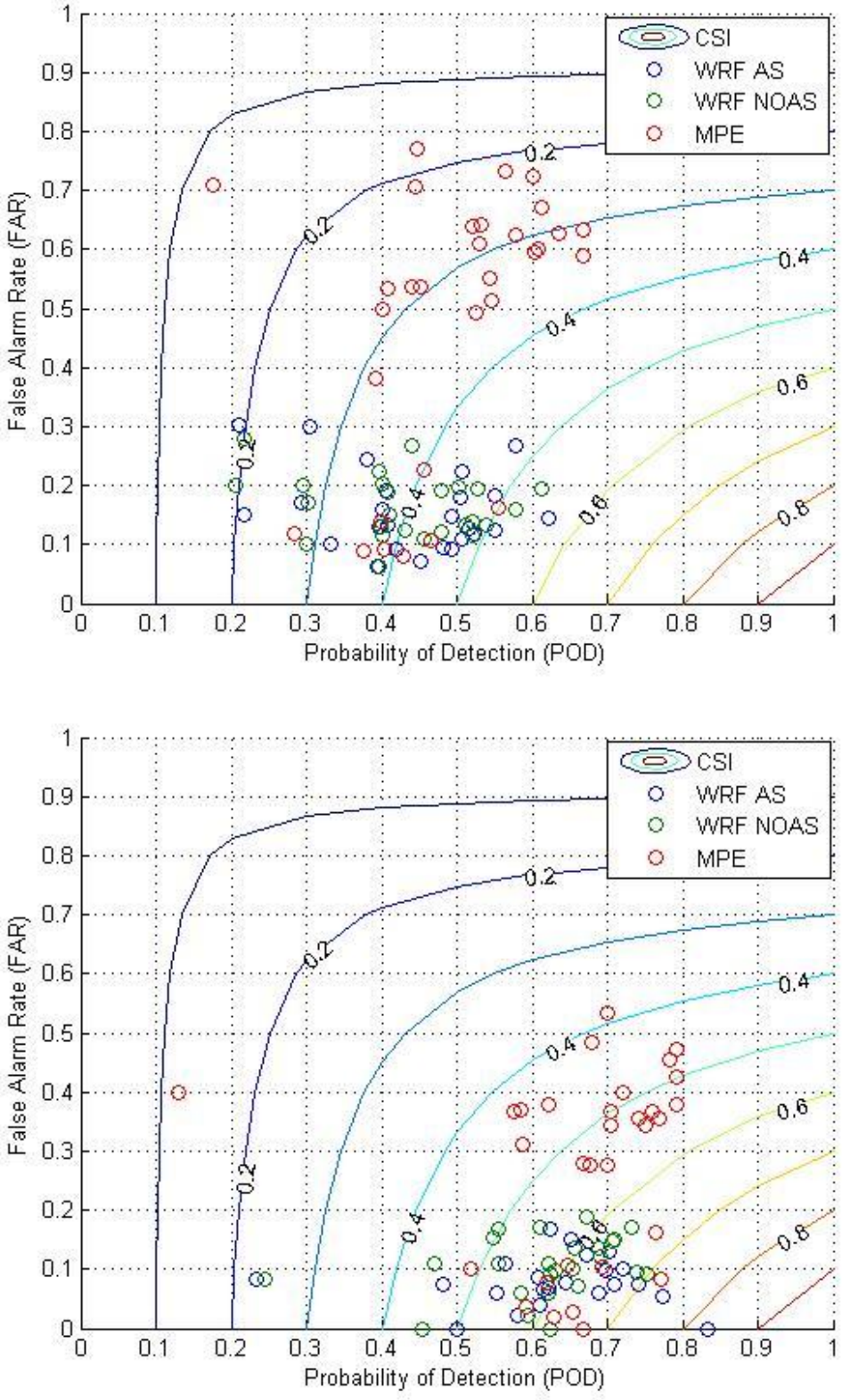

Figure 3.43b: Station Based 6 (top) and 24 (bottom) Hourly POD, FAR, CSI Charts

CHAPTER 4

NOAH MODEL SIMULATIONS AND CALIBRATION

4.1 General Information

In this chapter, NOAH-hydro model simulations and calibration process are discussed. As an initial step, NOAH-hydro model simulations with WRF AS and WRF NOAS precipitation inputs are performed for each of 25 events with predefined default parameter sets before the calibration starts. Considering the improvement obtained with assimilation in WRF model, NOAH-hydro is simulated using WRF AS precipitation during calibration processes. With the calibration processes it is aimed that appropriateness of model results are increased until they match to measured stream flow data. As the heavy precipitation periods of sub-regions among selected 25 events are compared with limited stream flow data obtained, it is observed that limited stream flow data is not capable of representing every selected heavy rainfall event for 4 major basins (Filyos, Devrekani, Düzce, Bartın). After each basin and its available stream flow data are inspected in detail, it is decided that potentially the best calibration can be performed at Bartin basin according to the total available stream flow data size for multiple events that this basin has, and thus, later on test simulations, hydrographs belongs to this basin are tried to be calibrated. As the event list shown in Table 2.1 is considered, events 6 and 8 are selected for main calibration test simulations and on this basin, DSİ 13-39 Kocanaz Boğazköy and DSİ 13-49 Arıt Darıören stream gauge stations are determined as calibration stations. After calibration is performed, the validity of calibrated parameters is evaluated at other selected stream gauge stations and events.

Considering the hydrological functions of parameters in model structure, the calibration is performed in two steps. In first step, parameters controlling total water volume, infiltration factor (REFKDT) and retention depth (RETDEPRT) parameters are evaluated to fit the generated hydrograph peaks as close as possible to observe hydrograph peaks. In the second step, parameters controlling hydrograph shape (or temporal structures of streamflow), surface roughness factor (OVROUGHRT) and channel Manning roughness factor (MANN) are used to fit the simulated hydrograph shapes with those of observed hydrographs. Calibration is performed with step-wise approach and calibrated parameters from first step are implemented as fixed values on second step. Inside the model structure, while REFKDT and MANN parameters are defined on individual parameter input tables and remain constant for whole model domain, RETDEPRT and OVROUGHRT parameters are individually adjustable for each sub-basins defined, so these are basin-specific parameters. These basin specific parameters are calibrated by using a scaling factor over default model values. Scaling factor is a constant that is multiplied with a parameter value. For example, each of the grids having the retention depth parameter (RETDEPRT) is multiplied with a scaling factor of RETDEPRTFAC to change its parameter value. Similarly, grids having surface roughness parameter (OVROUGHRT) are multiplied with a scaling factor of OVROUGHRTFAC to change its parameter values.

On stepwise calibration approach, best parameter values are found by making statistical analyses between calculated and observed streamflow values. In these statistical analyses

following parameters are calculated: root mean square error (rmse); mean-normalized root mean square error (nrmse mean); standard deviation normalized root mean square error (nrmse stdev); bias; bias percentage (biasp); correlation coefficient (RR); Nash-Sutcliffe efficiency index (nash-sutcliffe). While other statistical parameters are commonly used; Nash-Sutcliffe efficiency index (Nash and Sutcliffe, 1970) is being calculated with the following formula:

$$E = 1 - \frac{\sum_{t=1}^{T}(Q_0^t - Q_m^t)^2}{\sum_{t=1}^{T}(Q_0^t - \overline{Q_0})^2} \quad (4.1)$$

where;

Q_o observed discharge [m^3/s]

Q_m modeled discharge [m^3/s]

Q_o^t observed discharge at time t [m^3/s]

With these analyses targeted parameter values are: in rmse and bias values, zero; in Nash-Sutcliffe and correlation coefficients, '1'. Negative values on Nash-Sutcliffe parameter mean that simulated discharge values are lower than observed mean discharges and therefore, this points the sign of substantial low performance from the model. In addition, after examining the statistical parameters, it is observed that while bias and error stats show more sensitivity towards hydrograph volumes; correlation coefficients show more sensitivity towards temporal variation of discharges. In calibration process, these features of statistical parameters are considered. During the calibration of NOAH-hydro model parameters for Bartın Basin, calibration parameters are systematically changed within their logical ranges until they are closest to the targeted parameter values based on acceptable statistical behaviors. Since, NOAH-hydro model requires high computational time, the use of automated calibration methods is not appropriate for the model.

4.2 Calibration

4.2.1 Infiltration Parameter (REFKDT) Calibration

Infiltration parameter defines soil water absorption capacity until soil is fully saturated. After this state, excess water from precipitation becomes surface runoff and flows through surface slope. In the model, default value for REFKDT is 1.4. For calibration, considering the default value, a physical and wide range of REFKDT between 1.1 and 1.9 is selected and with 0.1 increments along with this range. For all calibration steps, testing ranges are defined to evaluate both lower and higher values with respect to default values. NOAH-hydro simulations are performed for events 6 and 8 individually. For event 6, hydrograph and statistics charts for DSİ 13-39 are shown in Figure 4.1, and for DSİ 13-49, same charts are shown in Figure 4.2. Likely, for event 8, DSİ 13-39 charts are shown in Figure 4.3 and DSİ 13-49 in Figure 4.4.

As expected, with REFKDT value increases, soil sucks more water and that results in lower hydrograph volumes. By considering the fact that initial model outputs release generally lower hydrograph volumes than observed flows it is decided to use REFKDT values which are less than the model default value in the calibration process. On the other hand, since soil water absorption cannot be ignored, an infiltration factor higher than 1 should be selected. As a result, lowest REFKDT value of the parameter range used in calibration runs, 1.1, is selected as the best value in this step. With this value, model simulated hydrograph volumes are found closest to observed hydrograph volumes as the model is ran for event 6 and 8. As shown in related figures, when REFKDT value equals to 1.1, bias and rmse take

the lowest values and Nash-Sutcliffe index generally stays in ± 0.5 range. In addition, high correlation coefficients between 0.7 and 1.0 are observed.

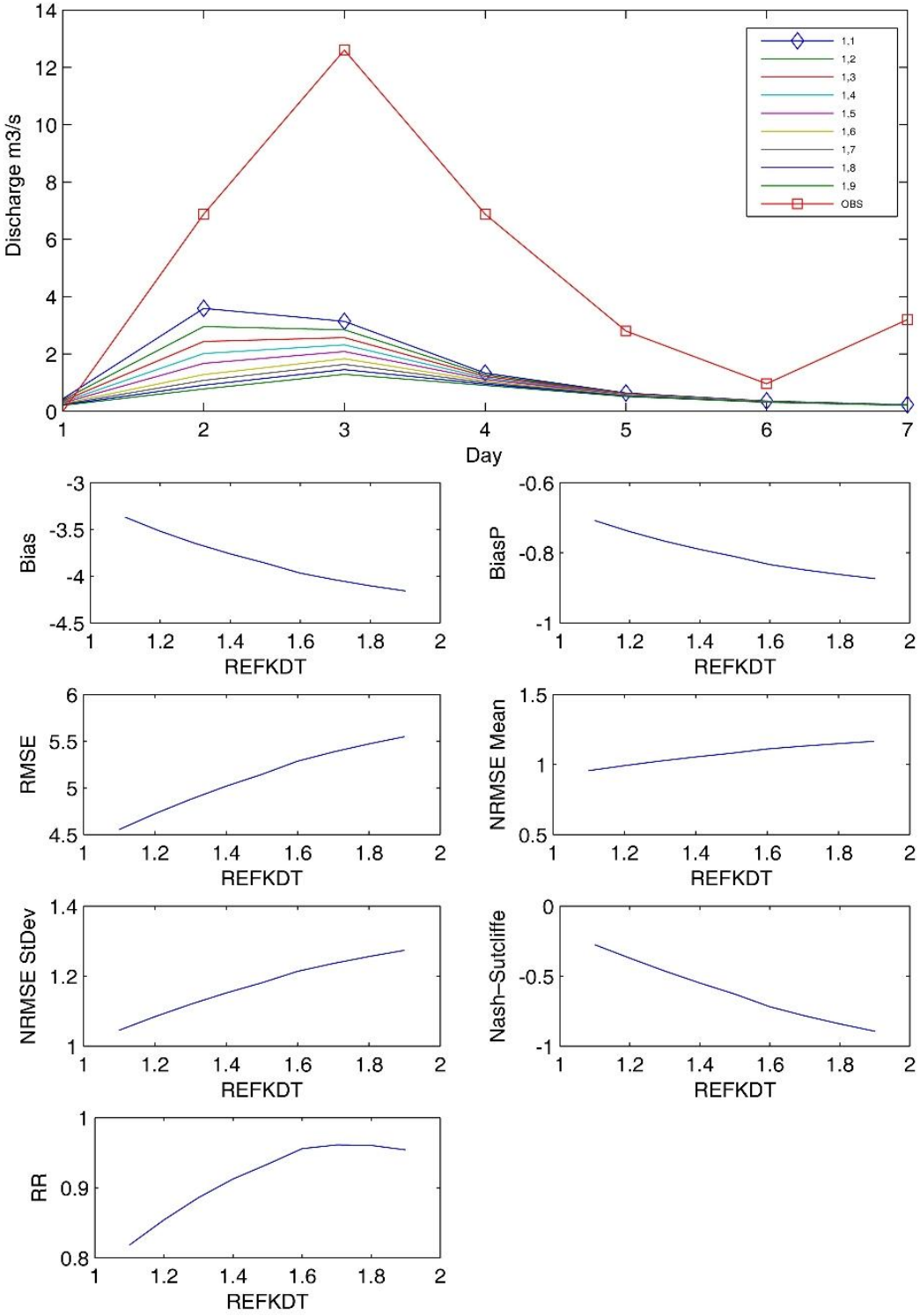

Figure 4.1: Event 6 DSİ 13-39 Station REFKDT Hydrographs and Stats

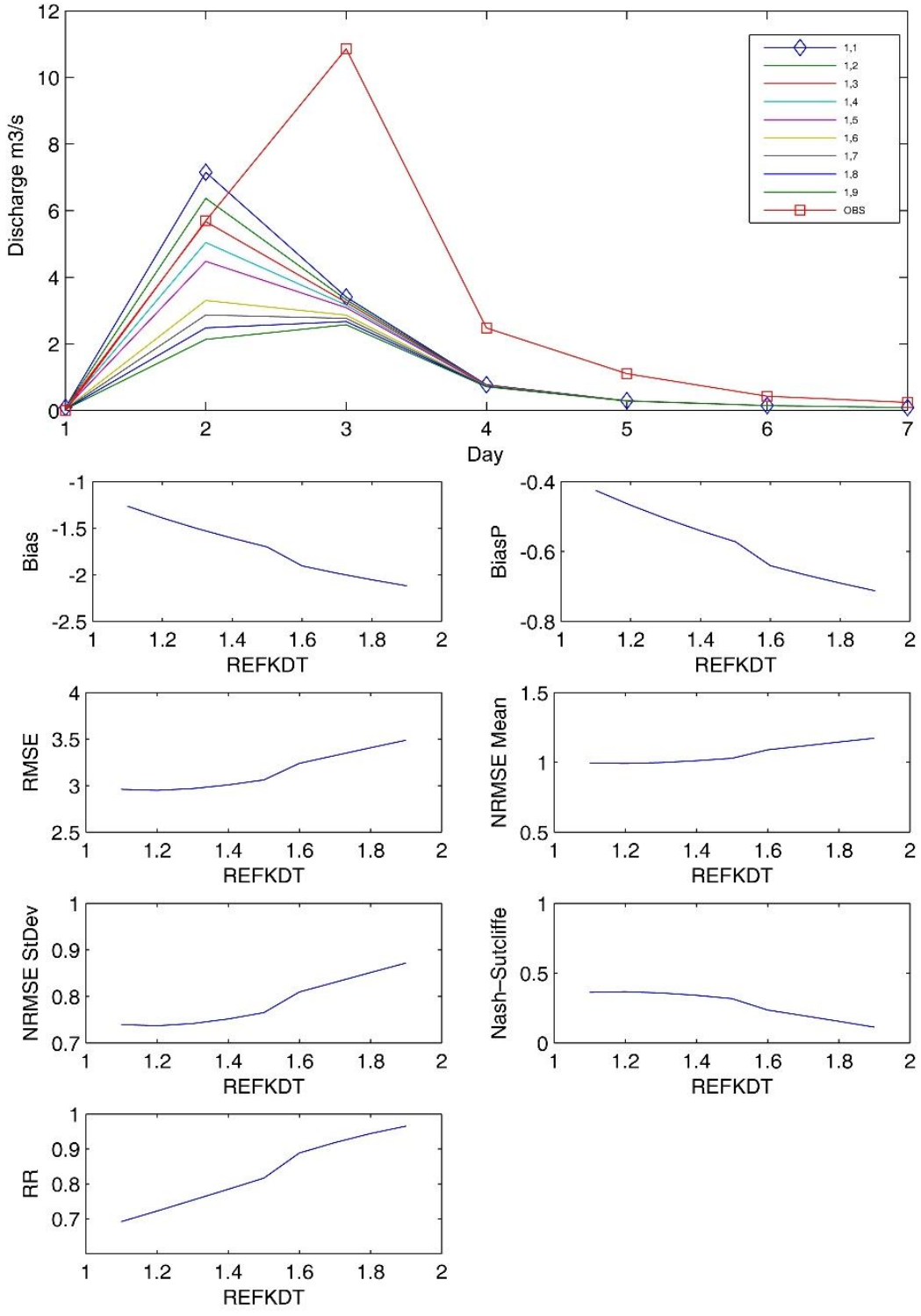

Figure 4.2: Event 6 DSİ 13-49 Station REFKDT Hydrographs and Stats

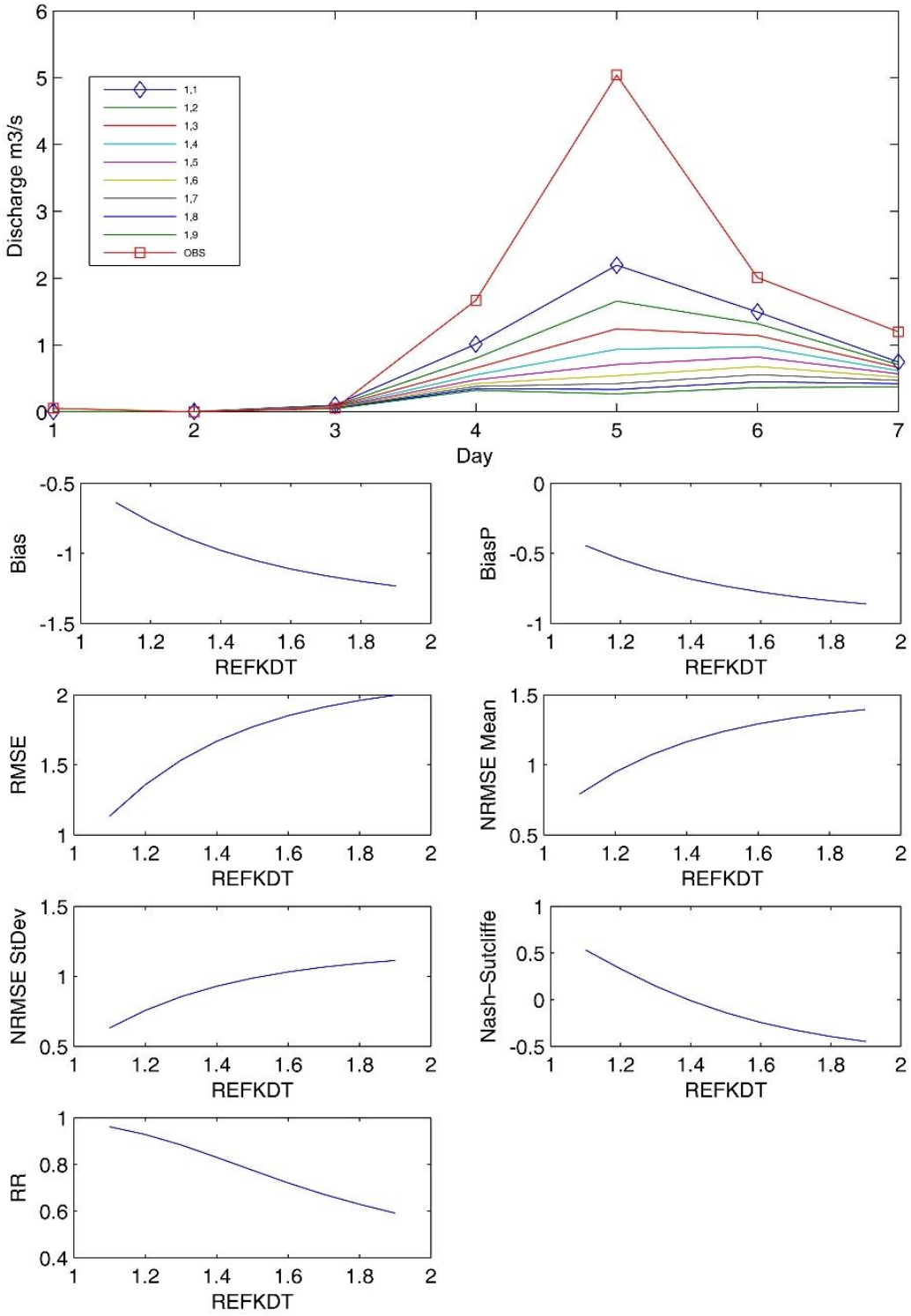

Figure 4.3: Event 8 DSİ 13-39 Station REFKDT Hydrographs and Stats

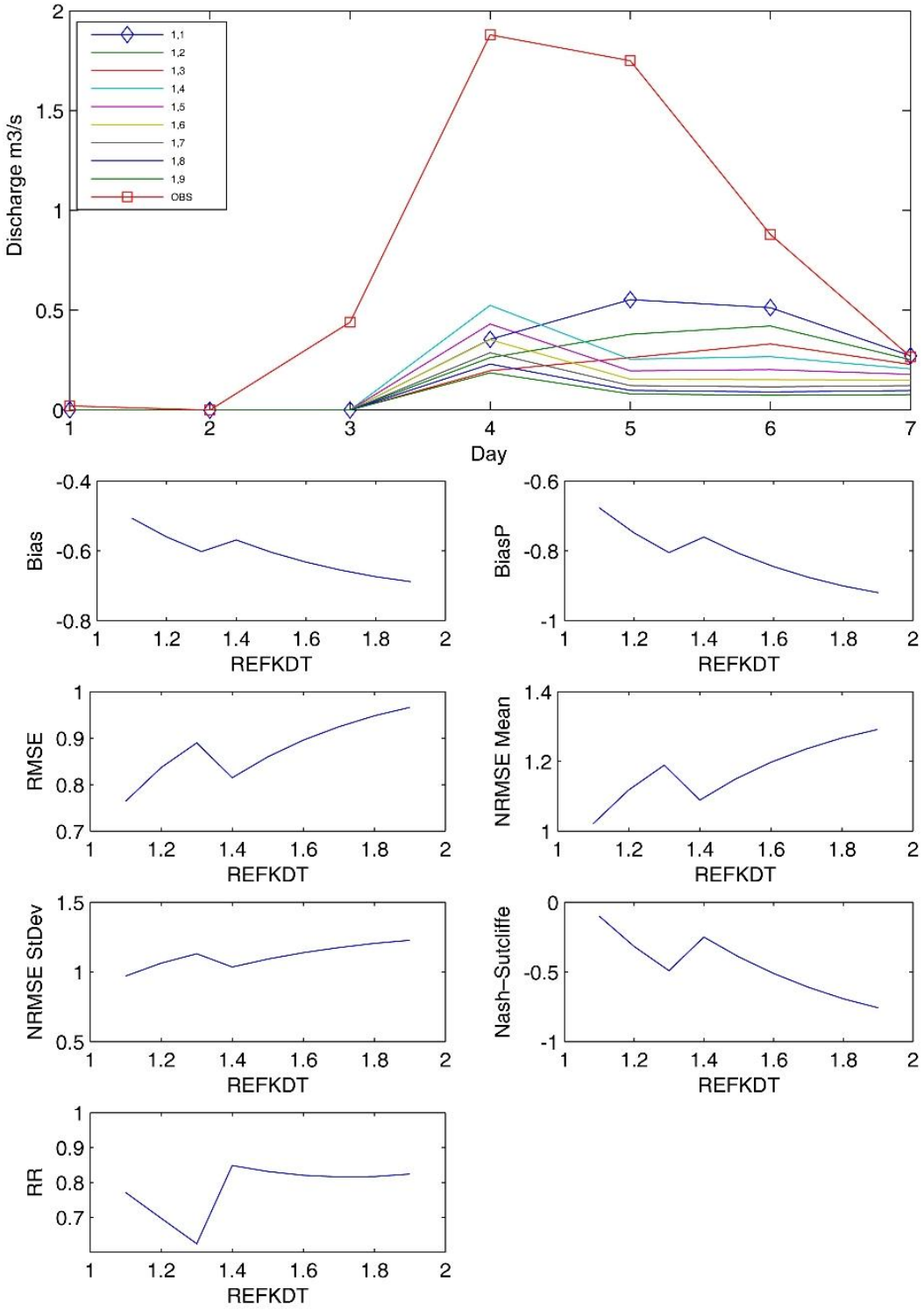

Figure 4.4: Event 8 DSİ 13-49 Station REFKDT Hydrographs and Stats

4.2.2 Retention Depth Parameter (RETDEPRT) Calibration

Retention depth is the parameter defining the depth of excess water accumulated on land before transforming into surface runoff. As retention depth increases, the surface runoff decreases and infiltration increases. In model the default value of retention depth parameter is defined 1 mm. Initial value of retention depth is adjusted depending on surface slope, and therefore, retention depth shows minor accumulation on steep surfaces while it takes higher depths on flat surfaces. Especially on plain and wetland regions, retention depth can be reached to significantly high values with a scaling factor. In general, on regions where slopes are higher than 30 º - 45º, retention depth shows no accumulation, so depth (REDEPRT) and scaling factor (RETDEPRTFAC) takes '0' value. For event 6, hydrograph and statistics plots for DSİ 13-39 are shown in Figure 4.5, and for DSİ 13-49, same plots are shown in Figure 4.6. Likely, for event 8, plots are shown for DSİ 13-39 in Figure 4.7 and for DSİ 13-49 in Figure 4.8. In calibration runs, RETDEPRTFAC to adjust the retention depth scale is used between values 0-10 with 1 increments to check correlation and nash-sutcliffe trends over various retention depth factors. While performing these simulations, previously calibrated REFKDT value of 1.1 is used.

As the plots are examined, it is observed that statistics varies with RETDEPRTFAC values changing between 0 and 1, while statistics are nearly same with scaling factor values between 1 and 10. Having correlation coefficients between 0.65 and 1.00, RETDEPRTFAC value is decided as "0" for this calibration step as expected, considering the steep mountainous topography of the region. Also with zero retention depth, statistics show lower rmse and bias results than other values within the simulation range. With selection of this zero value, it is assumed that no local accumulation is generated within the region and excess water immediately transforms into surface runoff after soil becomes fully saturated.

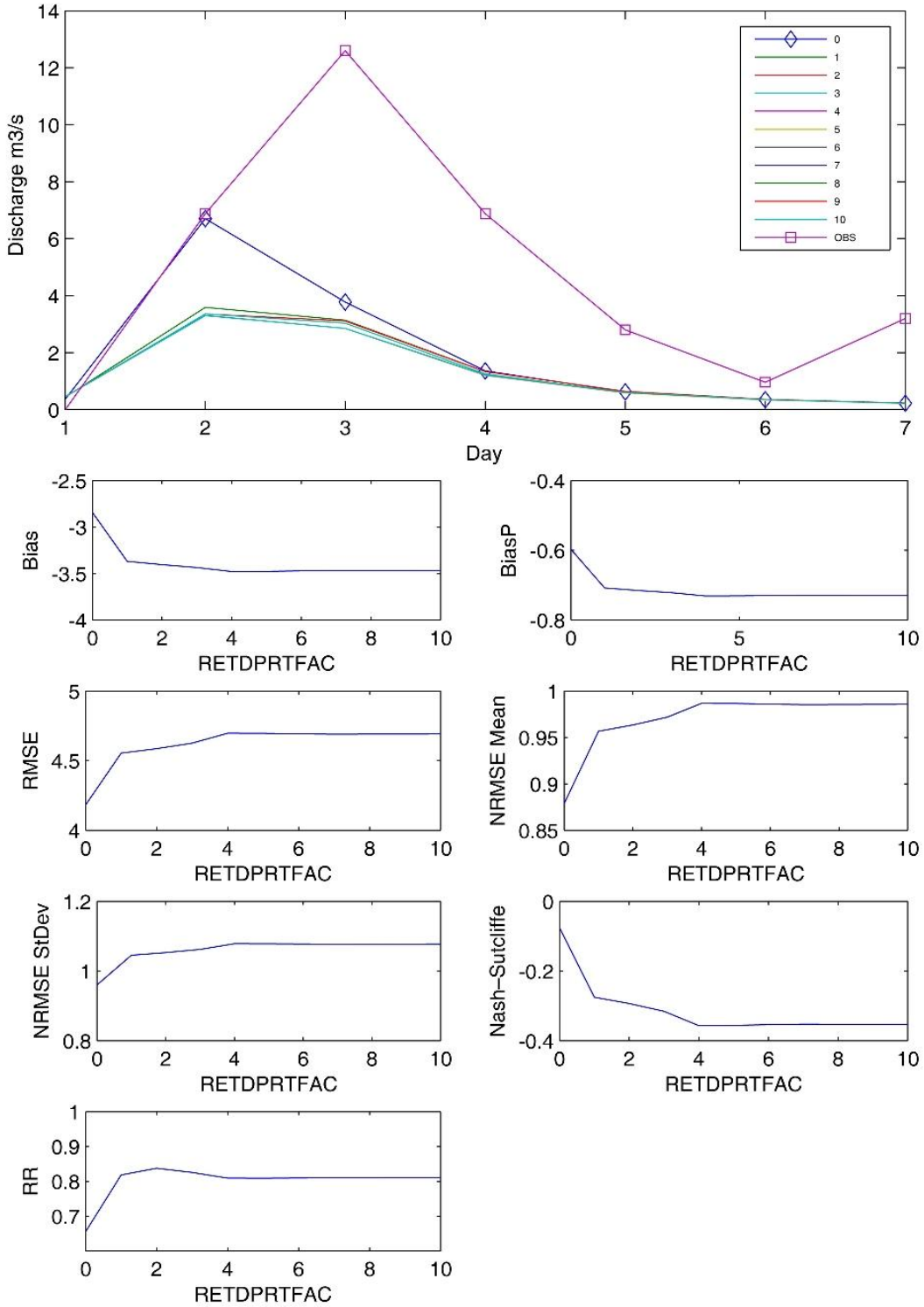

Figure 4.5: Event 6 DSİ 13-39 Station RETDEPRT Hydrographs and Stats

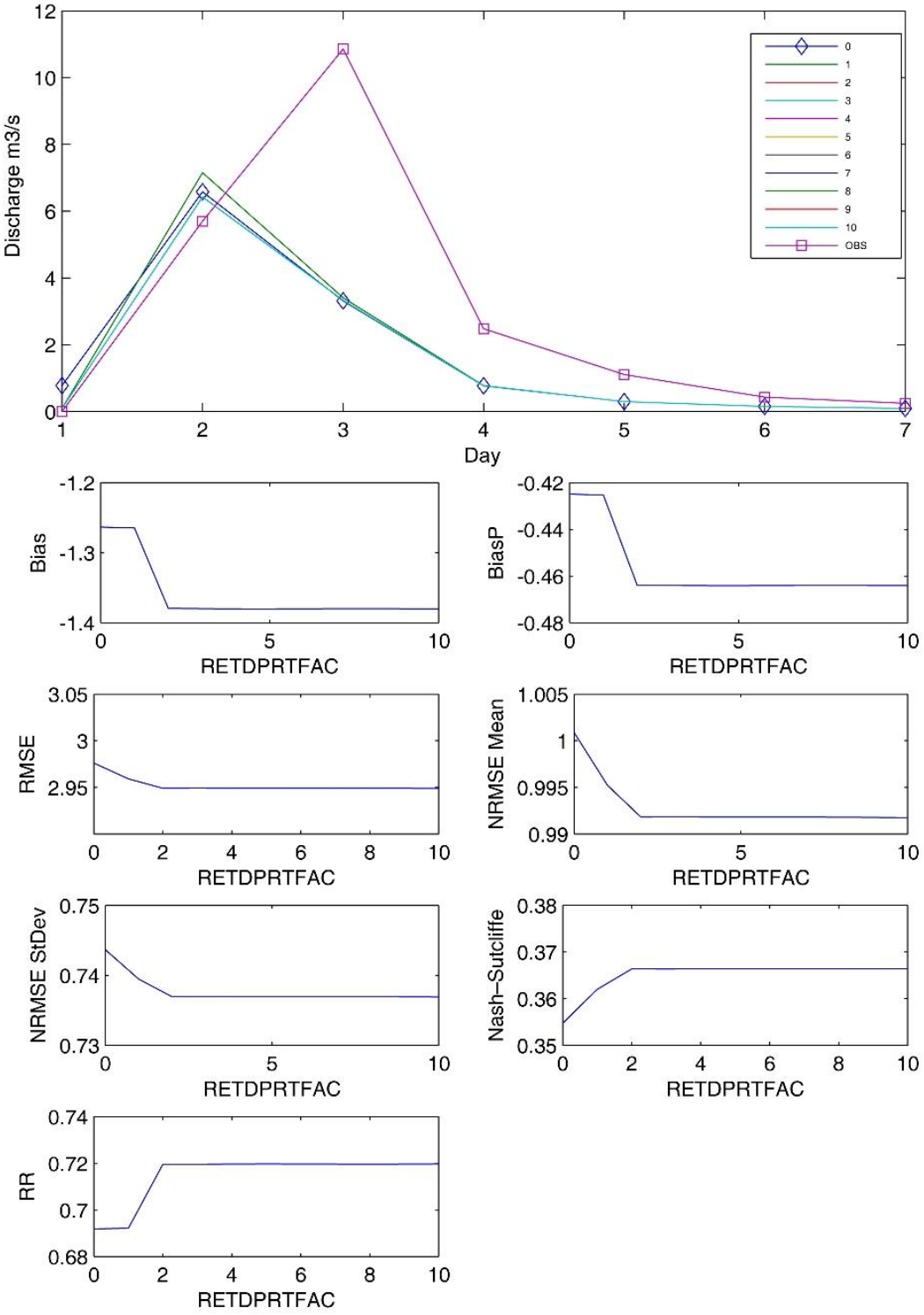

Figure 4.6: Event 6 DSİ 13-49 Station RETDEPRT Hydrographs and Stats

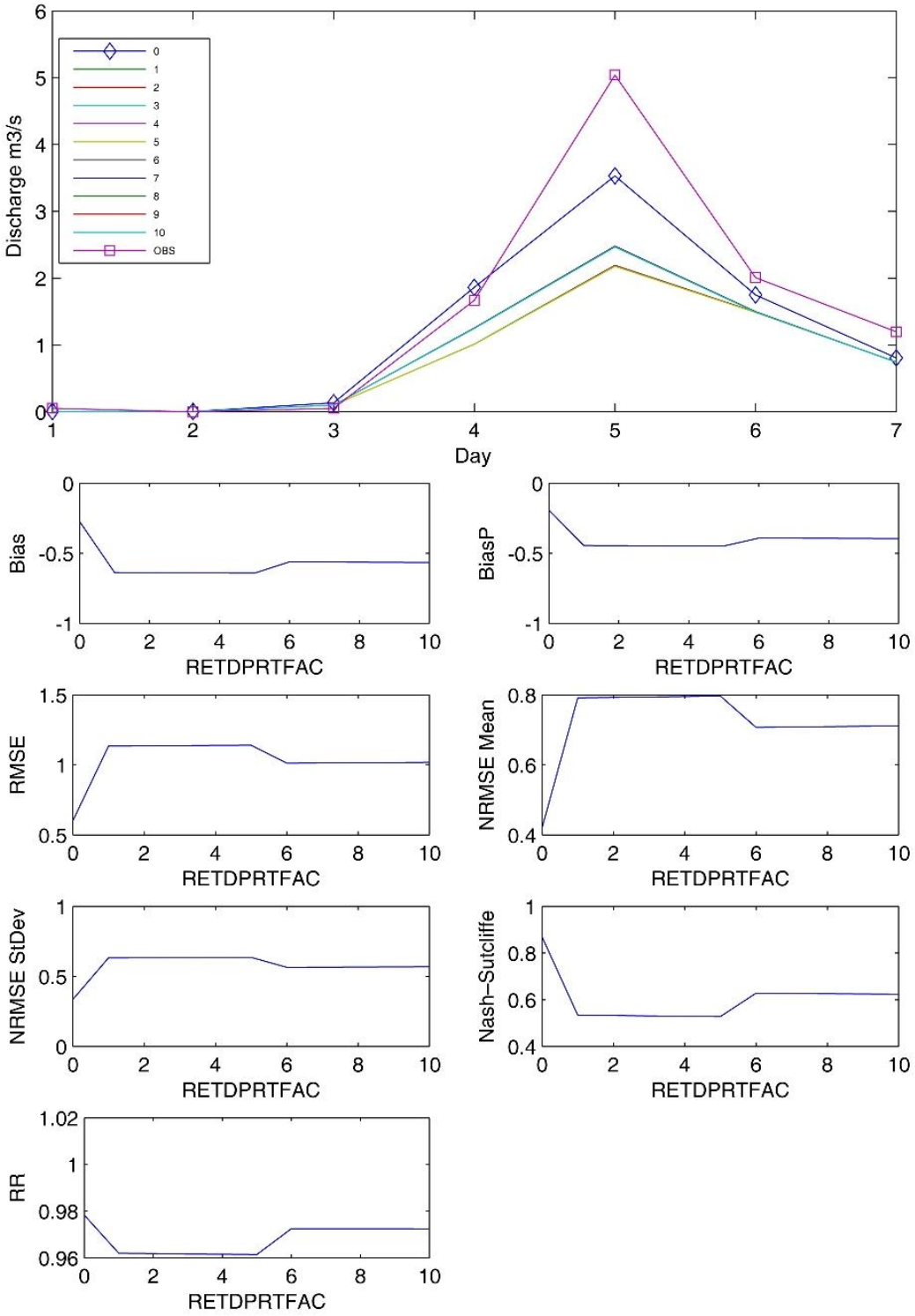

Figure 4.7: Event 8 DSİ 13-39 Station RETDEPRT Hydrographs and Stats

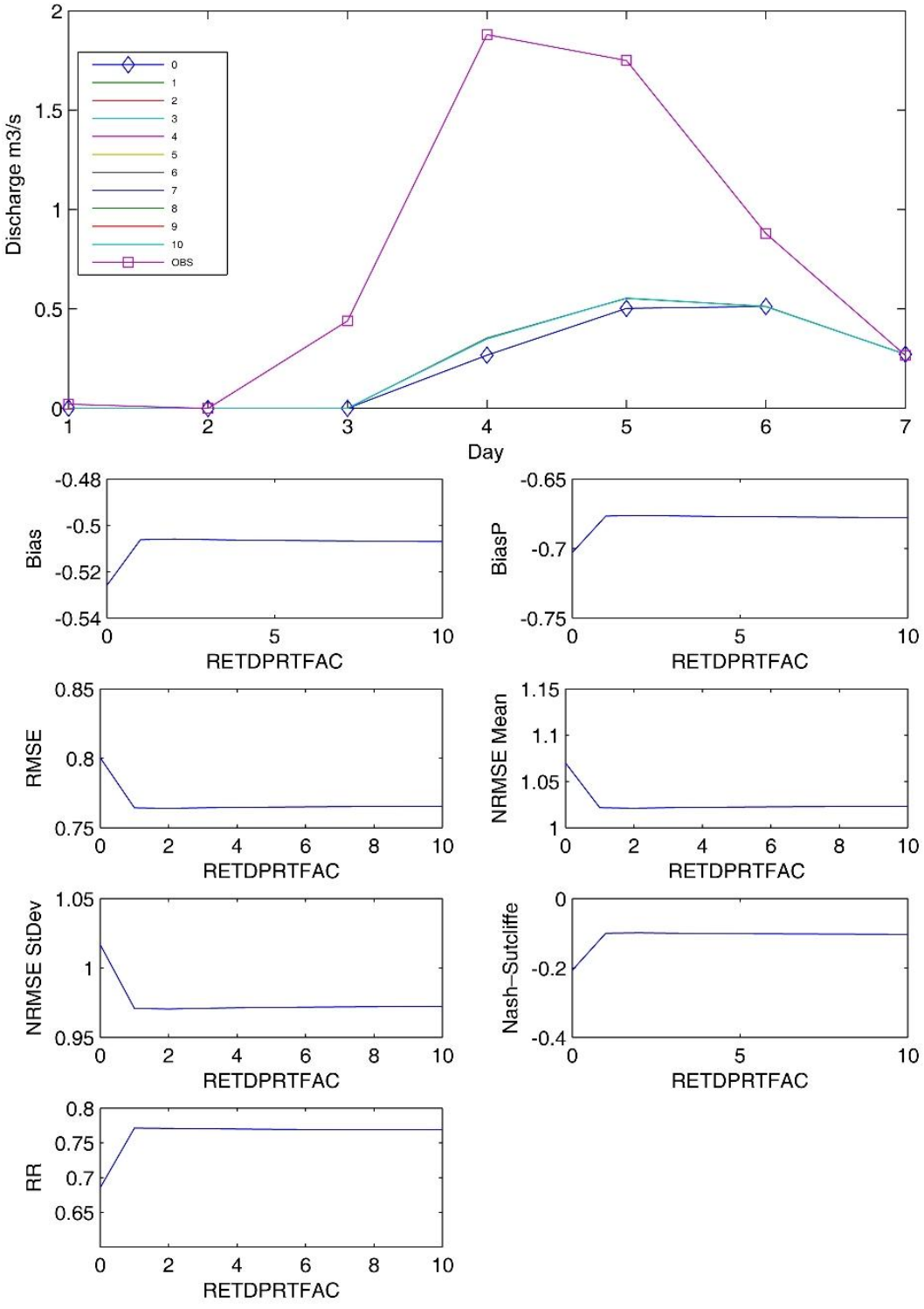

Figure 4.8: Event 8 DSİ 13-49 Station RETDEPRT Hydrographs and Stats

4.2.3 Surface Roughness Parameter (OVROUGHRT) Calibration

On the second main step of calibration, parameters controlling the temporal structure of hydrographs are aimed to be calibrated. Topography, vegetation and related parameter of surface roughness play an important role to transmit excess surface runoff to river networks. With changing the roughness parameter through calibration runs, unmatched peak times between modeled and observed hydrographs are tried to fit and increase statistical reliability on daily basis. Default value for surface roughness is defined with USGS land cover types (Table 2.6) used in land surface model (NOAH LSM). It is observed that Manning's equation performance for solving surface runoff becomes unstable when roughness values are assigned from out of the defined range. Surface roughness parameter is calibrated using roughness parameter scaling factor (OVROUGHRTFAC) between 0.1 and 1.0 with 0.1 increments in calibration runs. During testing of this parameter, REFKDT and RETDEPRTFAC values are taken as calibrated best-values (1.1 and 0.0, respectively). For event 6, hydrograph and statistics plots for DSİ 13-39 and DSİ 13-49 are shown in Figures 4.9, and 4.10, respectively. Similarly, for event 8, equivalent plots for DSİ 13-39 and DSİ 13-49 are shown in Figures 4.11 and 4.12, respectively.

As the plots are examined, for event 6, it is not clearly observed that OVROUGHRTFAC parameter has a strong positive effect on the improvement of temporal structure of the simulated hydrograph. For example, correlation coefficient stays around 0.6 along with parameter range and as roughness scaling factor increases, a substantial decrease in hydrograph volume is visible, which causes simulated hydrograph volumes much lower than observed hydrograph volumes. However, it is very distinctive that OVROUGHRTFAC value of 0.3 corresponds to the lowest rmse and largest Nash-Sutcliffe values for event 6. Furthermore, on event 8, the effect of OVROUGHRT is observed with higher correlation coefficients (0.9 ~ 1.0) and high Nash-Sutcliffe index (>0.9) with a very close matching of observed temporal trends. For this event, calibrated OVROUGHRTFAC value is decided as 0.3 and it is used in next calibration step.

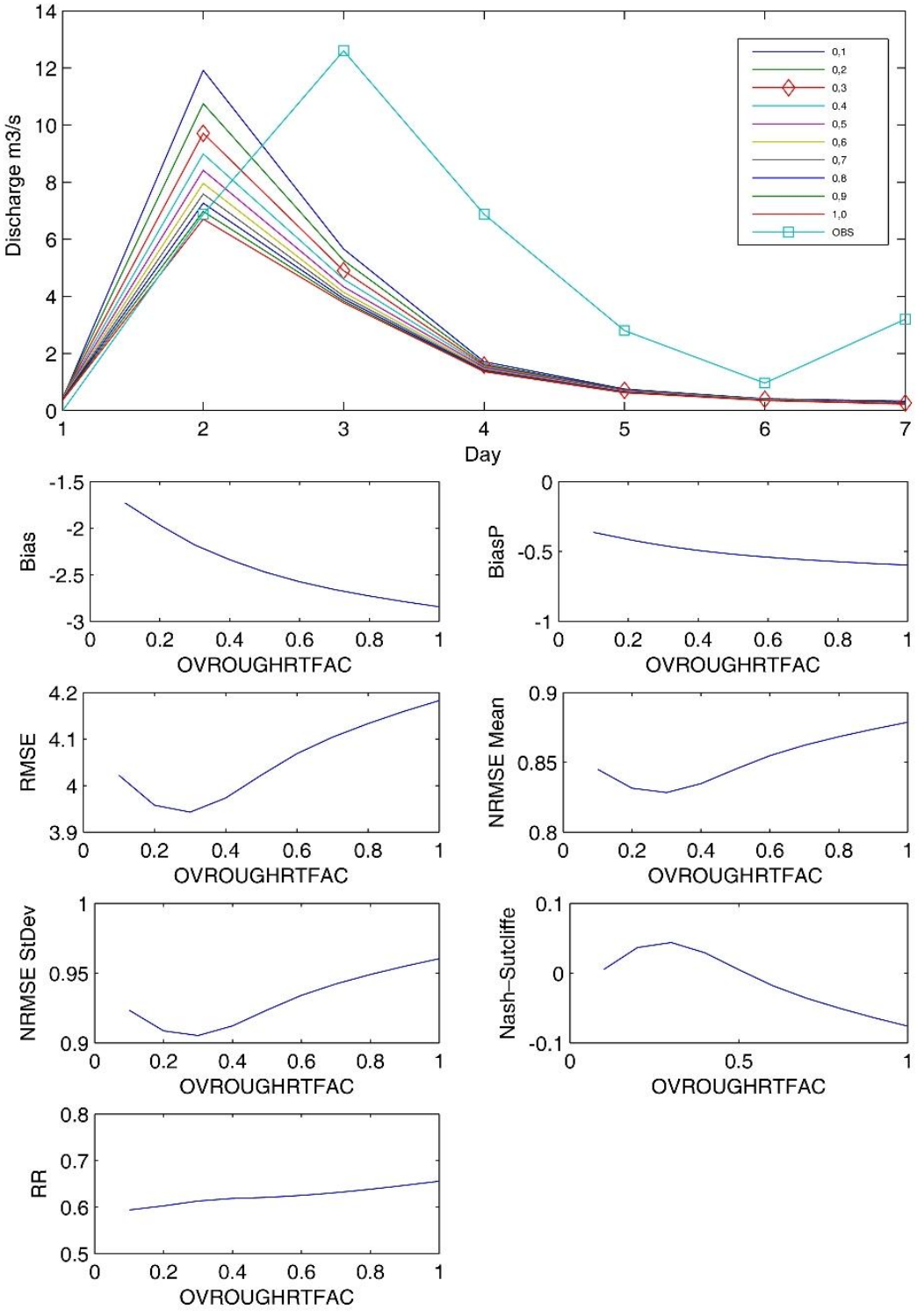

Figure 4.9: Event 6 DSİ 13-39 Station OVROUGHRT Hydrographs and Stats

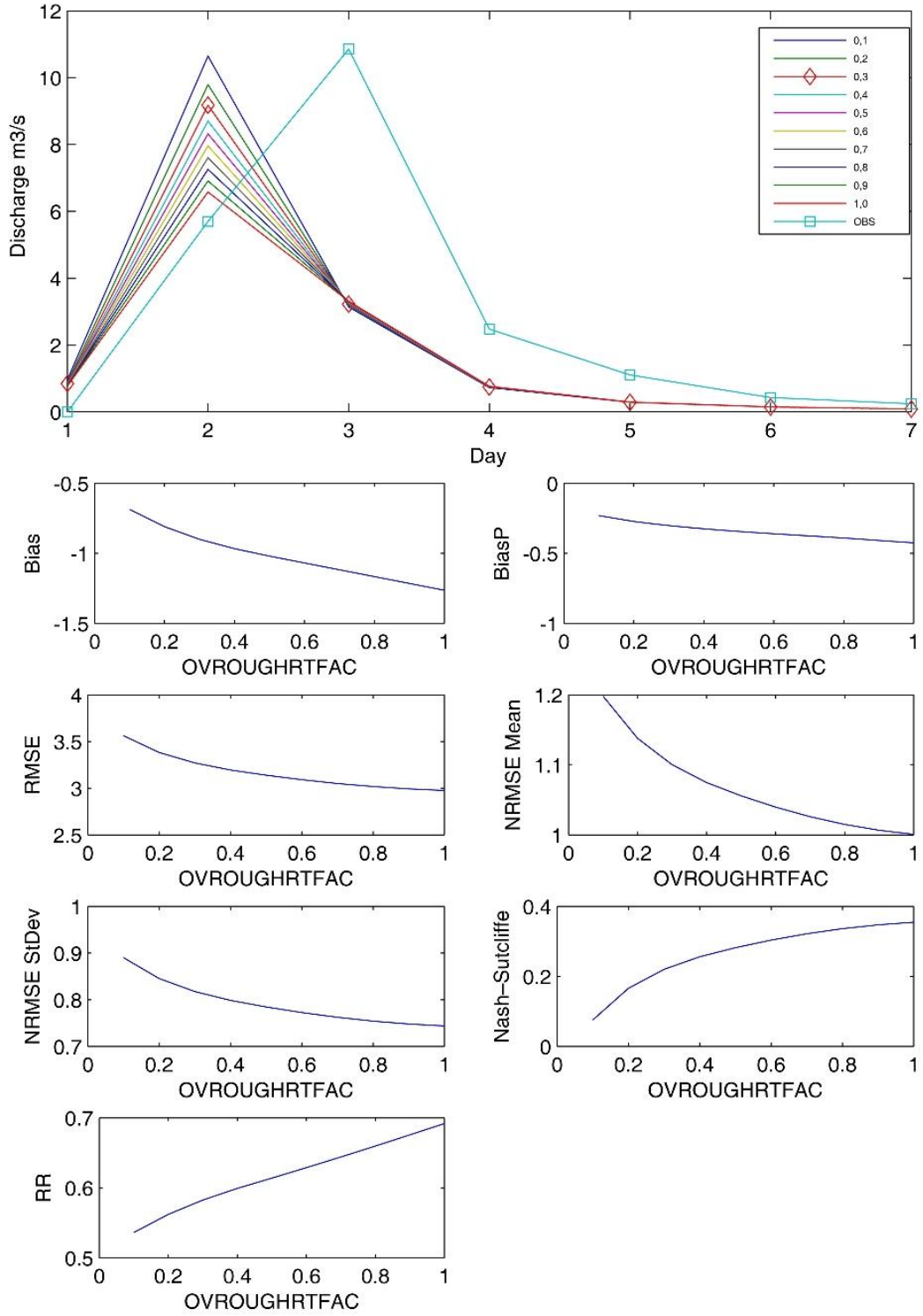

Figure 4.10: Event 6 DSİ 13-49 Station OVROUGHRT Hydrographs and Stats

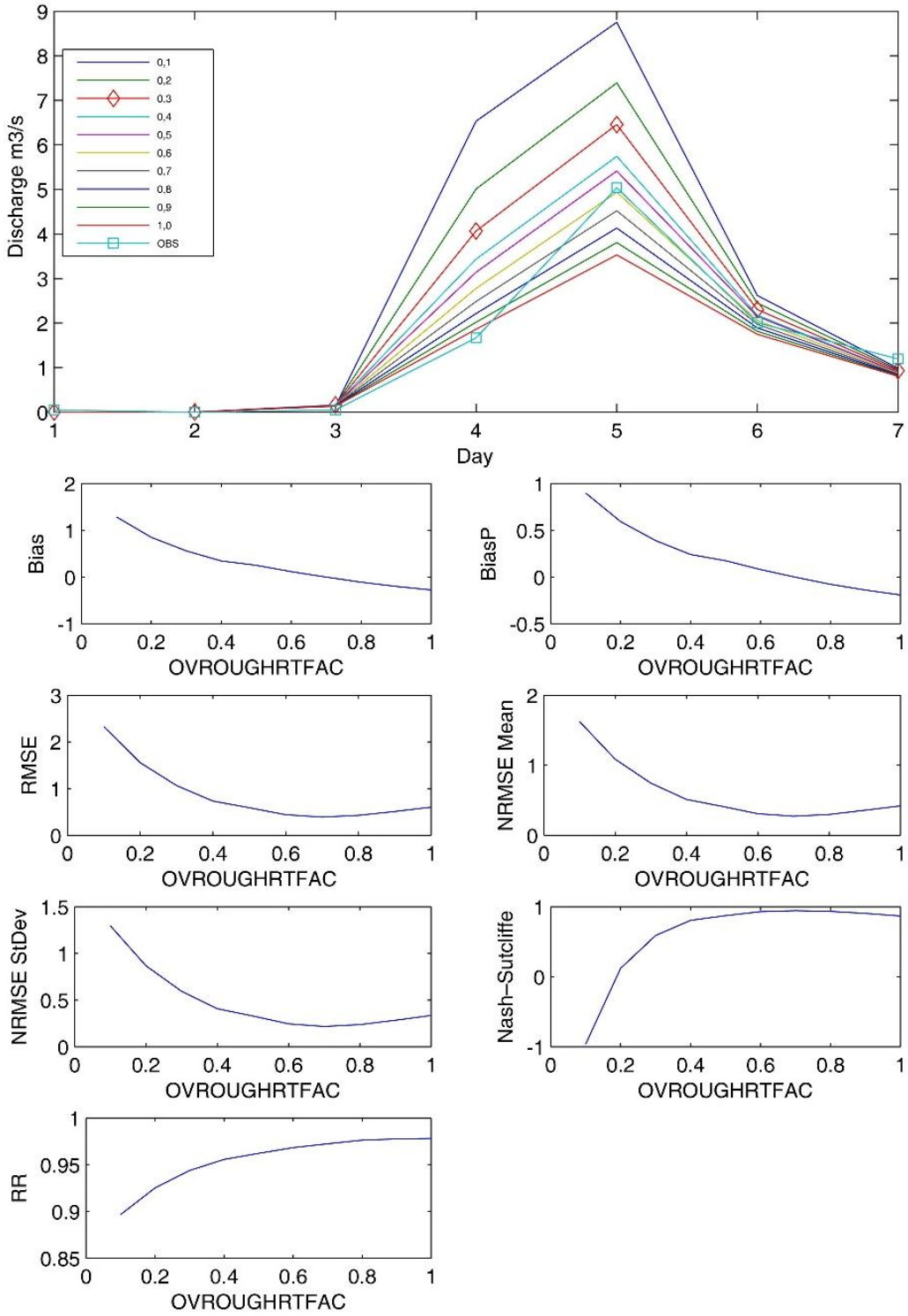

Figure 4.11: Event 8 DSİ 13-39 Station OVROUGHRT Hydrographs and Stats

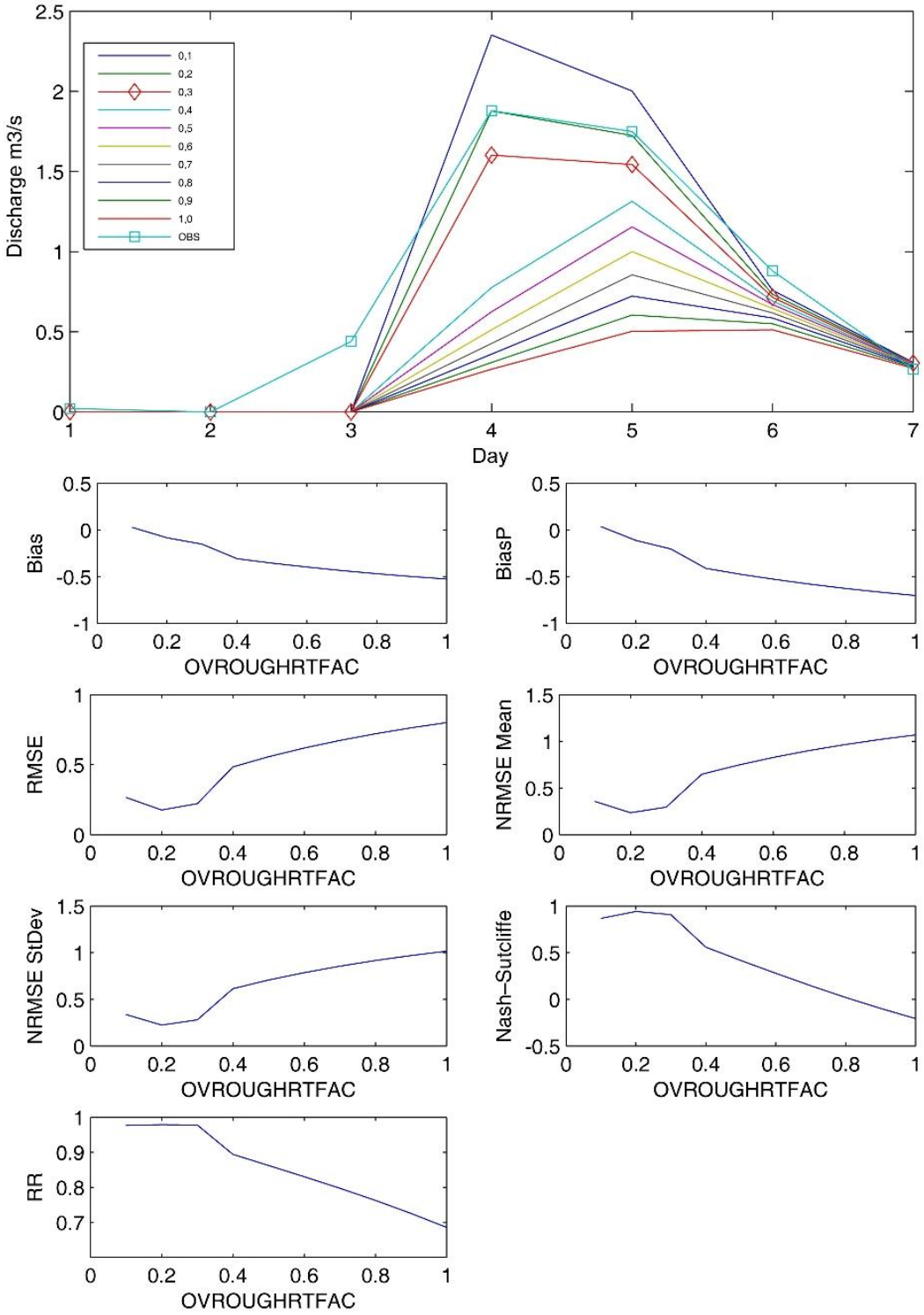

Figure 4.12: Event 8 DSİ 13-49 Station OVROUGHRT Hydrographs and Stats

4.2.4 Channel Manning Parameter (MANN) Calibration

After the surface runoff is transmitted to river network, the conveyance of water along the channels plays an important role on hydrograph shapes. Manning coefficients, defining the roughness of channels, determines the discharge velocity. Channel properties are introduced into the model as average channel base width (Bw), initial water depth (HLINK), channel slope (Ch SSlp), and Manning coefficient (MannN) based on each stream order (St Order). The standard channel parameter values are given in Table 4.1.

Table 4.1: Channel Parameter Table

St Order	Bw	HLINK	Ch SSlp	MannN
1	5	0.02	1	0.65
2	10	0.02	0.6	0.50
3	20	0.02	0.3	0.45
4	30	0.03	0.18	0.35
5	40	0.03	0.05	0.20
6	60	0.03	0.05	0.12
7	60	0.03	0.05	0.03
8	60	0.10	0.05	0.03
9	60	0.30	0.05	0.03
10	60	0.30	0.05	0.03

While channel parameters are evaluated for best fitting, channel geometric properties are selected as model default values since there is no available average channel cross-section data for the region with respect to stream orders. Only channel roughness (Manning Factor) parameter is evaluated for calibration. As seen on table, as the stream order increases (rivers combine into larger branches), manning coefficients decreases (channel roughness decreases), hence discharge increases. Because the channel manning parameters shown in Table 4.1 are assigned based on a specific theoretical background, it is decided that rather than changing manning parameters individually, multiplying the whole manning coefficients with same multiplier factor (scaling factor) is a more logical approach for parameter calibration. With a multiplier range between 0.6 – 2.1 with 0.1 increments, manning parameter is tested for all branches of river network in the basin. In calibrating channel roughness parameter, the values of three calibrated parameters obtained previously are used. For event 6, hydrograph and statistics plots for DSİ 13-39 and DSİ 13-49 are shown in Figure 4.13 and 4.14, respectively. Similarly, for event 8, the equivalent plots are shown for DSİ 13-39 and DSİ 13-49 in Figures 4.15 and 4.16, respectively.

As seen in plots, high correlation and high Nash-Sutcliffe index values (0.9 ~1.0) are observed for Manning scaling factor ranging between 1.3 and 1.8. Since in this interval, generally lower bias and rmse values are obtained, it is found out to be appropriate to take an average value within this range. A value of 1.5 is selected as appropriate Manning scaling factor, which resulted in a Manning coefficient range between 0.975 – 0.045 with respect to stream orders. With these calibrated parameter values, the channels are assumed to be rougher than model defaults.

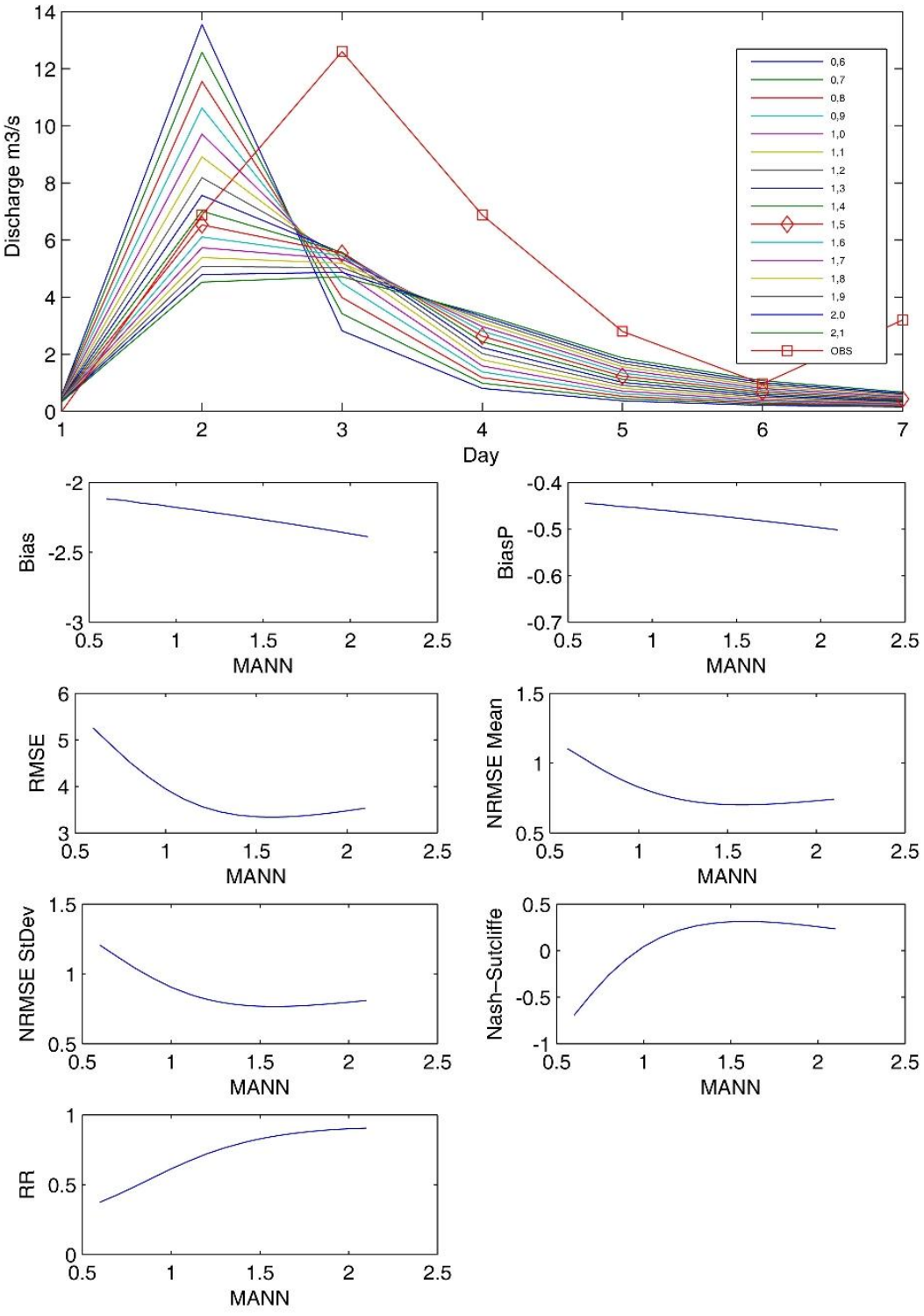

Figure 4.13: Event 6 DSİ 13-39 Station MANN Hydrographs and Stats

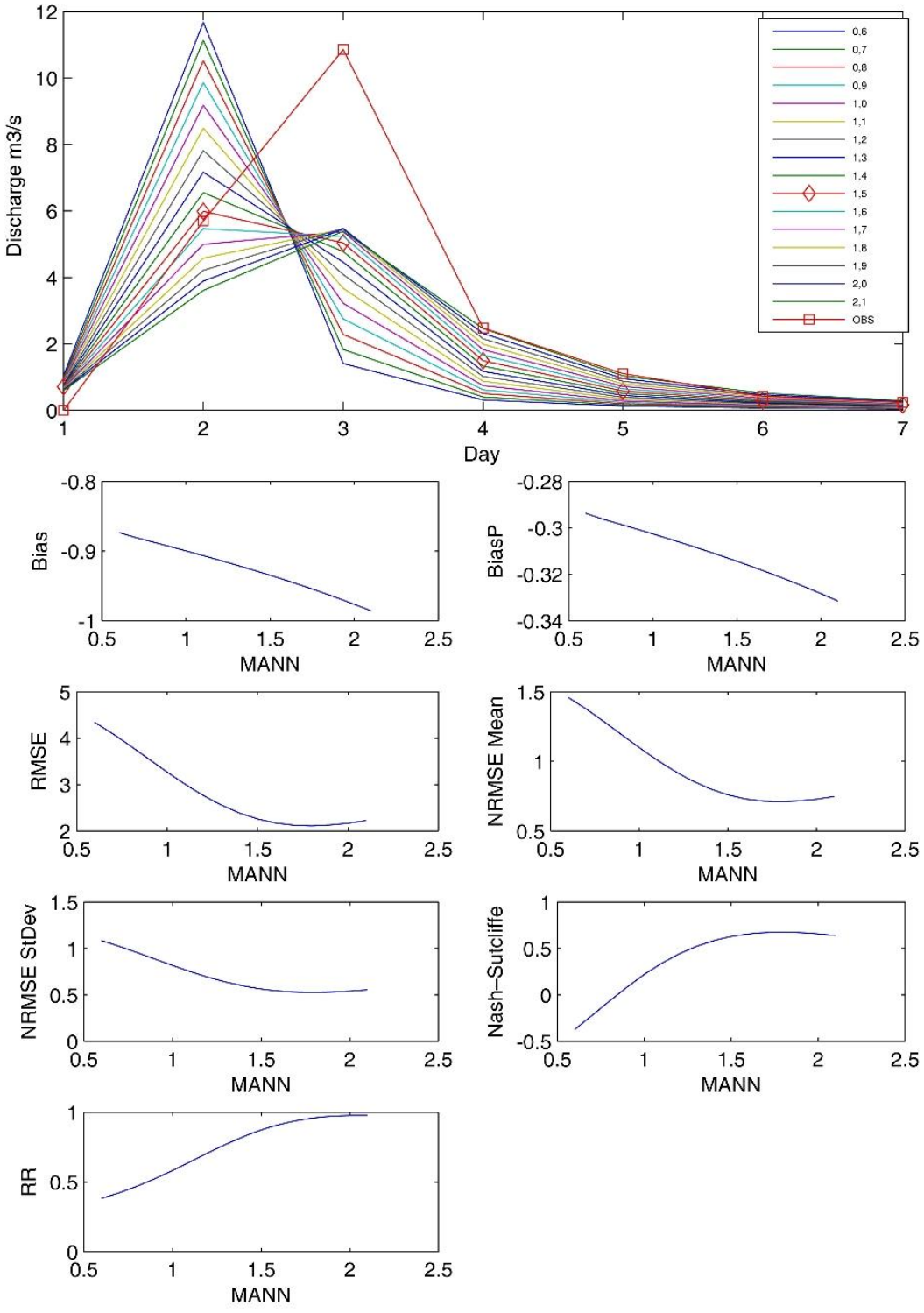

Figure 4.14: Event 6 DSİ 13-49 Station MANN Hydrographs and Stats

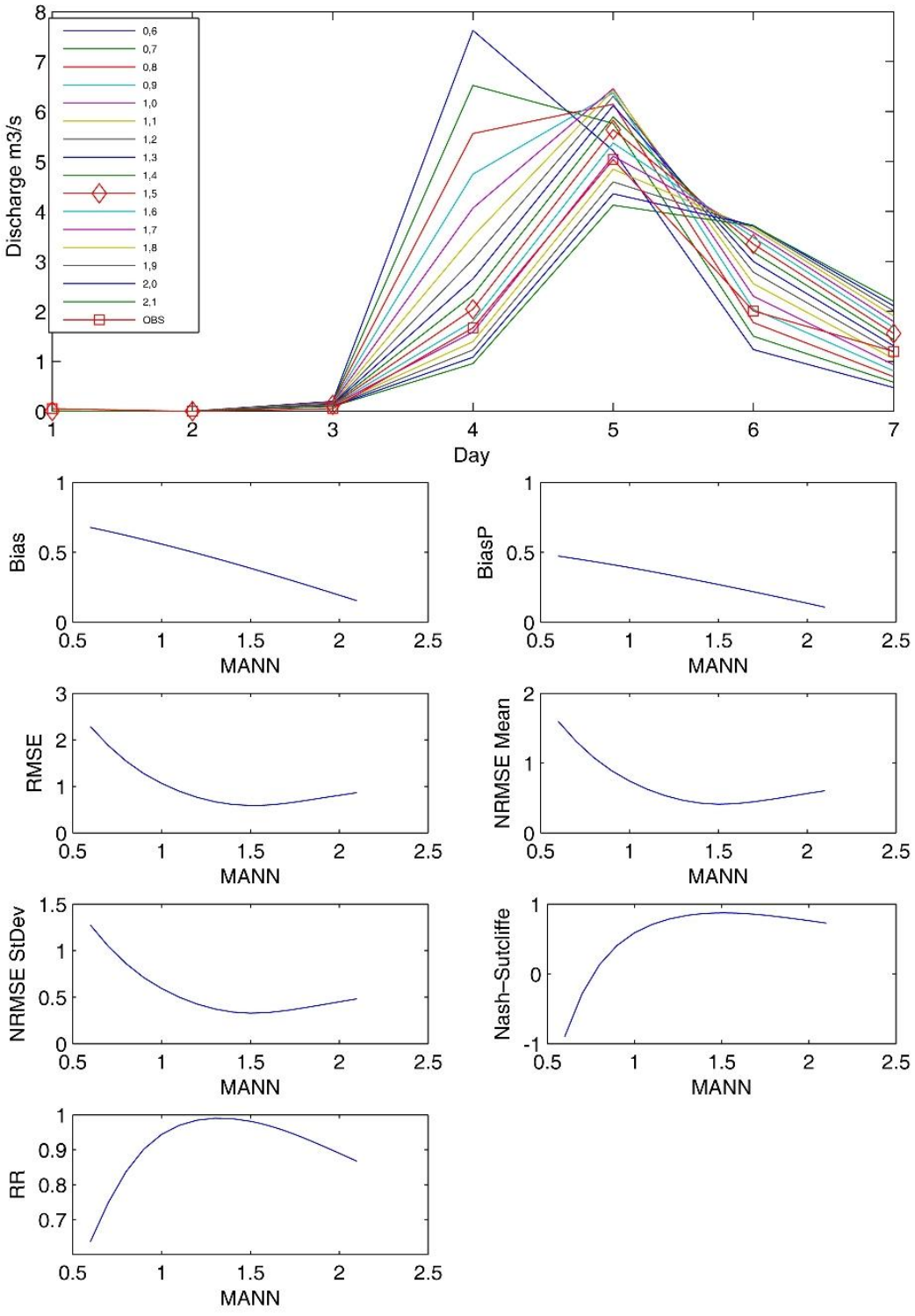

Figure 4.15: Event 8 DSİ 13-39 Station MANN Hydrographs and Stats

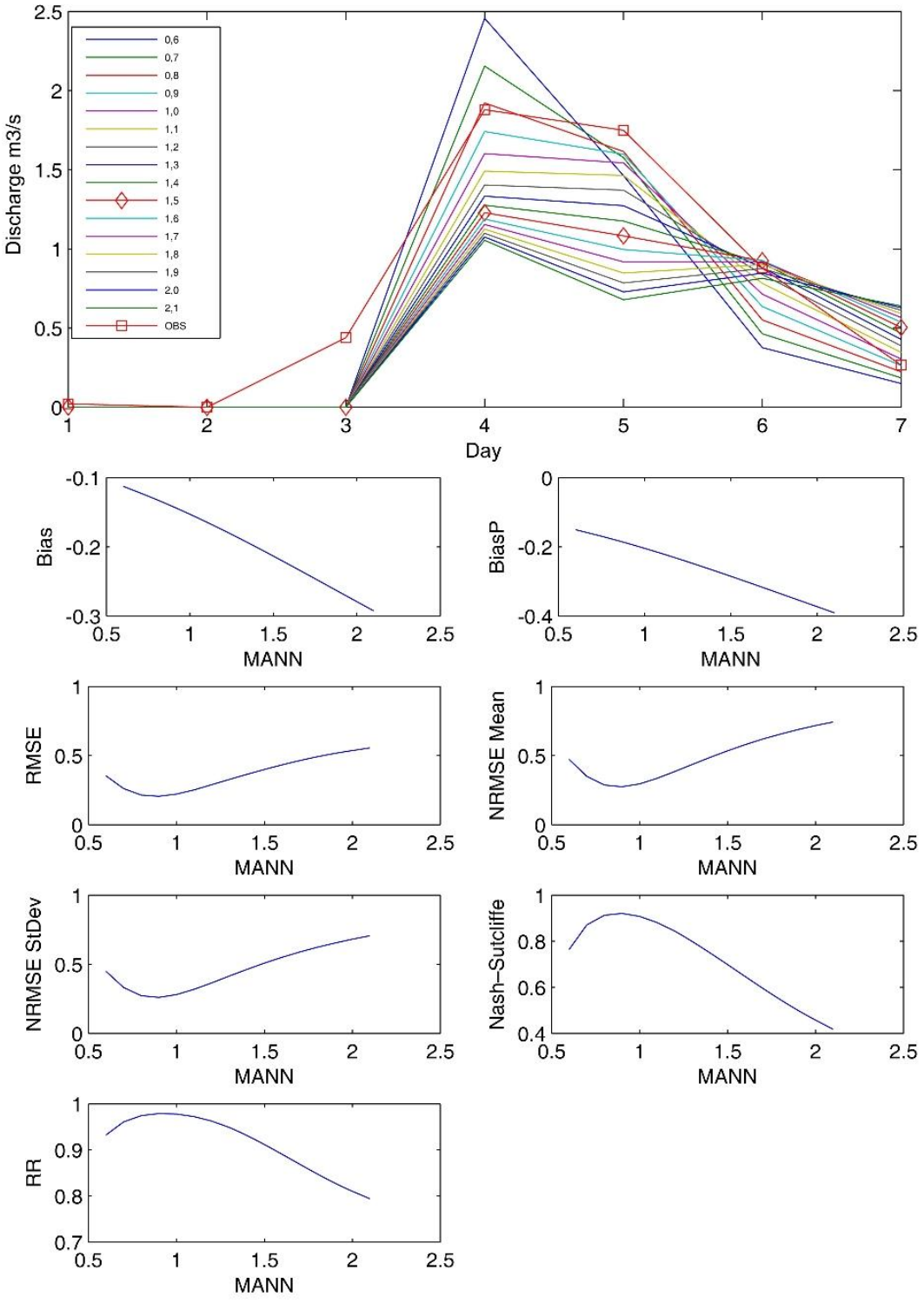

Figure 4.16: Event 8 DSİ 13-49 Station MANN Hydrographs and Stats

4.3 Calibration Results

In this section, results of calibration processes on simulated hydrographs for various events and stations are shown. Calibration evaluation is performed for non-assimilated WRF (NOAS), assimilated WRF (AS) and MPE precipitation. This section is discussed in 3 sub-sections; evaluation results of events used in calibration for Bartın basin (4.3.1), evaluation results of other events that show significant hydrographs and not used in calibration process for Bartın basin (4.3.2) and evaluation results of events observed on other three basins (4.3.3). Since observed discharge data, which are not used in calibration process, are utilized in sections 4.3.2 and 4.3.3, these sections provide evaluation to test the reliability of calibrated parameters.

4.3.1 Evaluation of Calibration Using Dependent Data in Bartın Basin

As widely discussed on previous section, calibration for NOAH-hydro model is performed with stream gauge stations (DSİ 13-39, DSİ 13-49) located in Bartın basin for selected events 6 and 8. Hydrographs compared at DSİ 13-39 and DSİ 13-49 for event 6 are shown in Figures 4.17 and 4.18, respectively. In these figures, comparative hydrographs are described as NOAH-hydro output with non-assimilated WRF precipitation (NOAH NOAS), NOAH-hydro output with assimilated WRF precipitation (NOAH AS), NOAH-hydro output with calibration performed non-assimilated WRF precipitation (CAL NOAS), NOAH-hydro output with calibration performed assimilated WRF precipitation (CAL AS), and observation (OBS). In these figures, it appears that calibration is unable to match the peak times between simulated (both CAL AS and CAL NOAS) and observed hydrographs on daily basis, however significant increase in volumes for both AS and NOAS precipitation is observed. Considering the calibration performed only with AS precipitation, the improvement on CAL AS hydrographs is slightly better than CAL NOAS hydrographs. Especially on rising limb stages, CAL AS shows nearly same slope trends with observations. Besides, NOAH AS hydrograph versus NOAH NOAS at DSİ 13-49 station shows much more relevant volume and peak value when comparing to observation.

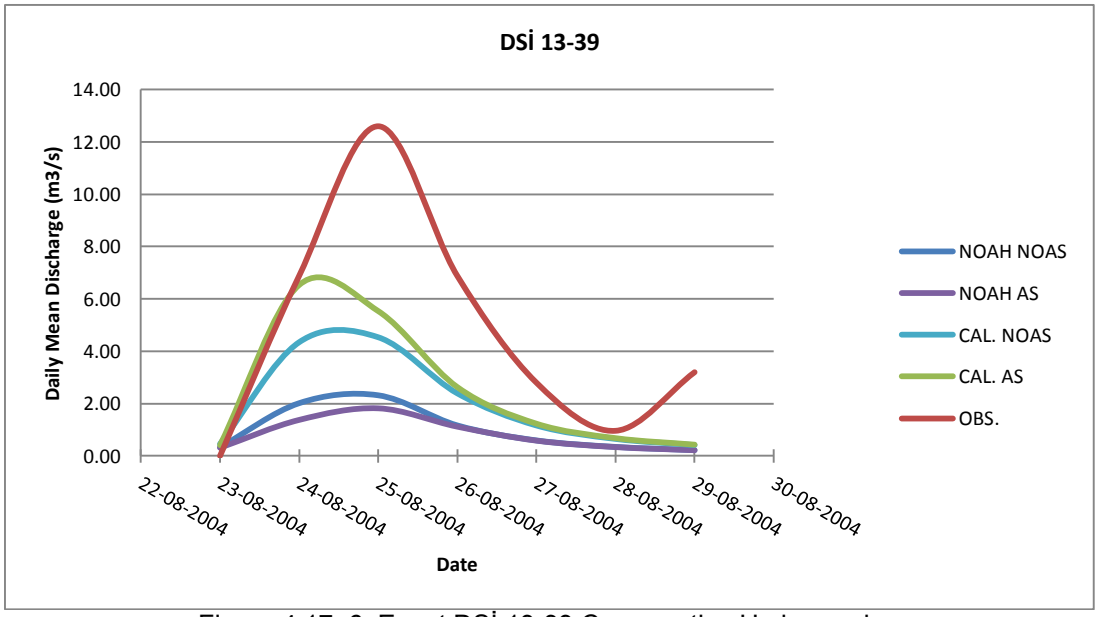

Figure 4.17: 6. Event DSİ 13-39 Comparative Hydrographs

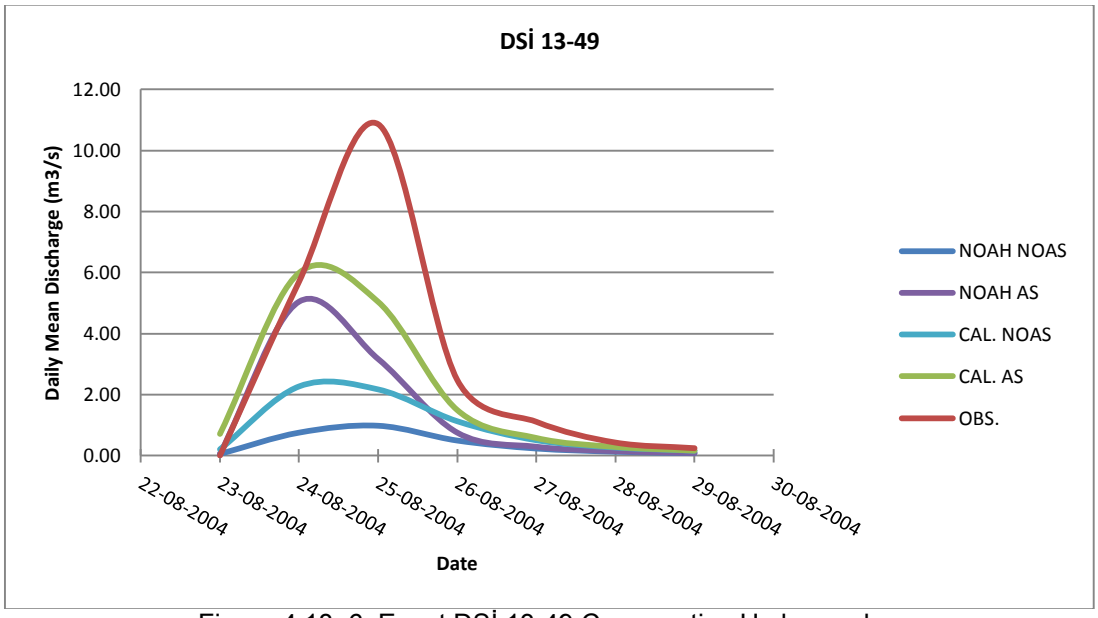

Figure 4.18: 6. Event DSİ 13-49 Comparative Hydrographs

The similar hydrograph comparisons for Event 8 are shown in Figure 4.19 for DSİ 13-39 and in Figure 4.20 for DSİ 13-49. In this case with calibration Event 8 hydrographs at both DSİ stations show larger volume improvement than Event 6 hydrographs. With matching peak times for both calibrated and non-calibrated graphs, CAL. AS hydrograph for DSİ 13-39 shows nearly same trend as observed hydrograph with minor volume difference. For same plot, while CAL NOAS also follows a similar trend, it shows an over-estimated volume than CAL AS. At DSİ 13-49, both simulated hydrographs remain in under-estimation but with much better representation of falling limb stage of hydrograph in CAL AS. In this part of the CAL AS hydrograph, the volume decrease is reduced with calibration and, thus it shows a closer volume to observed hydrograph.

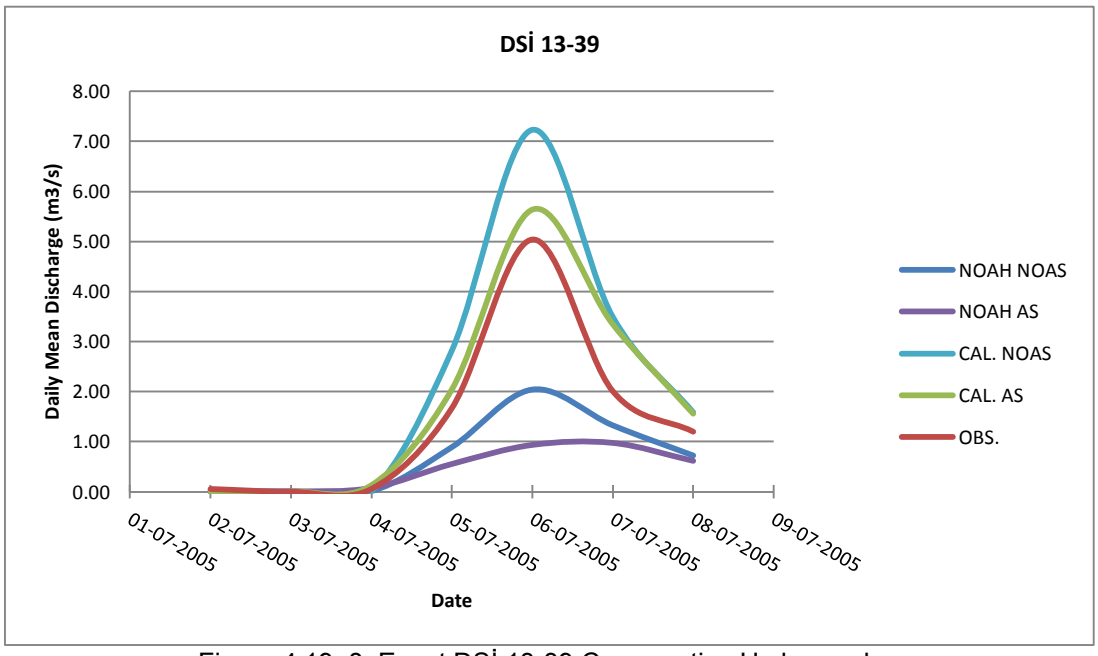

Figure 4.19: 8. Event DSİ 13-39 Comparative Hydrographs

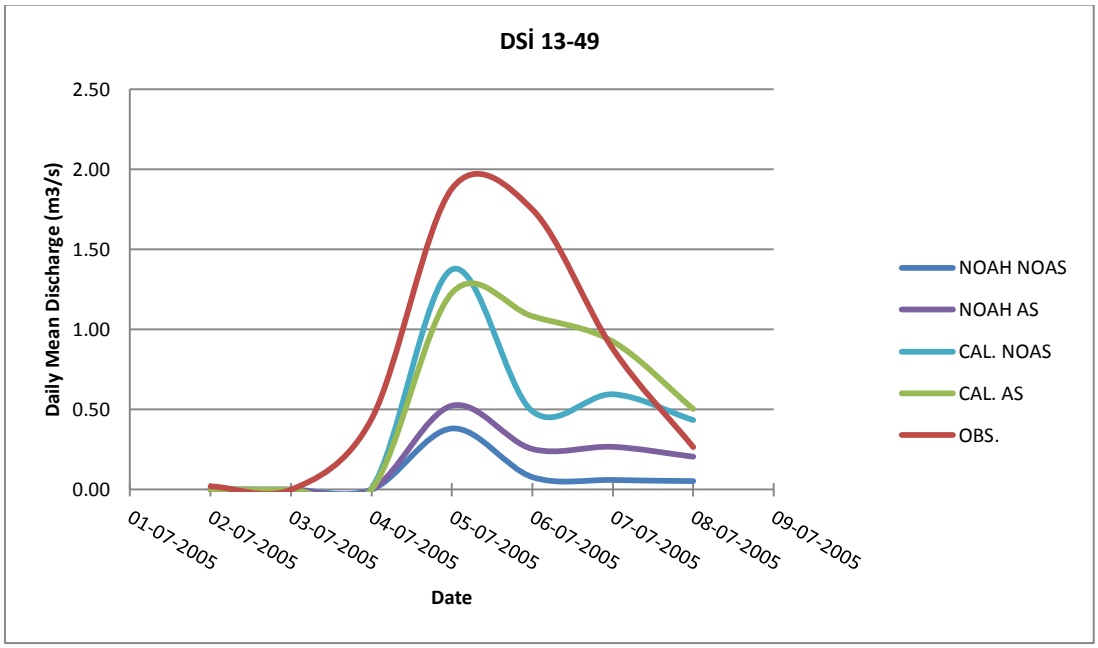

Figure 4.20: 8. Event DSİ 13-49 Comparative Hydrographs

Error and correlation statistics between simulated (with and without AS and CAL) and observed hydrographs at two DSİ gauging stations for events 6 and 8 are calculated and their values are shown in Table 4.2. Prior to calibration statistics results show that in most cases, NOAS has larger correlation coefficient but also larger rmse values than AS simulation. After calibration is applied, while correlation coefficients for AS are improved for both events and stations (except DSİ 13-39 for event 6 has shown nearly 0.1 decrease), NOAS shows correlation decrease for both stations in event 6, and increase for both stations in event 8. As rmse values show significant decrease for both events and stations with calibration, a higher mean reduction in AS (about 1 mm) is observed than NOAS (about 0.5 mm). In Table 4.3, error and correlation improvements are also given between pre-calibration and calibrated model outputs. As the results are investigated, up to nearly 74% improvement in error and 16% improvement in correlation per station are calculated. Also in this table, significance of assimilation improvement is remarkable with respect to no-assimilation. While correlation improvement shows inconsistency especially for Event 6, error improvement is present for stations by between 15% - 74%. For assimilation, average event 6 error improvement is calculated as 23.24% and for event 8, it is calculated as 52.57%. For no-assimilation, while statistics are worse than assimilation, calibration still shows positive increase in improvement (16.67% for Event 6, 40.72% for Event 8).

Table 4.2: Error and Correlation Statistics for Event 6 and 8

		RMSE (m^3/s)				Correlation Coefficient			
		AS	NOAS	CAL. AS	CAL.NOAS	AS	NOAS	CAL. AS	CAL. NOAS
EVENT 6	DSİ 13-39	7.5336	7.7675	5.8146	6.3417	0.9127	0.9443	0.8279	0.8972
	DSİ 13-49	3.3940	4.6735	2.5911	3.9728	0.7849	0.9616	0.8737	0.9063
	AVG.	*5.4638*	*6.2205*	4.2029	5.1572	0.8488	*0.9529*	0.8508	0.9018
EVENT 8	DSİ 13-39	2.2031	1.7717	0.5820	0.8231	0.8311	0.9677	0.9819	0.9944
	DSİ 13-49	1.2707	1.3816	0.8443	0.9962	0.8485	0.7658	0.9119	0.8182
	AVG.	*1.7369*	*1.5767*	0.7132	0.9096	0.8398	*0.8667*	0.9469	0.9063

Table 4.3: Error and Correlation Improvements for Event 6 and 8 Calibrations

		Improvement in RMSE (%)		Improvement in Cor. Coefficient (%)	
		AS	NOAS	AS	NOAS
EVENT 6	DSİ 13-39	22.82%	18.36%	-10.24%	-5.25%
	DSİ 13-49	23.65%	14.99%	10.16%	-6.10%
	AVG.	*23.24%*	16.67%	*-0.04%*	-5.67%
EVENT 8	DSİ 13-39	73.58%	53.54%	15.36%	2.68%
	DSİ 13-49	33.56%	27.89%	6.95%	6.40%
	AVG.	*53.57%*	40.72%	*11.16%*	4.54%

4.3.2 Evaluation of Calibration Using Independent Data in Bartın Basin

In this section, except events 6 and 8 through which model calibration is performed, simulated hydrographs for events 1, 4, 5, 7, 9, 14 and 17 with significant precipitation in Bartın basin are evaluated. Because these events are not used during calibration process, they provide an evaluation to test the performance of the calibrated parameters.

Figure 4.21 shows comparison of hydrographs from AS, NOAS and OBS at DSİ 13-14 for event 1. Having very close hydrographic trends of AS and NOAS to observations prior to calibration, the hydrograph trends after calibration shows a delay in peak times and increase in volume, since performed calibration forces increase on hydrograph volumes. Since there in no observation data for this station except first event, DSİ 13-14 observations are not available to for other events. As seen on daily spatial precipitation distribution in Figure 4.22, observation and both WRF precipitation show peak values on June 3, 2000 especially on Bartın basin. These precipitation peaks are reflected on hydrographs and, thus simulated hydrographs of AS and NOAS provide a good match with observed hydrograph.

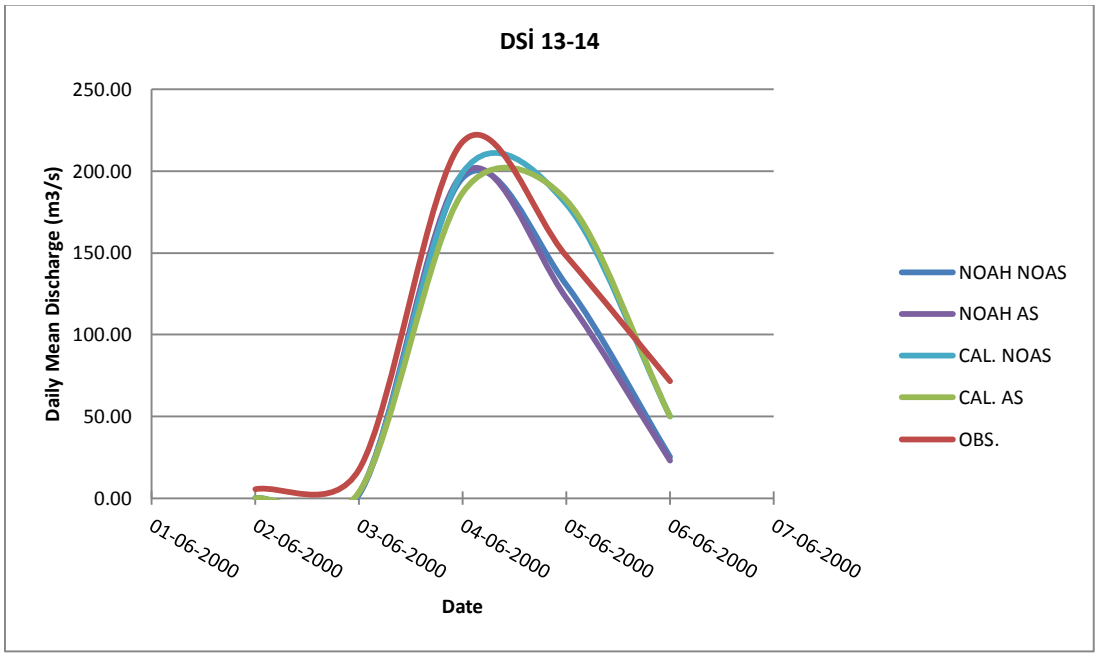

Figure 4.21: 1. Event DSİ 13-14 Comparative Hydrographs

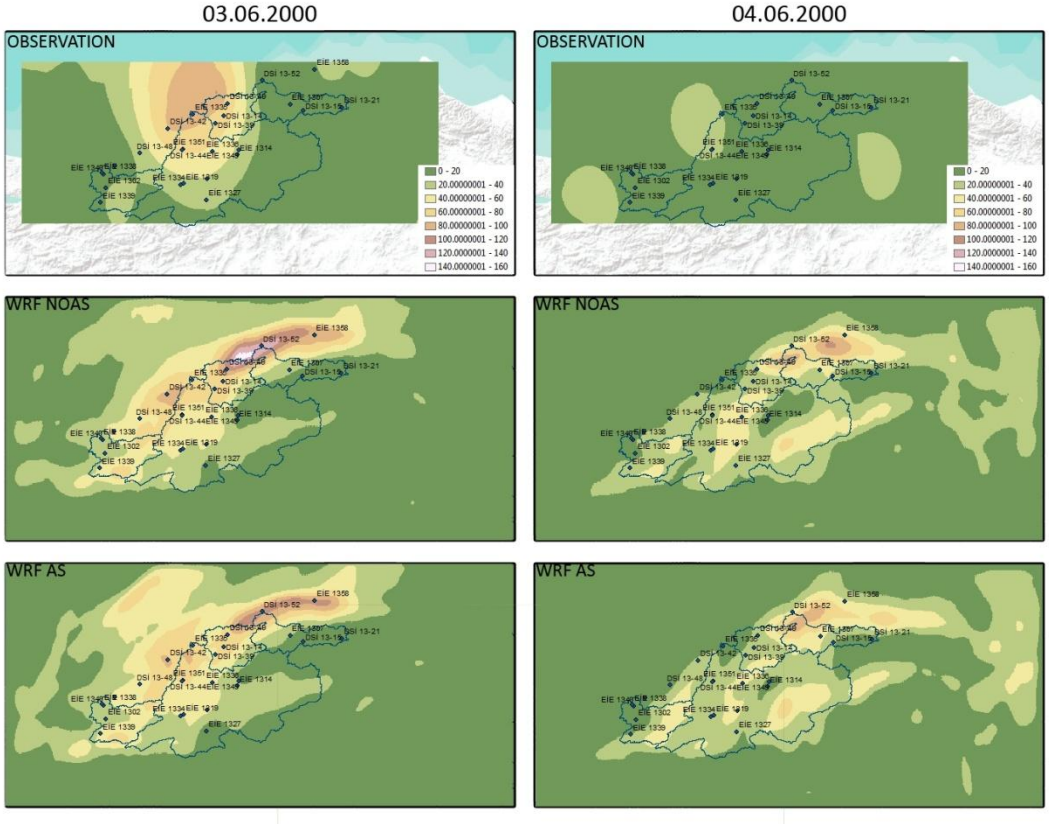

Figure 4.22: 1. Event Daily Rain Distribution for Peak Days

The similar hydrographs for stations DSİ 13-39 and DSİ 13-49 are shown for event 4 in Figures 4.23 and 4.24, respectively. On DSİ 13-39, while it is observed that calibration increases the hydrograph volume in a desired way, it is unable to relocate the peak time to match with observed hydrograph peak time in both CAL AS and CAL NOAS. On DSİ 13-49, though a minor volume increase is observed, calibration process manages to match peak time of CAL AS hydrograph with observed hydrograph.

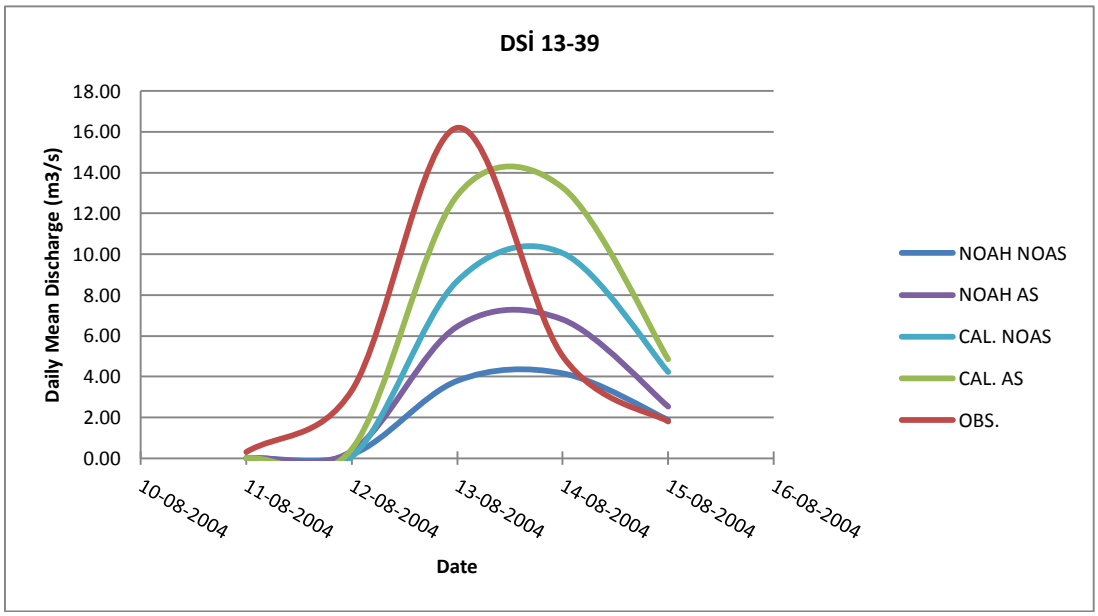

Figure 4.23: 4. Event DSİ 13-39 Comparative Hydrographs

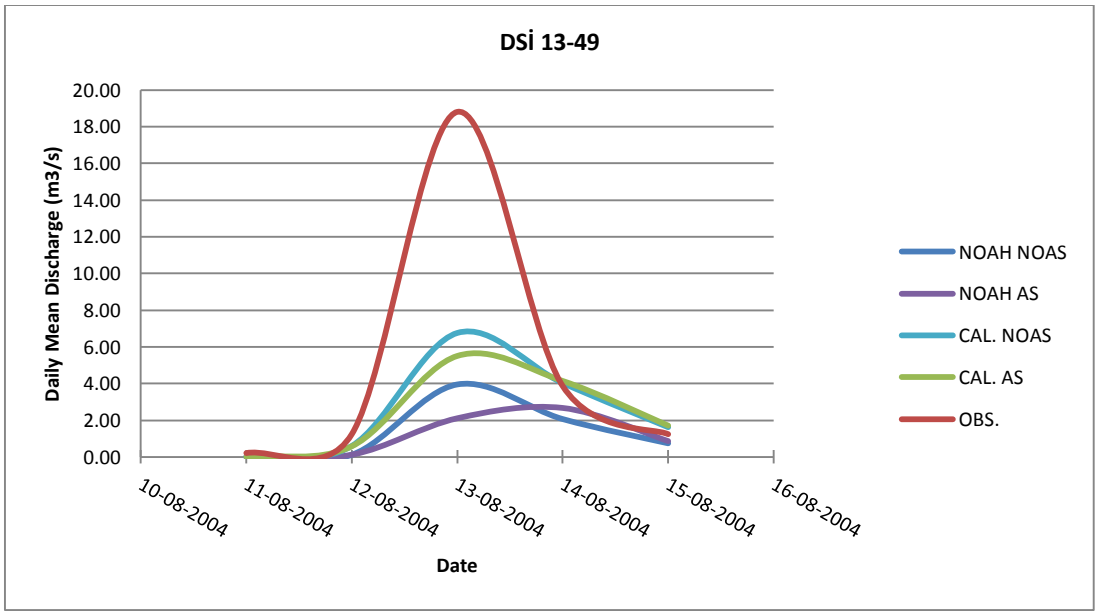

Figure 4.24: 4. Event DSİ 13-49 Comparative Hydrographs

For event 5, hydrographs for DSİ 13-39 and DSİ 13-49 are shown in Figure 4.25 and Figure 4.26, respectively. With a significant mismatch between hydrograph trends, volume increase is observed with calibration. As seen on DSİ 13-39 hydrographs, assimilation greatly reduces the overestimation tendency of WRF model in precipitation for this event. For example, with this feature NOAH AS hydrograph statistically provides much better results than NOAH NOAS hydrograph as it reduces the simulated hydrograph volume with respect to observed hydrograph. For DSİ 13-49, volume increase generated by calibration is also present with matching peaks. Precipitation reduction by assimilation in WRF model visible for both stations is also shown on daily spatial precipitation distribution for the event (Figure 4.27). While NOAS precipitation shows 140 mm/day for August 18, 2004, AS shows 60 mm/day for the same day in Bartin basin. Being close to, DSİ 13-39 station is located close to maximum precipitation region, so it reflects these high rain amounts in NOAS hydrograph.

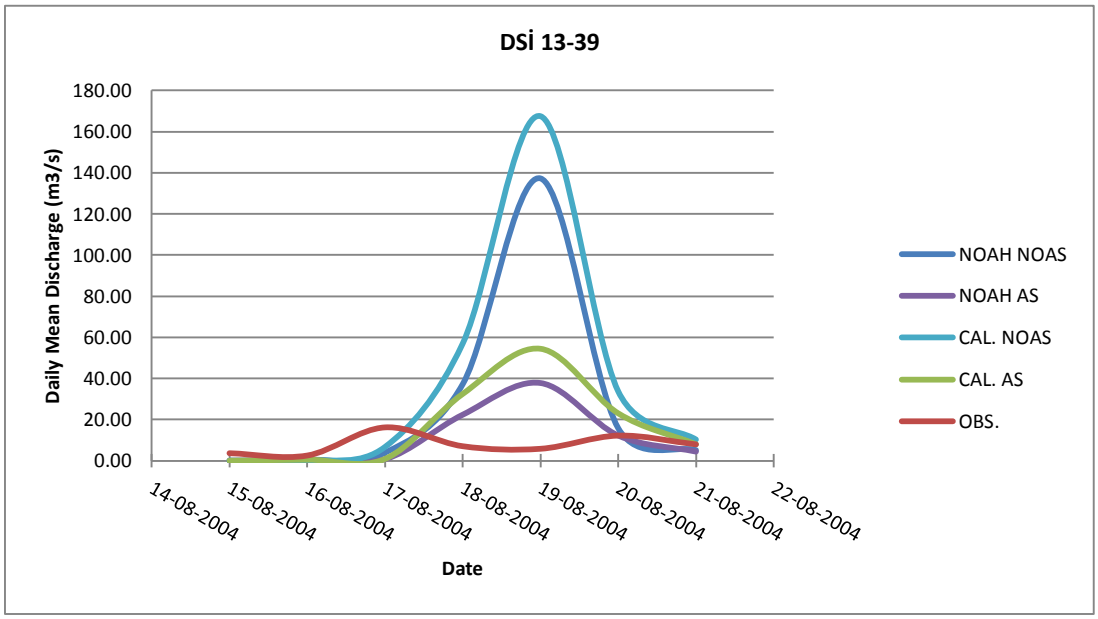

Figure 4.25: 5. Event DSİ 13-39 Comparative Hydrographs

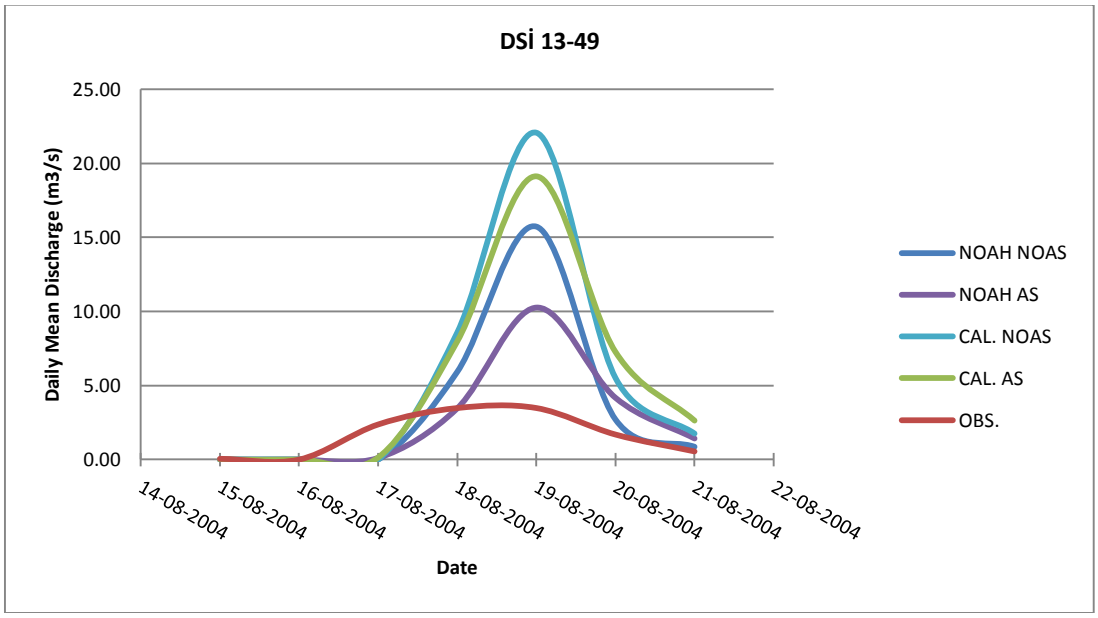

Figure 4.26: 5. Event DSİ 13-49 Comparative Hydrographs

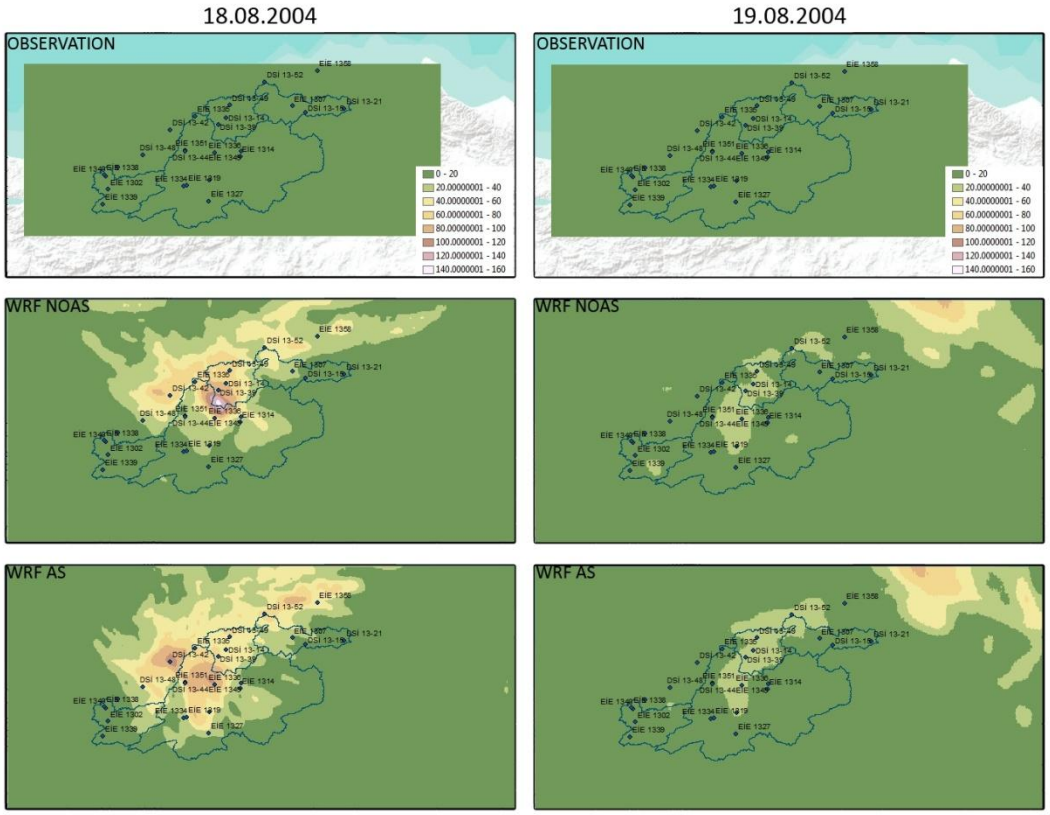

Figure 4.27: 5. Event Daily Rain Distribution for Peak Days

For event 7, simulated and observed hydrographs for DSİ 13-49 are shown in Figure 4.28 While pre-calibration hydrographs show irrelevant trends with respect to observation, after calibration, insufficient but visible low-volume peaks are generated with a temporal backward shift. This improvement with volume increase appears particularly for CAL NOAS hydrograph in this event. Daily spatial precipitation distribution for this event is shown in Figure 4.29 for rainfall peak days on 1-2 May 2005. On May 01, precipitation amount in Bartin basin and particularly around DSİ 13-49 station show that both WRF precipitation (AS and NOAS) is about 5-15 mm/day, while observed precipitation is around 20-25 mm/day. Generally for the event, it is commented that WRF precipitations are consistent with their simulated hydrographs.

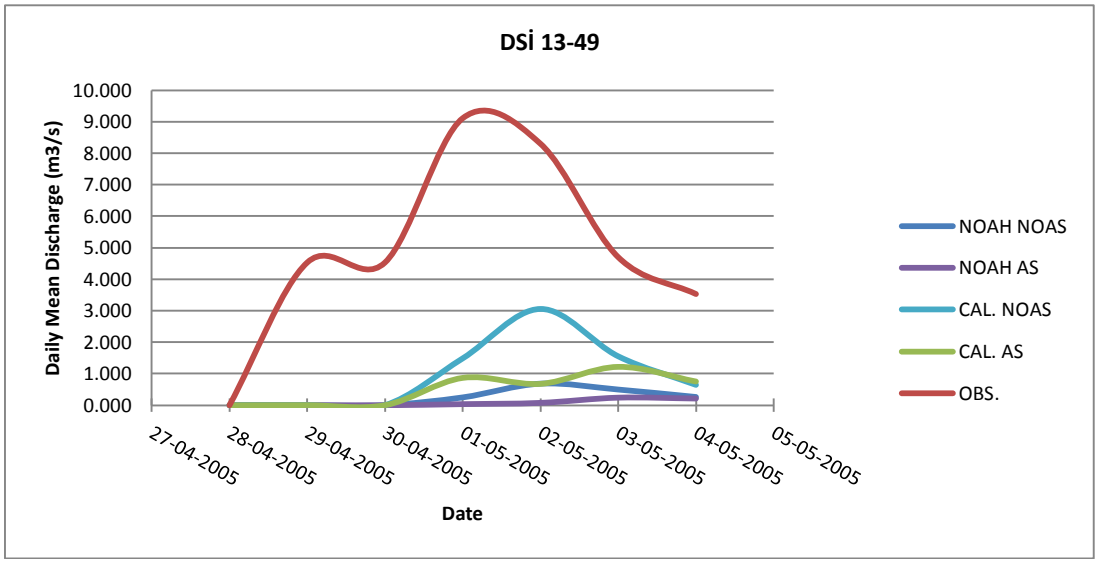

Figure 4.28: 7. Event DSİ 13-49 Comparative Hydrographs

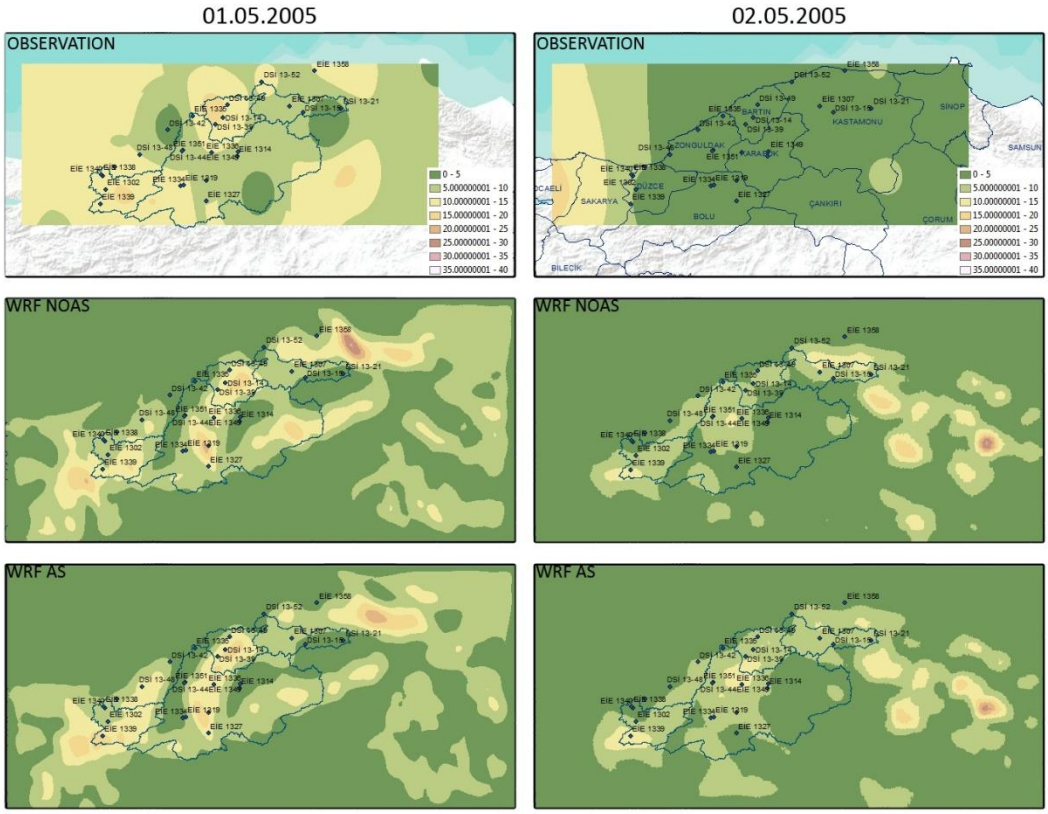

Figure 4.29: 7. Event Daily Rain Distributions for Peak Days

For event 9, DSİ 13-39 is selected and hydrographs comparison at this station is shown in Figure 4.30. As the chart is examined, it is observed that pre-calibration NOAS hydrograph (NOAH NOAS) shows under-estimation, while AS hydrograph (NOAH AS) show over-estimation with respect to observation. It is significant that with calibration both simulated hydrograph volumes are increased and this results in better match particularly with the timing and value of peak for CAL NOAS hydrograph. Additionally, CAL AS provides better temporal trend in hydrograph comparing to NOAH AS hydrograph.

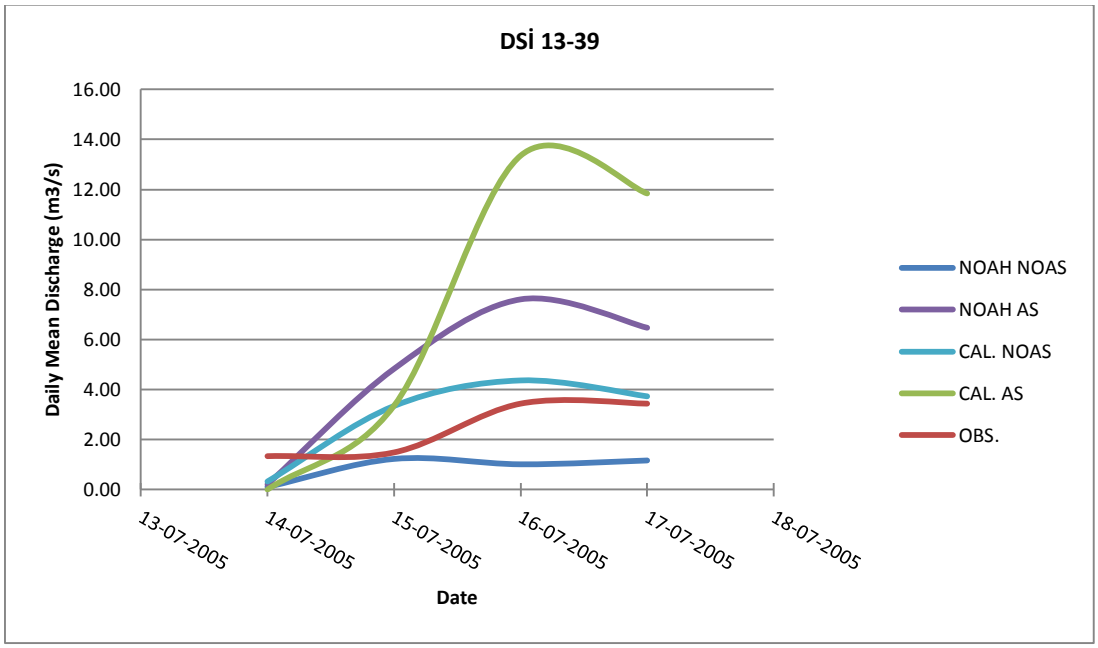

Figure 4.30: 9. Event DSİ 13-39 Comparative Hydrographs

For event 14, DSİ 13-49 is selected and hydrographs at this station are shown in Figure 4.31. Despite high observed hydrograph, NOAH-hydro outputs show under-estimation with significant discrepancy. Even though calibration increased model hydrograph volumes, still the improvement is insufficient to match the observation. With a forward shift, calibration adjusts the peak time for AS while NOAS peak remains unchanged. In this chart, MPE hydrograph is also shown and it produces almost no hydrograph because of its previously mentioned under-estimation trend. In Figure 4.32, daily spatial distribution of precipitation for peak days (14-15 July 2009) is shown. For two days from July 14 to 15, 2009, precipitation amount for the region around DSİ 13-49 is observed as 40-60 mm for AS; 60-100 mm for NOAS and 80-120 mm for observation, which are consistent with their corresponding hydrographs. Additionally, observed precipitation around the gauging station reached maximum rains so that the corresponding high peak discharge is formed at this station. Under-estimation trend of MPE can also be seen for rain peak days (July 14-15) with minor precipitation.

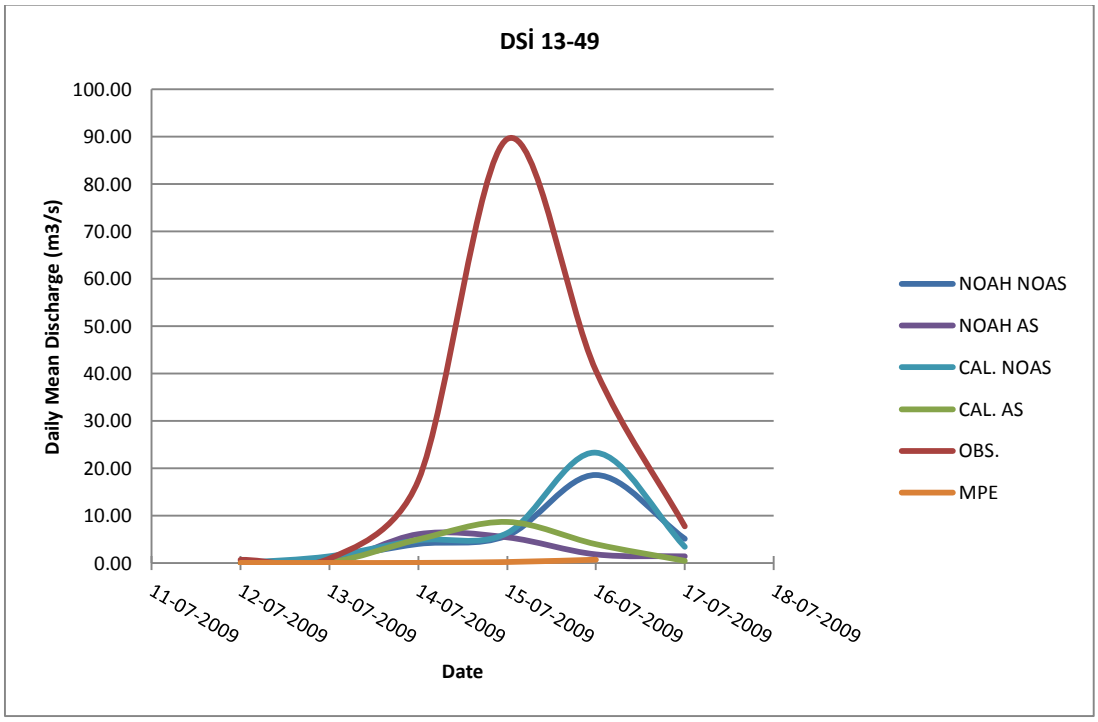

Figure 4.31: 14. Event DSİ 13-49 Comparative Hydrographs

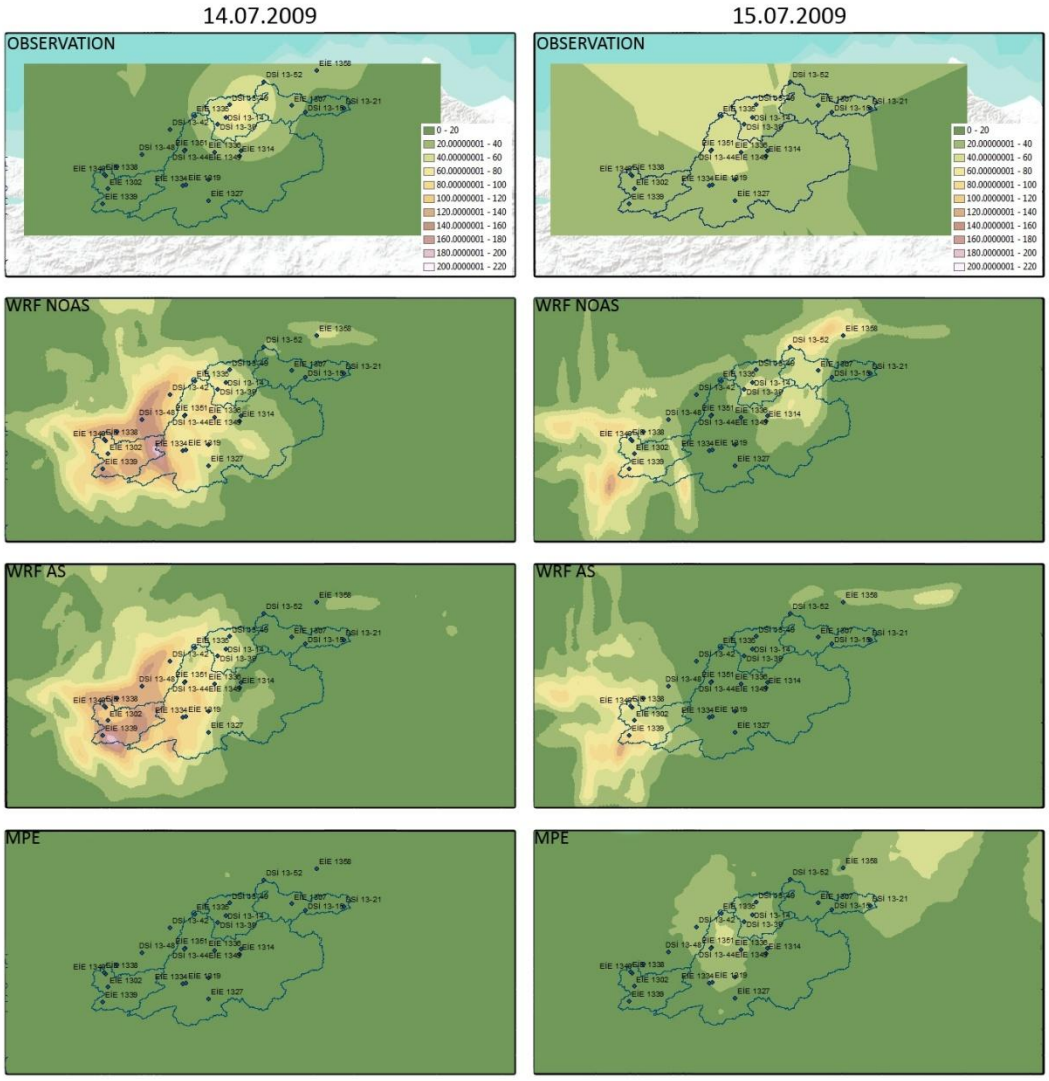

Figure 4.32: 14. Event Daily Rain Distributions for Peak Days

For event 17, DSİ 13-49 is selected and corresponding hydrographs are shown in Figure 4.33. For the station, while peak times are not adjusted with calibration to observation peak, the expected increase in hydrograph volume is observed. With significant discrepancy between AS and NOAS hydrographs, the effect of assimilation is witnessed by lowering the hydrograph volume and letting it closer to observation trend. Calibration causes deterioration in statistics with increasing already higher volumes seen with AS and NOAS hydrographs. In Figure 4.34, daily spatial distribution of precipitation for peak days on September 21-22, 2009 is shown. As spatial precipitation distributions from WRF AS and WRF NOAS on September 21 are compared, the decrease (about 25-30 mm/day) in AS rain is clearly visible around DSİ 13-49 station in Bartin basin. For this event, significant under-estimation of MPE is also evident while calibration shows minimal increase in MPE hydrograph volume.

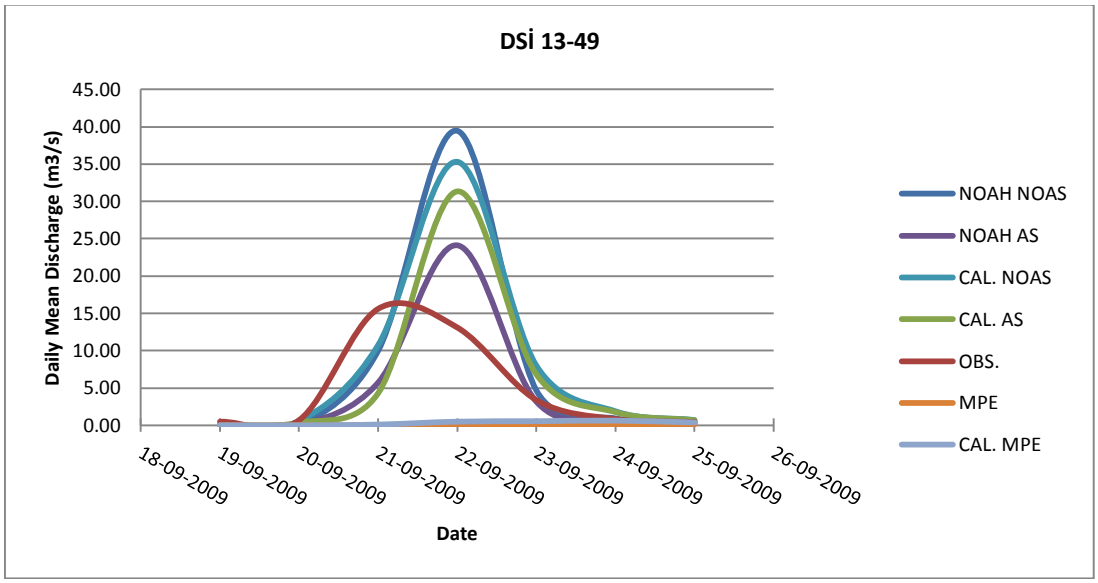

Figure 4.33: 17. Event DSİ 13-49 Comparative Hydrographs

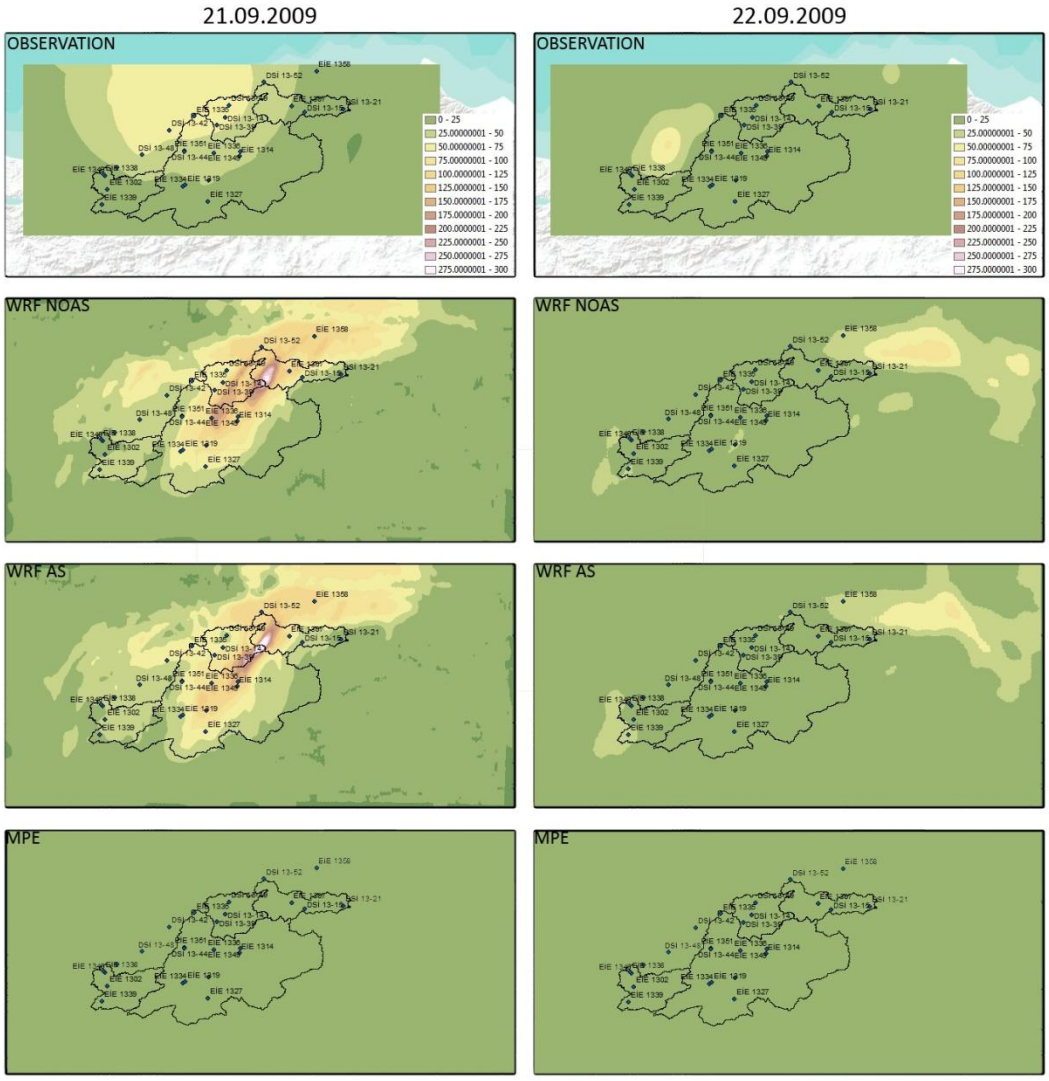

Figure 4.34: 17. Event Daily Rain Distributions for Peak Days

Error and correlation statistics between simulated (AS, NOAS, CAL AS, and CAL NOAS) and observed hydrographs at DSİ gauge stations for the number of events are calculated and shown on Table 4.4. For the selected stations, an overall increase in correlation coefficients is observed except few stations. Since the calibration process is constructed with assimilated precipitation (WRF AS), the mentioned increase is observed in AS more significantly. In some cases, calibration decreased the correlation for NOAS evaluations. For RMSE values, a general tendency to decrease is also observed. Except both AS and NOAS for events 1, 5 and AS for event 9, 17; all other events show decrease in rmse for stations used in this section. Finally, as average statistics for all data together are examined; despite the average rmse increase both in CAL AS and CAL NOAS; for correlation, calibration shows about 0.1 increases in for CAL AS, and about 0.04 increase for CAL NOAS.

Table 4.4: 8. Error and Correlation Statistics for Event 1,4,5,7,9,14 and 17

		RMSE (m^3/s)				Correlation Coefficient			
		AS	NOAS	CAL. AS	CAL.NOAS	AS	NOAS	CAL. AS	CAL. NOAS
EVENT 1	DSİ 13-14	*60.0440*	*59.4714*	80.7531	79.9635	*0.7093*	*0.7206*	0.6129	0.6379
EVENT 4	DSİ 13-39	*4.2721*	*5.2686*	4.0282	4.0605	*0.7138*	*0.6560*	0.7234	0.6399
	DSİ 13-49	*6.8665*	*6.1465*	5.5877	5.0896	*0.4539*	*0.8449*	0.7048	0.8095
EVENT 5	DSİ 13-39	*14.7604*	*51.2540*	21.9843	64.6218	*-0.1047*	*-0.1531*	-0.0652	-0.1153
	DSİ 13-49	*2.6647*	*4.5380*	6.1606	7.0924	*0.7002*	*0.7363*	0.7383	0.7396
EVENT 7	DSİ 13-49	*5.6687*	*5.4624*	5.2082	4.5962	*-0.0680*	*0.5684*	0.4619	0.7469
EVENT 9	DSİ 13-39	*2.6127*	*1.5937*	5.4048	1.1211	*0.8710*	*0.7025*	0.9675	0.8255
EVENT 14	DSİ 13-49	*37.8782*	*36.3755*	36.6981	35.1112	*0.8127*	*0.3018*	0.9195	0.4063
EVENT 17	DSİ 13-49	*5.6013*	*10.1996*	8.2217	8.7737	*0.7218*	*0.7360*	0.6324	0.7575
TOTAL AVG.		*15.5965*	*20.0344*	19.3385	23.3811	*0.5344*	*0.5682*	0.6328	0.6053

4.3.3 Evaluation of Calibration Using Independent Data in Other Basins

In this section, the parameters calibrated only for Bartın basin with assimilated rain (WRF AS) are applied to events showing significant hydrographs on 3 other basins (1. Filyos; 2. Devrenkani; 3. Düzce). The purpose of this evaluation is to test the reliability of calibrated parameters for different basin characteristics. On a general perspective, hydrographs in these basins show higher bias than previously mentioned hydrographs which can be explained as a side-effect of calibration being performed by only using Bartin basin. In this section, hydrographs from events 2, 3, 7, 8 and 10 are evaluated.

For event 2, the hydrographs at EİE 1340 station in Düzce basin are shown in Figure 4.35. As pre-calibrated AS and NOAS hydrographs match the peak time of observation, after calibration is applied, significant increase in volumes are observed with forward shifted peak times. Since simulation periods are limited to specific days shown on Table 2.1 (Event list), it is unavailable to witness calibrated hydrographs' exact peak times and recession limbs.

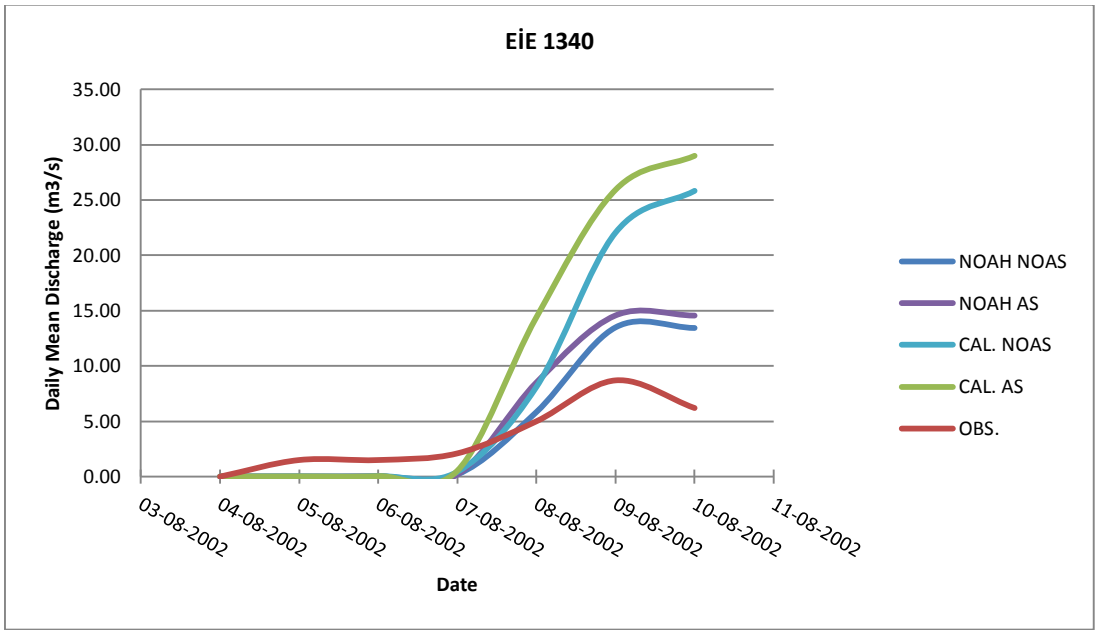

Figure 4.35: 2. Event EİE 1340 Comparative Hydrographs

For event 3, hydrograph comparisons at DSİ 13-52 station located at outlet of Devrekani basin are shown in Figure 4.36. As the figure is inspected, nearly no discharge showing with assimilated precipitation gains minor volume increase with calibration while non-assimilated precipitation shows a distinctive volume increase. Calibration is unable to match the peak time for NOAS but it provides good matching for peak times between AS and observation with a substantial underestimation in peak value. Also in Figure 4.37, daily spatial distributions of precipitation for peak days (August 21-22, 2002) are shown for the event. As stream observation and rain observation are compared for Devrekani basin, the consistency in between is observed. For low volume model hydrographs, the corresponding precipitation distributions also show this consistency. In this figure, on August 22, 2002, decreasing trend in precipitation with assimilation is obvious within model domain. Low AS precipitation results in low AS hydrographs for the station located on basin outlet. Also the 1-day delay between observation and NOAS hydrograph peaks is caused by WRF NOAS precipitation peaked on August 22, 2002 shown on daily spatial distributions.

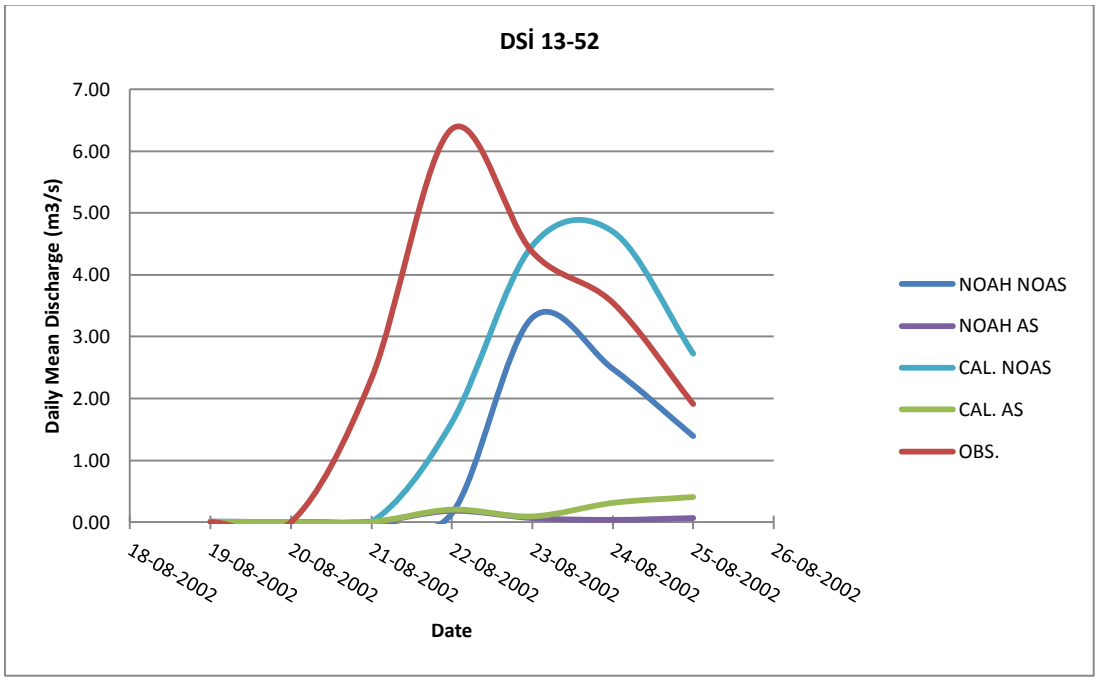

Figure 4.36: 3. Event DSİ 13-52 Comparative Hydrographs

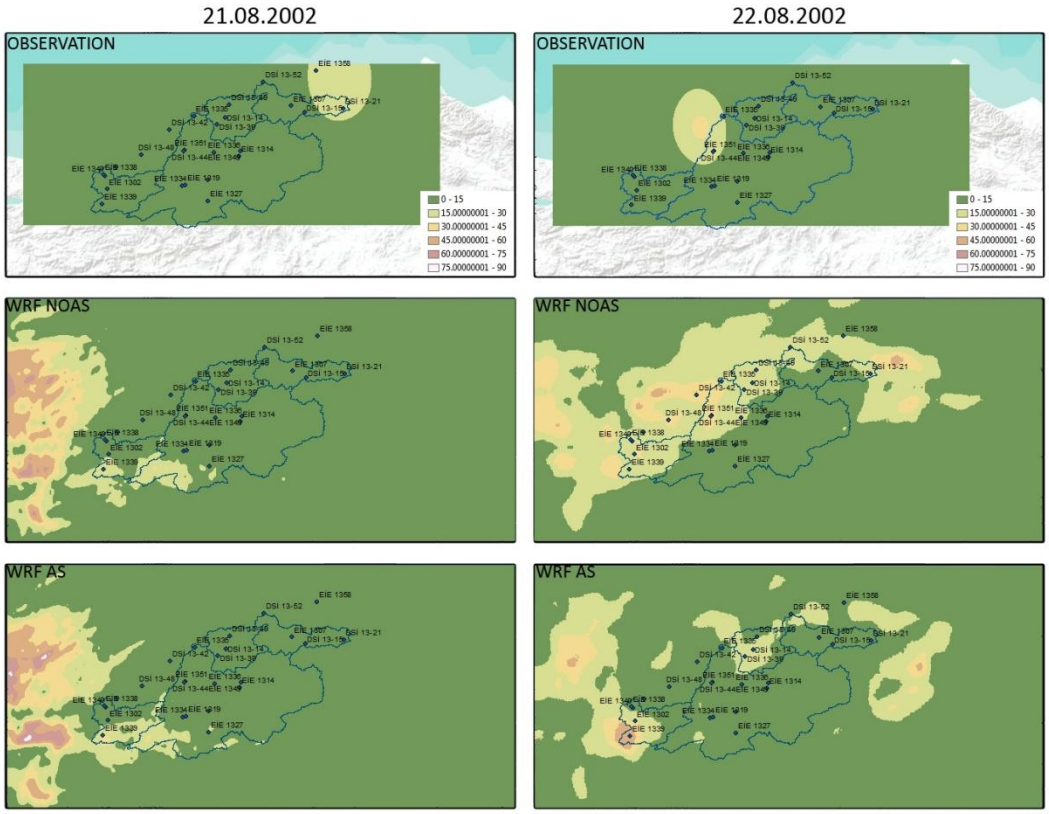

Figure 4.37: 3. Event Daily Rain Distributions for Peak Days

For event 7, hydrograph comparisons at EİE 1302 station in Düzce basin are shown in Figure 4.38. While pre-calibrated NOAH-hydro hydrographs show minor discharge, hydrograph volumes are increased significantly after using calibrated parameters. As the timing of the peaks does not match for the event, rising limb of CAL AS hydrograph shows significant resemblance with the rising limb trend of observed hydrograph. For the station, selected event period is also insufficient to complete simulated hydrograph shapes.

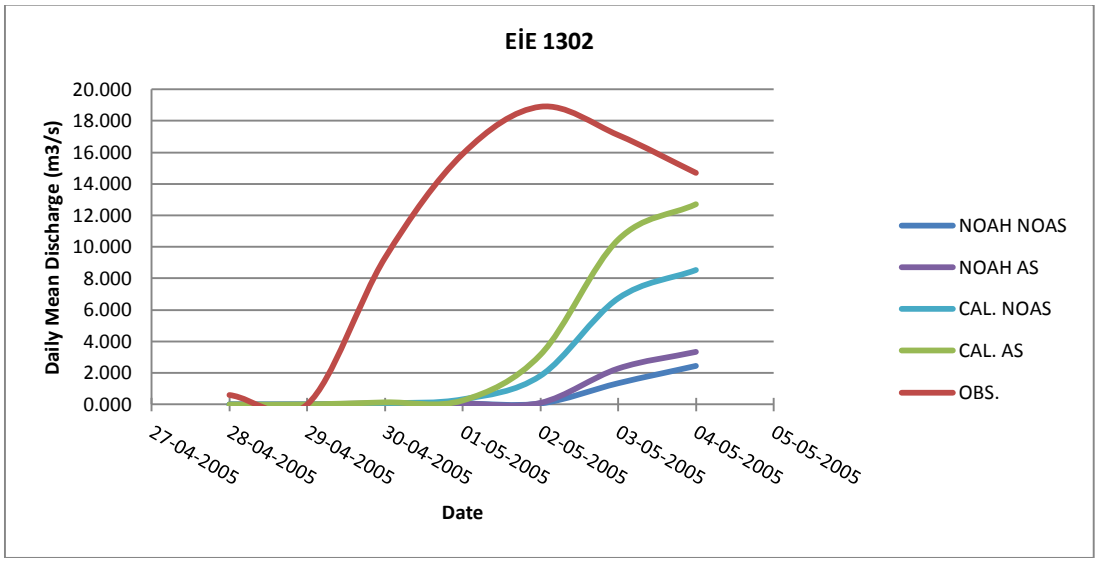

Figure 4.38: 7. Event EİE 1302 Comparative Hydrographs

For event 8, hydrograph comparisons at EİE 1302 located in Düzce Basin and at EİE 1334 located in Filyos Basin are shown in Figure 4.39 and 4.40 respectively. For EİE 1302, calibration adjusts peak times of simulated hydrographs to match the observation perfectly. With expected volume increase, calibration tends to fit simulated hydrographs of AS and NOAS at EİE 1302 successfully. However, for EİE 1334, calibration results in forward time shift away from observation peak with increased volume for AS. Moreover, NOAS hydrographs show unexpected trends both for pre-calibration and calibrated cases. Also in Figure 4.41, daily spatial distributions of precipitation are shown for the event peak days on July 4-5, 2007. While observation and WRF precipitations on July 04-05, 2007 on Düzce Basin (around EİE 1302) give peak values in hydrographs on the same day (July 06, 2007), intensity of precipitations during these two days are observed as 60-80 mm/day for observation; 60-70 m/day for NOAH AS and 40-60 mm/day for NOAH NOAS. The variation of these amounts is reflected on hydrograph magnitudes. In Filyos basin, trend on EİE 1334 with NOAH AS hydrograph shows a close resemblance to observation trend because at this station precipitation is adjusted by assimilation. Around this station, while WRF AS has shown an intensity of 30-40 mm/day, WRF NOAS has shown 10-20 mm/day.

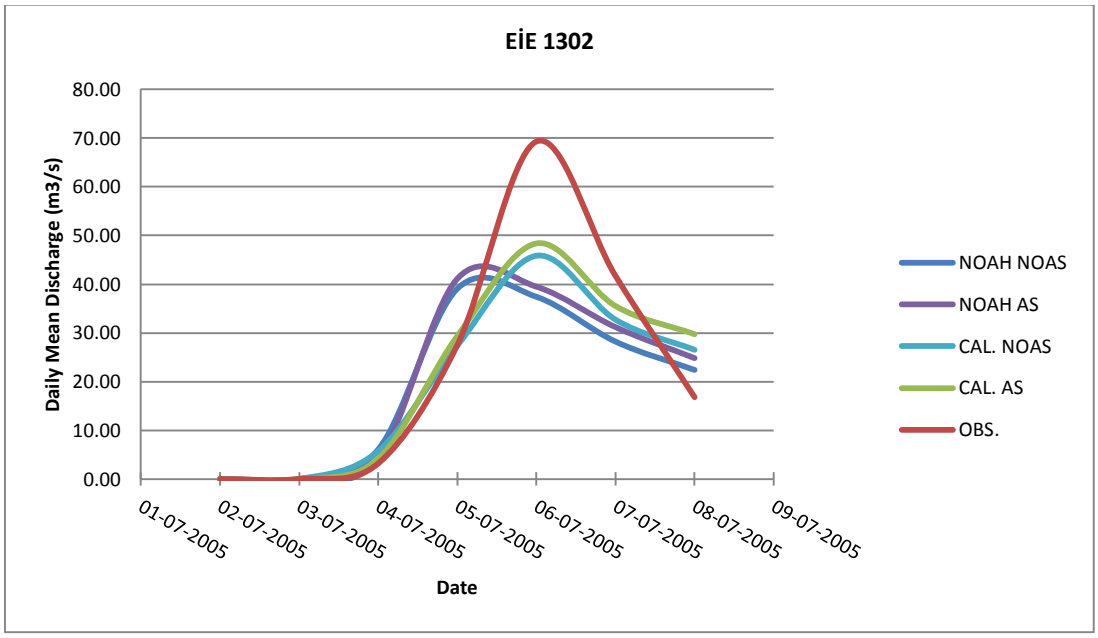

Figure 4.39: 8. Event EİE 1302 Comparative Hydrographs

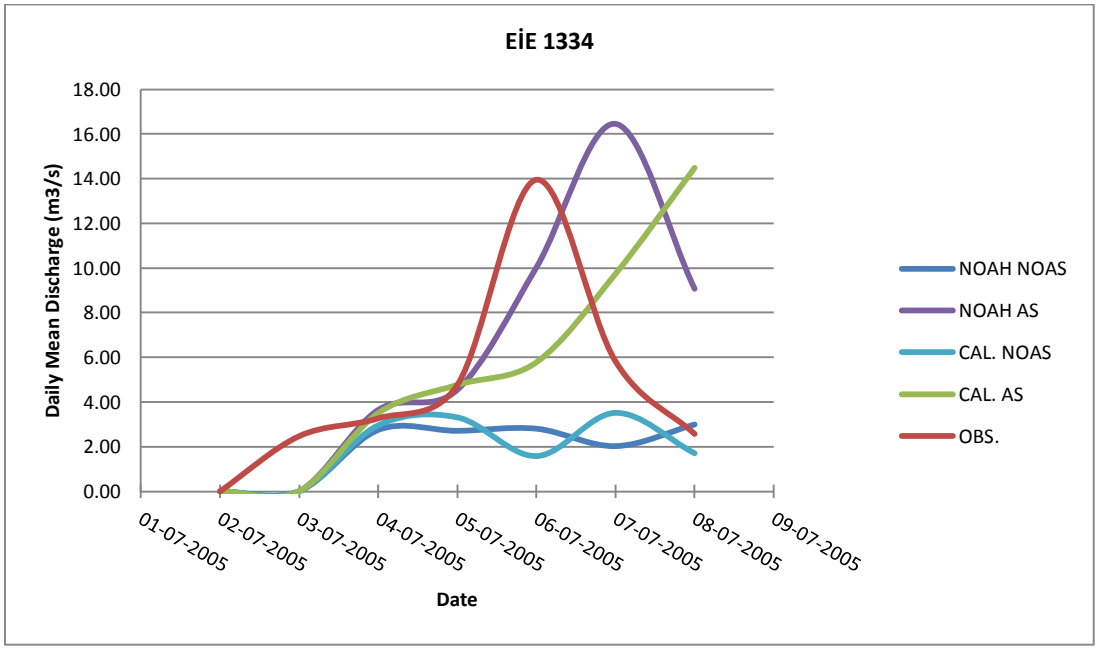

Figure 4.40: 8. Event EİE 1334 Comparative Hydrographs

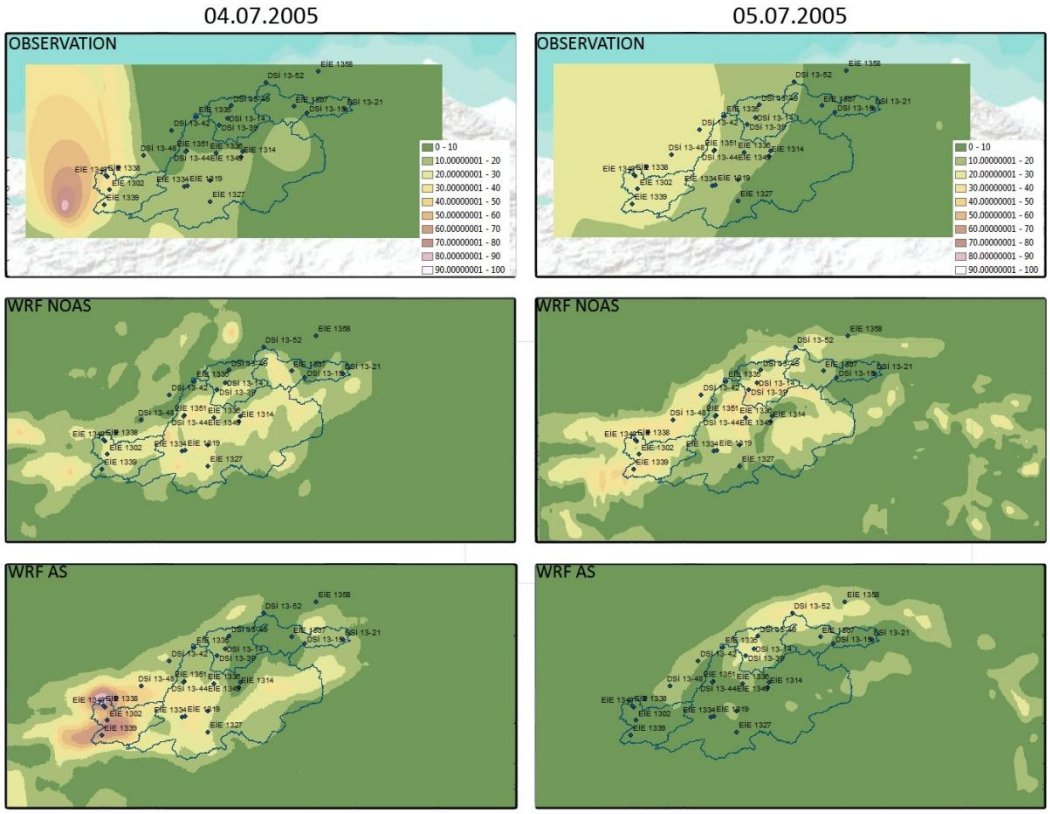

Figure 4.41: 8. Event Daily Rain Distributions for Peak Days

For event 10, hydrograph comparisons at EİE 1307 in Devrekani Basin, at EİE 1339 in Düzce Basin and at EİE 1351 in Filyos Basin are shown in Figures 4.42, 4.43 and 4.44, respectively. In addition to AS, NOAS, MPE and calibrated MPE (CAL MPE) are also included to hydrographs. For EİE 1307, it is observed that with the volume increase calibrated parameters improved the hydrographs of AS and NOAS. Calibration process is unable to adjust AS peak time to observation peak, while both NOAH NOAS and CAL NOAS peaks match with observed hydrograph temporally. Especially for this event, CAL NOAS shows a close trend resemblance to observed hydrograph. For MPE, despite a rare occasion of over-estimated volume, calibrated parameters force MPE peak time to match with observation, and adjust the hydrograph to enter recession phase. For EİE 1339, calibrated parameters generate irregular CAL AS and CAL NOAS trends with medium volume increase. For this station, calibrated MPE does not manage to match peak time and shows only volume increase. Nevertheless; calibrated AS hydrograph shows a closer resemblance to observation than NOAS and MPE. Finally, on EİE 1351, it is observed that pre-calibration NOAS hydrograph shows more resemblance than other hydrographs. While significant volume increase by calibration is observed for all evaluating hydrographs, CAL AS and CAL NOAS hydrographs are unable to show recession trend during simulation period.

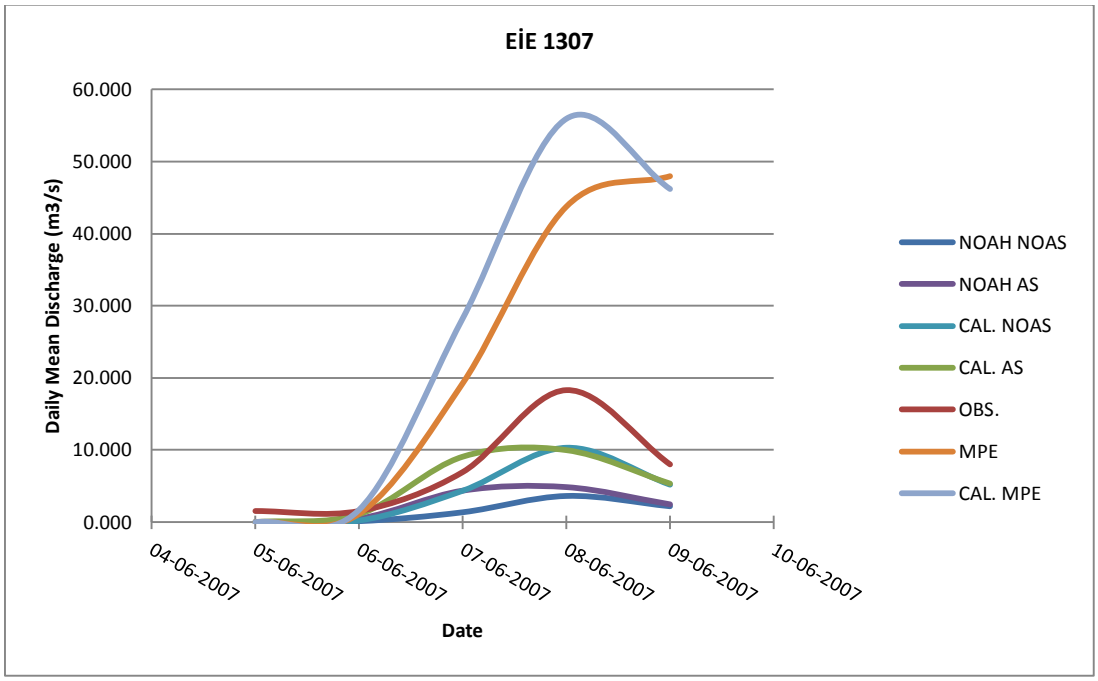

Figure 4.42: 10. Event EİE 1307 Comparative Hydrographs

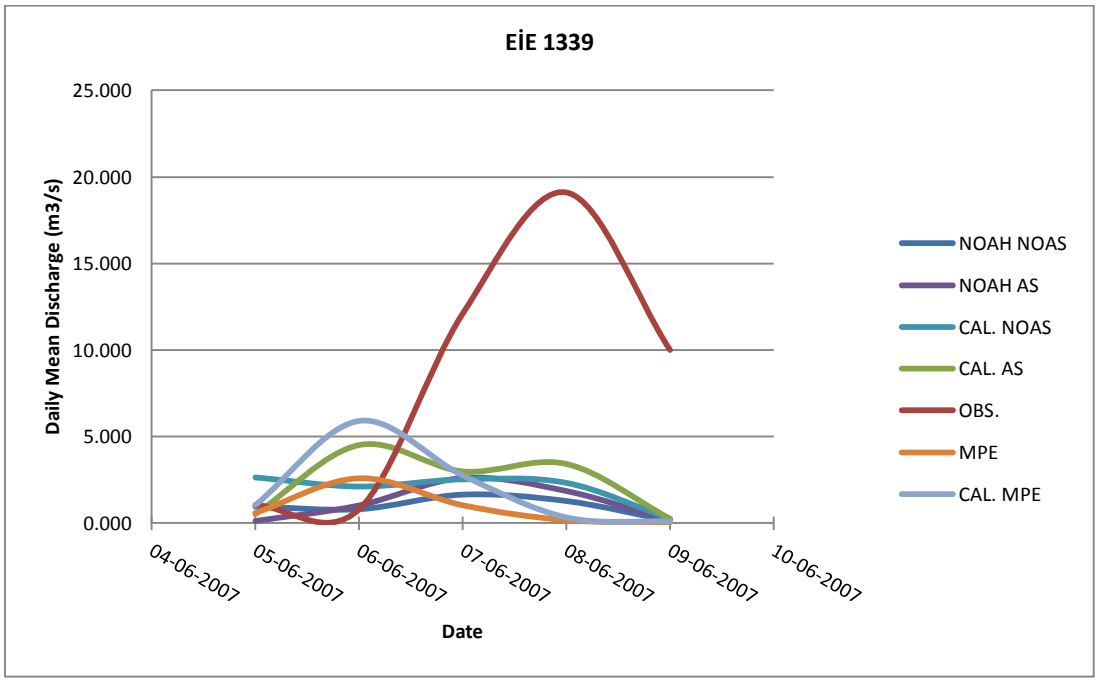

Figure 4.43: 10. Event EİE 1339 Comparative Hydrographs

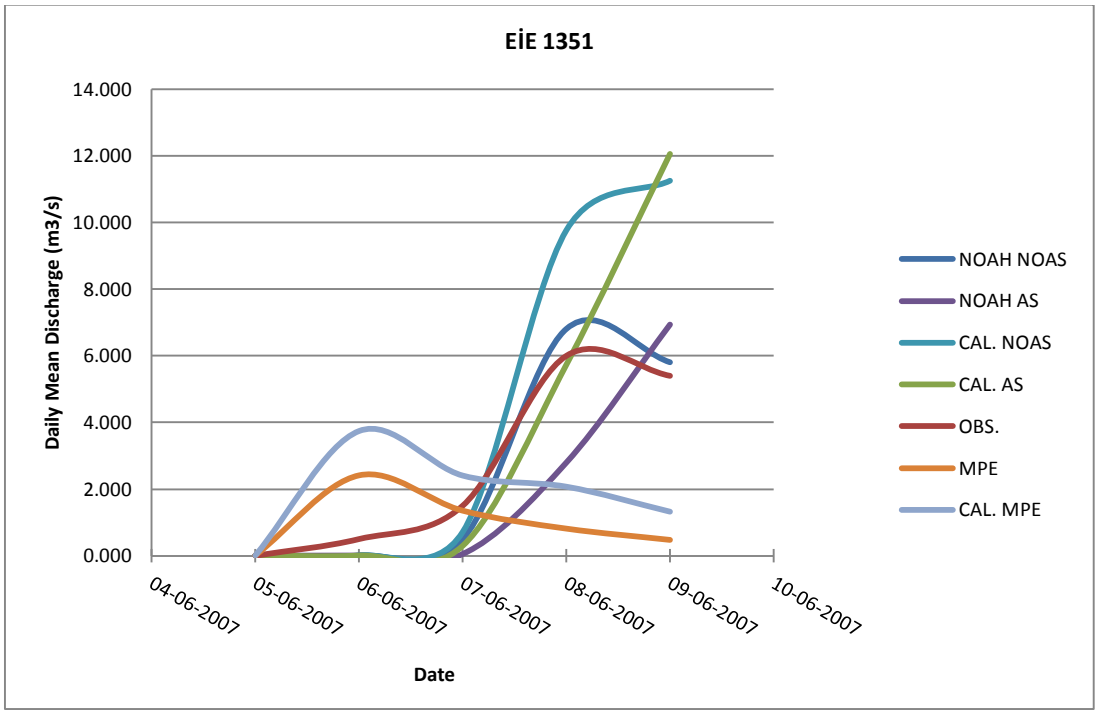

Figure 4.44: 10. Event EİE 1351 Comparative Hydrographs

CHAPTER 5

CONCLUSION AND RECOMMENDATIONS

In this study, a regional-scale hydro-meteorological model system, containing WRF atmospheric model, land surface and hydrologic model applications, is used for simulations of heavy-rainfall and major flooding events observed in the Western Black Sea region and the performance of model system is tested with data assimilation scheme and satellite data. Obtained from the WRF model, atmospheric inputs such as precipitation, temperature, humidity, wind speed and radiation are used in fully distributed, high grid resolution (250 m) NOAH-hydro hydrological model to create event-based flow hydrographs for the selected periods. In this research, 25 major hydrometeorological events selected between years 2000-2011 are used in the analysis as a large sample dataset and therefore a wide performance test is provided for model system.

Assimilated and non-assimilated WRF model outputs and satellite precipitation measurements are tested with observation by applying comprehensive statistical analyses. On mean areal time series of each event, especially assimilated WRF model is managed to match temporal observation trends and rain amounts up to significant levels. While temporal consistence shows variance for each event, in some events this consistency is observed much significantly. Except very few events, MPE generally shows under-estimation on rain amounts; it also manages to match the observation trends occasionally. As the under-estimation tendency of MPE is compared with WRF model, it is seen that MPE does not manage to match dense local rain gradients observed on WRF.

As the time resolution is decreased (from 1-hourly to 3, 6, 24 hourly intervals gradually), correlation is increased and scattering (divergence from 1:1 trend) is decreased. With assimilation, WRF precipitation gives less bias and error and higher correlation than other data sets, also best statistical results are obtained from 3-hourly analyses. While WRF gives significantly better statistical results than MPE, its under-estimation tendency is validated with negative biases calculated for most of the cases. As whole available data is considered, the improvement in AS is calculated as ~4%. For every threshold performance, WRF AS shows higher success scores than WRF NOAS, and MPE shows lesser success than both WRF rains. With MPE showing ETS Bias values lower than 1, lower estimation tendency of MPE algorithm with respect to WRF and observation is statistically validated. This condition is also observed significantly on higher threshold levels. However at the same levels, WRF generates more precipitation. For AS, the improvement in ETS on matching threshold levels is more significant than CSI scores for the same cases.

In event basis analyses, where spatial variations in precipitation are investigated, generally assimilated rainfall shows more error, bias reduction and correlation increase with respect to non-assimilated rainfall. Satellite rainfall generally shows dry-trend (negative bias). In most cases WRF AS gives better statistical results than WRF NOAS and MPE. Spatial variations in precipitation for each event can also be explained by different rain types and regimes. In station based analyses, a statistical evaluation is calculated by combining all events. In this evaluation, improvement in assimilation has also observed. Especially in 3-hourly evaluations, the amount of improvement is more significant. Assimilation resolves the temporal influence better than spatial influence for the events. In this research, as mainly summer events are investigated, rains are generated by convective systems and in this type

of rains, uncertainty in spatial influence occurs more than uncertainty in temporal influence. In station based analyses, while WRF error scores are observed lower than event based analysis scores, MPE error scores are observed higher in station based analyses. Temporal resolutions are established better than spatial resolutions by WRF. With topography and convective periods, uncertainties in spatial resolutions are more significant. While AS shows an improvement of 5.13% for 3-hourly evaluations, as direct WRF improvement percentages are investigated, the improvement ratio is calculated up to 11.39%. With similar studies, it is seen that assimilation forced improvement can be increased with more reliable observations. Moreover, with respect to bias and error calculations, correlation statistics are better with assimilation and thus, the change of trend in precipitation is resolved by assimilation with respect to precipitation amounts.

POD, FAR and CSI values are evaluated to investigate their tendencies with respect to events and stations. As a result of these evaluations, it is observed that WRF model shows more scattered, higher POD and lower FAR values than MPE. As evaluation time intervals are increased (from 1-hourly to 24-hourly), convergence to higher POD and lower FAR is observed for all datasets. In station based POD, FAR, CSI charts, same type centered accumulation trend for MPE and WRF is observed and this accumulation correctly matches the temporal gradients for both WRF and MPE precipitation. According to these results, it can be commented that spatial uncertainties are observed more than temporal uncertainties. In both event and station based charts, MPE values generally shows higher FAR and lower CSI trends while showing close POD values with respect to WRF.

Hydrologic model is calibrated by a 2-step calibration process based on hydrograph volume and hydrograph structure (peak value, time to peak) adjustments. With limited stream gauge observation data, calibration process is constructed for Bartın basin by best-fitting volume and trend controlling parameters and validity of these parameters are maintained for other sub-basins. To best-fit the calibration for more reliable and accurate results, more stream gauge observation data, hourly rather than daily, are needed. With this type of data, hydrograph of a flooding event can be calibrated more precisely by using shorter durations. In calibration, the fitting process is carried out by selecting relatively best statistics for corresponding stream gauge stations per event and done for each step manually. An automated optimization process should act more accurate for this complex model, however, because of technical restrictions, automated optimization process is inapplicable and forces the process to be done manually. Flood hydrographs reacts sensitively to WRF rain input and their consistencies show variance over events. If the rain input (both temporal and spatial) shows consistency, the generated hydrographs also show the related correlations with the stream gauge observations even when volume difference is present. In most cases, the improvements generated by AS rain is also reflected on hydrographs based on AS rains, and results in more compatible hydrographs with observations. For trial calibration events, calculated error and correlation improvements shows up to nearly 74% improvement in error and up to 16% correlation improvement for assimilation per station with mean error improvements by 23.34% for Event 6 and 53.57% for Event 8. While no-assimilation also shows improvements, it is lower than assimilation statistics. For the few MPE shown hydrographs, satellite performance again shows under-estimation on streams and with the lack of spatial resolution, MPE gives inconsistent results. With calibration, structural and volumetric fitting are especially significant on Bartın basin. Use of a fully distributed hydrological model enables basin-based calibration and this situation plays an important role on regions having complex topography.

With this research, applicability of a potential flood early warning system is shown. In this context, the use of WRF or another NWP model via data assimilation technique is important for providing more accurate precipitation distribution in space and time and using such products in a hydrological model is critical for flood forecasting. With a fully distributed hydrometeorological model, more reliable forecast of a flood event is possible with proper calibration processes for different regions with adequate observation inputs.

REFERENCES

Allen, M. R., and Ingram, W. J., (2002). Constraints on future changes in climate and the hydrologic cycle. *Nature, 419*, 224-232.

Amengual, A., Romero, R., Gómez, M., Martin, A. and Alonso, S., (2002). A hydrometeorological modeling study of a flash flood event over Catalonia, Spain, *J. Hydrometeor., 8*, 282–303.

Anderson, J. R., Hardy, E. E., Roach, J. T. and Witmer, R. E., (1976). *A land use and land cover classification system for use with remote sensor data*. Geological Survey Professional Paper 964, USGS, Reston, VA.

Barker, D. M., Huang, W., Guo. Y-R. and Bourgeois, Al, (2003). *A three-dimensional Variational (3DVAR) Data Assimilation System for use with MM5*. NCAR Technical Note, NCAR/TN-453+STR, pp68.

Brito-Castillo, L., Douglas, A. V., Layva-Contreras, A., and Lluch-Belda, D., (2003). The effect of large-scale circulation on precipitation and streamflow in the Gulf of California continental watershed. Int. *J. Climatology, 23*, 751-768.

Chen, F., and Dudhia, J., (2001). Coupling an advanced land surface-hydrology model with the Penn State-NCAR MM5 modeling system. Part I: Model implementation and sensitivity. Mon. *Wea. Rev., 129*, 569–585.

Choi, H., Ha J., Lee, D. and Kuo, Y., (2011). Analysis and Simulation of Mesoscale Convective Systems Accompanying Heavy Rainfall: The Goyang Case, *Asia-Pacific J. Atmos. Sci., 47(3),* 265-279.

Chokngamwong, R. and Chiu, L., (2008). Thailand Daily Rainfall and Comparison with TRMM Products. *Journal of Hydrometeorology 9:2*, 256-266.

Colle, B. A., Mass, C. F., and Westrick, K. W., (2000). MM5 precipitation verification over the Pacific Northwest during the 1997–1999 cool seasons. *Wea. Forecasting, 15*, 730–744.

Dudhia, J., (1989). Numerical study of convection observed during the winter monsoon experiment using a mesoscale two-dimensional model. *J. Atmos. Sci., 46,* 3077-3107.

Faccani, C., Ferretti, R. and Visconti, G., (2003). High-resolution weather forecasting over complex orography: Sensitivity to the assimilation of conventional data. *Mon. Wea. Rev., 131,* 136–154.

Held, I. M., and Soden, B. J., (2006). Robust responses of the hydrological cycle to global warming. *J. Climate, 19,* 5686-5699.

Heinemann, T., Lattenzio, A. and Roveda, F., (2002). *The Eumetsat Multi Sensor Precipitation Estimate (MPE),* Eumetsat.

Hong, S.-Y., and Pan, H.-L., (1996). Nonlocal boundary layer vertical diffusion in a medium-range forecast model. Mon. *Wea. Rev., 124,* 2322-2339.

Julien, P.Y., Saghafian, B. and Ogden, F. L., (1995). Raster-based hydrological modeling of spatially-variued surface runoff. *Water Resour. Bull., AWRA, 31(3*), 523-536.

Kain, J. S., and Fritsch, J. M., (1992). Convective parameterization for mesoscale models: The Kain-Fritsch scheme. The representation of cumulus Convection in Numerical Models, *Meteor. Monogr., No. 46, Amer. Meteor. Soc*., 165-170.

Kidd, C., Bauer, P., Turk, J., Huffman, G.J., Joyce, R., Hsu, K-L. Braithwaite, D., (2011). Inter-comparison of high-resolution precipitation products over northwest Europe, *Journal of Hydrometeorology Early Online Release*.

Lee, S., Lee D. and Chang, D., (2004). Impact of Horizontal Resolution and Cumulus Parameterization Scheme on the Simulation of Heavy Rainfall Events over the Korean Peninsula, *Advances in Atmospheric Sciences, Vol. 28, No. 1*, Page 1-15.

Lim, K-S.S and Hong, S-Y., (2010). Development of an Effective Double-Moment Cloud Microphysics Scheme with Prognostic Cloud Condensation Nuclei (CCN) for Weather and Climate Models, *Mon. ea. Rev., 138*, 1587–1612.

Liu, J., Bray, M. and Han, D., (2012). A study on weather radar data assimilation for numerical rainfall prediction, *Hydrol. Earth Syst. Sci. Discuss., 9*, 10323–10364.

Liu, Y., Zhang ,D.-L. and Yau, M. K., (1997). A multiscale numerical study of hurricane Andrew (1992). Part I: Explicit simulation and verification. *Mon. Wea. Rev., 125*, 3073–3093.

Nash, J. E. and Sutcliffe, J. V., (1970). River flow forecasting through conceptual models part I — A discussion of principles, *Journal of Hydrology, 10 (3),* 282–290.

Neelin, J. D., Munnich, M., Su, H., Meyerson, J. E., and Holloway, C. E., (2006). *Tropical drying trends in global warming models and observations*. PNAS, 103, doi: 10.1073/pnas.0601798103.

Parrish, D. F., and Derber, J. C., (1992). The National Meteorological Center's Spectral Statistical Interpolation analysis system*. Mon. Wea. Rev., 120,* 1747-1763.

Roebber, P. J., Schultz, D. M., Colle, B. A. and Stensrud, D. J., (2004). Toward improved prediction: High-resolution and ensemble modeling system in operations. *Wea. Forecasting, 19*, 936–949.

Skamarock, W. C., Klemp, J. B., Dudhia, J., Gill, D. O., Barker, D. M., Wang, W., and Powers, J. G., (2005). *A description of the Advanced Research WRF Version 2*. Tech. rep., NCAR.

Gochis, D. J., and Chen, F., (2003). *Hydrological enhancements to the community NOAH land surface model. NCAR Technical Note,* NCAR/TN-454+STR, 68 pgs.

Gochis, D. J., Leal, J. C., Shuttleworth, W. J., Watts C., and Garatuza-Payan J., (2003). Preliminary Diagnostics from a New Event-Based Precipitation Monitoring System in Support of NAME, *J. Hydrometeor., 4*, 974-981.

Gochis, D. J., Brito-Castillo, L. and Shuttleworth, W. J., (2006). Hydroclimatology of the North American Monsoon region in northwest Mexico., *J.Hydrology 316*, 53-70.

Gochis, D. J., Yu W., and Yates, D. N., (2012). *The NCAR Distributed Hydrological Modeling 818 System (NDHMS): User's Guide and Technical Description*. NCAR Science and Technical 819 Note: Under Review. Tech. rep., NCAR.

Rummler, T., Kuntsmann, H. and Gochis, D. J., (2012). Towards fully coupled regional atmospheric-hydrologic simulations: Performance of a hydrologically-enhanced regional atmospheric model in complex terrain. *Journal of Hydrometeorology Manuscript Draft.*

Ogden, F. L., (1997). *CASC2D Reference Manual*. Storrs, CT, University of Connecticut.

Trenberth, K. E., (1998). Atmospheric moisture residence times and cycling: Implications for rainfall rates and climate change. *Climatic Change, 39*, 667-694.

Trenberth, K. E., (1999). Conceptual framework for changes of extremes of the hydrological cycle with climate change. *Climatic Change, 42*, 327-339.

Trenberth, K. E. and Jones, P. D., (2007). *Observations: Surface and Atmospheric Climate Change. In: Climate Change 2007*. Cambridge University Press. Cambridge, U.K. and New York, NY, USA, 235-336.

Wigmosta, M. and Lettenmaier, D. P., (1999). A comparison of simpli_ed methods for routing topographically driven subsurface ow*. Water Resour. Res., 35 (1),* 255-264.

Wigmosta, M., L. W. Vail, and Lettenmaier, D. P., (1994). A distributed hydrology-vegetation model for complex terrain. *Water Resour. Res., 30 (6),* 1665-1679.

Xiao, Q., Kuo, Y.-H., Sun, J., Lee, W.-C., Lim, E., Guo, Y.-R. and Barker, D.M. (2005), Assimilation of Doppler radar observations with a regional 3D-VAR system: Impact of Doppler velocities on forecast of heavy rainfall case*, J. Appl. Meteor., 44,* pp. 768-788.

Yucel I., Shuttleworth W. J., Pinker R. T, Lu L., and Sorooshian S., (2002). Impact of ingesting satellite-derived cloud cover into the Regional Atmospheric Modeling System. *Mon. Wea. Rev., 130*, 610–628.

Yucel I., Shuttleworth W. J., Gao X., and Sorooshian S., (2003). Short-term performance of MM5 with cloud-cover assimilation from satellite observations. *Mon. Wea. Rev., 131*, 1797–1810.